Exploring Charge-Transfer Properties of Donor-Acceptor Functionalized Squaraine Dyes

By:

Austin Stanley

A Thesis Submitted in Partial Fulfillment of the Requirements for the Degree of

MASTER OF SCIENCE

in the Department of Chemistry

Supervisory Committee

Exploring Charge-Transfer Properties of Donor-Acceptor Functionalized Squaraine Dyes

By:

Austin Stanley

Supervisory Committee

Dr. Erin Chernick, Supervisor

Department of Chemistry

Dr. David Leitch, Supervisor

Department of Chemistry

Dr. Violeta Iosub, Member

Department of Chemistry

Dr. Robin Hicks, Member

Department of Chemistry

Abstract

In the realm of optoelectronics and solar technology, the demand for efficient and cost-effective materials has intensified. Squaraine dyes have emerged as a promising class of compounds for these applications, owing to their ability to absorb light and facilitate charge transport across different layers within materials. This thesis aims to present the synthesis and characterization of a novel donor-acceptor (DA) functionalized squaraine dye, featuring redox-active phenols that can be oxidized to phenoxyl radicals. Our objective is to investigate the charge-transfer (CT) properties of these compounds using spectroscopic techniques and computational modeling.

Chapter 1 provides an introduction to organic DA compounds, the probing of intramolecular charge-transfer (ICT) in such systems, and a background on stable free radicals and squaraine dyes. The chapter sets the context for the application of these molecules in materials and outlines the goals of the thesis.

Chapter 2 focuses on the synthetic methodology and nuclear magnetic resonance (NMR) spectroscopic characterization of a series of previously unreported DA compounds and squaraine dyes. The synthesis of compounds **2.14** and **2.15** is described using Suzuki-Miyaura chemistry, followed by the coupling of **2.14** to a known squaraine dye via Suzuki-Miyaura cross-coupling to form **2.25**. The synthesis and NMR characterization of these compounds are presented, along with the proposal of a structural motif (**2.31**) and the discussion of attempts to synthesize it. Preliminary data supporting oxidative addition to form **2.30** are also provided.

Chapter 3 focuses on the photophysical and redox properties of compounds **2.14, 2.15**, and **2.25**. UV-Visible and fluorescence spectrophotometry techniques are employed to demonstrate the CT characteristics of each compound. Cyclic voltammetry is used to investigate the oxidation

potentials of the phenols in **2.14** and **2.25**, while the attempt to isolate stable free radicals is discussed. Computational data using density functional theory (DFT) and time-dependent DFT (TD-DFT) are used to support the experimental findings, including the plotting of frontier molecular orbitals (FMOs) and natural transition orbitals (NTOs).

Chapter 4 provides a comprehensive summary of the results presented in this thesis and suggests future experiments for further investigation. Additionally, preliminary computational results for compound **2.31** are briefly discussed. In conclusion, this thesis explores the CT properties of novel compounds, particularly focusing on the influence of donor character on the photophysical properties. This research contributes to the understanding and potential applications of DA functionalized squaraines in optoelectronics and solar technology.

Contents

List of Figures

List of Schemes

List of Tables

List of Abbreviations

K	degrees Kelvin
ACN	Acetonitrile
B3LYP	Becke, 3-paramater, Lee-Yang-Parr functional
BHJ	Bulk heteojunction
BTD	benzothiadiazole
cataCXium A	Di(1-adamantyl)-*n*-butylphosphine
cm	centimeters
COSY	correlated spectroscopy
CT	charge transfer
CV	cyclic voltammetry
DA	Donor-acceptor
DBU	1,8-Diazabicyclo[5.4.0]undec-7-ene
DCM	dichloromethane
def2-SVP	Split valence basis set
def2-TZVP	Triple zeta split valence basis set
DFT	Density functional theory
DMABN	Dimethylaminobenzonitrile
EA(A)	Electron affinity of acceptor
EDA	Electron donor-acceptor
E_{LE}	Local excitation energy
E_{ox}	Oxidation potential
$E_{ox/red}$	Reversible oxidation potential
EPR	electron paramagnetic resonance
ESI	electrospray ionization
E_{TICT}	TICT energy
EtOAc	Ethyl acetate
EtOH	Ethanol
eV	electron volts
FMO	Frontier molecular orbital

FQY	Fluorescence quantum yield
g	grams
GHz	Gigahertz
HMBC	heteronuclear multiple bond correlation
HOMO	highest occupied molecular orbital
HRMS	high resolution mass spectroscopy
HSQC	heteronuclear single quantum coherence
HTS	High throughput screening
ICT	intramolecular charge transfer
IP(D)	Ionization potential of donor
IP(FC)	potential of internal standard, ferrocene
ISC	Intersystem crossing
LE	locally excited state
λ_{max}	Wavelength of maximum absorption
LUMO	lowest unoccupied molecular orbital
M	molar
mA	Miliamps
MePhos	Dicyclohexylphosphino-2′-methylbiphenyl
mg	milligrams
mL	millileters
mM	millimolar
mmol	millimoles
mol	moles
mol%	Percent molar equivalent
NaHMDS	Sodium bis(trimethylsilyl)amide
NIR	Near infrared
nm	nanometers
NOE	nuclear overhauser effect
NOESY	nuclear overhauser effect spectroscopy
NTO	Natural transition orbital
OLED	organic light emmiting diodde

OSC	organic semi-conductor
OSC	Organic solar cell
PCE	power conversion efficency
PICT	Planar intramolecular charge transfer
PivOH	pivalic acid
R_f	retention factor
RICT	Rehybridized intramolecular charge transfer
RISC	reverse intersystem crossing
s	seconds
S_0	Singlet ground state
S_1	First singlet excited state
SCE	Saturated calomel electrode
SFR	stable free radical
SMC	Suzuki-Miyaura cross-coupling
S_N2	Bimolecular nucleophilic substitution
SOC	spin orbit coupling
SOMO	singulary occupied molecular orbital
T_1	First triplet excited state
TADF	thermally activated delayed flouresence
TDDFT	Time-dependent density functional theory
TICT	twisted intramolecular charge transfer
TLC	Thin-layer chromatography
TSCT	Through-space charge-transfer
UV	ultra violet
V	Volts
Vis	visible
WICT	Wagging intramolecular charge transfer
ΔE_{ST}	singlet-triplet energy gap

Acknowledgements

I would like to start by acknowledging my late supervisor Dr. Erin Chernick. Erin provided me with an amazing opportunity to conduct research under her supervision, and she always reminded me that it was okay to set boundaries as a student, and to take care of myself first. These lessons have been very valuable to me during my time as a graduate student, and I am lucky to have gotten to experience that support.

I would also like to sincerely thank Dr. David Leitch for taking us in after Erin passed away. Dave has been nothing short of selfless in his efforts to incorporate us into his group, and work towards understanding the research we do despite it not being his field of expertise. Thanks for laughing at all my stupid jokes during our group meetings. I still haven't received that Christmas bonus, but I'm sure it's just something on the back end. I'd also like to thank the remainder of the Leitch group for helping in any ways they could.

I'd like to extend a thank you to my committee members Dr. Violeta Iosub and Dr. Robin Hicks. Thank you for both of your unwavering support over the last 5 years here at UVic. You two have served as fantastic mentors. I'd also like to acknowledge Chris Barr for NMR assistance, and Dr. Tyler Trefz for conducting HRMS experiments.

Next, I'd like to thank the friends I've made here. Bennett, thanks for the frequent uplifting and support, laughs, oil changes, dinners, and overall friendship you have provided me. Nahia, thank you for insisting on helping me with high throughput experiments, and for helping me land that 231 position. Thank you to Chris Tremblay for all the help with CV, and the rest of the Buckley group for frequent office breaks. Thank you to Mitch Nascimento for help with growing crystals, and Etienne LaPierre for his help in navigating EPR as well as revising this thesis. I'd also like to thank the rest of the Manners group of which there are too many to name.

Thank you to my mom, dad, aunt, and sisters. Even though none of you understand what I do, I appreciate you pretending. And to the homies; Fiona, Hannah, Ash, Gaelin, Lew, Jonah, Doro, Colin, and the rest of you who have been by my side this whole time. You have all provided me so many outlets and reminded me there is far more to life than school.

Finally, thank you to my girlfriend who has listened to me complain endlessly, and who is picking up sushi for me at this very moment. Love you boney!

Chapter 1 Introduction

1.1 Organic Donor-Acceptor (DA) Systems

Organic donor-acceptor containing molecules are an important class of compounds for a variety of applications across organic and materials chemistry. They are used as synthetic intermediates in organic synthesis,[1] as building blocks for organic materials such as polymers,[2–4] and as catalysts[5,6] and sensors in analytical chemistry.[7,8] In addition, organic donor-acceptor containing molecules can be used in the development of drug delivery systems, such as nanoparticles[9,10] and liposomes.[11,12] These molecules can be used to modify the properties of the drug delivery system, such as its stability and its release profile.

Organic donor-acceptor containing molecules are composed of two components: an electron donor group and an electron acceptor group. The donor group is typically an electron-rich moiety such as a phenoxyl, *N*-amine or thiophene, while the acceptor group is an electron-deficient moiety such as a carbonyl, nitrile, or imine. Some common examples of both donors and acceptors are shown in **Figure 1-1**. The groups are generally connected by a covalent bond and contain a high degree of π-conjugation to facilitate intramolecular communication between the two. These molecules can also form strong intermolecular interactions, such as hydrogen bonds and π-stacking, between the donor and acceptor groups. This enables them to form highly stable complexes with other molecules.

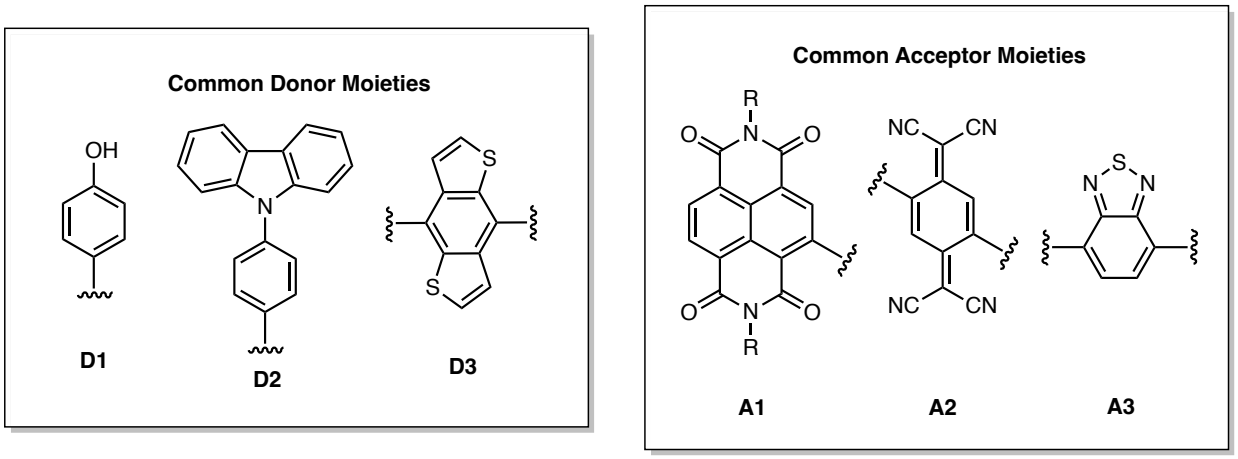

Figure 1-1. Common electron donor and acceptor moieties.

The photophysical properties of donor-acceptor (DA) systems are highly tunable. One example of this is from a study by Kumar and co-workers. The study probed the effect of extending π-conjugation between a triphenylamine donor and triazine acceptor, as shown in **Figure 1-2**. An increase in absorption and a redshift in the emission spectra of each compound was seen as a result of extending the conjugation.[13] This is a demonstration of how simple extension of π-conjugation can have a strong effect on the photophysical properties of DA molecules.

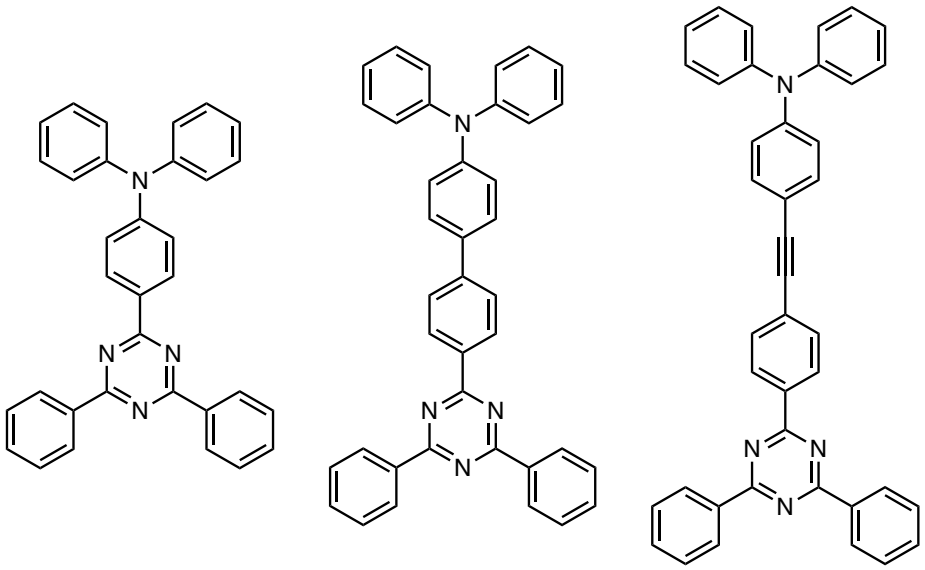

1.1 1.2 1.3

Figure 1-2. DA molecules as published by Kumar *et al.* displaying increased absorption and red-shifted emission as a function of extended π-conjugation.

Another common application of DA systems are as thermally-activated delayed fluorescence (TADF) emitters. This type of fluorescence finds use in third-generation organic light emitting diode (OLED) technology due to their potential high internal quantum efficiencies (IQE).[14–16] In traditional fluorescent emitters, singlet and triplet excitons exist in a 1:3 ratio, where only singlet excitons are utilized in fluorescence, and triplet excitons decay non-radiatively. TADF emitters are an attractive solution to this issue as they contain energy gaps between the S_1 and T_1 states of around 0.3 eV, known as ΔE_{ST}. This energy gap is short enough such that ambient heat can repopulate the excited singlet state from the excited triplet state. This process is known as reverse intersystem crossing (RISC) and can be shown using a simple Jablonski diagram in **Figure 1-3**.[17,18] Through this mechanism, it is theoretically possible that emitters of this type could reach photoluminescent quantum yields (PLQY) of 100%.

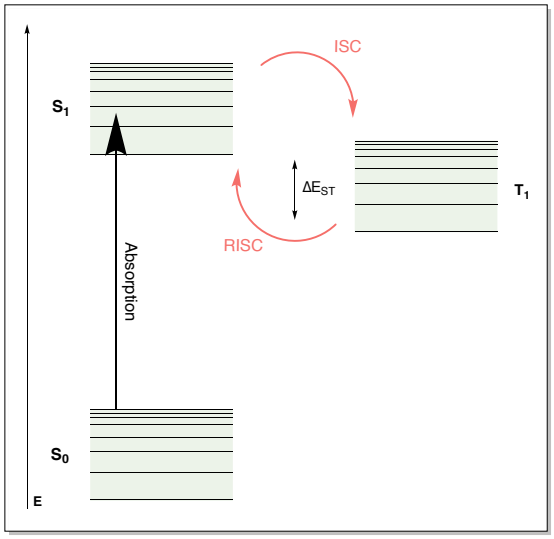

Figure 1-3. Jablonski Diagram showing ISC and RISC of an electron from the singlet excited state to the triplet excited state. In the case of TADF, ΔE_{ST} is small enough that thermal energy can promote RISC.

Examples of TADF are abundant and the literature on such compounds is expanding quickly. For example, earlier this year Hojo *et al.* published work on copolymers capable of TADF and through-space charge transfer (TSCT) shown in **Figure 1-4**.[19] The copolymers feature nodes, which are breaks in conjugation, that still display charge-transfer (CT) characteristics by holding the donor and acceptor moieties in close spatial proximity to one another. Polymers such as these may find use in materials such as optoelectronics, by utilizing spin-coating and inkjet printing. These polymer-based materials have also given rise to flexible devices.[20,21] Currently the best TSCT-TADF emitters have shown an efficiency of up to 12%, comparable to other less versatile DA systems used in similar devices.[20]

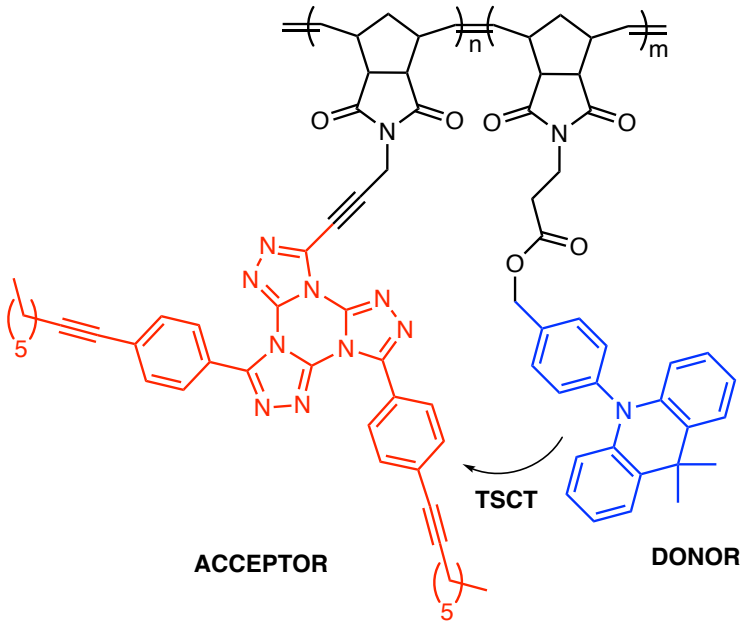

Figure 1-4. TADF-TSCT polymer as published by Hojo *et al.*

Spatial separation of the frontier molecular orbitals is necessary in the design of TADF emitters. The general design of these molecules is therefore reliant on intramolecular DA connectivity as these ensure there exists such spatial separation between the HOMO and LUMO.[22] It is not enough to just spatially separate these orbitals, however, as there still exists electron exchange correlation energies which can increase ΔE_{ST}.[23] The design of such structures should therefore also reduce the overlap between the spatially separated frontier molecular orbitals.[24] A comprehensive review of such structures is beyond the scope of this chapter, and the interested reader can consult the literature for specific examples.[25,12,13,14,29] What is important is that intramolecular interactions in molecules can have drastic effects on the photophysical properties of DA systems.

More recently, Stephenson *et al.* reported a catalytic cross-coupling method that utilizes intermolecular charge transfer. The process first involves photochemically generating a catalytically active DA complex. The acceptor containing a leaving group then generates a radical intermediate to form new carbon-carbon bonds between the leaving group and an aromatic heterocycle.[30] The structures and overall mechanism of this process is shown in **Figure 1-6**. This type of catalysis is an attractive option in forming new carbon-carbon bonds as it bypasses the use of transition metal complexes that are often expensive, air-sensitive, and occasionally toxic.

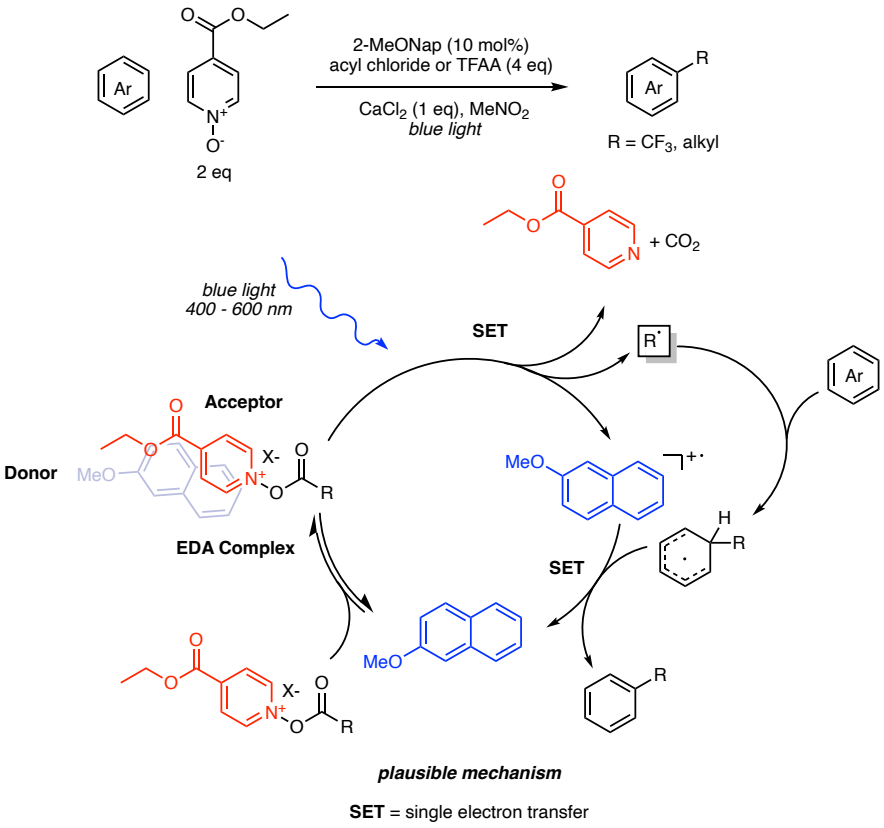

Figure 1-5. Mechanism of photocatalysis using EDA complex.

1.2 Intramolecular Charge-Transfer (ICT)

One of the main advantages of DA compounds is their ability to facilitate CT between the electron-rich donor and the electron-poor acceptor. This can happen both intermolecularly and intramolecularly. When electrons are passed from donor to acceptor through conjugated bonds within the same molecule, the process is known as intramolecular charge-transfer (ICT). As mentioned to in the previous sub-chapter, CT in the absence of conjugation is TSCT. Although both mechanisms are important, the remainder of this chapter will focus primarily on the former process; the interested reader is directed to the literature for examples of TSCT.[31,32]

CT is an important mechanism of electron-transfer in both biology and materials science.[33–37] The mechanism of CT typically occurs under photoexcitation, where an electron is transferred from an electron-rich donor to an electron-poor acceptor. The charge distribution of this charge-separated state is different than that of the ground state as shown in **Figure 1-7**, and can therefore be stabilized by polar solvents. For this reason, CT molecules typically exhibit solvatochromic fluorescence, where the emission of the molecule redshifts with increasing solvent polarity. It is therefore important to understand the mechanism of ICT when studying DA systems.

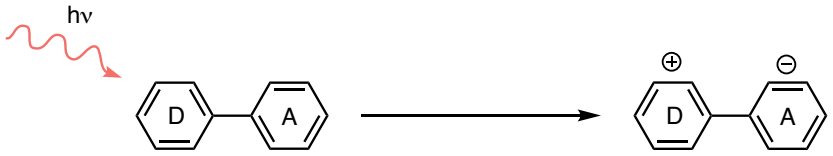

Figure 1-6. Charge transfer upon excitation with light.

The mechanism of ICT is still debated, and relies heavily on quantum theory. Systems of this type often display dual fluorescence resulting from different energies between the locally

excited (LE) state and the ICT state. This can be best shown using a Franck-Condon diagram as seen in **Figure 1-8**. Photoexcitation from the S_0 to S_1 state creates a LE which can undergo prompt fluorescence. This fluorescence is typically nearer in energy to the blue end of the visible spectrum and does not have a significant Stokes shift. To reach the ICT state, the system needs to overcome an activation energy. From here, there can be radiative decay from the ICT S_1 state to a vibrational mode in the S_0 state that is higher in energy than the ground vibrational state, before non-radiative relaxation back to the ground state. This will result in a red-shifted (lower energy) fluorescence.

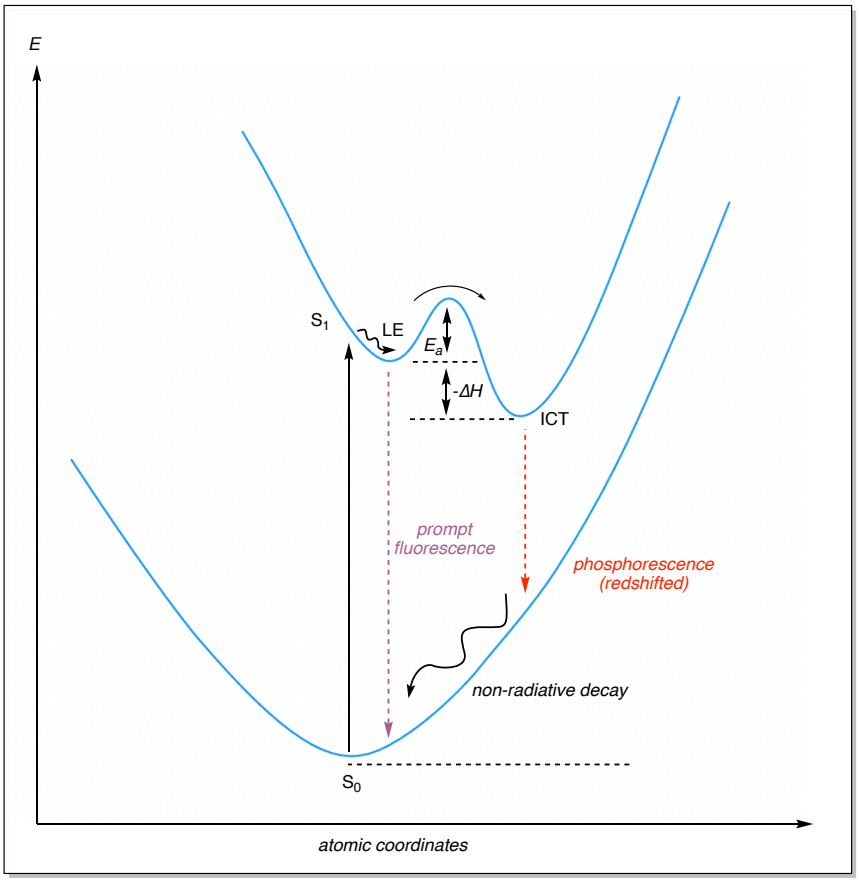

Figure 1-7. Franck-Condon diagram for ICT.

One mechanistic insight into the excited state geometry leading to dual fluorescence can come from the twisted intramolecular charge-transfer (TICT) state theory. First described by Grabowski *et al* in 1973,[38] a LE state can undergo an adiabatic rotation about the bond connecting the donor and acceptor. This twisting decouples the donor and the acceptor units by forming a radical cation and radical anion at the respective ends of the molecule. This twisted state is lower in energy than the LE state, and from here the exciton can relax to a twisted ground state structure before complete relaxation to the ground state geometry.[39,40] This is best shown using a Jablonski diagram in **Figure 1-9**.

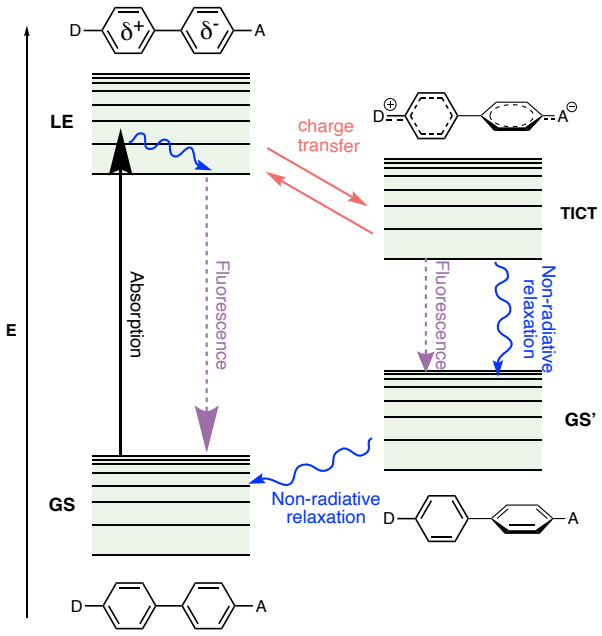

Figure 1-8. Jablonski diagram showing TICT.

TICT was used to describe the unique dual fluorescence seen in 4-dimethylaminobenzonitrile (DMABN) as published by Lippert in 1961.[41] Since then, there have

been countless studies done to try and find evidence for the TICT mechanism. The simplest way to do this is by structural modification to the DMABN structure as shown in **Figure 1-10**. The results of such studies were able to confirm that the TICT is the reason for seeing dual fluorescence in DMABN. A comprehensive review of the results of these structural modifications can be found in the literature.[42]

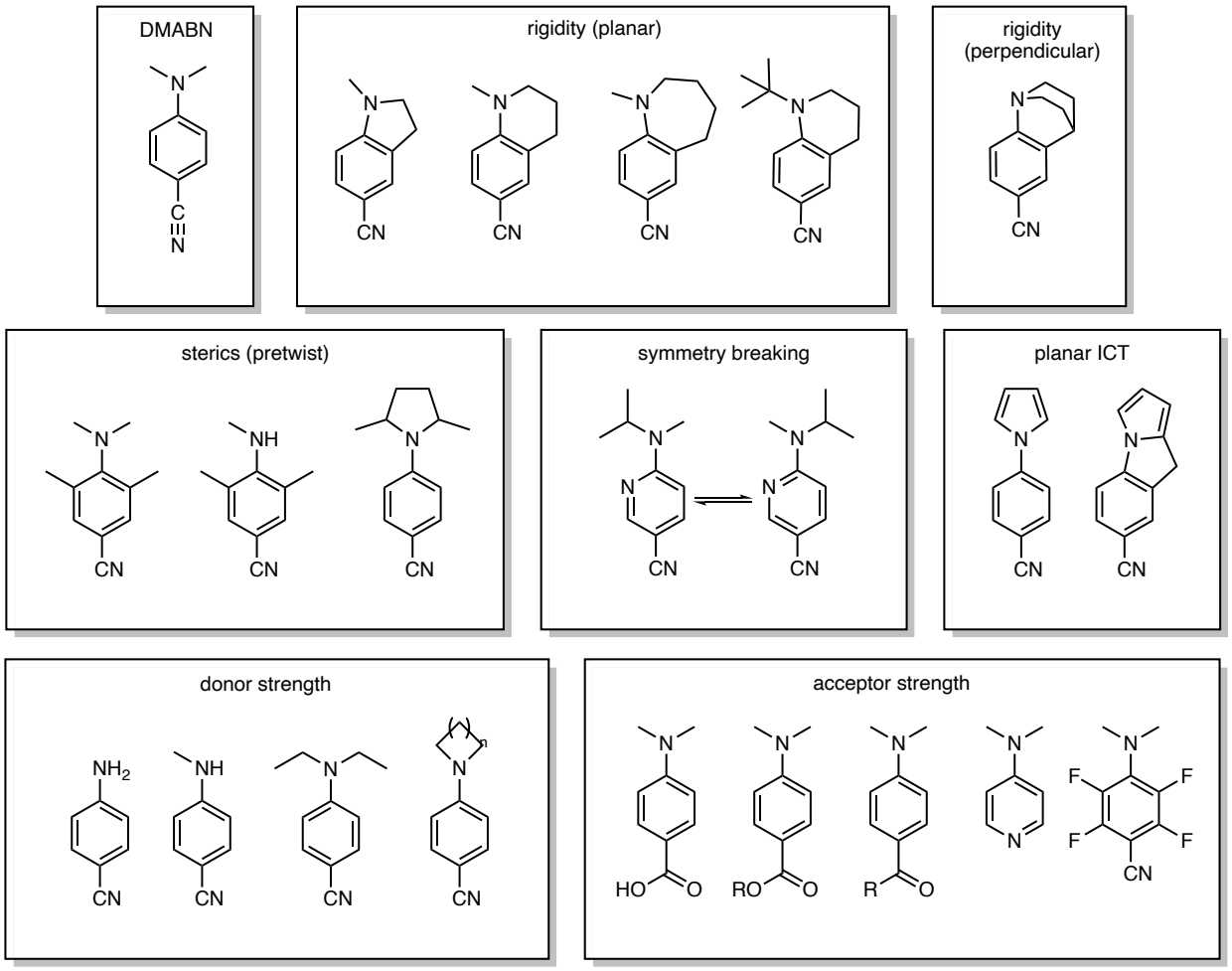

Figure 1-9. Structural modifications made to DMABN.

There are several other models explaining the excited state geometries of CT systems. For example, planar intramolecular charge transfer (PICT), rehybridized intramolecular charge transfer (RICT) and wagging intramolecular charge transfer (WICT), all of which are detailed in the literature.[39,43,44] Currently, TICT is considered the best representation of the excited state geometry leading to dual fluorescence.

1.3 Organic Stable Free Radicals

Much of the current literature on organic DA systems focuses on diamagnetic compounds. It is also possible for organic paramagnetic species to display CT characteristics. Open-shell molecules are key intermediates in many types of organic reactions and are ubiquitous in nature.[45] However, most of these examples are highly unstable due to their incomplete valence and corresponding electron-deficiency. Despite this, there are several examples of organic stable free radicals (SFRs). Since the early 1900s, there have been many examples of organic SFRs that have been isolated pure and characterized crystallographically in their open-shell states.[46]

One of the first examples of an organic SFR was published in 1900 by Gomberg where he claimed to have isolated triphenylmethane as a carbon based free radical.[47] This was disputed in the years following this publication and is currently known to exist as Gomberg's dimer in solution seen in **Figure 1-11**.[48] A comedic historical account of this research for those interested can be found in the literature.[49] Gomberg's publication paved the way for chemists interested in SFRs, as it gave insight to how open-shell molecules may be stabilized. Although rationally it would make sense to consider that a higher degree of saturation would better stabilize the trivalent carbon, here it is clear that the degree of unsaturation leads to delocalization of the lone electron over the entire system as shown in **Figure 1-12**. The system was also postulated to utilize the bulky phenyl rings

as protecting groups towards radical quenchers. However, it has since been proven that this system readily forms peroxide dimers in the presence of oxygen.

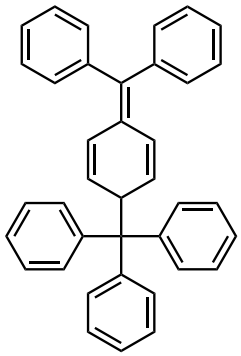

1.4

Figure 1-10. Gomberg's dimer.

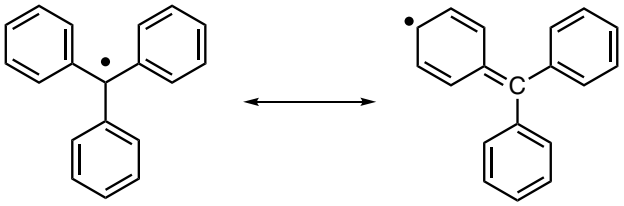

1.5

Figure 1-11. Triphenylmethyl radical showing resonance at the *para*-position of aromatic rings.

A more recent example of trivalent carbon is shown below in **Figure 1-13**. Reported by Veciana *et al.*, this substituted analog of the triphenylmethyl radical postulated by Gomberg features a perchlorotriphenylmethyl (PTM) appended to a tetrathiafulavene (TTF) donor. This open-shell compound was shown to be stable under ambient conditions, and when single crystals were exposed to high pressure displayed semiconductor behavior.[50] More examples of stable PTM-based radical DA systems can be found in the literature.[51,52]

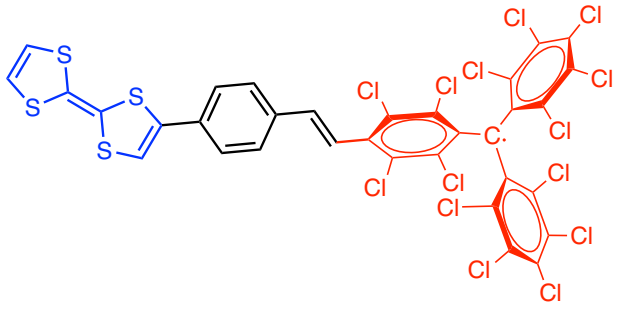

Figure 1-12. PTM-TTF radical.

Another prominent example of an organic SFR that has been known for several decades is the tetramethylpiperidinoxyl (TEMPO) radical whose structure can be seen in **Figure 1-14**. This system contains an *N*-oxyl based radical with a high degree of saturation with four nearby methyl groups. This system has been studied extensively since originally being isolated in 1960 and is the subject of a recent review article.[53]

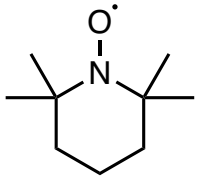

Figure 1-13. TEMPO.

Sugano *et al.* published one of the first organic π-donor systems where a TTF donor was appended to a TEMPO radical via an imine linker. The TTF-TEMPO SFR was then combined in solution with a tetracyanoquinodimethane (TCNQ) acceptor and the resulting CT salt was studied using magnetization and EPR. Results determined there was weak interaction between TTF-

TEMPO and TCNQ, but this work was an important stepping stone in learning how paramagnetic DA systems might interact with one another.[54]

SFRs have found use in organic semiconductors as DA systems,[55] as pure organic magnets,[56] donors in spintronics,[57,58] energy storage,[59] and in other applications. A recent example of a radical system for use in organic semiconductors was published in 2021 by Li *et al.*[60] The work examined a pair of quinoid diradicals that formed preferentially under aggregation with a narrow bandgap as a result, whose structures are shown in **Figure 1-15**. The results highlight an insightful mechanism to the design of organic photovoltaic systems utilizing open-shell systems.

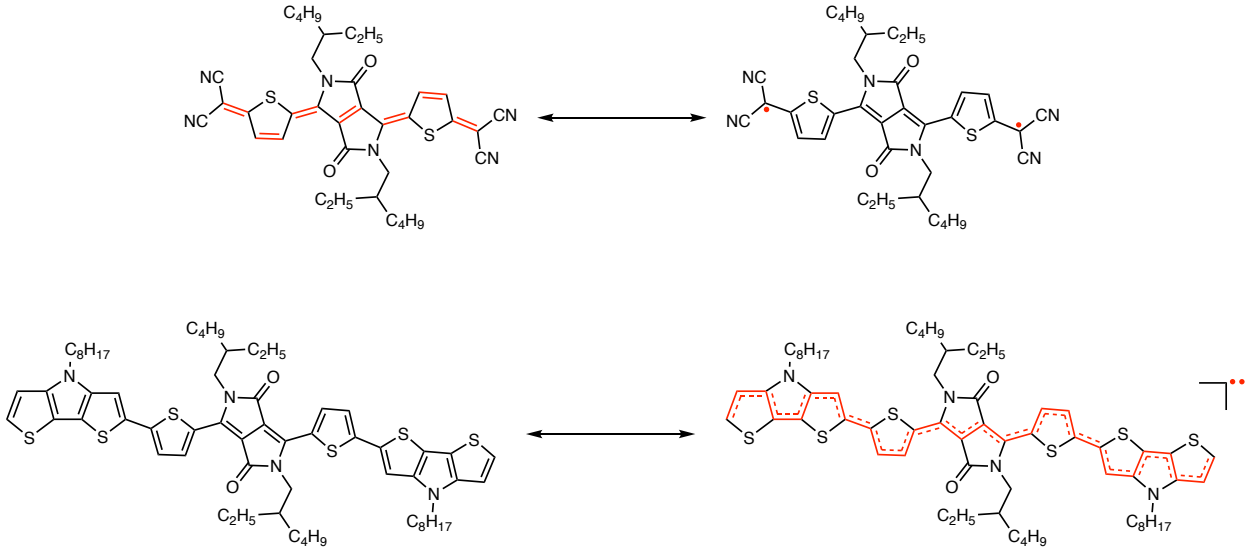

Figure 1-14. Radicals reported by Li *et al.*

The myriad applications of open-shell systems have led to new fields of research, one of which is organic spintronics. This field involves paramagnetic species in spintronics devices that harness the response of spin to external stimuli to then conduct some logical operation. Mannini

et al.[61] published an article in 2018 on nitronyl nitroxide radicals appended to electron transport layers of gold or lanthanum strontium manganite (LSMO) as seen in **Figure 1-16**. An external magnetic field applied to the coated surface showed paramagnetic character up to 250 K with increased injection efficiency below 50 K. This work demonstrates the applications of hybrid materials in the field of spintronics.

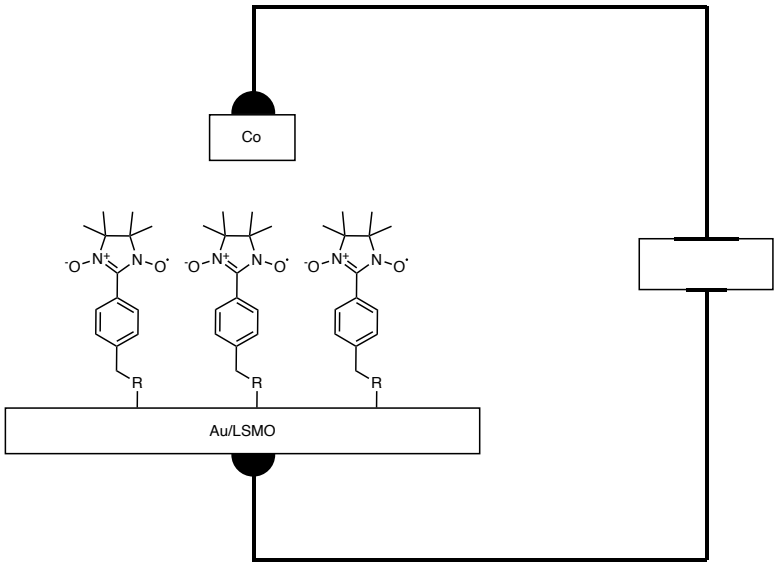

Figure 1-15. Organic spintronics device as published by Mannini *et al.*

The chemistry of SFR's has been the topic of significant research ever since Gomberg's publication in 1900. There has since been the discovery of several types of stable organic paramagnetic species. This includes phenoxyl radicals, verdazyls, and quinoid radicals which are discussed in depth in the literature.[62–64] Although a full review is not necessary here, it is important to highlight the commonalities between them – a high degree of unsaturation with delocalization of the radical, and bulky substituents to protect the radical from radical quenchers. This thesis will

focus specifically on phenoxyl radicals whose redox and EPR properties will be formally introduced in Chapter 3.

1.4 Squaraine Dyes

Due to the extensive research on open-shell systems over the decades, there are endless opportunities to functionalize SFR's. Organic dyes in particular have potential for synergetic optoelectronic effects when couple to an SFR. Many organic dyes typically contain extensive π-electron delocalization and in some cases may be charged or zwitterionic due to CT.

A relevant example of a class of dyes exhibiting both properties are squaraines. First published in 1966 by Ziegenbein,[65] these dyes are characterized by their cyclobutadienolate core derived from squaric acid as seen in **Figure 1-17**. Squaraines are zwitterionic at physiological pH and in some cases are soluble in aqueous media. This makes them suitable candidates for biomedical imaging in cells, tissue and organs.[66–69] Their zwitterionic character can also lead to strong ion-dipole interactions which have been exploited to detect polar molecules.[70]

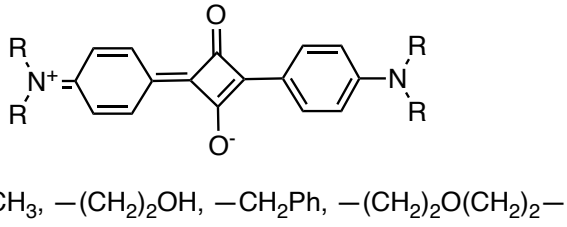

R = –CH_3, —$(CH_2)_2OH$, —CH_2Ph, —$(CH_2)_2O(CH_2)_2$—

Figure 1-16. First published squaraine dye.

A 2020 Nature publication from Yang *et al.* reported a squaraine dye that could resolve the fine cristae structure of mitochondria using stimulated emission depletion (STED) nanoscopy.[67]

Typical imaging techniques are insufficient for imaging these fine structures, and by use of a squaraine dye were able to achieve an image resolution of 35.2 nm using its fluorescent properties. The high photostability of the dye is crucial in this technique and demonstrates the versatility of this class of dyes.

Another characteristic of squaraine dyes is their intense visible light absorbance, with extinction coefficients on the scale of 10^5 M^{-1} cm^{-1} and sharp emissions at low concentrations.[71] These properties are a result of their rigid planar structures, which leads to extensive electron delocalization. This results in absorbance and emission maxima reaching into the near-infrared (NIR) which falls between 780 nm and 2500 nm. Because of this, squaraines have found use in non-linear optics,[72] light-emitting diodes,[73] solar cells,[74] phototransistors[75] and other applications.

In 2023 Al-Horaibi *et al.* synthesized two novel squaraine dyes for use in dye-sensitized solar cells (DSSCs). The cosensitized dye demonstrated significant photostability, strong NIR absorption, and a high photocurrent output of 22.3 mA cm^{-2} with an efficiency of 4.8%.[76] Efficiencies of squaraine dyes in DSSCs range from 0.06% to the highest being 8.9%.[77,78] These dyes are typically adsorbed onto a TiO_2 conducting surface, and the structures of these dyes can be symmetrical or unsymmetrical. In both cases they have been shown to effectively act as DSSC sensitizers. A select few structures demonstrating the highest PCEs for squaraine dyes can be seen in **Figure 1-18**.

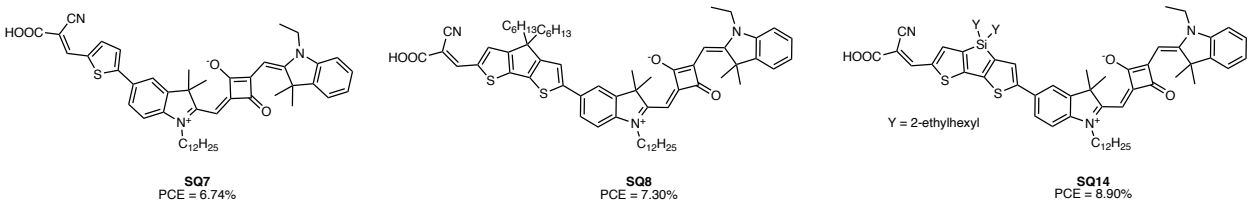

Figure 1-17. Squaraine structures with published application in DSSCs.

Squaraines are prone to aggregation due to their intermolecular π-π interactions and H-bonding. Aggregation can have a significant effect on their ability to inject electrons. A study in 2015 explored adding different surfactants to manipulate and interrupt the aggregation of a specific squaraine dye. The effect of this interruption leads to changes in the visible properties of the dye.[79] These results may have use in biological contexts as they could act as a quick and efficient way to detect the presence of such surfactants in human urine samples or water.

In some cases, aggregation has been shown to improve efficiency in photovoltaics. Chen *et al.* were able to show that by use of different solvents, there can be control over the type of aggregation that occurs. By selectively choosing a solvent that promotes J-aggregation, the squaraine aggregate showed strong absorbance at 850 nm and significantly improved photocurrent. This property was determined to be a result of better intermolecular CT character for this type of aggregate.[80]

Another photovoltaic application of squaraines are as components of organic solar cells (OSCs). First demonstrated in 1976,[81] squaraines initially were not considered viable species for use in OSCs due to poor power-conversion efficiencies (PCEs). In 2008 Marks *et al.* published a study where a squaraine as part of a bulk heterojunction (BHJ) showed a PCE of 1.24%, up from the 0.02% that was shown in 1976.[82] BHJ-OSCs have since garnered a lot of attention, with one of the highest PCEs reaching 6.3% for a symmetrical squaraine,[83] and 7.41% for an unsymmetrical squaraine.[84] Squaraine dyes have also been shown to effectively act as cosensitizers in advanced solar cells and perovskite solar cells.[85–88]

1.5 Thesis Objectives and Scope

The objective of this thesis is to build on the field of organic paramagnetic DA systems containing a strong chromophore core. First, chapter 2 covers the synthetic protocol towards two new DA functionalized squaraine dyes. The DA moiety was first synthesized using 4-bromo-2,6-di-*tert*-butyl phenol as the electron-donor starting material, and then coupled via Suzuki-Miyaura chemistry to 4,7-dibromo-2,1,3-benzothiadiazole (BTD) as electron-acceptor. The resulting DA compound contains one bromine on the BTD acceptor as a coupling handle for downstream cross-coupling.

A previously reported literature procedure is followed to form a pinacol boronate ester squaraine which is cross-coupled to our DA compound to form our first target squaraine dye. The results towards the second target squaraine dye are presented, and current synthetic troubles are discussed. The ^{1}H NMR spectroscopy and ^{13}C NMR spectroscopy of all novel compounds are assigned and discussed including isolated side products of interest.

Chapter 3 discusses the photophysical and redox properties of all novel compounds, as well as the computational results for these compounds. Ultraviolet-visible (UV-Vis) spectrophotometry and fluorimetry are used to characterize the absorbance and emission profiles of all compounds. Cyclic voltammetry is used to characterize the redox properties of the isolated phenol-containing dyes, and the results of oxidation reactions are also examined. Finally, computational studies investigate the orbital energies of all relevant compounds, and explore possible methods of oxidation towards the biradical DA squaraine dyes proposed in this thesis.

Chapter 2 Synthesis

2.1 Introduction

2.1.1 Catalysis in Chemical Synthesis

Catalysis is a crucial part of synthetic chemistry. Used to accelerate chemical reaction rates, catalysts enable new chemical transformations by providing a lower energy pathway from reactants to products. With respect to the actual form of the catalyst, there are two main branches – heterogeneous catalysis and homogeneous catalysis. Heterogeneous catalysis involves a catalyst that exists in a different phase than the reactants (usually a solid catalyst), where homogeneous catalysis involves a catalyst in the same phase as the reactants (usually a dissolved catalyst in the reaction medium).

One of the most useful and well exploited examples of a heterogenous catalyst is palladium on carbon (Pd/C), used predominantly in the hydrogenation of unsaturated hydrocarbons. In this example, both hydrogen gas and an unsaturated hydrocarbon such as an alkene or alkyne are adsorbed onto a palladium metal surface before undergoing a *syn* addition of the hydrogen atoms to the unsaturated bond. Hydrogenation was first described by Paul Sabatier in the late 19th century, and is still used industrially on a multi-ton scale today.[89] This reduction method is possible with more catalysts than just Pd/C: other metals like platinum, rhodium, and nickel are also capable of catalyzing this reaction.

Catalytic converters are another widely employed heterogenous catalyst used in vehicles to break down toxic gases such as carbon monoxide and nitrogen oxides.[90] Catalytic converters work by utilizing metals such as platinum or palladium to adsorb the toxic gas molecules. The adsorbed gases can then be converted to less toxic molecules through oxidation (e.g. CO to CO_2)

or reduction (e.g. NO_2 to N_2) before exiting through the exhaust system. Both this and the previous hydrogenation mechanism rely on high surface areas to catalyze these reactions efficiently.

Heterogeneous catalysis oftentimes exploits the poor solubilities of transition metal elements and catalyst support materials in organic solvents containing organic reactants. This keeps the catalyst and reactants/products in different phases. Homogeneous catalysis on the other hand relies on both the catalyst and reactants being soluble in the same phase as one another. This enables alternative and (in principle) easier to control catalytic mechanisms, due to our ability to tune the electronic and steric properties of transition metals.[91] This will then influence how these catalysts can react with other organic reagents.

It is important to recognize that homogeneous catalysis can involve metals or other non-metal catalysts: from a simple proton to large organometallic complexes. An example of a homogenous metal-catalyzed reaction is the oxidation of iodide anions by use of iron(III) metal complexes.[92] A non-metal case is the addition of alcohol functional groups onto olefins via a sulfuric acid catalyst, where all reagents are in the liquid phase.[93] There are myriad examples of both metal and non-metal homogeneous catalysis and processes like these are ubiquitous in nature and industry.

2.1.2 Palladium-Catalyzed Cross-coupling

One of the most prominent metals used in catalysis for organic synthesis is palladium. In particular, palladium-catalyzed cross-coupling is among the most frequently used reactions in organic synthesis. First pioneered by Prof. Richard Heck in 1972,[94] palladium is used catalytically in his namesake Heck reaction, which involves the alkenylation of aryl halides. Other Pd-catalyzed carbon-carbon bond forming reactions include the Suzuki-Miyaura reaction, Sonogashira reaction,

Stille coupling, and more.[95] The activity of palladium has found application in the formation of carbon-nitrogen as well as carbon-carbon bonds using aromatic hydrocarbons or other unsaturated systems. Palladium catalysis for cross-coupling is most often done homogeneously, but there are examples of cross-coupling by heterogeneous catalysts. For example, cross-coupling with palladium has been achieved by silica-supported catalysis,[96] polymer supported catalysis,[97] or even with simple Pd/C.[98]

Despite its relatively high cost, palladium remains the major catalytic metal for cross-coupling. Palladium catalysts have repeatedly demonstrated high product yields and good turn over numbers (TON), which is the yield as a function of number of cycles. It is however understood that yields and high TON cannot truly describe the long-term recyclability of a catalyst, as the recyclability has more to do with the kinetics of catalysis that monitor the inductive periods of the active species.[99] Recyclability is difficult to study and as such the literature on the topic to date is quite limited.

A general catalytic cycle for homogeneous palladium-catalyzed cross-coupling reactions is shown in **Figure 2-1**. The process generally begins with a palladium(II) or palladium(0) precursor, which is combined with an ancillary ligand to form a reactive LPd(0) or L_2Pd(0) complex. This palladium(0) complex undergoes oxidative addition with an organohalide, where the organic R and halide X coordinate to the palladium(0) centre. Transmetallation involves addition of an electron rich R' group and base, which substitutes R' for X at the palladium centre. The final step is the reductive elimination of R and R' to form the new cross-coupled product, and regenerate the catalytically active palladium(0) complex. The mechanism of catalysis for many specific reactions has been studied extensively, and although the catalytic cycle is generally well

understood, there exists much debate over the exact mechanisms of each step. The interested reader may consult the literature to learn more about the topic.[100–104]

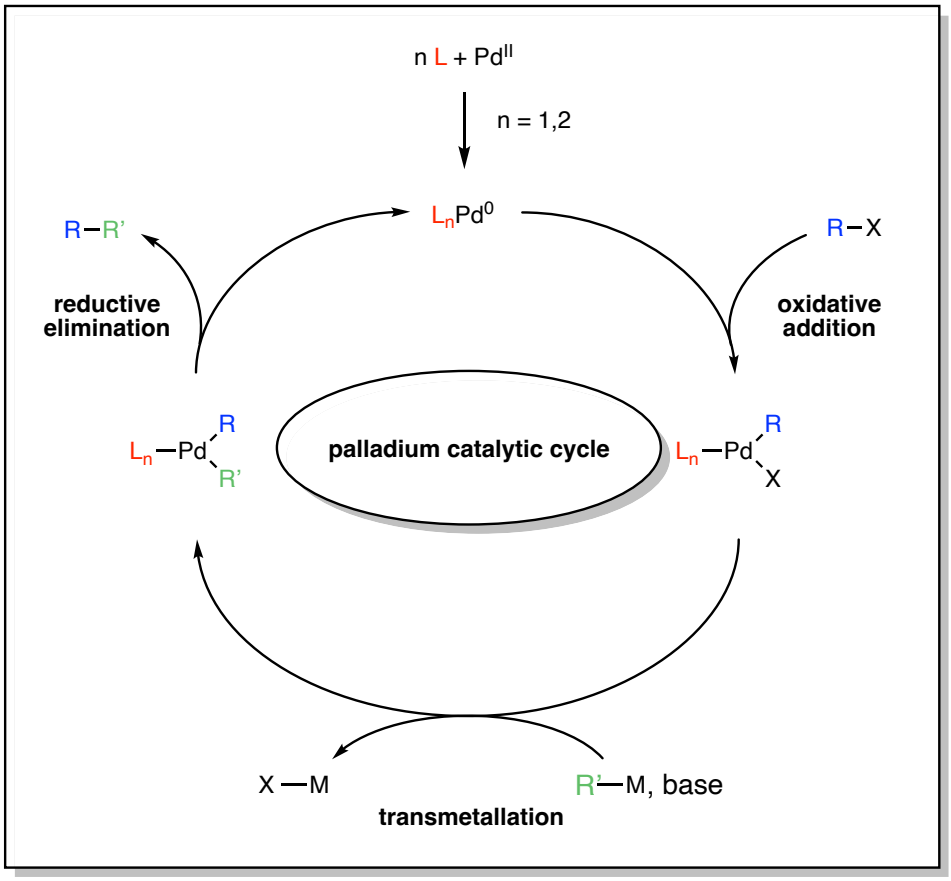

Figure 2-1. General catalytic cycle for palladium-catalyzed cross-coupling.

Palladium catalysis has had a profound impact on the practice of organic synthesis, from small scale to manufacturing scale. It has been used in the synthesis of agrochemicals,[105] pharmaceuticals,[106] organic materials,[107,108] and natural products.[109,110] In the realm of organic materials chemistry, palladium catalysis is used to generate highly conjugated polyaromatic compounds. Dessi *et al.* showed in a recent publication a method to synthesize hole-transport materials used in perovskite solar cells with catalyst loadings of as low as 1%, improving previous literature procedures.[111] Later that year, Gessner *et al.* published a method in the synthesis of di-

and triarylamines, some of which are used in light emitting materials, also improving previous synthetic methodology for such compounds.[112] Such advancements in synthetic protocols continue to advance materials chemistry which can have outlasting positive effects on the environment.

2.1.3 Suzuki-Miyaura Cross-Coupling

Perhaps two of the most well-known palladium catalyzed reactions are the Miyaura borylation and Suzuki-Miyaura cross-coupling reactions, the latter of which is often abbreviated as SMC. First published in 1979 by Miyaura and Suzuki,[113] the SMC reaction utilizes electron-poor organohalides with electron-rich organoborane compounds to create new aryl carbon-carbon bonds. Since then, it has become one of the most prolific palladium-catalyzed reactions which has found use in myriad fields of organic chemistry. For example, SMC has been used in the synthesis of pharmaceuticals,[114–117] materials,[118] total synthesis,[119–122] and can be done in the presence of water and under generally ambient reaction conditions.[123–125] It has become one of the most widely employed synthetic tools in organic chemistry thanks to its regio- and stereoselectivity,[126–128] and low catalyst loadings.[129,130] In some cases, SMC is possible in both solvent-free and ligand-free conditions.[131,132] A full review of SMC can be found in the literature.[133]

Upon development of the synthetic plan towards the products presented in this thesis, it was clear the most efficient way to create the highly-conjugated systems would be via SMC chemistry. A publication from Kuster and Geiger utilized SMC in the synthesis of various squaraine dyes as shown in **Figure 2-2**. They were able to convert squaraines containing halides easily and efficiently into their corresponding boronic acid pinacol ester before coupling to other aryl groups.[134] The work presented the compatibility between squaraine dyes and SMC conditions and is one of the primary motivators behind the research presented herein.

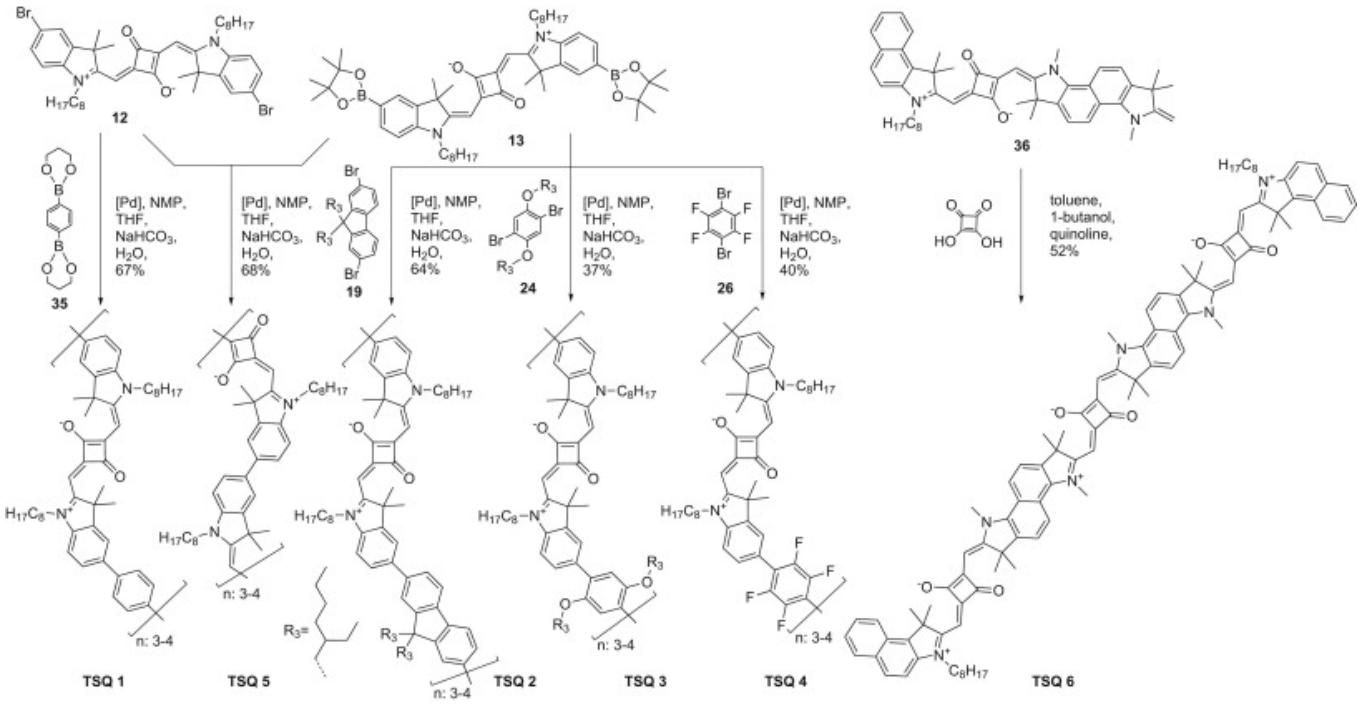

Figure 2-2. Various squaraine polymers synthesized via SMC. Reprinted with permission from Kuster S.; Geiger T. Strategies and Investigations on Bridging Squaraine Dye Units. *Dyes and Pigments*. **2012**, *95* (3), 657-670. DOI: https://doi.org/10.1016/j.dyepig.2012.06.017

More recently, Würthner and coworkers presented an isoindigo-based phenoxyl biradical which was synthesized via SMC.[135] By converting the readily available 4-bromo-2,6-di-*tert*-butylphenol (DTP) into its respective pinacol boronate ester via Miyaura borylation, the phenol can be coupled to the halogenated isoindigo to produce the precursor to the radical. This was important for two reasons. First, it was shown that oxidation of the phenol into the radical could be done two different ways and using relatively mild oxidation conditions as shown in **Figure 2-3**. Second, the stability of the biradical when appended to a dye such as isoindigo supported our hypothesis of creating a squaraine-based radical. This work inspired us to investigate phenols as our precursor towards a SFR in the design of our target molecules.

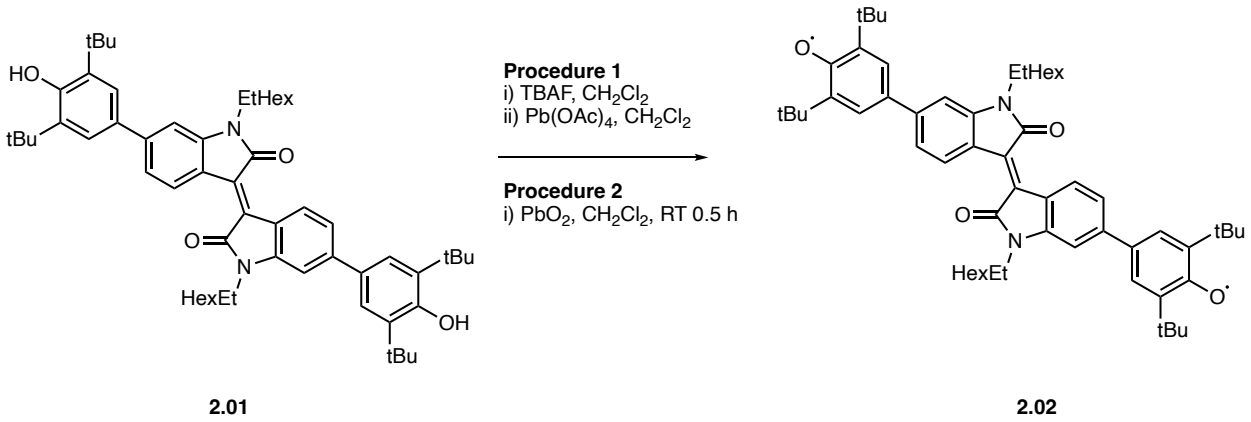

2.01 **2.02**

Figure 2-3. Biradical as prepared by Würthner *et al.*

There have been several publications utilizing the pinacol boronate ester of DTP in SMC. Recently, Abe *et al.* were able to demonstrate the photochromism of two new DTP-containing systems. The mechanism carries forward via a biradical pathway when irradiated with light of the proper wavelength.[136] The redox-active DTP unit acts as a type of molecular switch within the system that can control the absorption profile of these compounds. This work highlights the tunability of DTP when appended to different chromophores and shows the relevance of such work in the present day.

Previous work by the Chernick group used 4,7-dibromo-2,1,3-benzothiadiazole (BTD) as an electron acceptor in a 2020 publication featuring DA scaffolds, seen in **Figure 2-4**.[137] Here the acceptor was easily synthesized from readily available starting materials and showed reactivity using palladium catalysis. It should be noted that the work utilized Stille coupling in the procedure towards the final compound. This did not present any concern as SMC utilizes electron-poor organohalides in the oxidative addition step of the catalytic cycle. For this reason, we chose to use

BTD as our electron acceptor in the design of our target compounds. Much like DTP, there exist many current publications involving the use of BTD and SMC for materials chemistry.[138–141]

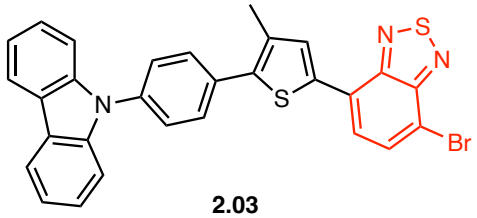

2.03

Figure 2-4. DA compound reported by Junge *et al.*, BTD acceptor highlighted in red.

2.1.4 Synthetic Roadmap

Considering the recent publications from Junge and Würthner, we decided to investigate the synthesis of a novel DA compound involving a DTP donor and BTD acceptor. We hypothesized the phenol would be readily oxidized to its corresponding SFR based on the surrounding *tert*-butyl groups and a *para*-attachment to a strong acceptor. By utilizing a remaining bromine handle on BTD akin to **2.03**, we could then use SMC to couple our DA compound to a boronate squaraine dye whose synthetic procedure is already known.

The full retrosynthetic analysis towards **2.25** is shown in **Scheme 2-1**. Access to DA compound **2.14** can be achieved from commercially available BTD, N-bromosuccinimide (NBS), and 4-bromo-2,6-di*tert*butylphenol to access our DA compound **2.14**. Procedures for the forward synthesis from **2.16/2.17** to **2.24** are published by Kuster and Geiger.[134] Boronate squaraine **2.24** can then be coupled to **2.14** through SMC to yield our first DA functionalized squaraine dye **2.25**.

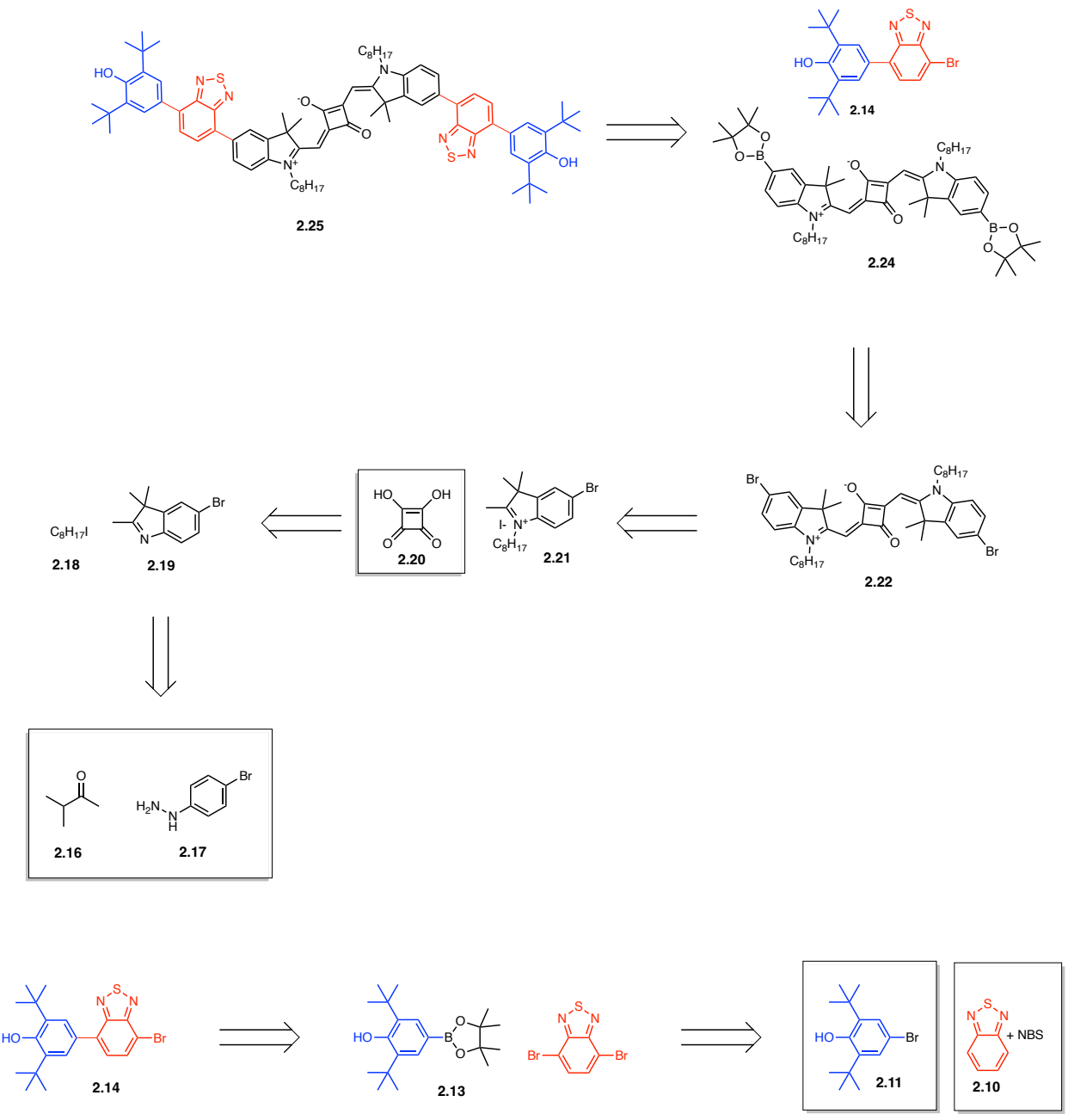

Scheme 2-1. Retrosynthetic analysis of target compound **2.25** back to commercially available starting materials.

Based on the retrosynthesis in **Scheme 2-1**, we further proposed a retrosynthesis to previously unexplored squaraine dyes **2.29** and **2.31** shown in **Scheme 2-2**. The approach would be analogous to the known procedures towards **2.24**, but use 2-bromophenylhydrazine **2.26** as a key starting material. We hypothesized that alkylation of **2.27** to form **2.28a-c** would be difficult due to steric hindrance near the nucleophilic nitrogen on the indoline. Our approach involved testing three different iodoalkane reagents to form an *N*-alkyl-indolinium salt (**2.28**). From here, a base-catalyzed condensation is used to form squaraine dye **2.29**. As for **2.25**, borylation and subsequent coupling would form functionalized squaraine dye **2.31**.

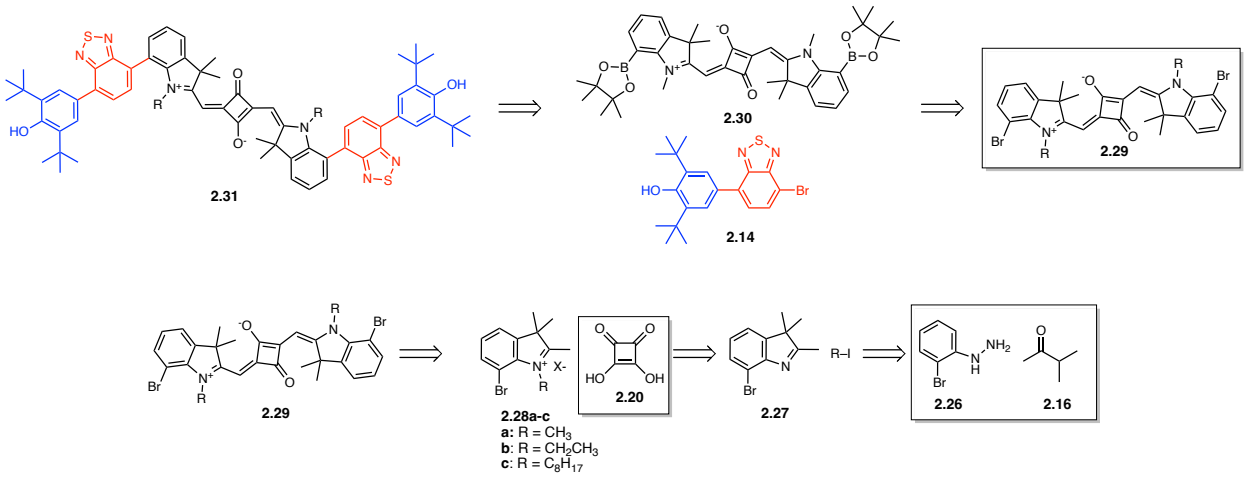

Scheme 2-2. Retrosynthetic analysis towards target compound **2.31**.

2.2 Donor Acceptor Compound **2.14**

2.2.1 Synthesis and Purification

Scheme 2-3 highlights the key steps discussed in this chapter following previously reported procedures.[135,142] The synthetic procedure for compounds **2.13** and **2.12** involved a Miyaura

borylation shown in **Figure 2-5** and electrophilic aromatic substitution shown in **Figure 2-6**, respectively. These procedures were carried out following previous reports, giving compounds **2.13** and **2.12** in isolated yields of 64% and 99% respectively. Compound **2.13** was purified by column chromatography, while **2.12** was easily carried forward without purification.

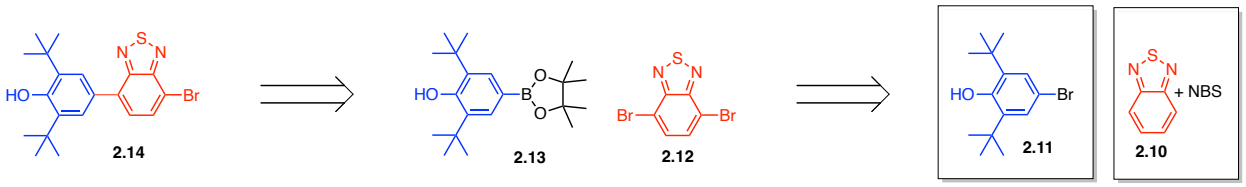

Scheme 2-3. Retrosynthesis towards **2.14**.

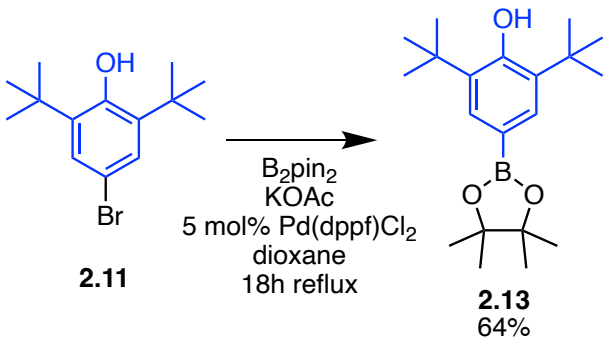

Figure 2-5. Synthesis of **2.13**.

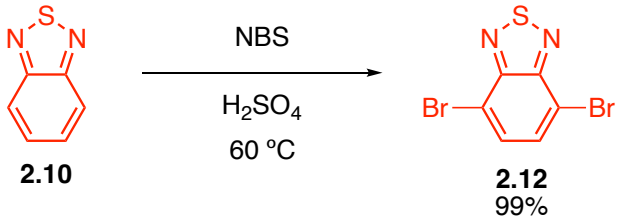

Figure 2-6. Synthesis of **2.12**.

Suzuki cross coupling reactions are extremely sensitive to almost all components of the reaction conditions and procedure. This means that careful choice of base, palladium (0) source, ligand and solvent is needed. To best determine which conditions would favor the synthesis of **2.14** in highest yields, a 24-well screening experiment was conducted. A test reaction shown in **Scheme 2-4** using $Pd(dppf)Cl_2$ showed evidence of successful coupling via NMR spectroscopic analysis and was used as a benchmark reaction.

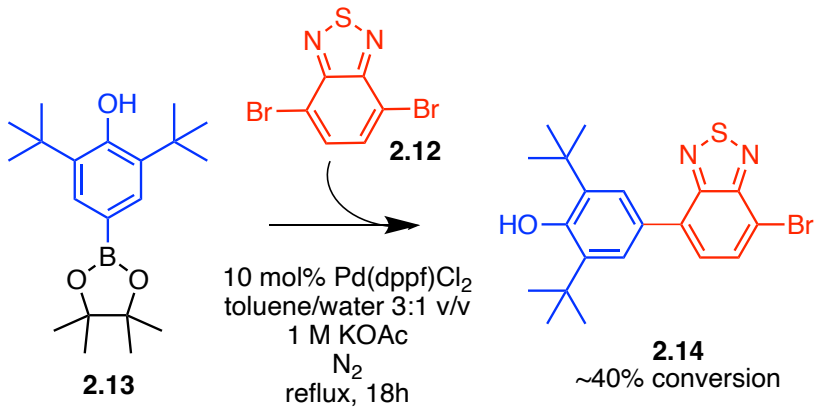

Scheme 2-4. Pilot reaction of **2.14.**

Table 2-1 shows the design of the screening experiment along with the quantitative results. THF is a polar aprotic solvent and was chosen as the organic phase for this reaction. Additionally, since **2.13** is a boronic acid pinacol ester, it is possible that water may be necessary to hydrolyze the pinacol ester a boronic acid. Formation of the boronic acid is crucial in the transmetallation

step of the catalytic cycle,[143] so the inclusion of water as a co-solvent was a further factor in the experiment design.

Two palladium sources were used in the reaction screen; palladium (II) acetate and a palladium (0) precatalyst previously reported by our group.[144] Potassium acetate was used as a base as well as six commonly used ligands shown in **Figure 2-7**.

Results from this screening reaction highlight the necessity for water to be present in these reactions. We also were able to identify by ^{1}H NMR spectroscopy the formation of **2.15**. As seen below, only reaction vials containing water showed successful formation of the new cross-coupled product based on the appearance of two doublets in the ^{1}H NMR spectroscopy. Reactions containing DAB-Pd-MAH showed much higher yields than the corresponding reactions containing $Pd(OAc)_2$. From this screening, we determined that 6 mol% DAB-Pd-MAH with P(*o*-tol)$_3$ in a 4:1 mixture of THF and water to be the best reaction conditions to form **2.14** with as little **2.15** as possible.

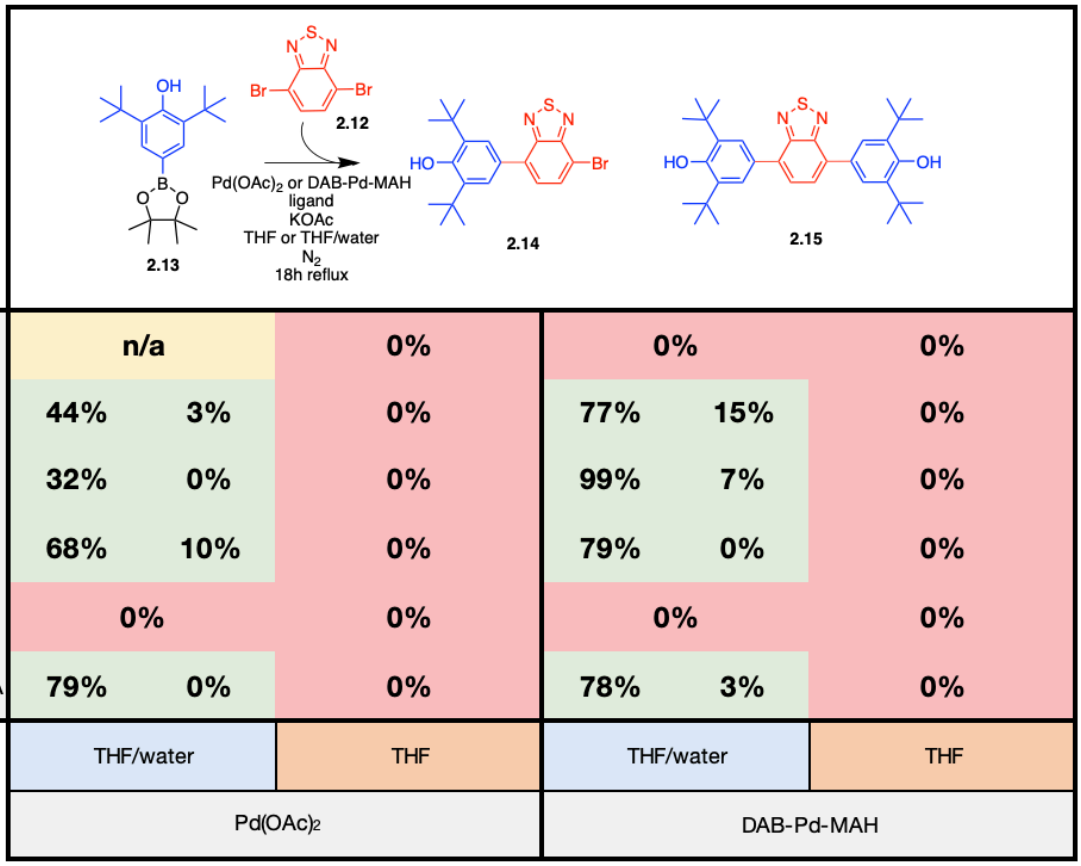

Table 2-1. 24-well reaction screening setup. The green cells indicate successful reaction and the corresponding yields of both **2.14** and **2.15** from left to right, respectively. Red cells indicate no evidence of successful reaction, and yellow cells indicate inconclusive results. Yields calculated using NMR spectroscopy with 1,3,5-trimethoxybenzene as an internal standard and a measurement error of 10%.

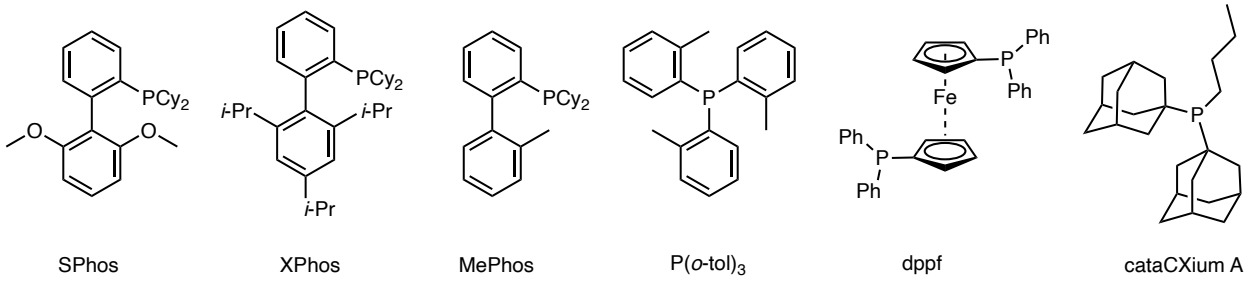

Figure 2-7. Ligands used in HTS experiment.

With the reaction conditions now optimized, several purification methods were explored. The crude solid was fully soluble in every solvent tested except water, so recrystallization was not attempted. Column chromatography using solvent mixtures containing various combinations of ethyl acetate, dichloromethane, hexanes, pentane, petroleum ether, toluene, methanol, acetic acid, and diethyl ether were tested in different ratios. A 1:1 v/v mixture of dichloromethane and light petroleum ether gave the apparent best separation by TLC analysis, as shown in **Figure 2-8**. Despite extensive testing, these very similar R_f values for three separate components represents the best separation observed. Although it was not possible to spot it on the TLC plate, **2.13** is present as an impurity.

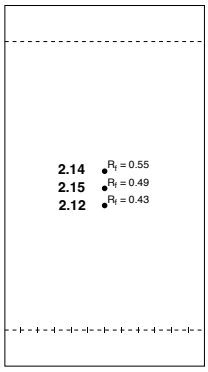

Figure 2-8. TLC Plate showing R_f values of the crude reaction mixture in synthesizing **2.14** using DCM and light petroleum ether as eluent. The compounds corresponding to the points are labeled.

A sample containing **2.14**, **2.15** and **2.12** was isolated after rigorous column chromatography in a 22% crude yield in a ratio of 1 : 0.33 : 1.5, removing any remaining **2.13** (**Scheme 2-5**). This mixture could be carried forward to the next reaction step, as only **2.14** contains the reactive bromine handle for cross-coupling. Over-reacted product **2.15** could then be removed by purification of **2.25**, and there was no evidence of **2.12** coupling to **2.24** based on NMR spectroscopic analysis.

Still, it was necessary to isolate both **2.14** and **2.15** to fully characterize both molecules. First, a basic extraction using 1 M aqueous NaOH was attempted to extract **2.14** out of solution. This would allow separation of **2.14** into the aqueous phase, leaving **2.15** in the organic phase. The results of this were not successful, so we turned to a recrystallization from hot ethanol using water as anti-solvent. This also led to a mixture of starting materials and product as none of the materials are water soluble. However, it was found that taking the mixture from the first column attempt and subjecting it to a second column with 100% dichloromethane as eluent led to isolation of **2.14** and **2.15** in 14% and 2% yields respectively to use for analysis. This product was used to fully characterize both molecules using the full suite of NMR spectroscopy spectroscopy experiments,

mass spectrometry, along with UV-Visible and fluorescence spectroscopies. The complete reaction scheme can be seen in **Scheme 2-6**.

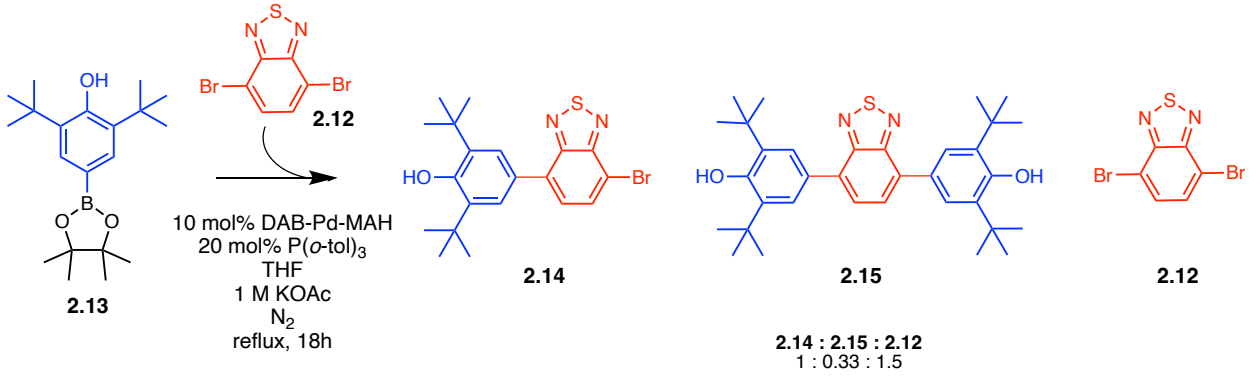

Scheme 2-5. Crude reaction mixture carried forward in the synthesis towards **2.25**.

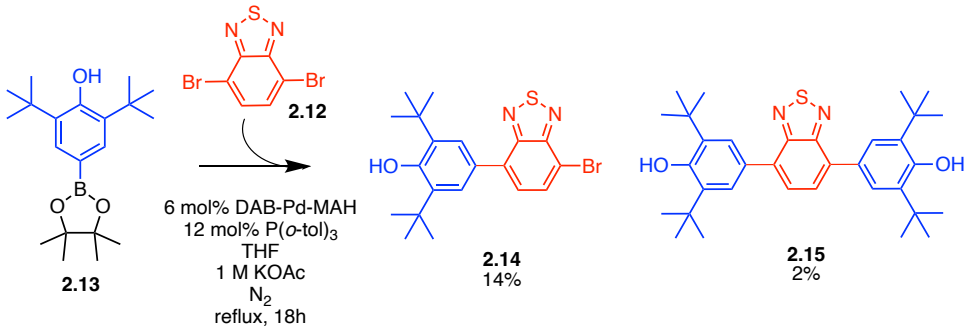

Scheme 2-6. Optimized conditions to synthesize **2.14**.

2.2.2 NMR Spectroscopy Assignments

NMR spectroscopy provides the best method to confirm the connectivity of both compounds. A comprehensive overview of the ^{1}H and ^{13}C NMR signal assignments for **2.14** is presented in **Table 2-2**. The assignments for C3, C4, C8, and C12 were established through their ^{1}H-^{13}C heteronuclear single quantum coherence (HSQC) correlations. Initially, the assignments for H3 and H4 were attempted using nuclear Overhauser effect spectroscopy (NOESY), as it was hypothesized that H8 and H4 would exhibit through-space interactions. Surprisingly, the

experiment yielded no correlation between these two protons. Consequently, the assignments for these protons, along with the remaining carbons, were determined by leveraging resonance structures and heteronuclear multiple bond correlation (HMBC) correlations.

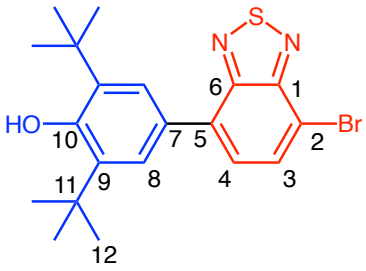

#	^{1}H	^{13}C
1	-	154.23
2	-	112.08
3	**7.89**	**132.66**
4	**7.52**	**127.66**
5	-	135.26
6	-	153.76
7	-	128.06
8	**7.75**	**126.62**
9	-	136.43
10	-	154.97
11	-	34.85
12	**1.52**	**30.66**
OH	5.44	-

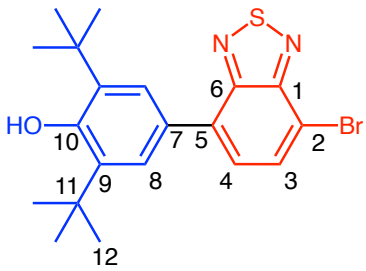

#	^{1}H-^{13}C HMBC
C1	H3
C2	H3, H4
C3	H4
C4	H3, H4
C5	H3, H8
C6	H4
C7	-
C8	H4, H8, H12
C9	OH, H12
C10	OH, H8
C11	H8, H12
C12	OH, H8, H12

^{1}H-^{1}H NOESY Correlations

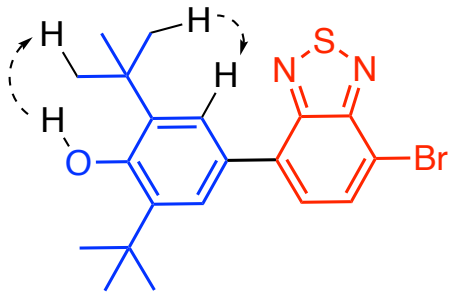

Table 2-2. ^{1}H and ^{13}C assignments for **2.14**, including 2D and NOESY correlations. Bolded entries indicate ^{1}H-^{13}C HSQC correlations.

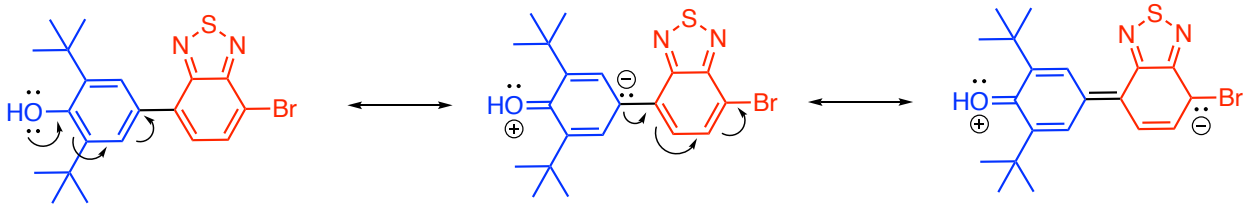

Figure 2-9. Resonance structures showing shielded carbons in **2.14**.

Figure 2-9 illustrates how the resonance in **2.14** leads to shielding effects at specific sites, consistent with the observed upfield shifts for C7 and C2 in comparison to C5 and C3. This phenomenon also accounts for the nearly 0.4 ppm separation between H3 and H4 in the ^{1}H NMR spectrum. In **Table 2-3**, the HMBC correlations provide further insights. The electron-deficient nature of C1 and C6 enables clear assignment through ^{3}J correlations with H3 and H4, respectively. Notably, C5 exhibits ^{3}J correlations with both H3 and H8 and is shifted to higher chemical shifts due to its deshielding effect, as depicted in the resonance scheme. Consequently, the assignments of C9 and C10 were relatively straightforward, leveraging resonance considerations and HMBC correlations.

Compound **2.15** possesses an internal mirror plane, simplifying the NMR signal assignments, as indicated in **Table 2-3**. The singlet resonance observed in the ^{1}H NMR spectrum at 7.82 ppm was unequivocally assigned to H5, given its relative integration value of 4. Likewise, the singlet resonance observed at 7.71 ppm, with a relative integration of 2, was assigned as H1. Once again, no NOESY correlations were observed between protons on the phenol and benzothiadiazole rings. However, notable NOESY correlations were observed between H9 and H5, as well as between H9 and the phenolic proton, as depicted in **Figure 2-10**.

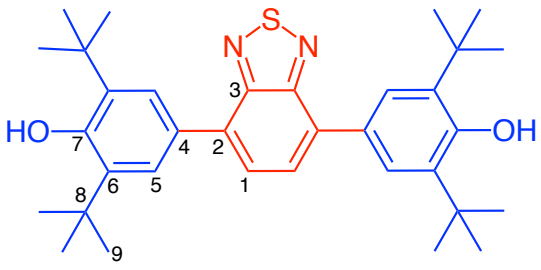

#	^{1}H-^{13}C HMBC
C1	-
C2	H1
C3	H1
C4	H5, H1
C5	H5, H9
C6	H5, H9, OH
C7	H9, OH
C8	H5, H9
C9	H9

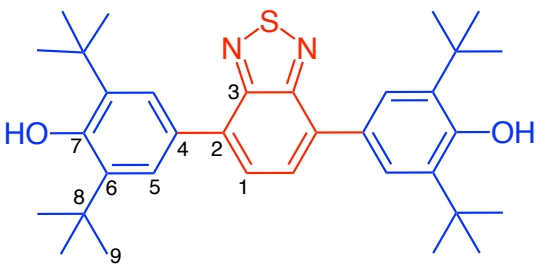

#	^{1}H	^{13}C
1	**7.71**	**127.71**
2	-	129.10
3	-	154.75
4	-	133.57
5	**7.82**	**126.62**
6	-	136.24
7	-	154.55
8	-	34.88
9	**1.54**	**30.73**
OH	5.39	-

Table 2-3. ^{1}H and ^{13}C assignments for **2.15**.

^{1}H-^{1}H NOESY Correlations

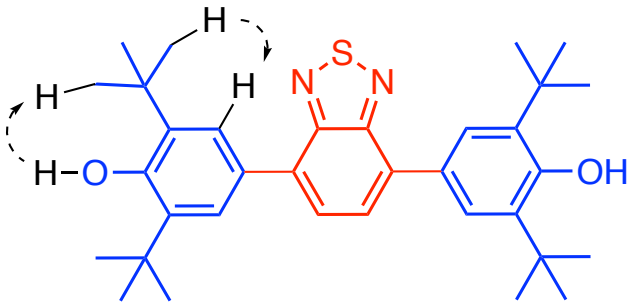

Figure 2-10. ^{1}H-^{1}H NOESY correlations in **2.15**.

Consistent with previous findings, the ^{1}H-^{13}C HSQC correlations, highlighted in bold, facilitated the assignments of H1, H5, and H9 to their respective carbons. The remaining assignments were accomplished employing ^{1}H-^{13}C HMBC experiments. Notably, the correlation between C3 and H1, combined with its pronounced downfield shift, led to its assignment as depicted. The resonance at 129.10 ppm was attributed to C2. Surprisingly, this chemical shift appears slightly upfield compared to the corresponding C5 resonance in **2.14**. However, this observation can be rationalized by the symmetry of **2.15**, whereby it becomes evident that C2 experiences shielding relative to its counterpart carbon in **2.14**, as illustrated in the resonance scheme presented in **Figure 2-11**. The remaining ^{13}C resonances were successfully assigned based on their respective HMBC correlations.

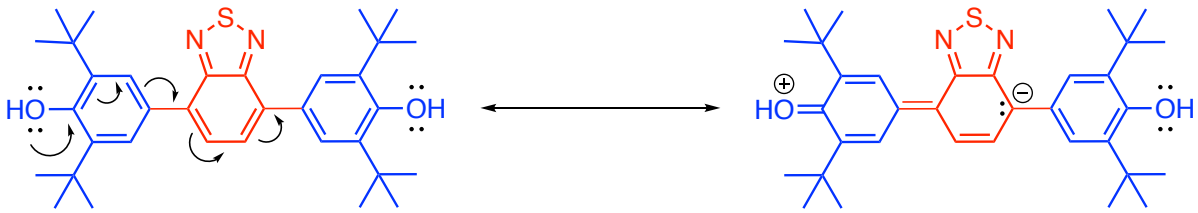

Figure 2-11. Resonance structure showing shielding at C3.

2.3 Squaraine Dye Target Compound **2.25**

2.3.1 Synthesis and Purification

Having successfully optimized the synthesis of the desired DA building block **2.14**, we next approached one of the two envisioned final dye compounds detailed in this thesis. To chart the synthetic path towards **2.25**, an excerpt of the previously described retrosynthetic analysis is shown in **Scheme 2-7**. The forward synthesis begins with readily accessible 4-bromophenylhydrazine (**2.17**) and 3-methyl-2-butanone (**2.16**) and follows previous reports.[134,145]

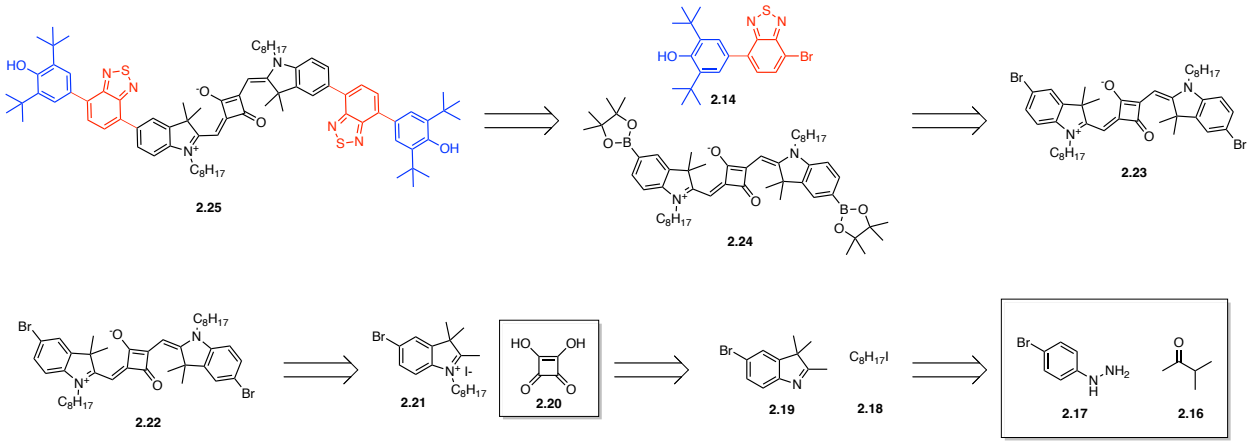

Scheme 2-7. Retrosynthetic analysis towards the synthesis of the final dye compound **2.25**.

This initial stage of the synthesis involved the Fischer indole synthesis, as depicted in **Scheme 2-8**, between compounds **2.16** and **2.17**. Refluxing both compounds in acetic acid for 4 hours followed by isolation generated a red oil product in 90% yield. The nitrogen in the indolenine moiety can then be alkylated using standard S_N2 substitution, seamlessly progressing from the Fischer indole synthesis product.

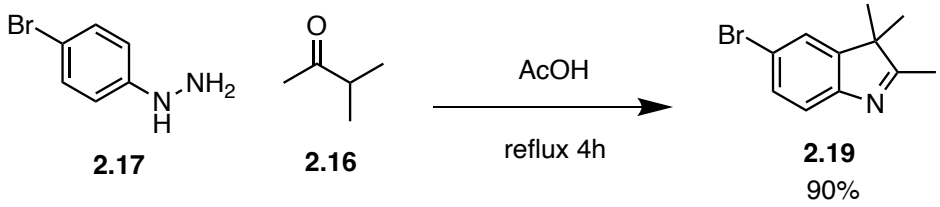

Scheme 2-8. Synthesis of **2.19**.

Initially, we postulated that the target squaraine dye **2.25** could suffer from poor solubility. To enhance the solubility of the target dye compound in organic solvents, we sought to incorporate a long alkyl chain. To achieve this, a well-established method from the literature was employed to

install a hexadecyl chain through substitution with the corresponding iodoalkane, as illustrated in **Scheme 2-9**.[146] The quaternization process involved refluxing compound **2.19** with iodohexadecane (**2.32**) in acetonitrile for 4 hours, resulting in a 46% yield of the desired product. Isolation of the product was achieved by washing with diethyl ether to remove soluble impurities including unreacted **2.32**.

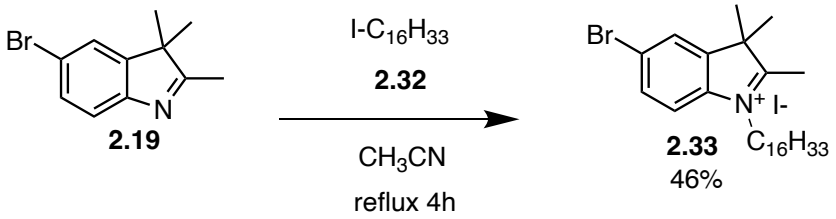

Scheme 2-9. Synthesis of **2.33**.

Subsequently, a condensation reaction between **2.33** and **2.20** to form squaraine dye **2.23** would be performed by refluxing overnight in a 1:1 mixture of toluene and 1-butanol shown in **Scheme 2-10**. In the literature procedure, a Dean-Stark apparatus was utilized to drive the reaction towards the product by removing water from the reaction flask. However, in our experiments, it was determined that the use of the Dean-Stark apparatus was unnecessary, as our yields were comparable to those reported in the literature without its use.

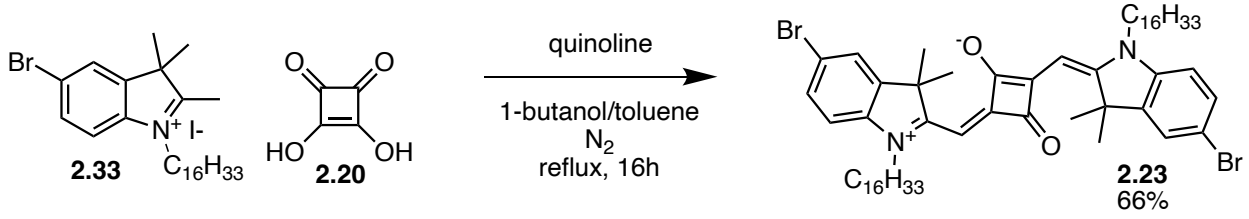

Scheme 2-10. Synthesis of **2.23**.

As anticipated, compound **2.23** exhibited good solubility in a wide range of organic solvents, expanding its potential applications. However, this high solubility posed challenges during the purification process. To address this, we employed column chromatography over silica gel using a 3:1 mixture of light petroleum ether and ethyl acetate as the eluent. After successfully isolating the pure compound, we noted that it exists as a sticky blue solid rather than a crystalline solid, likely due to the presence of the long alkyl chains. This led to challenges in material handling of this compound.

Considering these handling challenges, we explored the use of iodooctane as an alternative alkylating agent following the synthetic route described in **Scheme 2-11**, as previously reported by Kuster and Geiger.[133] The yields achieved using iodooctane were comparable to those obtained with the hexadecyl chain in both the quaternization and condensation steps. Notably, during the condensation reaction depicted in **Scheme 2-12**, we discovered that purification could be conveniently accomplished by employing a mixture of ethanol and a 10% aqueous citric acid solution, which facilitated the precipitation of the solid product. The resulting compound was isolated an iridescent green powder, rendering it easier to handle, while demonstrating similar solubility properties to **2.23**. Consequently, this variant was selected as the squaraine core for the synthesis of the final dye compounds.

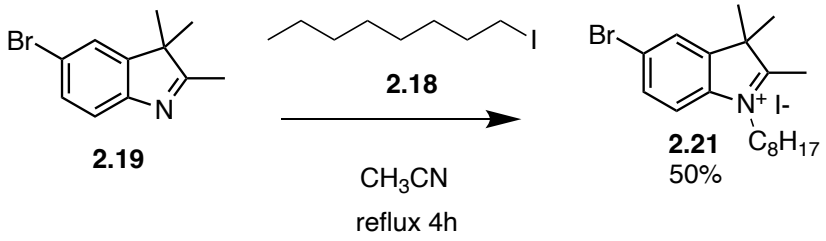

Scheme 2-11. Synthesis of **2.21**.

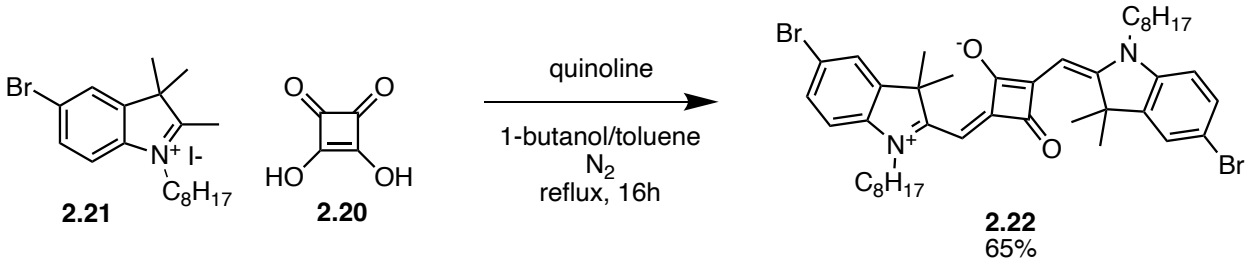

Scheme 2-12. Synthesis of **2.22**.

The installation of pinacol boronate esters at both ends of the squaraine framework was achieved through Pd-catalyzed Miyaura borylation reaction, following the synthetic procedure outlined in **Scheme 2-13**. The literature protocol was executed without any modifications,[133] resulting in the isolation of compound **2.24** in 77% isolated yield.

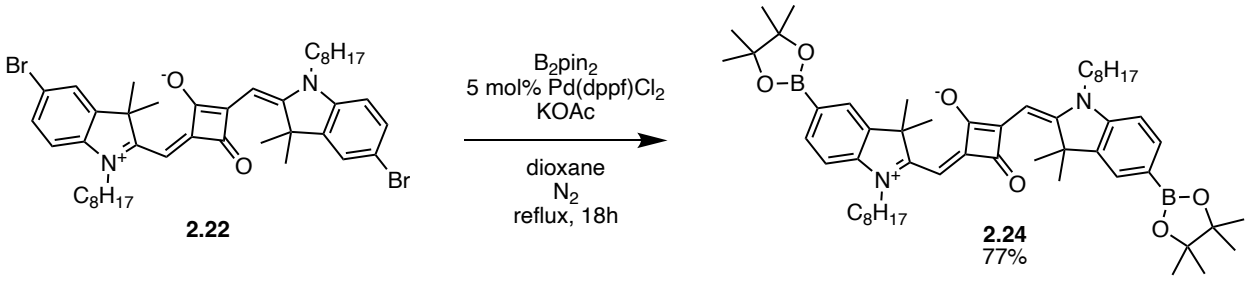

Scheme 2-13. Synthesis of **2.24**.

After successfully isolating **2.24**, we proceeded to investigate the feasibility of the Suzuki cross-coupling reaction using the previously described mixture of **2.14** and **2.15** (**Scheme 2-14**). To achieve this, we used 10 mol% of $Pd(P(tBu)_3)_2$ catalyst in a mixture of THF and water with a 1:1 ratio, while potassium acetate served as the base. The reaction mixture was heated to reflux and allowed to proceed overnight under an inert atmosphere. Subsequently, the crude reaction mixture was subjected to filtration, followed by concentration and recrystallization in ethanol at -4°C. Through this process, compound **2.25** was obtained in a satisfactory yield of 52% and the chemical formula was confirmed using high-resolution electron-spray ionization mass spectrometry (HRESI-MS).

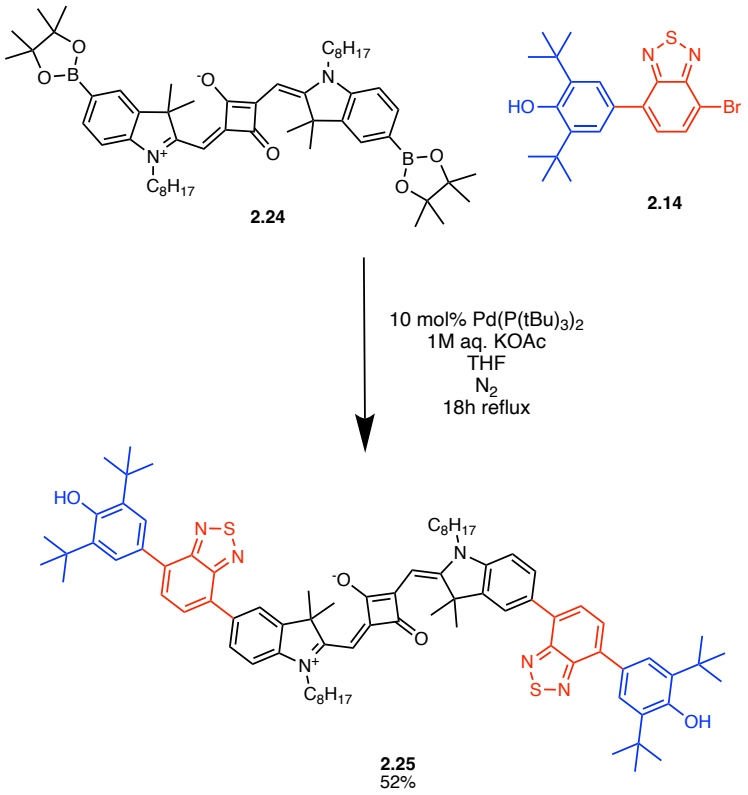

Scheme 2-14. Synthesis of final dye compound **2.25**.

2.3.2 NMR Spectroscopy Characterization of **2.25**

The NMR spectroscopy assignments for **2.25** are presented **Table 2-4**, obtained using a comprehensive range of NMR spectroscopy experiments. While the symmetry of the compound facilitated straightforward assignments of the ^{1}H NMR spectroscopy spectrum, the ^{13}C NMR spectroscopy assignments necessitated the utilization of ^{1}H-^{13}C HMBC and ^{1}H-^{13}C HSQC NMR spectroscopy techniques.

Compound **2.25** contains 33 distinct carbon atoms. Notably, resonance structures associated with the cyclobutenolate core, as depicted in **Scheme 2-15**, illustrates equivalence of the two carbonyl groups. Thus, these two carbons appear as one signal at 179.84 ppm in the ^{13}C NMR spectrum. Additionally, resonance between the two indolenine nitrogens, as illustrated in **Scheme 2-16**, leads to a high degree of symmetry, and therefore simplifies NMR spectroscopy assignments.

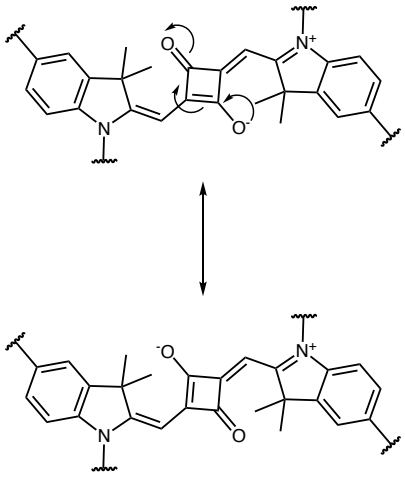

Scheme 2-15. Resonance structure between the two oxygens on the cyclobutenolate core of **2.25**.

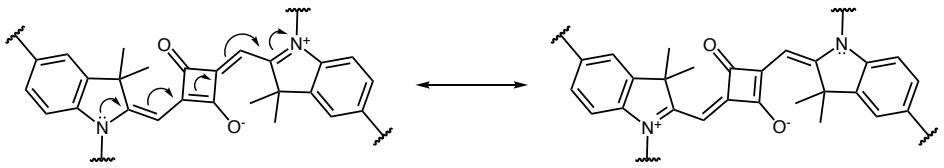

Scheme 2-16. Resonance structure between the two indolenine nitrogens in **2.25**.

The C4 carbon exhibits a substantial downfield chemical shift owing to its pronounced electron deficiency resulting from the presence of the cationic nitrogen. Assignments of quaternary carbons were made based on the ^{1}H-^{13}C HMBC correlations as outlined in **Table 2-4**.

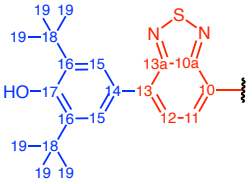

#	^{1}H	^{13}C	#	^{1}H	^{13}C
14	-	154.58	10	-	131.90
15	**7.84**	**126.53**	10a	-	154.33
16	-	136.20	**11**	**7.79**	**128.06**
17	-	154.61	**12**	**7.74**	**127.43**
18	-	34.74	13	-	134.33
19	**1.54**	**30.56**	13a	-	128.68
OH	5.42	-			

#	^{1}H-^{13}C HMBC	#	^{1}H-^{13}C HMBC
C14	OH, H15	C10	H8, H6, H12
C15	H19	C10a	H11
C16	OH, H15, H19	C11	-
C17	OH, H15	C12	-
C18	H15, H19	C13	H15, H11
C19	H15	C13a	H12

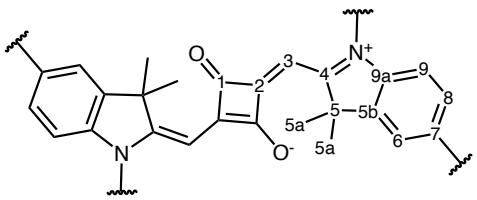

#	^{1}H	^{13}C	#	^{1}H-^{13}C HMBC
1	-	179.84	1a	-
2	-	132.52	2	-
3	**6.05**	**87.42**	**3**	-
4	-	170.11	4	H5a
5	-	49.61	5	H6, H2, H5a
5a	**1.90**	**27.39**	**5a**	H5a
5b	-	142.95	5b	H6, H9, H5a
6	**7.92**	**123.31**	**6**	H8
7	-	133.56	7	H9
8	**8.02**	**129.35**	**8**	H6
9	**7.15**	**109.56**	9	-
9a	-	142.70	9a	H8, H6

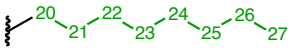

#	^{1}H	^{13}C	#	^{1}H-^{13}C HMBC
20	**4.05**	**44.16**	**20**	-
21		31.96	21	H27
22		30.51	22	-
23	1.50-1.25	29.56	23	-
24		29.37	24	-
25		27.33	25	-
26		22.80	26	H27
27	**0.89**	**14.27**	**27**	-

Table 2-4. ^{1}H, ^{13}C and 2D NMR spectroscopy assignments for **2.25**. Bolded entries indicate HSQC correlations.

2.4 Toward the Synthesis of a Sterically-Hindered Squaraine Dye

To assess the effect of substitution pattern on the properties of our dye compounds, we sought access to an unreported squaraine dye **2.29**, as depicted in **Scheme 2-17**. Building upon the synthetic protocol used for the synthesis of compound **2.22**, we reasoned that the formation of compound **2.29** can be achieved through a similar condensation reaction involving quaternized indolinium compounds **2.28** and compound **2.20**. The synthesis of compounds **2.28a-c** can be achieved using an S_N2 reaction with an electrophilic iodoalkane, while the precursor compound **2.27** can be prepared using readily available starting materials **2.26** and **2.16**. From **2.29**, we hypothesized that **2.31** would be accessible via Suzuki-Miyaura chemistry using **2.14** and boronate pinacol ester **2.30,** as shown in **Scheme 2-18.**

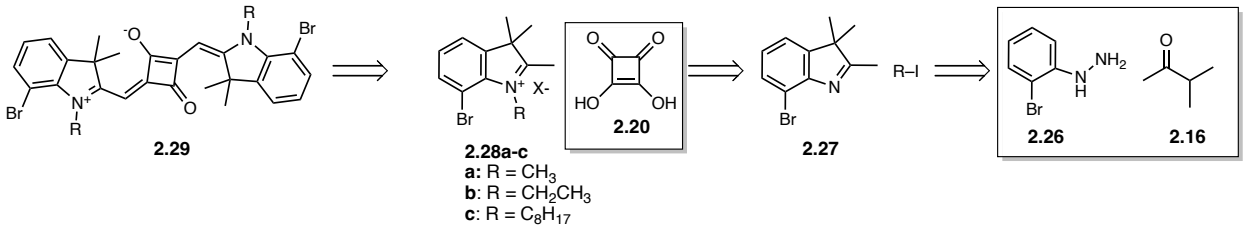

Scheme 2-17. Retrosynthesis towards **2.29**.

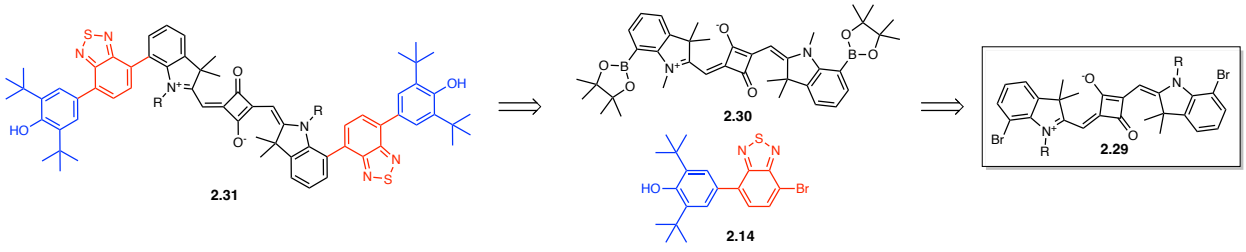

Scheme 2-18. Synthetic proposal towards **2.31**.

To access compound **2.27**, we conducted a Fischer indole synthesis, as illustrated in **Scheme 2-19**. This synthetic transformation yielded a deep red oil with an isolated yield of 85%. The resulting compound **2.27** was subsequently characterized using both ^{1}H and ^{13}C NMR spectroscopy techniques to confirm its structural identity.

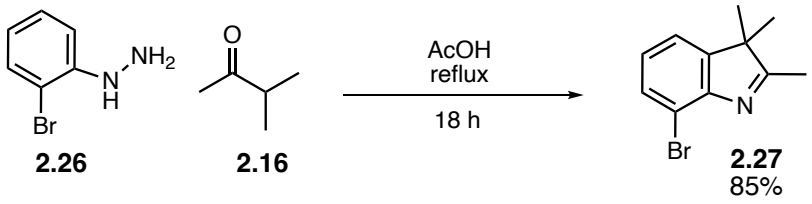

Scheme 2-19. Synthesis of **2.27**.

The obtained product was subsequently used in the quaternization reaction. Our aim in synthesizing compound **2.31** was to enhance the steric interaction between the substituent at the 7-position of the squaraine core and the appended substituent. We hypothesized that the alkylation of this nitrogen would pose challenges due to the use of alkyl chains ranging from 8 to 16 carbons in length, and our experimental results confirmed this hypothesis. **Scheme 2-20** illustrates the attempted reaction conditions employed for this alkylation process.

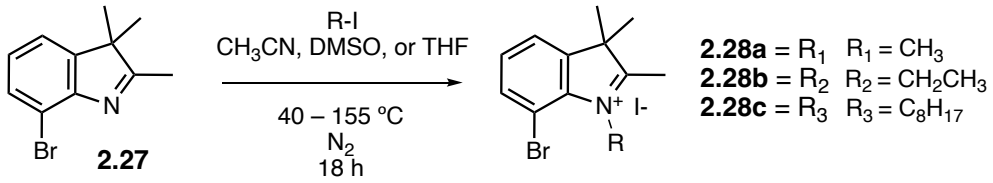

Scheme 2-20. Synthetic scheme for synthesis of **2.28a-c**.

The optimization of the quaternization reaction was conducted by undergraduate research student Max Strasser, as depicted in **Table 2-5**. Three different alkylating agents, namely iodooctane, iodoethane, and iodomethane, were explored. Initially, acetonitrile with R_1 was tested but did not yield any desired product. Subsequently, THF and DMSO were tested, considering their varying polarities and boiling points, yet they also failed to produce the desired compound. Among the electrophilic candidates, iodomethane proved to be the only successful reagent. Refluxing the reaction mixture in THF resulted in the formation of compound **2.28a** with a yield of 31%. Initially, it was speculated that the volatility of iodomethane might be affecting the reaction yield. To mitigate this issue, the reaction was performed in an air-tight vial, but the yields remained unaffected. Ultimately, it was discovered that increasing the equivalents of MeI and heating the reaction overnight neat (without solvent) allowed for the isolation of a significant quantity of **2.28a**, facilitating its further use in the synthesis process (**Scheme 2-21**).

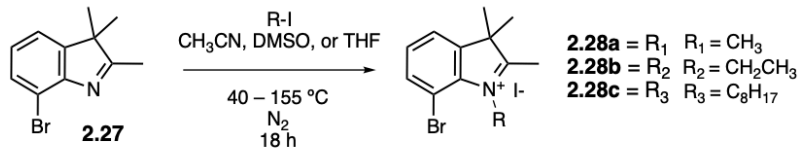

R-I	Conditions	Yield
$C_8H_{17}I$	CH_3CN, 80 °C	0%
	THF, 120 °C	0%
	DMSO, 155 °C	0%
CH_3CH_2I	CH_3CN, 80 °C	0%
	DMSO, 155 °C	0%
CH_3I	THF, 40 °C	7%
	THF, 60 °C	14%
	DMSO, 60 °C	4%
	DMSO, 130 °C	7%
	THF, 80 °C	31%

Table 2-5. Optimization screen for synthesis of indolinium **2.28a-c**.

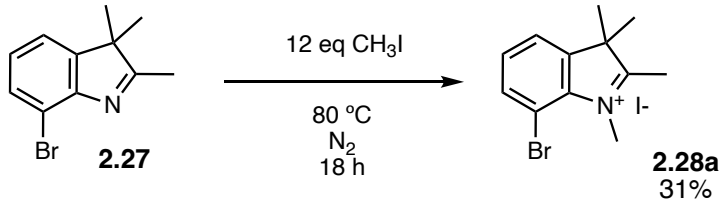

Scheme 2-21. Optimized synthesis of **2.28a**.

Clearly, the positioning of the bromine proved to have a significant impact on the alkylation of the indolenine nitrogen. Fortunately, this positioning did not affect the condensation reaction of **2.28a** with squaric acid, enabling the production of compound **2.29** with a yield of 92% (**Scheme 2-22**).

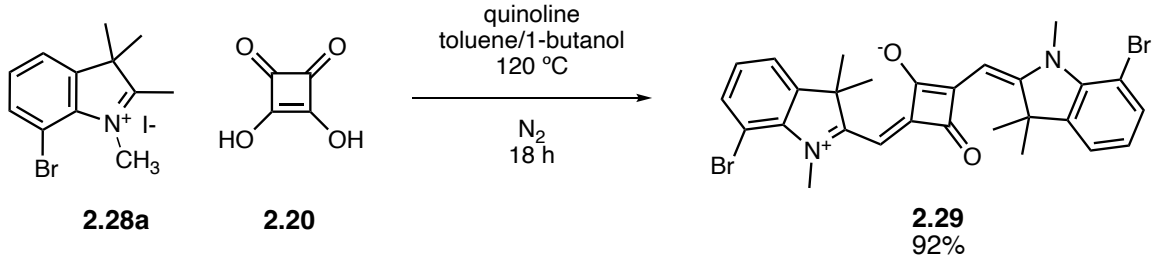

Scheme 2-22. Synthesis of **2.29**.

Considering the difficulties encountered in methylating the nitrogen, we anticipated challenges in borylating this position using B_2pin_2. Initial attempts, following the conditions used in the synthesis of **2.24** (**Scheme 2-23**), proved unsuccessful as observed by ^{1}H NMR spectroscopy. Subsequently, we explored alternate ligands. SPhos, known for its high catalytic activity and air stability in Suzuki cross-coupling reactions, was chosen.[147,148] However, after conducting two reactions in dioxane and THF, no evidence of reaction was observed by ^{1}H NMR spectroscopy. We also investigated PCy_3, known for its large cone angle,[149] but once again, ^{1}H NMR spectroscopy revealed no signs of reaction.

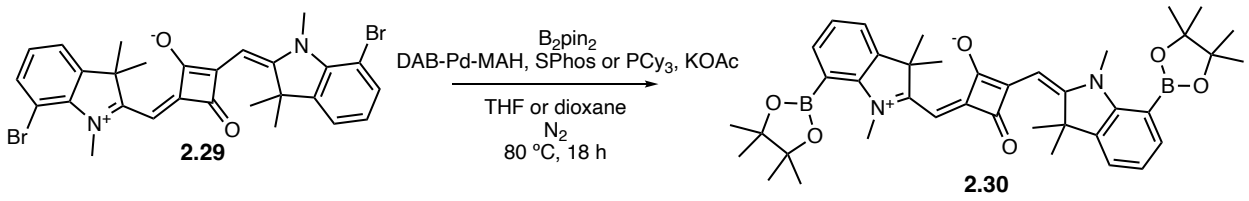

Scheme 2-23. Synthetic pilot reactions towards **2.30**.

Based on the outcomes of the four attempted Miyaura borylations, a high-throughput screening experiment was conducted. This involved testing two Pd sources, six ligands, two bases, and one solvent. The layout and results of this screening are presented in **Table 2-6** including the structures of all ligands used in **Figure 2-13**. Surprisingly, no evidence of the borylated compound **2.30** was observed. However, in two cases, we observed 100% conversion of the starting materials to the protodehalogenated compound **2.35** (**Figure 2-12**). While this does indicate that oxidative addition can occur at this hindered position, there are clearly further challenges to installing the boronic pinacol ester group. Due to time constraints, this avenue was not pursued further, though additional screening and optimization could reveal successful conditions.

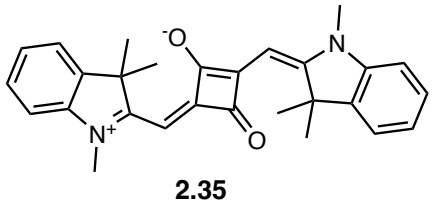

Figure 2-12. Compound **2.35** as the protodehalogenated product of the Miyaura borylation reaction from **Scheme 2-21**.

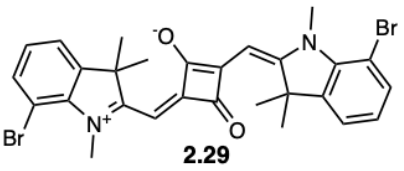

B_2pin_2
Pd source, ligand, base
THF
N_2
80 °C, 18 h

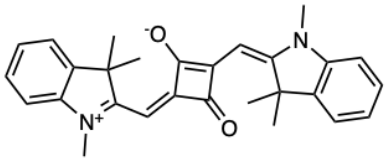

CyJohnPhos	0%	0%	43%	100%
MePhos	0%	0%	0%	0%
DavePhos	0%	0%	0%	100%
RuPhos	0%	0%	0%	0%
Cphos	0%	0%	0%	0%
P(o-OMePh)3	0%	0%	0%	0%
	KOAc	K_2CO_3/PivOH	KOAc	K_2CO_3/PivOH
	$Pd(OAc)_2$		DAB-Pd-MAH	

Table 2-6. Optimization conditions used for the synthesis of **2.30**. ^{1}H NMR spectroscopy yields are referring to yields of **2.35**. All red cells indicate no change from starting materials.

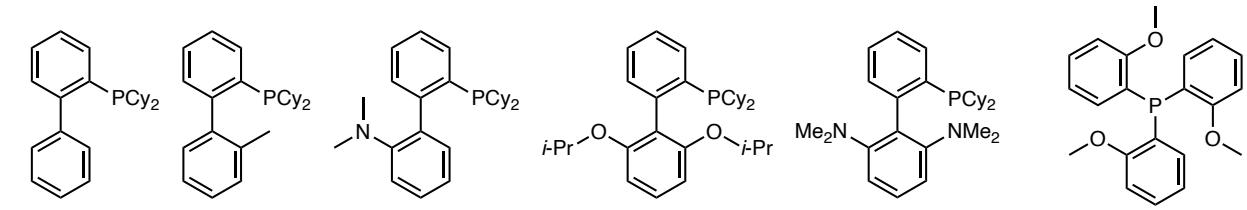

Figure 2-13. Ligands used in HTS experiment outlined in **Table 2-6**.

2.5 Conclusion

In conclusion, one of two target dye compounds were synthesized and characterized by NMR spectroscopy. The synthetic pathway to reach **2.25** was modified slightly in the synthesis

towards **2.31**. The increased steric hindrance arising from the position of the bromine in compound **2.27** had a pronounced negative effect on compound yields. Still, we were able to isolate and characterize **2.28a** and carry this compound forward to synthesize squaraine **2.29** in high yield.

Our subsequent attempts to install a boronate ester were unsuccessful using $B_2(pin)_2$, resulting in the protodehalogenated species **2.35**. We propose that by use of a HTS experiment utilizing $B_2(Epin)_2$ as a boron source based on the current literature, it may be possible to successfully synthesize the boronate ester required for Suzuki-Miyaura cross coupling to afford **2.31**.

We were also able to successfully isolate **2.14** and **2.15** in sufficient yields for complete characterization. Full NMR spectroscopic assignments were made, and the synthetic protocol was discussed in-depth. Further optimization is required to increase product yields, and further characterization of these compounds are discussed in Chapter 3.

Chapter 3 Properties of Key Compounds

3.1 Introduction

This aims of this chapter is to conduct comprehensive examination of the pivotal compounds, specifically **2.14**, **2.15**, and **2.25**, whose syntheses were outlined in Chapter 2. The primary objective was to delve into the characterization of CT character within these molecules, employing advanced photophysical techniques such as UV-Visible (UV-Vis) and fluorescence spectrophotometry. Building upon the discussions in Chapter 1, these experiments served as a powerful tool to monitor and analyze the changes in emission behavior as we explored solvents with varying polarities. Consequently, we aimed to observe the phenomenon of solvatochromic fluorescence, gaining valuable insights into CT properties.

In addition, our investigation delved into the redox properties of the key compounds. By employing cyclic voltammetry, we quantitatively assessed the oxidation and reduction potentials of our molecules to observe a change in the oxidation potentials with increasing acceptor strength. These experimental findings were pivotal in selecting an appropriate oxidant with the necessary strength to facilitate the oxidation of our compounds, enabling their transformation into their respective open-shell counterparts. The characterization of these open-shell forms could be further examined through techniques such as electron paramagnetic resonance spectroscopy.

To augment and reinforce our experimental observations, we employed density-functional theory in conjunction with cyclic voltammetry to investigate the electronic structures of our key compounds. This approach provided invaluable insights into the frontier molecular orbitals, including their respective energies, offering a deeper understanding of the electronic structure and properties of the investigated molecules.

3.1.1 General Analysis of DA Compounds

To characterize compounds **2.14**, **2.15**, and **2.25**, we sought to examine the photophysical data supporting CT. Characterization of CT properties in such compounds is done using photophysical techniques such as UV-Vis and fluorescence spectrophotometry. When used in conjunction, these methods can demonstrate solvent effects on either the ground or excited states. The key characteristics that are attributed to ICT character are solvent-dependent red-shifting and emission intensity.[150,151] Concentration-dependent fluorescence experiments can be used to show aggregation, or decreased fluorescence intensity as a function of solvent polarity.[152,153] These results may be supported qualitatively by time-dependent density functional theory (TD-DFT).

We additionally aimed to characterize the change in CT after oxidation of these key compounds. Hence, we further aim to explore the redox properties of **2.14, 2.15,** and **2.25** by cyclic voltammetry (CV). The resulting oxidation potentials are used to better understand the oxidation potentials of these compound. Using this, we can test different oxidants and employ the photophysical techniques discussed in the previous paragraph to monitor for oxidation. These are used to benchmark how ICT characteristics change with the loss of electron density on the donor or otherwise oxidized species. Again, these results can be compared the TD-DFT results to give a qualitative view of how the frontier molecular orbitals (FMOs) are affected.

As our aim was to isolate a phenoxyl radical, we sought to characterize these oxidized compounds using a variety of experiments. One of such experiments is proton NMR spectroscopy. In the case of closed-shell molecules, oxidation will lead to distinct changes in the proton NMR spectra. Key evidence for paramagnetism using this method is line-broadening. Line-broadening arises from perturbations of the Larmor frequency by the fluctuating local magnetic fields of nearby magnetic nuclei or unpaired electrons.[154] This method has been used in the literature to

monitor the presence of free radical intermediates.[155] By this method, one can easily conduct a single-electron oxidation experiment and check its success by proton NMR spectroscopy. However, it is not always the case that one will see line-broadening as the relaxation time for single electrons can occur outside of the NMR spectroscopy time-scale, resulting in NMR spectroscopy-silent radicals.[156] In this case, it is best to use the appearance of new absorption peaks together with EPR spectroscopy to confirm the presence of such NMR spectroscopy-silent paramagnetic species.

Using TD-DFT in tandem with experimental results, the natural transition orbitals (NTOs) where excited state transitions and energy levels lie can be determined. The highest occupied molecular orbital (HOMO) and lowest unoccupied molecular orbital (LUMO) can give insight to where oxidation and reduction occur, allowing us to better understand experimental CV results.

3.1.2 Cyclic Voltammetry of Phenolic Compounds and Squaraine Dyes

CV is a technique used to measure the redox potentials of redox active molecules. The general principle involves passing current through a solution containing pure analyte with a supplementary electrolyte. Solvent is an important parameter as it is necessary to examine all molecules within a redox window that does not lead to the deterioration of solvent or electrolyte. As the potential is scanned, any redox events will lead to a change in the current and thus leads to a potential versus current plot that gives information on the molecule such as chemical and electrochemical reversibility, each important for redox active molecules. A full review on the technique can be found in the literature.[157]

Specifically, the redox potentials of phenols have been studied at great lengths over the past century. Richards *et al.* showed the redox potentials of 2,4,6-tri-*tert*-butyl phenol in the polar

aprotic acetonitrile and polar protic ethanol/water mixture.[158] Using an alkaline ethanol and water mixture, it was shown that the oxidation of the phenoxide anion to the phenoxyl radical is highly reversible, where the resulting species are shown in **Figure 3-1**. This reversibility disappears at pH values lower than 10 due to the reactivity of the phenoxonium cation with water and eventual downstream reactivity to form 2,6-di-*tert*-butylquinone shown in **Figure 3-2**.

The radical species shown in **Figure 3-1** is destabilized due to the *para*-substituent being electron donating. This species has been examined in great depth, where stability of the tri-*tert*-butylphenoxy radical containing 35 different substituents was further examined in 1991 by Bordwell and Cheng.[159] The oxidation potential of this species has been officially characterized at +1.07 V with respect to Fc/Fc+ at pH below 10.

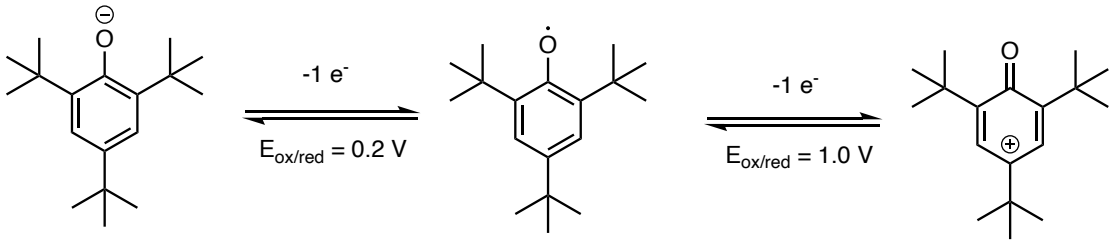

Figure 3-1. Redox activity of 2,4,6-tri-*tert*-butylphenoxide at pH 10 vs. SCE.

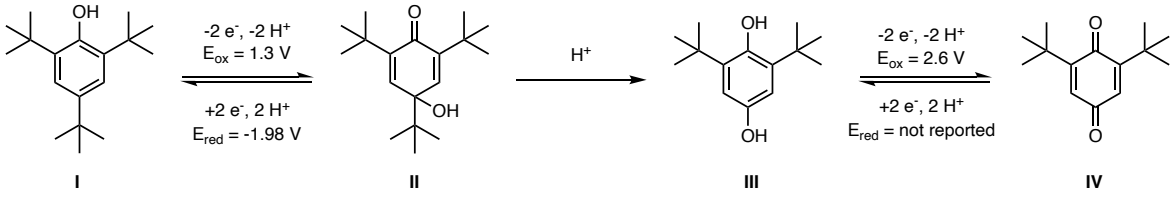

Figure 3-2. Redox activity of 2,4,6-tri-*tert*-butylphenol below pH 10 vs. SCE

Phenolate anions are more electron rich than their neutral counterparts. Subsequently, phenoxyl radicals have been reported to be accessed primarily in alkaline conditions. The oxidation potential of tri-*tert*-butylphenol for example has been reported to be -0.68 V in the presence of sodium hydroxide,[160] a 1.39 V difference compared to the oxidation potential under neutral conditions. Mechanistically, electron transfer from the anion to become the neutral radical is far simpler and does not involve the intermediate and reactive radical cation. When accessing the phenoxyl radical from the neutral phenol, the radical cation will tend to undergo another one electron oxidation to preferentially form the phenoxonium cation and a release proton as shown in the example above. It is therefore advantageous to utilize basic conditions when attempting to oxidize phenols.

The redox activity of squaraines has also been studied extensively. The cyclic voltammogram of non-functionalized indolenine-containing squaraine dyes has been reported to have two reversible oxidation events, one reversible reduction event and one irreversible reduction event. These oxidation and reduction events are not described in the literature, but the hypothetical oxidations and reductions are shown in **Figure 3-3**.[161] This can be used as a benchmark for understanding the redox properties of **2.25** which contains a indolenine squaraine core.

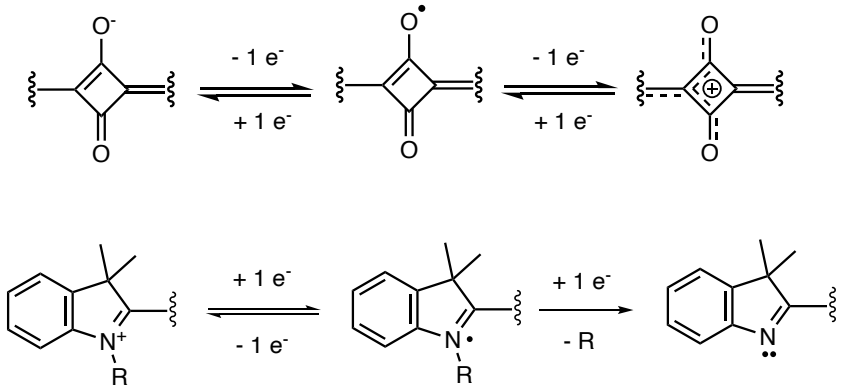

Figure 3-3. Two hypothetical reversible oxidation events (top) and two hypothetical reduction events (bottom) for unsubstituted bisindolenine squaraine dyes.

3.1.3 Electron Paramagnetic Resonance (EPR) of Phenoxyl Radicals

Phenoxy radicals are paramagnetic species with S = ½. In general, most phenoxyl radicals show isotropic g-tensor values between 2.003 and 2.007.[162] The EPR spectrum of 2,4,6,-tri-*tert*-butylphenoxy radical is reported to have three principal g-tensor components equal to 2.0072, 2.0043 and 2.0024 which can be resolved at frequencies higher than 95 GHz.[163] In solution the isotropic g-value is reported as 2.00495.[164] These values do not shift much in semiquinone like structures as reported by Prabhananda and this allows for easy characterization of such radicals by EPR spectroscopy.

3.2 Photophysical Studies

3.2.1 UV-Visible and Fluorescence Spectroscopy of **2.14**

After isolating and purifying **2.14**, we proceeded to perform UV-Visible and fluorescence spectroscopy experiments to detect any signs of charge transfer. Initially, we dissolved a small quantity of the compound in various solvents, which were then arranged in order of increasing polarity. Subsequently, the samples were exposed to UV light. The resulting qualitative fluorescence profile, captured in **Figure 3-4**, is presented below illustrative purposes.

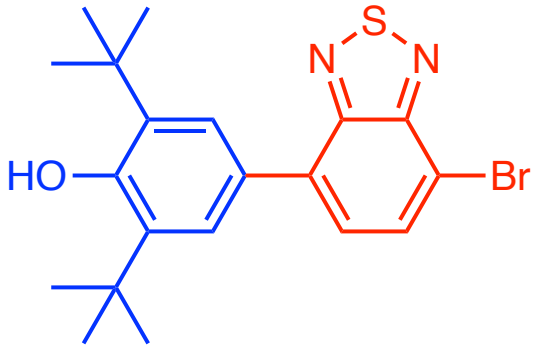

2.14

Figure 3-4. 2.14 illuminated with UV light displaying solvatochromic fluorescence.

To measure the absorption and emission characteristics, we gathered absorption and emission spectra for each of the solvents mentioned earlier. The absorption profile exhibited a consistent λ_{max} across varying solvent polarities, as depicted in **Figure 3-5**. However, the fluorescence profile revealed a noticeable redshift, providing compelling evidence of charge transfer taking place. These findings imply that solvent polarity has minimal impact on the stability of the ground state, but significantly influences the energetic behavior of the relaxation mechanism in the excited state.

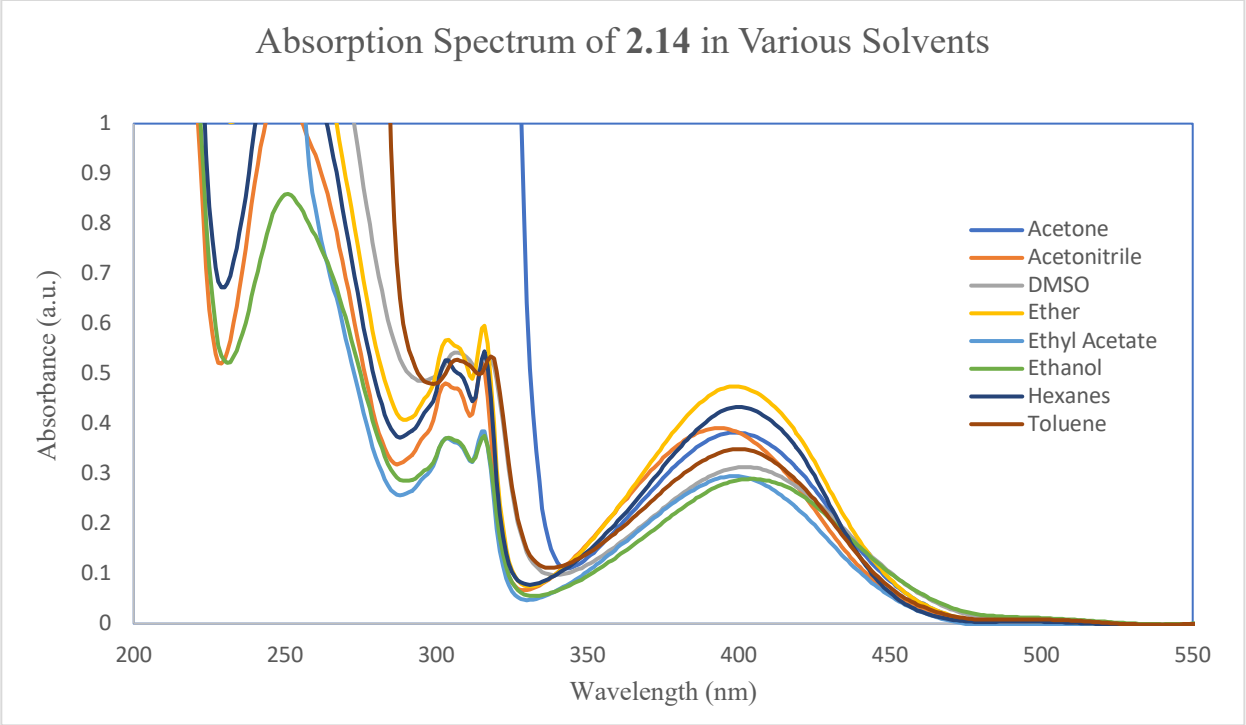

Figure 3-5. Absorbance spectra overlay of **2.14** in various solvents.

The emission profile of **2.14** was normalized to highlight the evident redshift in emission. Unfortunately, technical difficulties during the emission measurements in acetonitrile resulted in the loss of the curve's tail, as illustrated in **Figure 3-6**. Both the absorption and emission wavelengths can be found in **Table 3-1**. While the precise concentrations of the samples were not recorded due to a shortage of the compound, their estimated values were approximately in the range of 10^{-1} mM. This, coupled with the observed solvation effect, holds great promise as it indicates CT character.

Notably, no indication of dual fluorescence was observed in the compound's emission profile, suggesting that TICT may not be occurring. Furthermore, no emission was detected in DMSO or ethanol. It is well-known that polar solvents like water or alcohols can significantly reduce the fluorescent quantum yields (FQYs) of emitters due to the prevalence of nonradiative decay pathways.[165,166]

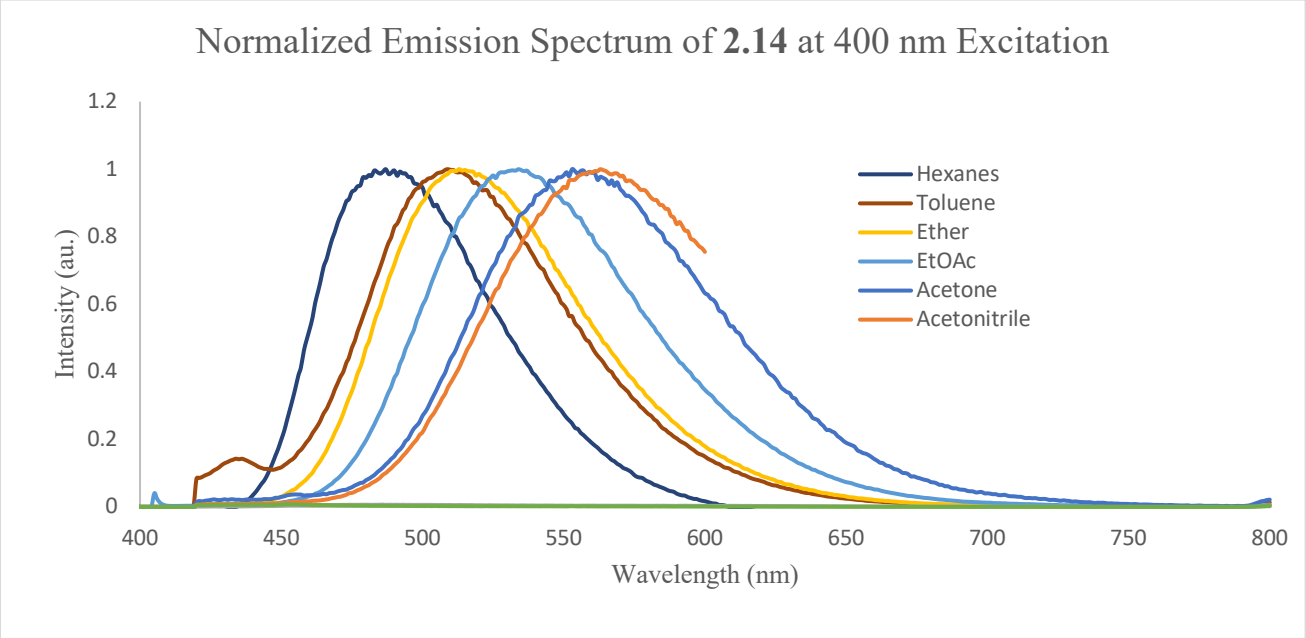

Figure 3-6. Normalized emission profile of **2.14** in various solvents.

Table 3-1. Absorption and emission wavelengths of **2.14** in various solvents.

Solvent	λ_{abs} (nm)	λ_{em} (nm)
hexanes	404	491
toluene	400	508
diethyl ether	402	512
ethyl acetate	397	536
acetone	400	557
ethanol	405	-
acetonitrile	398	567
DMSO	403	-

The lack of dual fluorescence can be a result of a few factors. The TICT state results from the decoupling of the donor and acceptor through a radical cation and anion. The strength of the donor and acceptor are therefore important in determining the likelihood of TICT occurring. This can be described using the following equations put forth by Rettig *et al.*[167,168]

$$E_{LE} - E_{TICT} > 0 \quad \textbf{(1)}$$

$$E_{TICT} = IP(D) - EA(A) + C + E_{solv} \quad \textbf{(2)}$$

The equation (**2**) considers the ionization potential of the donor (*IP(D)*) and electron affinity of the acceptor (*EA(A)*); *C* is the Coulombic attraction between the radical cation and anion; E_{solv} is the energy of the solvent stabilization and is typically negative. The energy of the LE (E_{LE}) state and TICT (E_{TICT}) state must be greater than zero described in equation (**1**). The IP(D) and EA(A) of **2.14** is not known but is presumably weaker than that of DMABN where TICT is well understood.[42] This is consistent with theory as alcohol π-donors are weaker than methylamine donors.

Another possible reason TICT may not be occurring is due to hydrogen bonding. The radical anion can end up on the nitrogen nearest the proton on the positively charged donor portion of the molecule as seen in **Figure 3-7**. This hydrogen bond may be interfering with the ability for the donor to rotate out of plane with the acceptor which would keep the two parts coupled through the planarity.

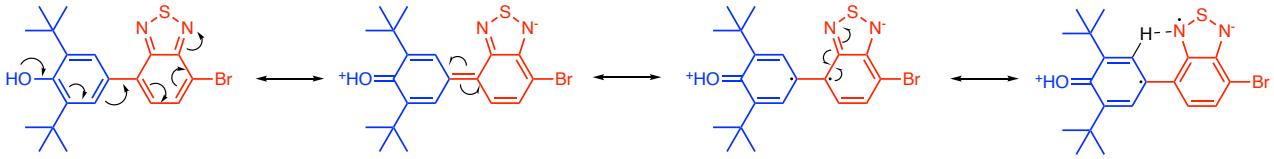

Figure 3-7. Plausible H-bonding restricting C-C bond rotation.

Experimental determination of molar absorptivity coefficients was conducted, and the results are presented in **Figure 3-8**. Notably, two prominent absorption peaks were observed at 305 nm and 317 nm, exhibiting a relatively sharp profile in comparison to the λ_{max} at 400 nm. According to the Frank-Condon Principle, this distinct behavior could be attributed to a certain degree of rigidity in the ground state, which more precisely defines the absorptions at these higher-energy wavelengths.[169] Intriguingly, when excited at these particular wavelengths, the resulting emission spectra matched that of the 400 nm excitation-emission wavelength corroborating a similar decay pathway to that of the aforementioned excitation wavelength.

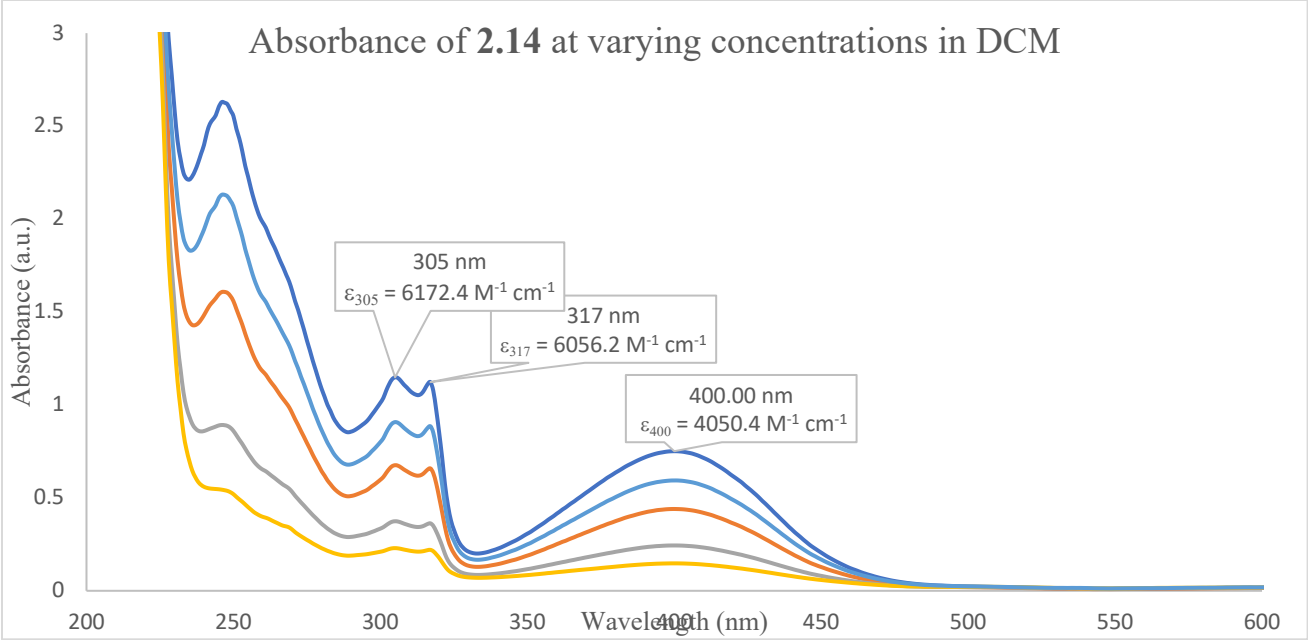

Figure 3-8. Concentration-dependent absorption profile of **2.14**.

The absorption characteristics of **2.15** were examined in DCM, revealing a peak absorbance at 415 nm, as illustrated in **Figure 3-9**. However, due to the limited yield of this compound and the challenges associated with isolating it in its pure form, there was an insufficient amount of material remaining to conduct additional absorption and emission measurements. As this particular compound did not hold substantial interest for our study, we decided against further exploration beyond its redox properties.

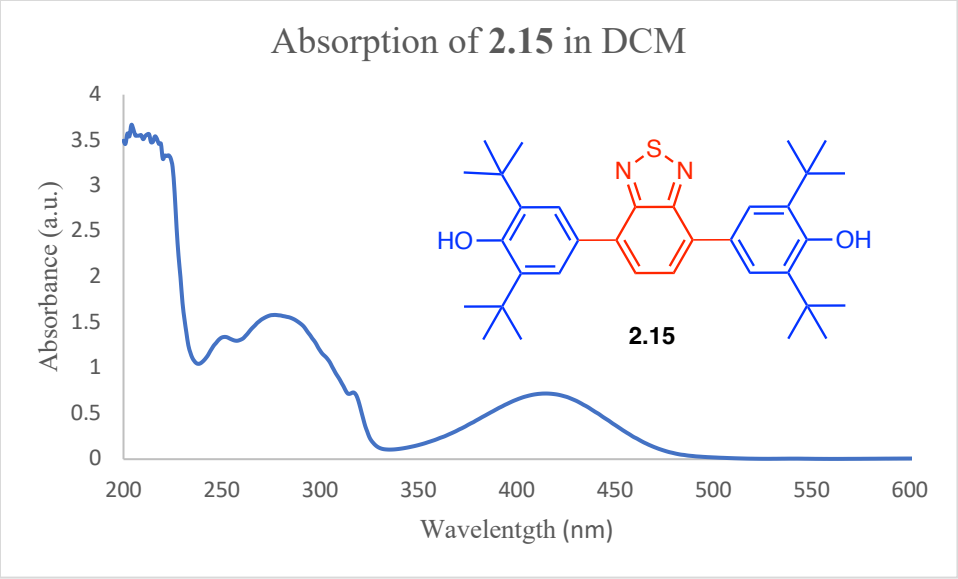

Figure 3-9. Absorption spectrum of **2.15** in DCM.

3.2.2 UV-Visible and Fluorescence Spectroscopy of **2.25**

The isolated squaraine dye **2.25** is a deep blue crystalline solid, while in solution displays a distinctive turquoise hue, as seen in **Figure 3-10**. UV-Vis measurements conducted on the compound in different solvents are presented in **Figure 3-11**. The molar extinction coefficient for the absorption peak around 675 nm is determined to be 1.65×10^5 M^{-1} cm^{-1}, which aligns with previously reported values for squaraine dyes in the literature. There also exists an absorption band at 410 nm with relatively weak compared to its maximum absorption, with an extinction coefficient of 9.52×10^3 M^{-1} cm^{-1}.

Notably, these measurements yield slightly varying outcomes compared to those of the precursor compound **2.14**. In the case of DMSO and toluene, a solvent-induced effect is evident, causing a redshift in absorbance up to 685 nm. For example, DMSO being a polar aprotic solvent with hydrogen bond acceptor properties, may engage in intermolecular hydrogen bonding with the dye molecules in solution leading to a redshifted absorption. Additionally, a secondary absorption

peak is observed towards the blue end of the spectrum, potentially arising from conformational barriers present in the ground state.

Figure 3-10. Solutions of **2.25** in various solvents.

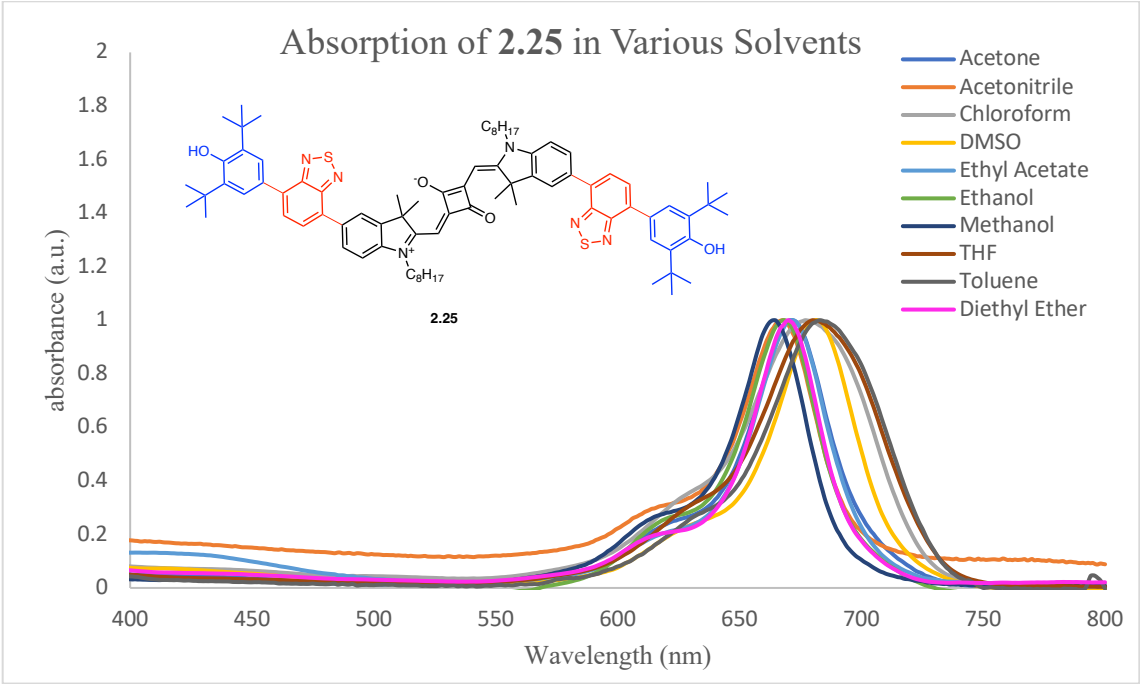

Figure 3-11. Normalized absorption spectra of **2.25** in various solvents.

The emission of the compound was subsequently monitored at concentrations of $2.0x10^{-3}$ mM using an excitation wavelength of 685 nm shown in **Figure 3-12**. In all tested solvents, a fluorescence band was observed at 708 nm, exhibiting a Stokes shift of approximately 20 nm. The results of this experiment revealed that the most intense fluorescence occurred in non-polar solvents such as diethyl ether and toluene. As the solvent polarity increased, there was a noticeable quenching of fluorescence at these concentrations matching the trend observed in the fluorescence profile of **2.14**. There is no indication of CT behavior in this compound, as no solvatochromism was observed in its fluorescence profile. To show the change in absorption with increased conjugation, **Figure 3-13** shows the absorbance profiles of **2.14**, **2.22**, **2.24** and **2.25**.

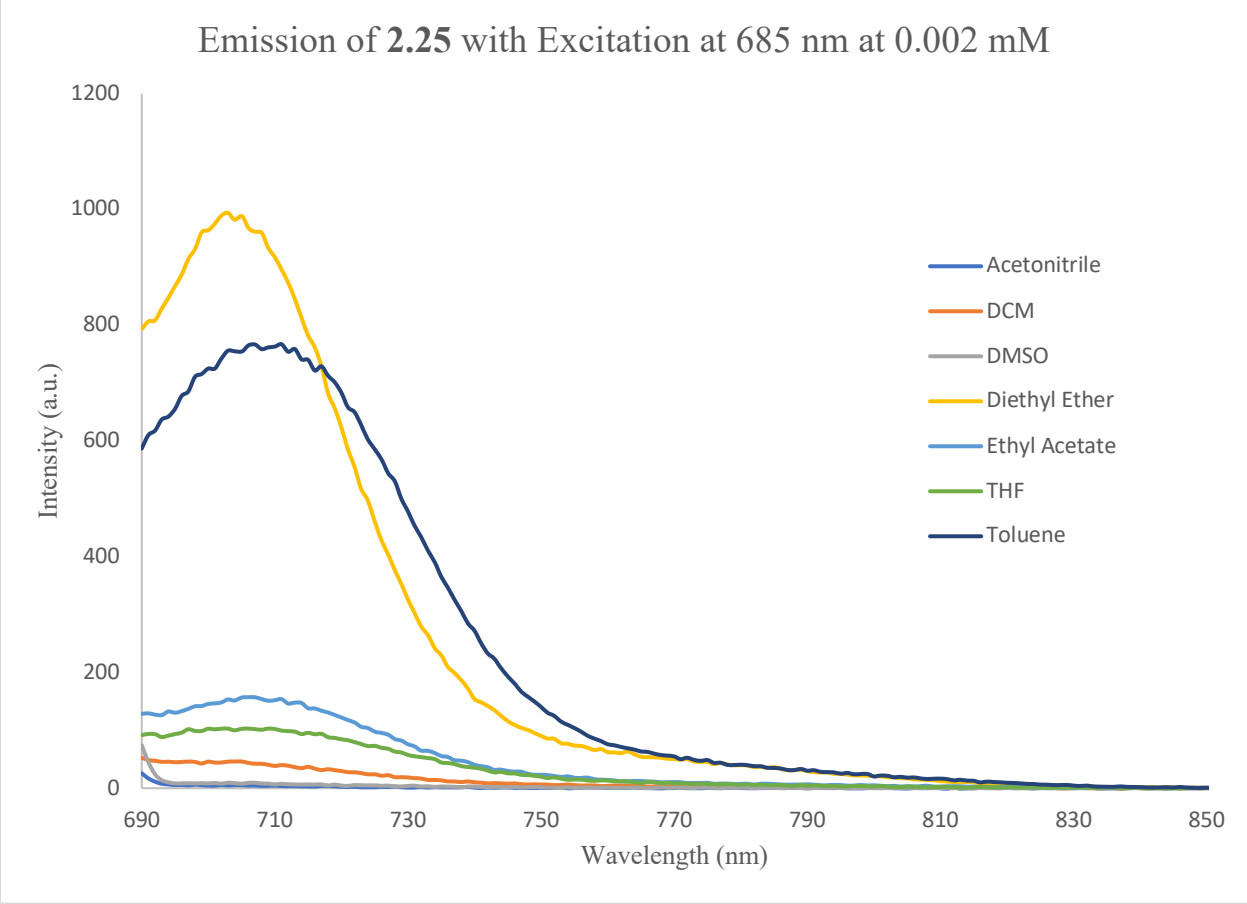

Figure 3-12. Emission of **2.25** at 0.002 mM in various solvents.

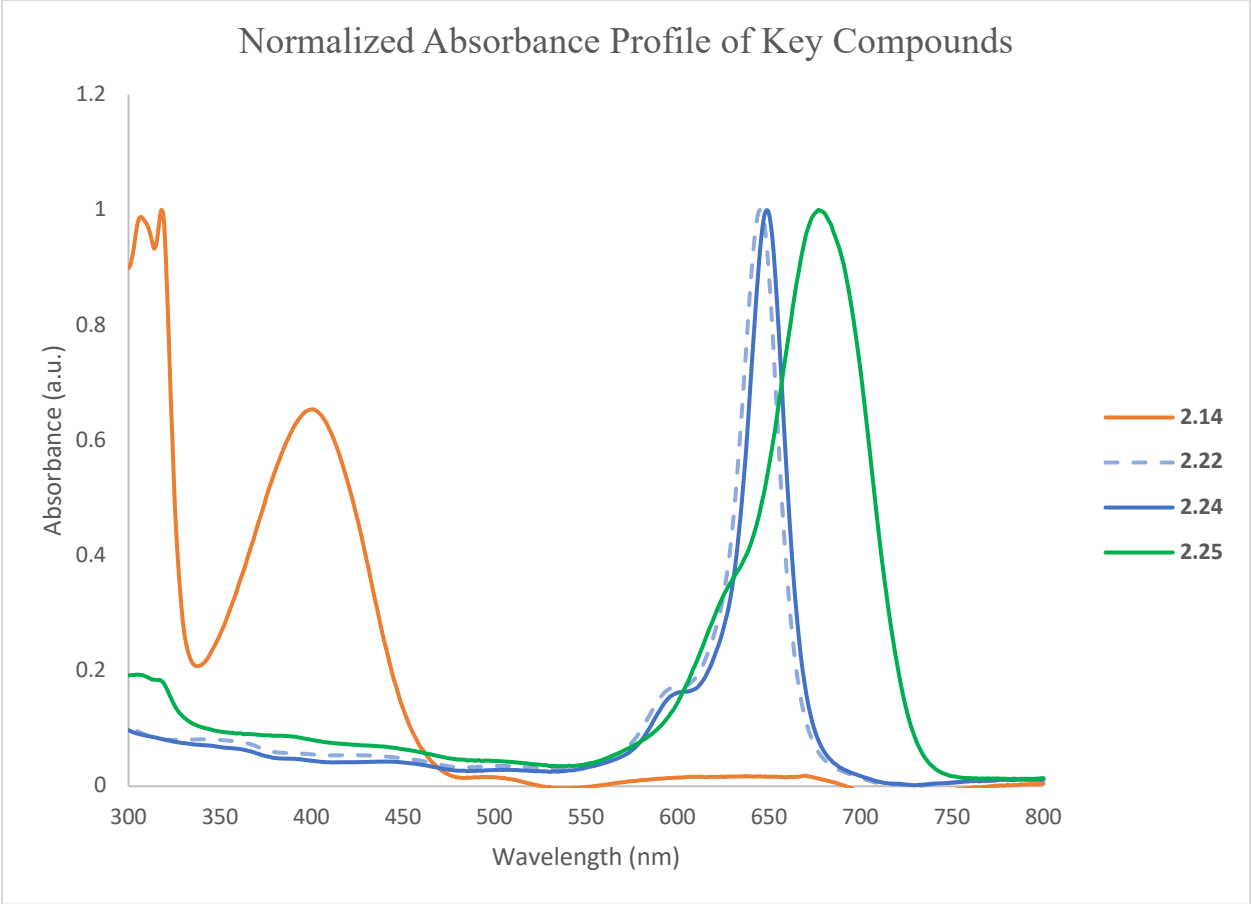

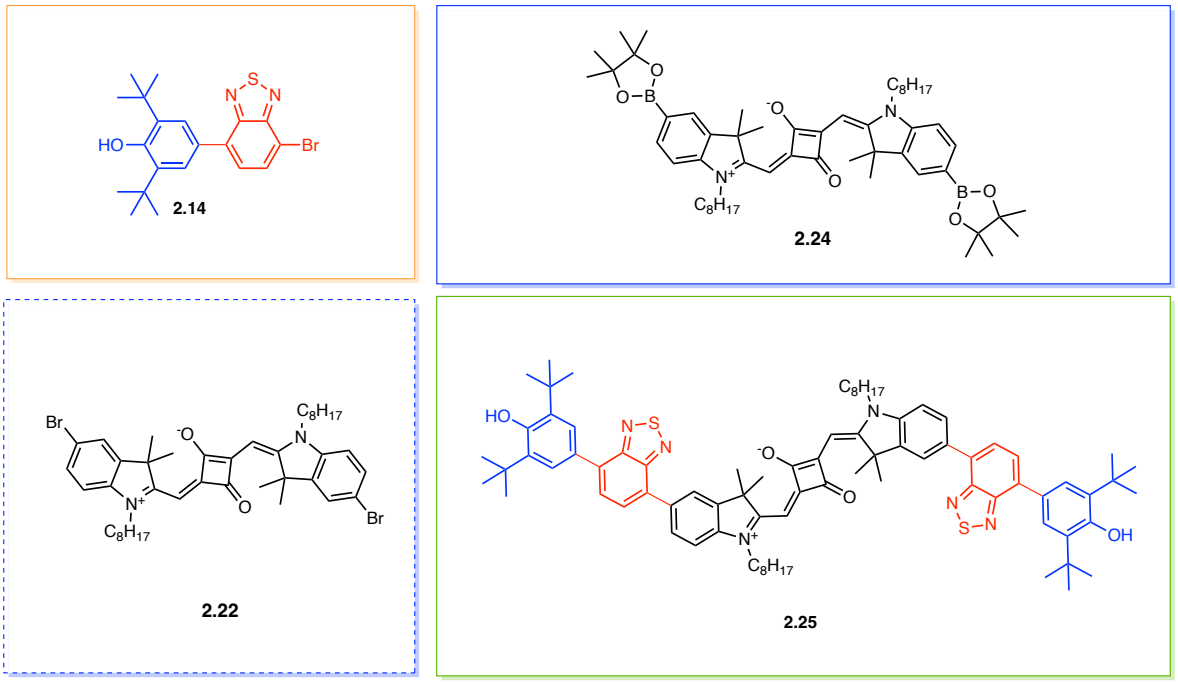

Figure 3-13. Absorption of **2.14, 2.22, 2.24** and **2.25** in DCM.

3.3 pH Dependence of Absorption and Emission

We conducted an investigation into the absorbance profiles of both **2.14** and **2.25** as varying equivalents of base were added. Due to solubility issues in methanol, **2.14** was dissolved in ethanol, and a 1M solution of NaOH in methanol was prepared (**Figure 3-14**). The base additions were carried out stoichiometrically in a quartz cuvette, starting with 0.25 equivalents and increasing in 0.25 increments. We did not observe a one-to-one reaction between the phenolic proton and the base; in other words, excess NaOH was required to observe all of the spectral changes that we attribute to deprotonation.

Upon the addition of base, **2.14** underwent a transformation from its fluorescent yellow color in solution to a deep blue opaque solution. The absorption profile of this compound exhibited a decrease in the absorbance band at 400 nm and the emergence of a new absorbance band at 564 nm (**Figure 3-15**). An isosbestic point, indicating a point of no change in absorbance, was observed at 460 nm. This indicates there are no intermediates observed in this transformation. Furthermore, we observed an increase in absorbance at 305 nm and 317 nm, which corresponds to the CT band. This increase is consistent with a strengthening of the donor moiety as the anionic charge becomes more pronounced.

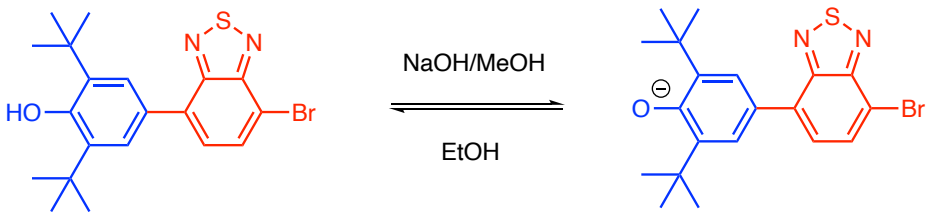

Figure 3-14. Deprotonation of **2.14**.

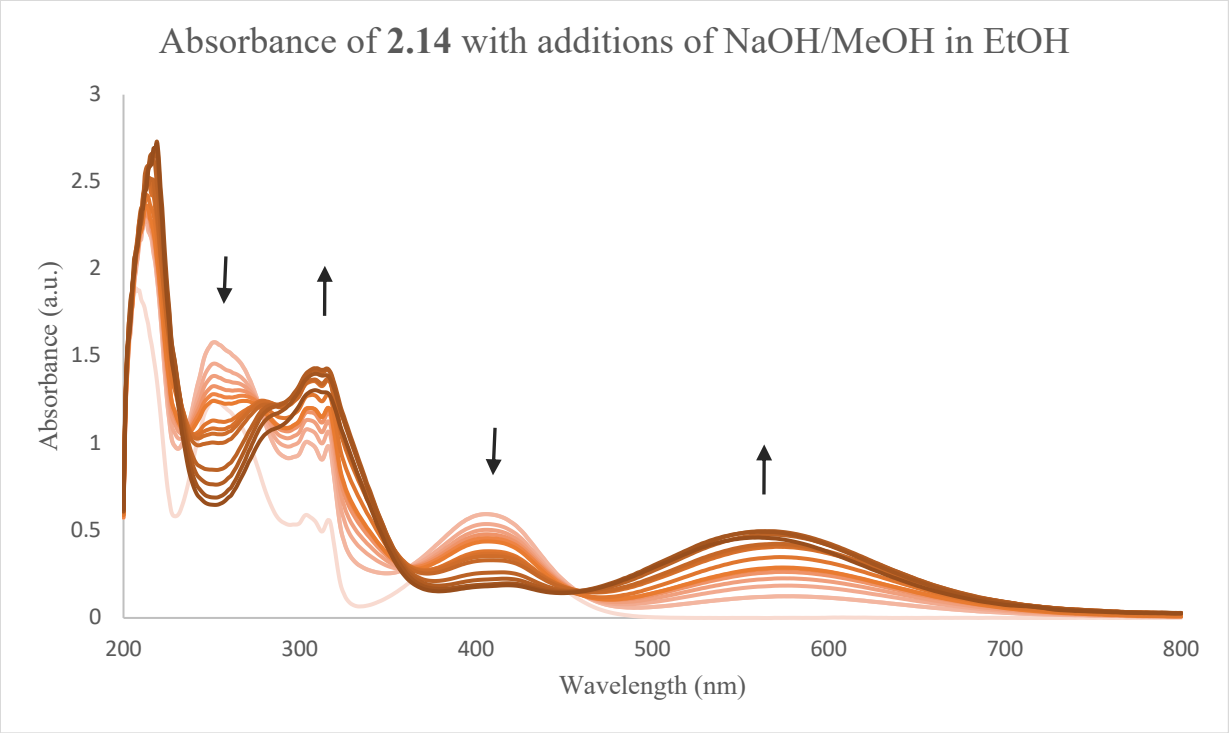

Figure 3-15. Absorption spectra of **2.14** in ethanol with additions of sodium hydroxide in methanol as base. Arrows indicate appearance or disappearance of absorption bands.

Building upon the findings of our previous experiment, we proceeded to investigate the same experimental setup on compound **2.25**, as illustrated in **Figure 3-16**. For this investigation, we employed three different bases: sodium hydroxide, DBU, and a 1 M solution of sodium bis(trimethylsilyl)amide in THF (NaHMDS). Among these bases, only NaHMDS exhibited any reactivity towards the phenolic protons, as confirmed through UV-Vis spectroscopic analysis. The resulting absorption profile, with successive base additions, is presented in **Figure 3-17**.

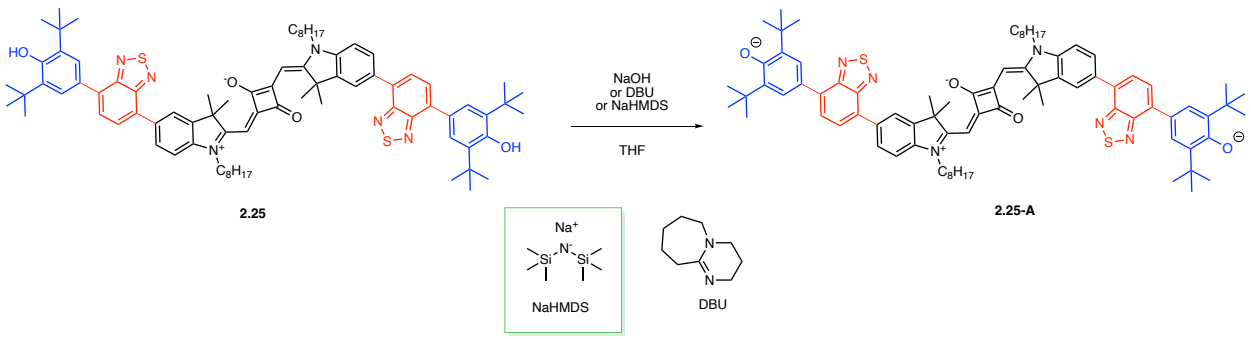

Figure 3-16. Deprotonation of **2.25**.

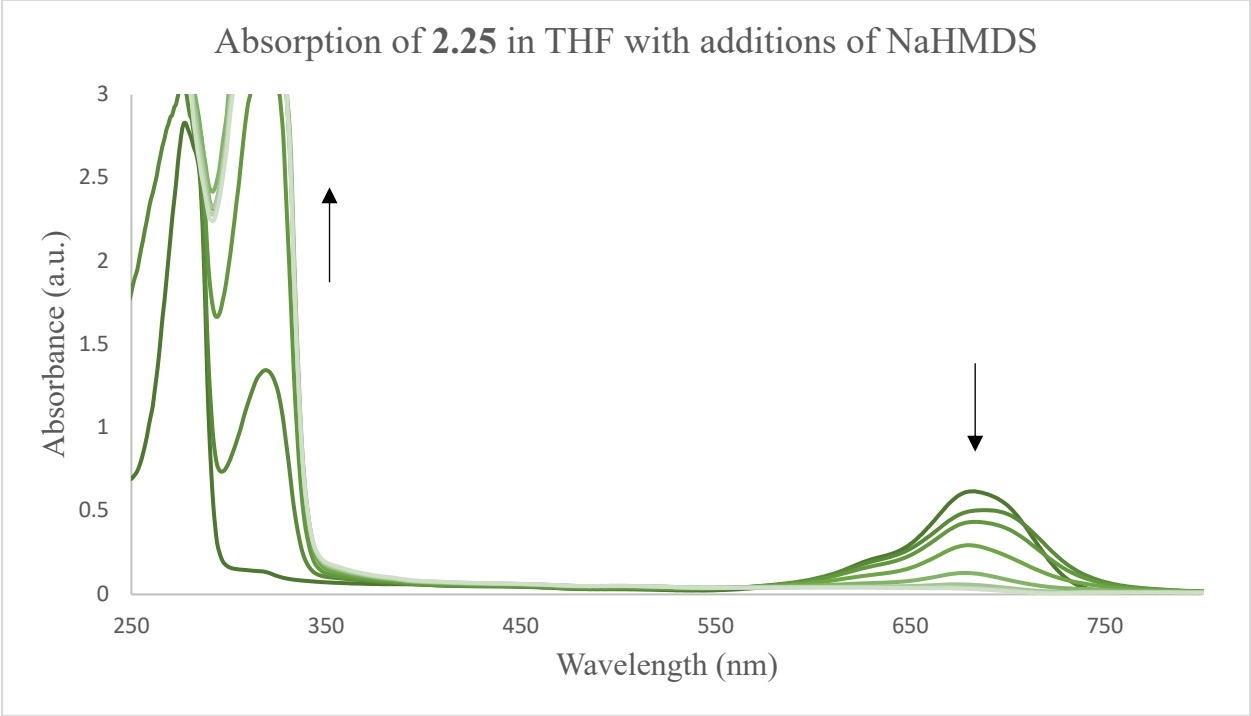

Figure 3-17. Absorption profile in THF of **2.25** with additions of NaHMDS.

The absorption profile exhibited a notable disappearance of the absorption band at 682 nm, accompanied by the emergence of a new absorption band at 324 nm. Consequently, the solution transitioned from its customary opaque blue hue to a colorless state. The appearance of the 324 nm band aligns with the absorption changes observed in **2.14**, providing further evidence to

support the notion that this absorption band corresponds to the escalating anionic character within the donor phenols.

No new absorption bands were observed between 682 nm and 900 nm. The anticipated augmentation of anionic character should lead to a destabilization of the HOMO relative to the LUMO, resulting in a red-shifted absorption band. Based on these findings, it is conceivable that **2.25-A** may absorb light in the NIR range, surpassing the detection limit of the employed spectrophotometer. A more detailed analysis of this aspect will be presented in Chapter 3.5.4, where the computational examination of **2.25-A** will be discussed.

3.4 Redox Properties

3.4.1 Cyclic Voltammetry

The redox properties of **2.14** and **2.25** were investigated using cyclic voltammetry. The voltammogram depicting the behavior of **2.14** can be observed in **Figure 3-18**. Within the anodic trace, two irreversible oxidations were observed. Of particular significance is the first oxidation occurring at 0.76 V, which is presumed to be the oxidation of the phenolic OH to the phenoxyl radical, as illustrated in **Figure 3-19**. Notably, this potential closely resembles the literature example of butylated hydroxytoluene (BHT), where the first oxidation to the phenoxyl radical occurs at 1.082 V relative to Fc/Fc+.[170] The lower voltage observed in our experiment supports the notion of stabilized oxidized species attributable to the BTD acceptor.

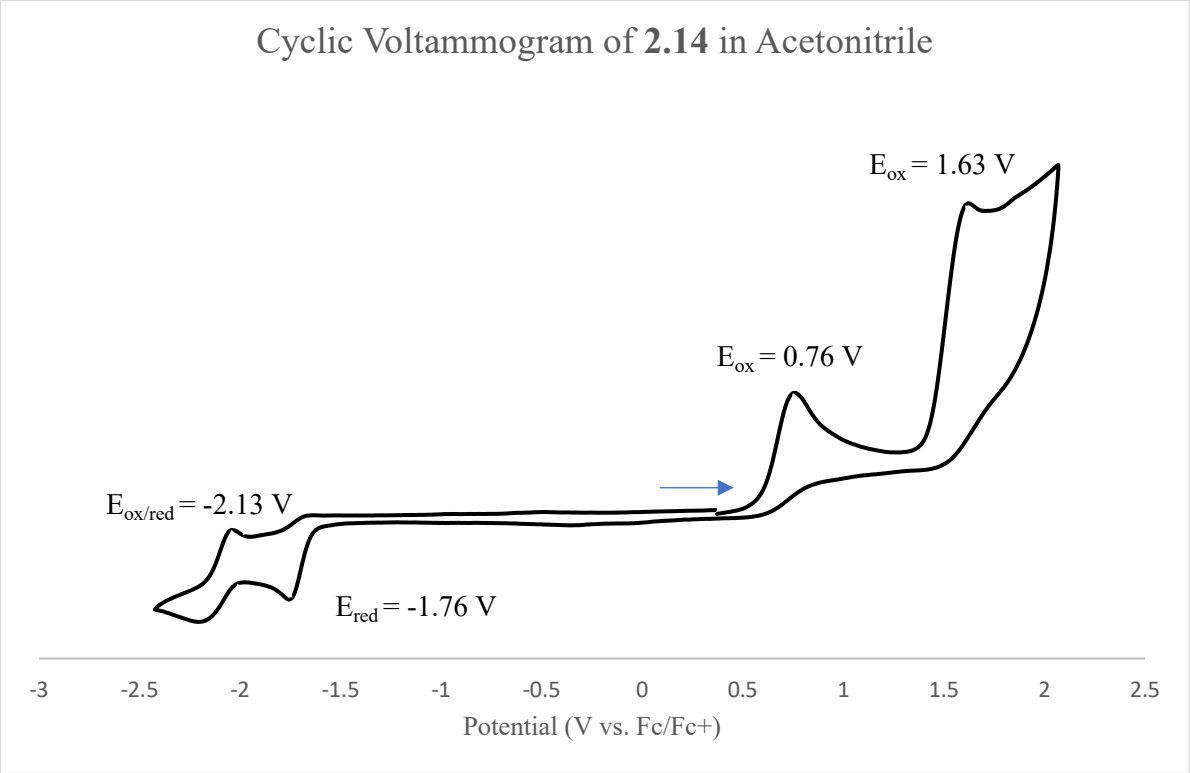

Figure 3-18. Cyclic voltammogram of **2.14** in ACN versus Fc/Fc^{+}.

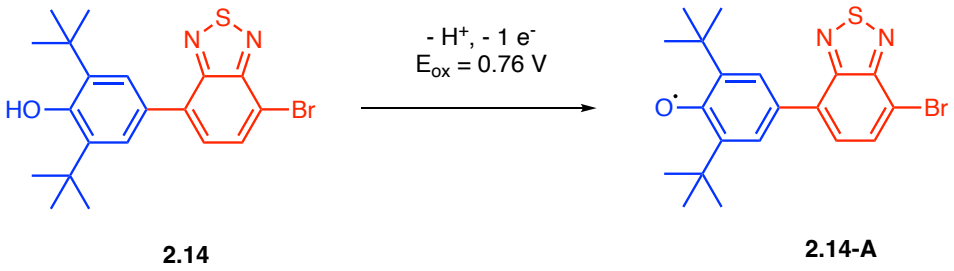

2.14 **2.14-A**

Figure 3-19. Irreversible oxidation of **2.14** to become **2.14-A** occurring at 0.76 V.

As described in Chapter 3.1.2, the oxidation of phenols in polar aprotic solvents is known to be an irreversible process attributed to proton loss. Nonetheless, phenoxyl radicals exhibit a propensity for reduction, leading to the formation of their corresponding phenolates. Regrettably, due to the exhaustion of the entire sample of **2.14** during the experiment, further scans were

unattainable, and no residual material was retained for subsequent analysis. Consequently, the interpretation of subsequent oxidations or reductions following the initial anodic signal proves challenging, necessitating additional experiments to comprehensively characterize the redox properties of this compound.

The voltammogram of **2.25** unveils two reversible redox events at -1.70 V and -2.14 V, as illustrated in **Figure 3-20**. Additionally, an irreversible oxidation is observed at -0.69 V, presumably originating from the oxidation of the phenolic OH group to form the phenoxyl radical. Notably, there has been a remarkable shift of approximately 1 V compared to the precursor compound **2.14**. This shift can be attributed to the extension of conjugation, resulting in a lowered energy level of the HOMO and facilitating electron removal. Regrettably, due to challenges in the purification process, further data acquisition on this compound was unfeasible, impeding a comprehensive understanding of the nature of the redox events occurring above 0.5 V.

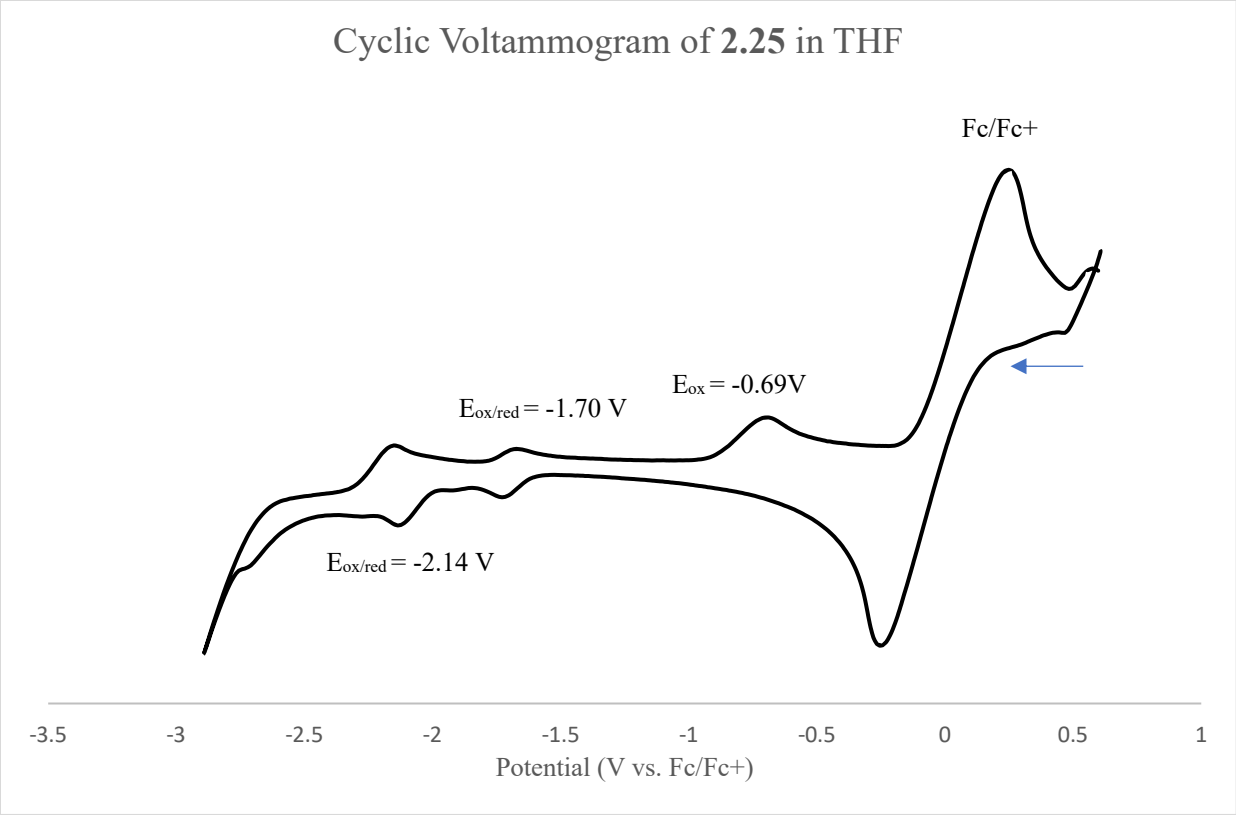

Figure 3-20. Voltammogram of **2.25** in THF versus Fc/Fc^{+}.

3.4.2 Oxidation of **2.14**, **2.15**, and **2.25**

During our investigation into the redox properties of **2.14** and **2.15**, we sought to explore their reactions with different oxidants. Our initial experiment involved dissolving a sample of **2.15** in DCM and stirring it with a mixture of aqueous 1 M NaOH and potassium ferricyanide (**Scheme 3-1**). The yellow solution rapidly transformed into a deep opaque fuchsia hue denoted as compound **2.36**. The solution was diluted and subjected to UV-Vis spectroscopic analysis, as depicted in **Figure 3-21**.

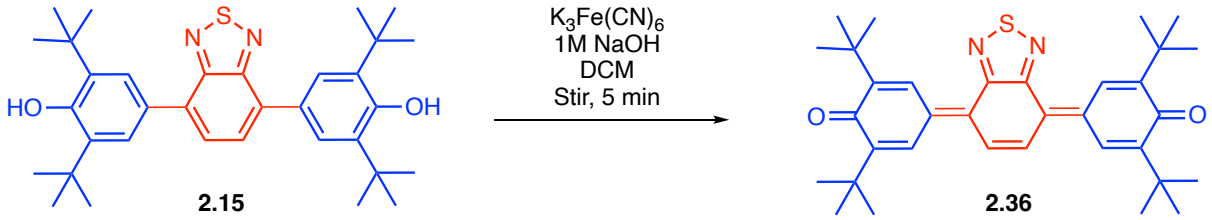

Scheme 3-1. Oxidation of **2.15**.

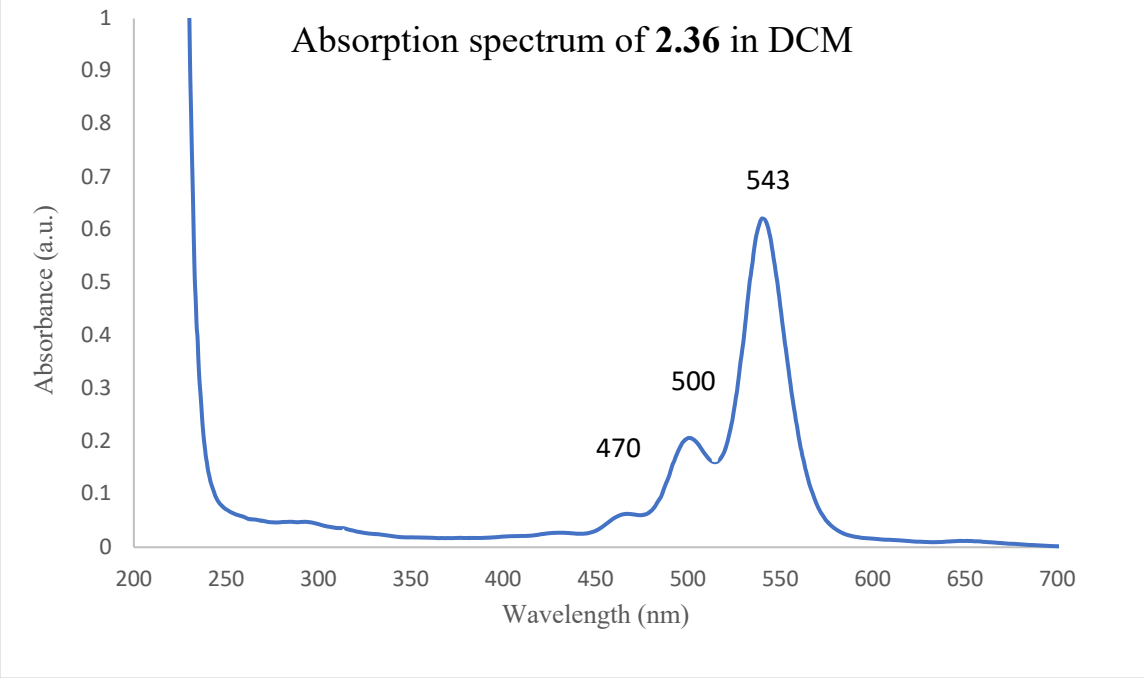

Figure 3-21. Absorption spectrum of **2.36** in DCM.

The obtained absorption spectrum reveals a notable absence of the previously observed absorption maxima within the range of 200 nm to 400 nm. Instead, three distinct absorption bands emerge at wavelengths of 470 nm, 500 nm, and 543 nm, exhibiting an ascending order of absorbance. These closely spaced absorption bands are indicative of compounds with a rigid excited state, a characteristic that can be effectively demonstrated through a Franck-Condon plot, as illustrated in **Figure 3-22**.

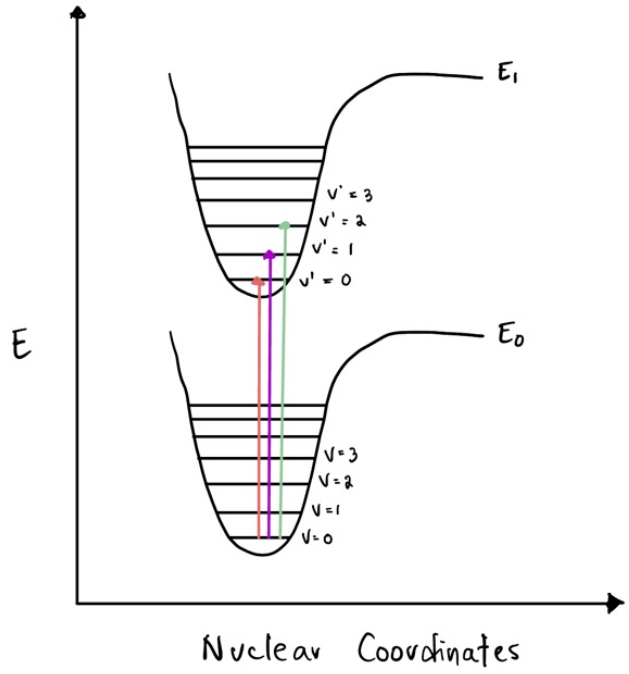

Figure 3-22. Franck-Condon diagram showing vertical transitions for structurally rigid polyaromatic hydrocarbons.

In cases where the atomic coordinates experience minimal changes between the ground and excited states, the most probable energetic transition occurs from the lowest vibrational state in E_0 to the lowest vibrational state in E_1, as depicted by the red arrow. Consequently, the subsequent likely transitions involve v = 0 to v' = 1, and so forth. As a result, the resulting absorbance spectrum exhibits a prominent absorbance band at the lowest energy level, gradually decreasing in intensity for the subsequent bands.

Taking into account the apparent rigidity inferred from the compound's absorption spectrum, we proceeded to analyze the NMR spectra of the compound. Proton NMR spectroscopy revealed a distinct symmetry change in the resulting oxidized molecule. Within the aromatic region, three resonances emerged, each corresponding to an integration of two protons. Notably, the signal attributed to the phenolic proton vanished, while the singlet for the *tert*-butyl groups

resolved into two separate singlets at 1.41 ppm and 1.40 ppm. These findings led to the proposal of the structure depicted as **2.36** in **Figure 3-23**.

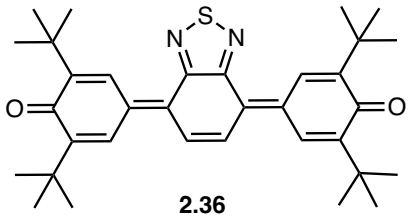

2.36

Figure 3-23. Compound **2.36**.

Over-addition of oxidant introduced uncertainty regarding the extent of oxidation. However, the reactivity of **2.15** under oxidative conditions showed promise. It was evident that there was no decomposition of the compound, and importantly, no peroxide-like side products were isolated. This is particularly noteworthy, as the oxidation of phenols under atmospheric conditions can often lead to the formation of such undesired byproducts.[171]

In an effort to obtain **2.14-A**, oxidation of **2.14** was conducted using 0.9 equivalents of $K_3Fe(CN)_6$ in DCM with aqueous 1 M NaOH, as illustrated in **Scheme 3-2**. The initial yellow solution underwent a rapid color transformation from yellow to a deep red hue. After removal of solvent and all insoluble residue, the resulting red solid was subjected to analysis.

2.14 **2.14-A**

Scheme 3-2. Oxidation of **2.14**.

To investigate the potential oxidation of the compound to the quinoidal form adjacent to **2.15**, ^{1}H NMR spectroscopy was conducted. Surprisingly, the obtained NMR spectrum displayed an identical profile to that of the starting material, suggesting that no significant structural changes occurred. Further analysis of the sample using UV-Vis spectroscopy revealed the emergence of two new absorption bands at 502 nm and 540 nm, accompanied by a slight broadening of the absorption at 400 nm, as depicted in **Figure 3-24**. For comparison, the absorption maximum for tri-*tert*butylphenoxyl radical in acetonitrile is 626 nm.[172]

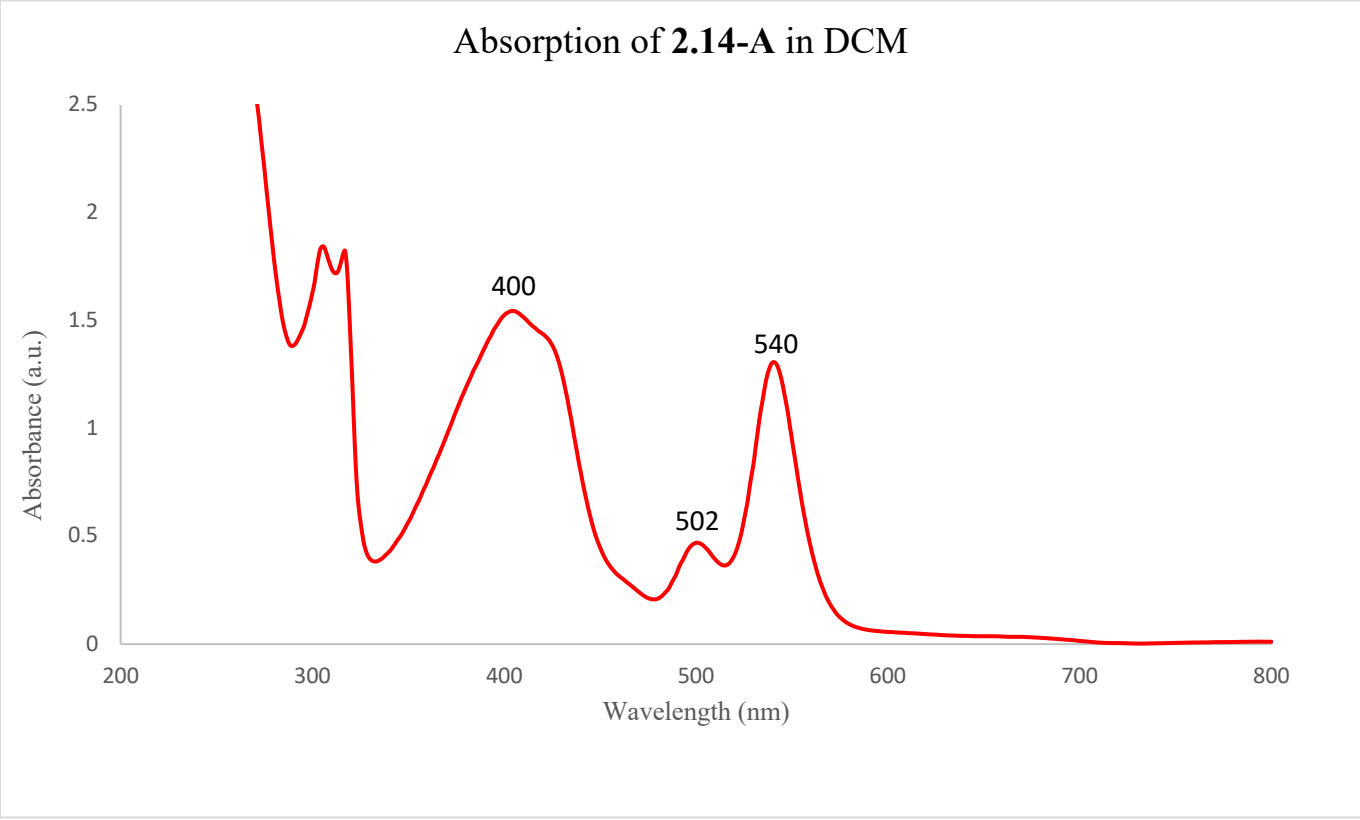

Figure 3-24. Absorption spectrum of **2.14-A** in DCM.

A small aliquot of the sample in DCM was utilized to obtain an EPR spectrum. The resulting spectrum exhibited the presence of a paramagnetic compound, indicated by a distinct singlet near g = 2.003. By adjusting the modulation and power settings, slight indications of coupling were observed in the spectrum, as depicted in **Figure 3-25**. This coupling could potentially arise from interaction with the *ortho*-substituted protons or a nitrogen atom on the acceptor unit. Unfortunately, due to limited resolution, precise coupling constants could not be extracted.

Confirmation of the chemical formula was obtained through HRMS analysis, albeit limited to negative ion mode. It is important to note that the observation of the radical species is not definitive, as reducing the radical to an anion would yield the same results as deprotonating **2.14** to form the anion. However, it is worth mentioning that no evidence of **2.14** was observed in positive mode.

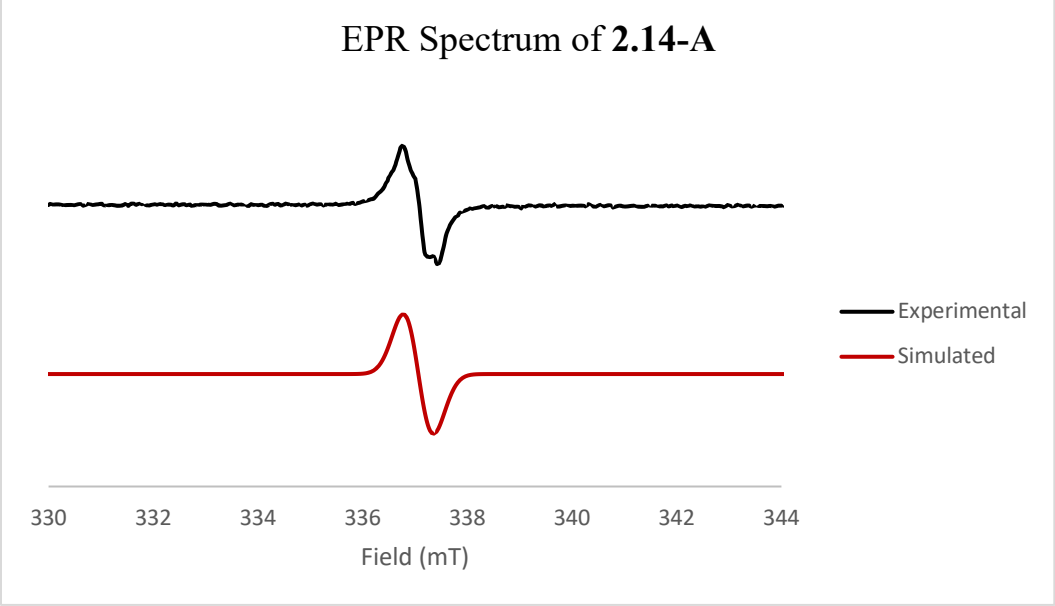

Figure 3-25. EPR spectrum of **2.14-A**.

An attempt was made to oxidize **2.25** into its corresponding SFR using the same conditions employed for the previous oxidations of the precursor compounds. There was no observable change in color, and the absorbance spectrum of the compound appeared identical to that of the neutral compound. To gain further insight, ^{1}H NMR spectroscopy was performed on the sample, revealing distinct line-broadening indicative of paramagnetism. However, subsequent analysis using EPR spectroscopy did not provide evidence of any paramagnetic species in solution.

Based on the electrochemical studies conducted on **2.25**, it was determined that an oxidant such as $K_3Fe(CN)_6$ possesses sufficient strength to remove an electron from the compound's HOMO. In acetonitrile, the reversible reduction event for $[Fe(CN)_6]^{3-}$ to $[Fe(CN)_6]^{4-}$ occurs at -1.397 V relative to ferrocene. However, no data regarding the redox potential in DCM is available, as the electrochemical window of the solvent does not encompass the redox potential of ferricyanide. The results of this experiment suggest that the oxidized species of **2.25** may be unstable in solution. Further investigations under anaerobic conditions would be necessary to shed light on this matter.

3.5 Computational Studies

3.5.1 TD-DFT of **2.14**

Computational studies were conducted on **2.14**, **2.15**, **2.25,** and **2.31**, with a specific focus on modeling the frontier orbitals of these compounds. Additionally, we aimed to investigate the energy gaps between the singlet and triplet excited states, as we hypothesized the potential for these luminescent materials to exhibit TADF.

The calculations involved a two-step process. Initially, a simple geometry optimization was performed using the def2-SVP basis set, followed by further optimization using the larger def2-TZVP basis set. The B3LYP and ωB97X-3D functionals were predominantly employed. The ωB97X-3D functional, a range-separated hybrid generalized gradient approximation, has been known to enhance accuracy in singlet excited state calculations.[173] However, in most cases, the B3LYP functional demonstrated better agreement with the experimental absorption profiles of all the molecules investigated.

Our initial focus was on examining the frontier molecular orbitals (FMOs) of **2.14**. Using the B3LYP functional and def2-TZVP level of theory, the HOMO was found to be primarily localized on the donor phenol, with some electron density observed on the BTD acceptor. Conversely, the LUMO was predominantly located on the BTD acceptor, consistent with theoretical predictions. The HOMO-LUMO energy gap was calculated to be 3.19 eV, and the distribution of electrons can be visualized in **Figure 3-26**.

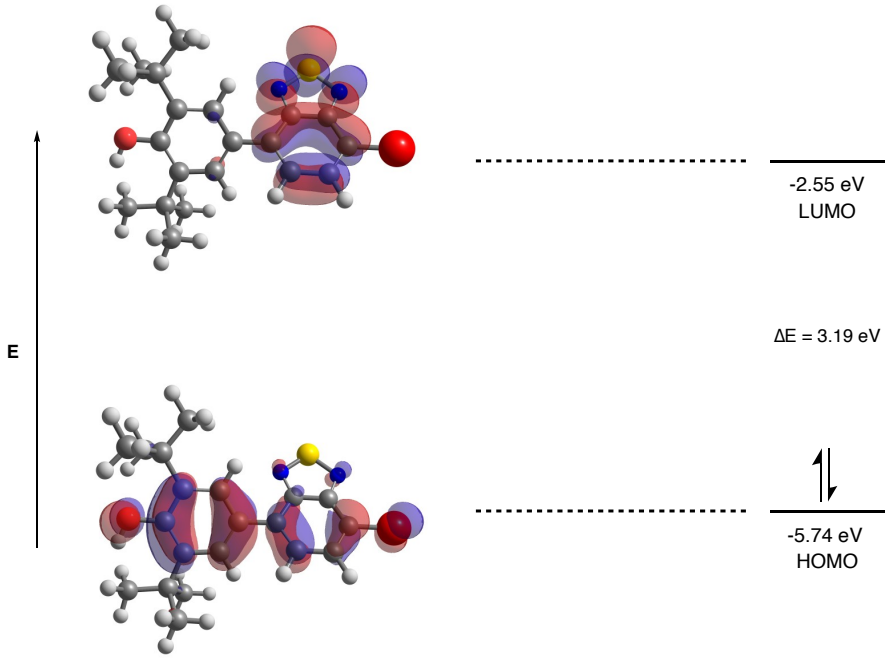

Figure 3-26. HOMO and LUMO of **2.14** calculated at the B3LYP/def2-TZVP level of theory.

The gas-phase absorption spectrum of **2.14** was modeled using TD-DFT, and the resulting Natural Transition Orbitals (NTOs) were visualized. The lowest energy transition to the singlet excited state (S_1) was observed at a transition energy of 2.780 eV, equivalent to 446 nm. These vertical energy transitions represent the energy gaps between the ground state and excited states, which were found to be slightly lower than the HOMO-LUMO gap of the ground state. It is noteworthy that this transition is spin-allowed. However, relaxation to the triplet excited state (T_1) can occur through ISC, which exhibits a transition energy of 2.13 eV or 583 nm from the HOMO (S_0) and is spin-forbidden. Nevertheless, under certain conditions, such as fluorescence monitoring, relaxation via ISC can be observed as the computational results are consistent with the experimental emission profile. The comparison of the calculated S_0-T_1 energy gap with the

emission profile of **2.14** reveals that both transitions correspond to π-π* transitions, demonstrating satisfactory agreement with experimental UV-Vis and fluorescence results.

Furthermore, the excited-state geometry of **2.14** was computed. The analysis revealed a rotation about the C-C bond between the phenol donor and BTD acceptor, resulting in a nearly planar geometry. While this geometry does not support TICT, it supports the coupling between the donor and acceptor coming from alignment of π-orbitals, thereby substantiating the CT character. The NTOs and excited-state geometries can be observed in **Figure 3-27**. Additionally, the experimental absorbance spectrum compared to the computational spectrum is depicted in **Figure 3-28**.

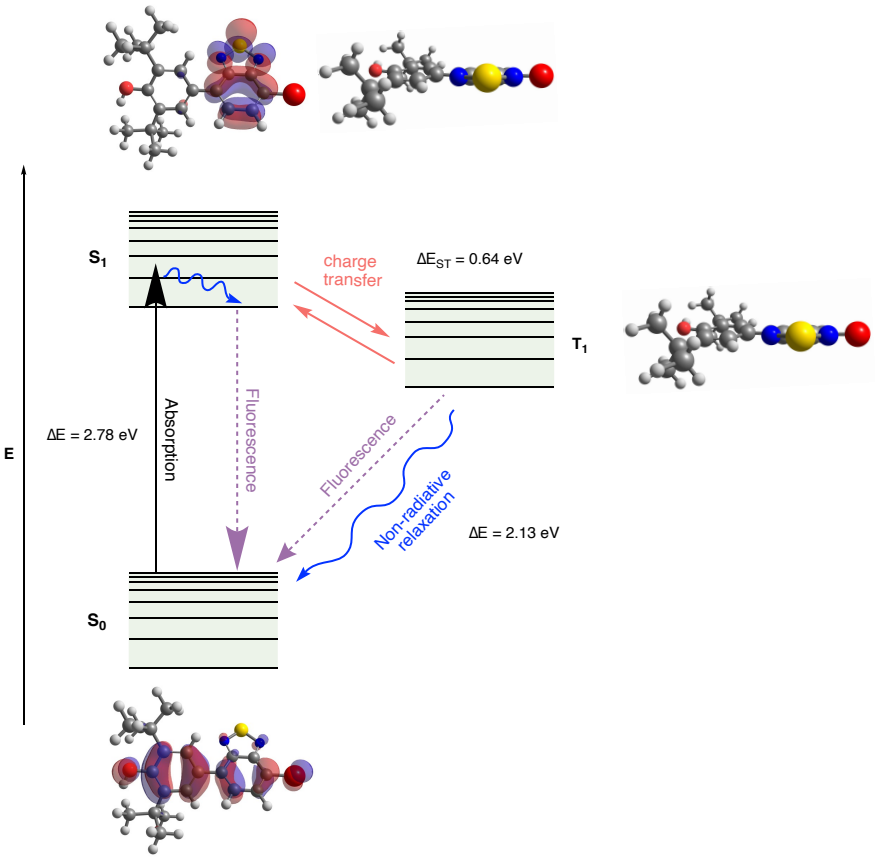

Figure 3-27. Jablonski diagram for excited state NTOs of **2.14** calculated at the B3LYP/def2-TZVP level of theory.

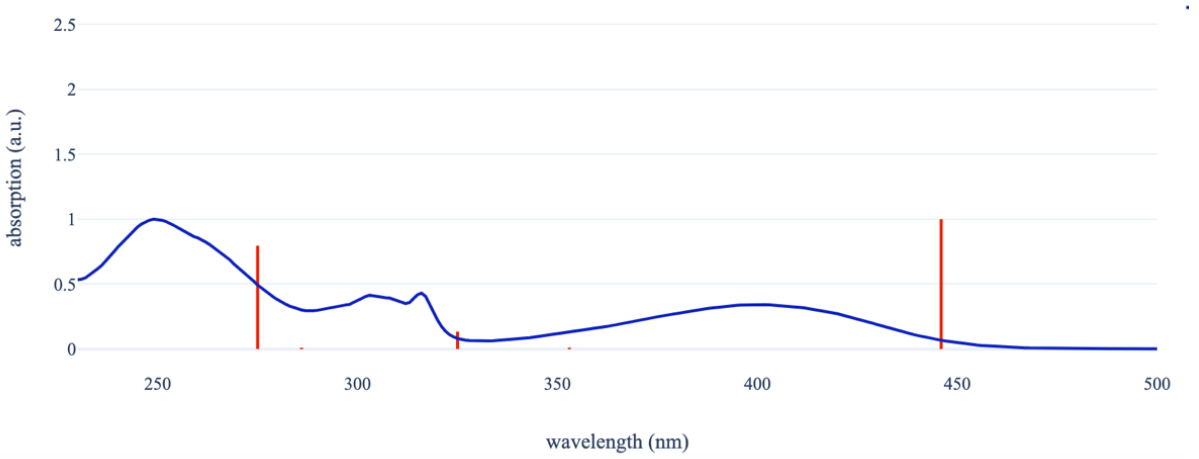

Figure 3-28. Experimental (blue) and computational (B3LYP/def2-TZVP, red bars) UV-Vis data. The bars indicate wavelengths with calculated absorption maxima.

Computational investigations were conducted on **2.14-A** employing the B3LYP functional and the 6-311G* basis set. The resultant alpha and beta molecular orbitals were visualized, and the absorption spectrum of the compound was predicted under gas phase conditions. A vertical energy gap between the α-SOMO and β-LUMO was computed, measuring 1.91 eV. Comprehensive insights into the electron distributions and corresponding energies of these ground state orbitals are provided in **Figure 3-29**. Notably, upon analyzing the distributions of the α-SOMO and β-LUMO, it is evident that the charge transfer (CT) character no longer prevails, assuming that the orbital transitions responsible for this characteristic arise from these specific orbitals. The oxidation of the phenol to the phenoxyl radical results in the creation of an electron-

deficient system, thus it is unsurprising that the CT character has been eliminated.

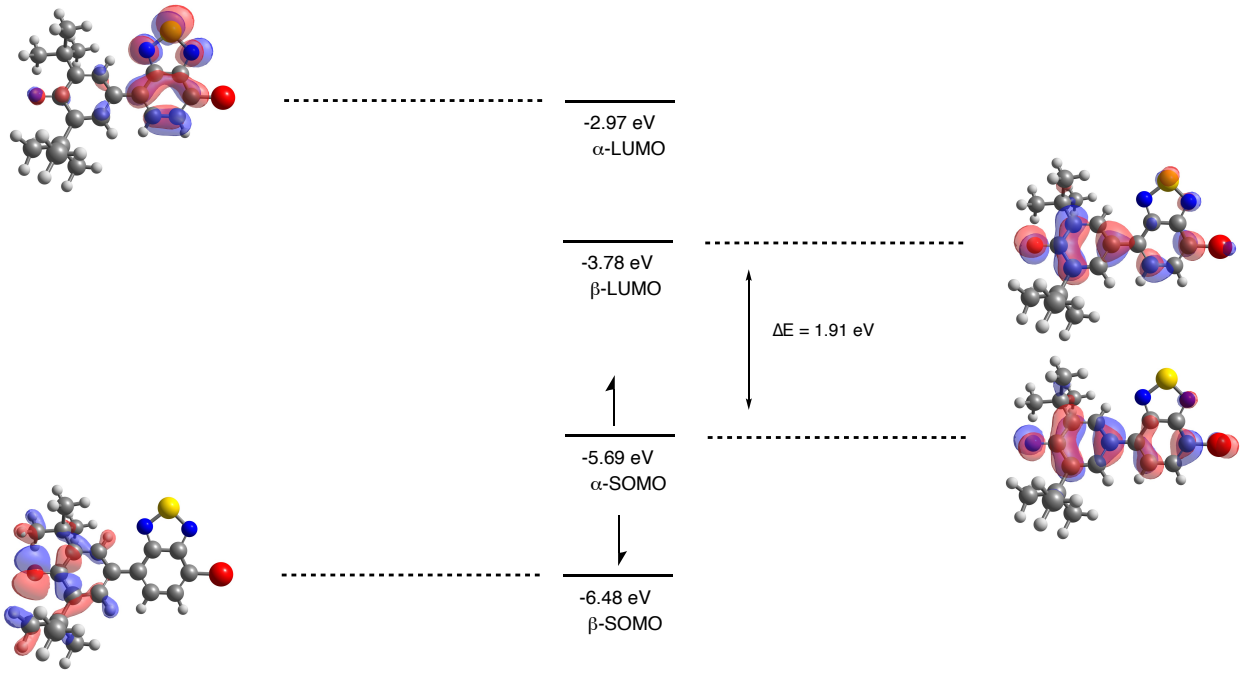

Figure 3-29. Alpha and beta SOMO and LUMO orbitals of **2.14-A** calculated at the B3LYP/6-311G* level of theory.

3.5.2 TD-DFT of **2.15**

Utilizing identical computational parameters as those employed for **2.14**, the frontier molecular orbitals (FMOs) of **2.15** were computed. The ground state HOMO and LUMO energies were determined to be -5.28 eV and -2.37 eV, respectively, resulting in an energy gap of 2.91 eV. The electron distribution reveals a substantial presence of HOMO density on the donor phenols, while the LUMO density predominantly resides on the BTD acceptor. For a visual representation of the electron distribution, please refer to **Figure 3-30**.

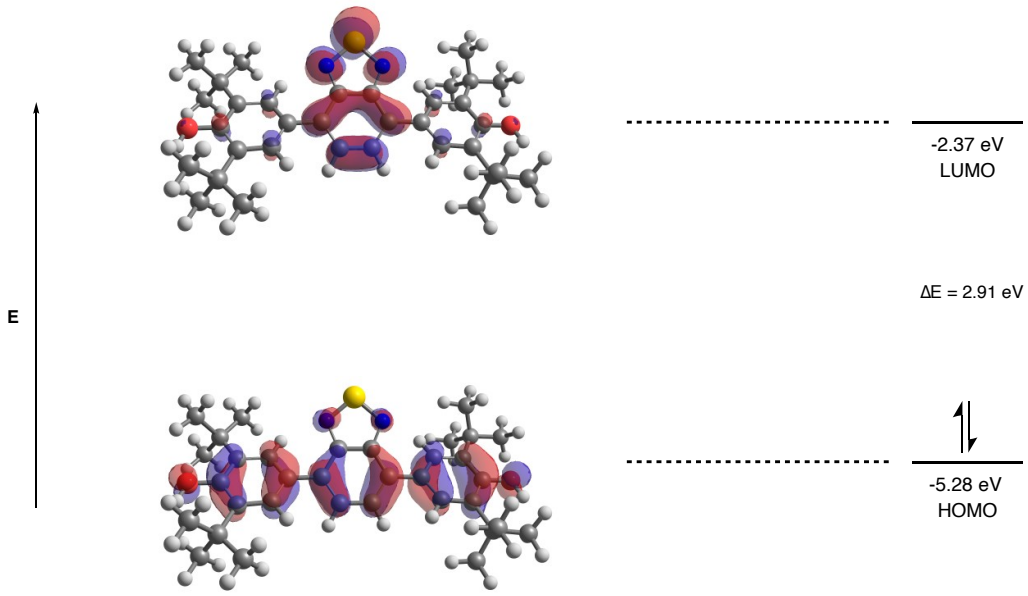

Figure 3-30. HOMO and LUMO of **2.15** calculated at the B3LYP/def2-TZVP level of theory.

In addition, we obtained the excited state NTOs to further explore the electronic transitions. Notably, **Figure 3-31** showcases the HOMO-LUMO transition, which corresponds to a vertical energy gap of 2.54 eV, equivalent to a wavelength of 487 nm. It is important to note that these computational results cannot be directly compared to the experimental data, highlighting the necessity for methodological refinements. In particular, the computed ΔE_{ST} value using this approach was determined to be 0.68 eV, indicating that this compound is unlikely to exhibit thermally activated delayed fluorescence (TADF). This observation is further supported by the results obtained using the ωB97X-3D/def2-TZVP method, which yielded an even higher ΔE_{ST} value of 1.37 eV.

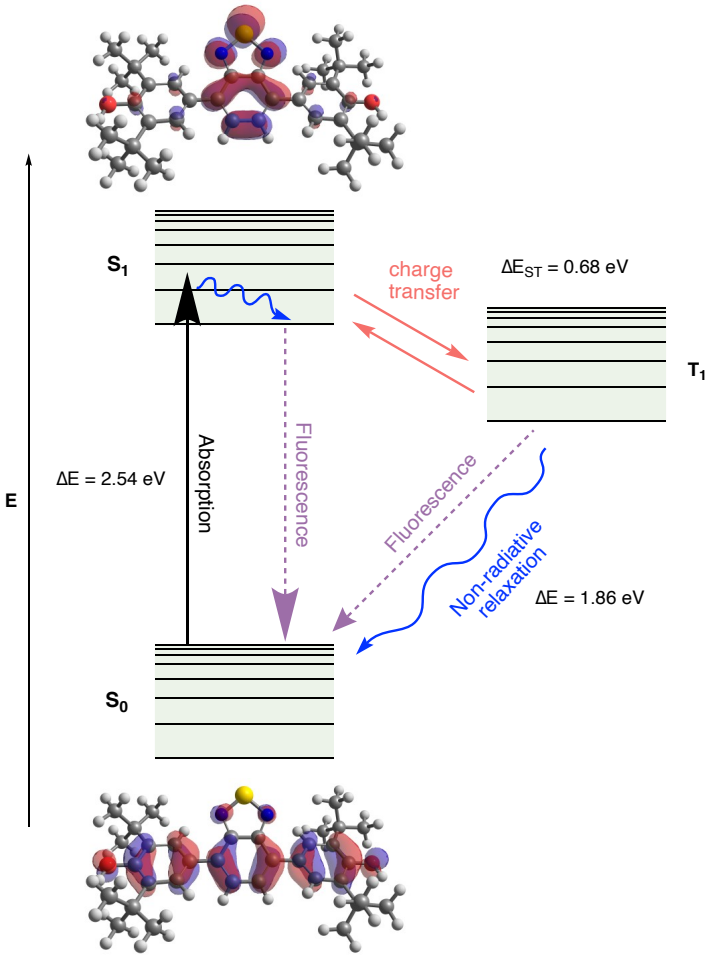

Figure 3-31. Jablonski diagram for excited state NTOs of **2.15** calculated at the B3LYP/def2-TZVP level of theory.

We also performed TD-DFT calculations on **2.36** to investigate its electronic properties. The computed ground state HOMO-LUMO energy gap was determined to be 5.36 eV, indicating a significantly larger gap compared to its reduced precursor. This disparity can be attributed to the loss of aromaticity resulting from the formation of a quinoidal structure. **Figure 3-32** illustrates the electron distribution associated with this ground state. The predicted absorption maximum was found to be at 436 nm, representing a blue-shift when compared to the calculated absorption maximum of 487 nm for **2.15**. However, it is worth noting that experimental observations show a

red-shift in the absorption of **2.36**, suggesting the need for further investigation and refinement of our computational approach.

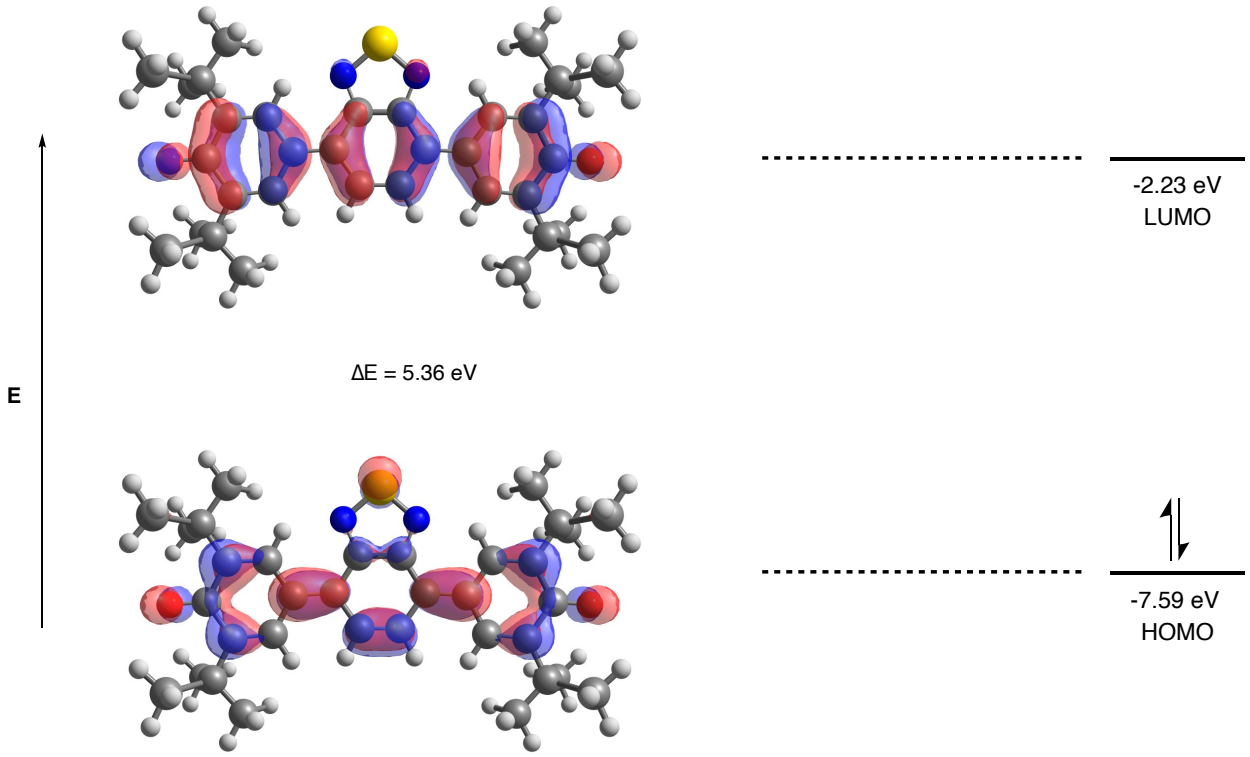

Figure 3-32. HOMO and LUMO of **2.36** calculated at the B3LYP/def2-TZVP level of theory.

3.5.3 TD-DFT of **2.25**

The gas-phase FMOs of **2.25** were calculated, revealing the HOMO density primarily localized on the cyclobutenolate core of the compound. Additionally, the LUMO density was observed to occupy both the core and the BTD acceptors, as depicted in **Figure 3-33**. The calculated HOMO-LUMO energy gap using the B3LYP/def2-TZVP level of theory was found to

be 2.05 eV. Notably, this combination of functional and basis set yielded results that exhibited better agreement with experimental values compared to ωB97X-3D/def2-TZVP. The vertical energy gap between the singlet ground state (S_0) and the first singlet excited state (S_1) was determined to be 1.85 eV or 667 nm, consistent with the experimental absorption findings. The calculated ΔE_{ST} value of 0.73 eV corresponds to an emission wavelength of 1.12 eV or 1105 nm. However, due to the limitations of the detection instruments, it is not currently possible to validate these results experimentally. Nevertheless, the computational analysis does predict a T_2 to S_0 energy gap of 1.73 eV or 718 nm, which aligns with the observed experimental outcomes.

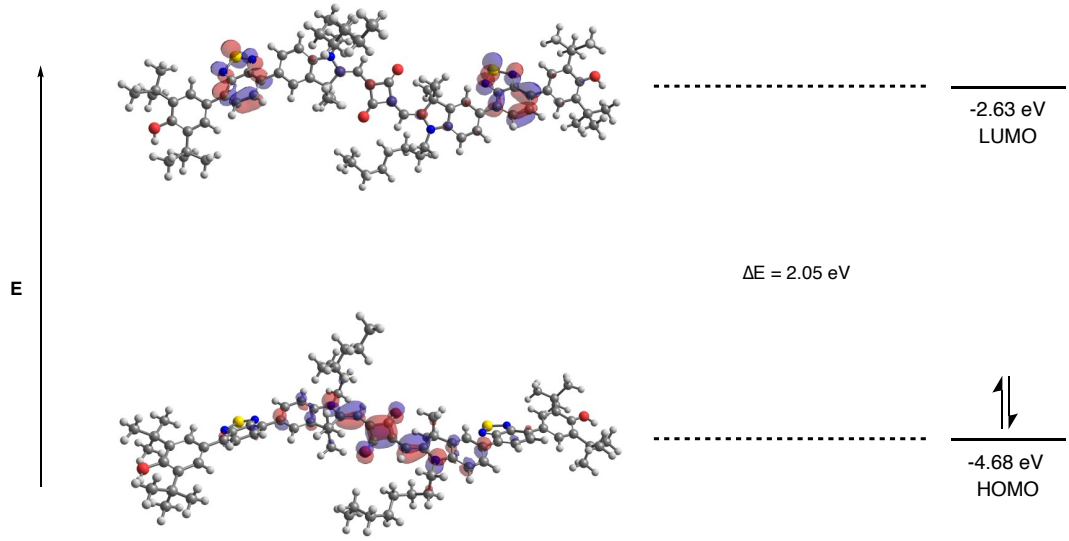

Figure 3-33. HOMO and LUMO of **2.25** calculated at the B3LYP/def2-TZVP level of theory.

We also employed the range-separated functional ωB97X-3D was to calculate ΔE_{ST}. Surprisingly, despite yielding similar HOMO-LUMO distributions, this alternative functional produced a significantly different HOMO-LUMO energy gap of 5.47 eV. Consequently, the calculated ΔE_{ST} for this compound amounted to 1.35 eV, surpassing the required 0.3 eV threshold for TADF. Additionally, the vertical transition energy from the HOMO to the LUMO was

determined to be 2.51 eV or 495 nm. Unfortunately, these computational results exhibited poor agreement with the experimental measurement of 675 nm, rendering the functional and basis set combination unsuitable for accurately modeling **2.25**. As a result, we opted to rely on the B3LYP/def2-TZVP approach for all calculations concerning this compound. The excited state NTOs of **2.25** are depicted in the Jablonski diagram found in **Figure 3-34**.

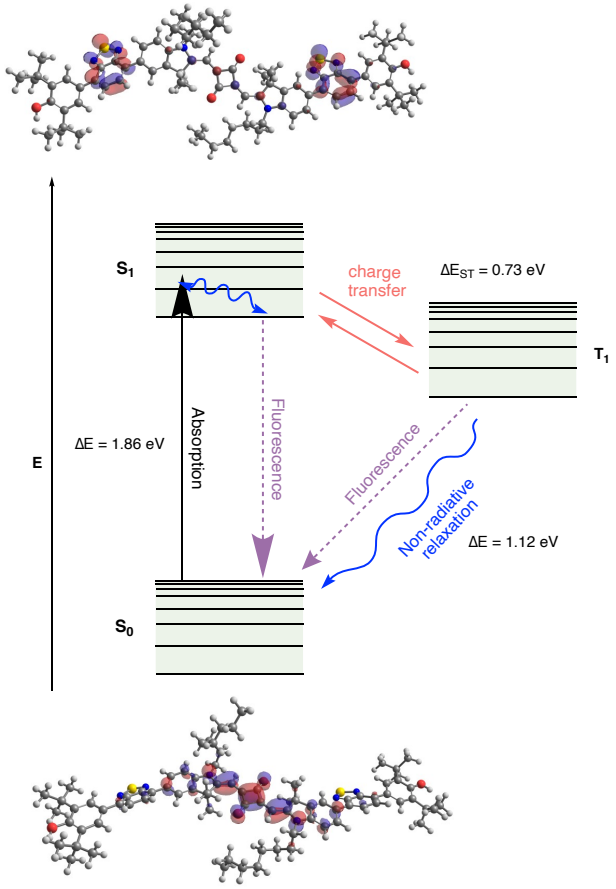

Figure 3-34. Jablonski diagram for excited state NTOs of **2.25** calculated at the B3LYP/def2-TZVP level of theory.

We further explored the FMOs of **2.25-A** using the B3LYP/def2-TZVP level of theory. As shown in **Figure 3-35**, the HOMO is located on the phenolate tails, while the LUMO exists on the

cyclobutenolate core of the squaraine moiety. These results are in support of our hypothesis, where we proposed deprotonating **2.25** to form **2.25-A** prior to oxidation will allow us to access the phenoxyl biradical squaraine dye due to the HOMO density exising on the phenolate tails.

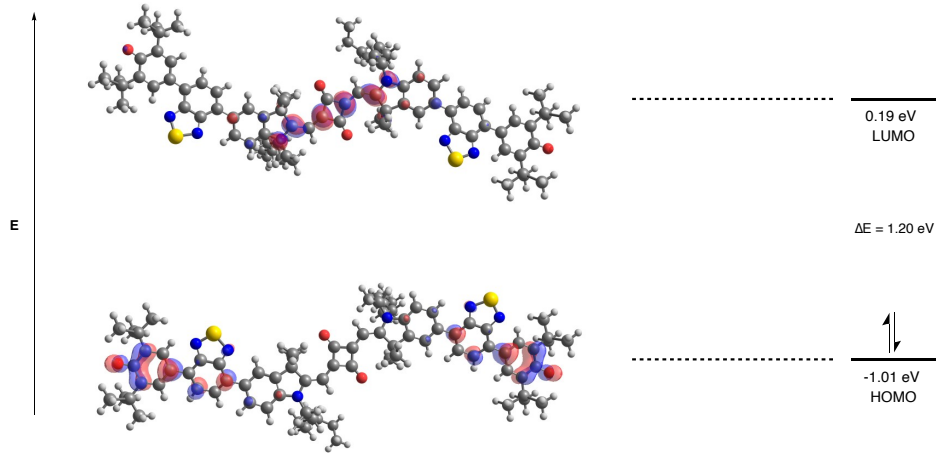

Figure 3-35. HOMO and LUMO of **2.25-A** calculated at the B3LYP/def2-TZVP level of theory.

TD-DFT results at the B3LYP/def2-TZVP level of theory predicts a S_0 to S_1 transition energy of 1.08 eV equal to 1147 nm corresponding to a HOMO to LUMO transition as shown by the excited state NTOs in **Figure 3-36**. The calculation also predicts a strong absorption at 690 nm consisting of 68% HOMO to LUMO and 22% HOMO-1 to LUMO excited state NTO transitions. The predicted UV-Vis absorption spectrum can be seen in **Figure 3-37**.

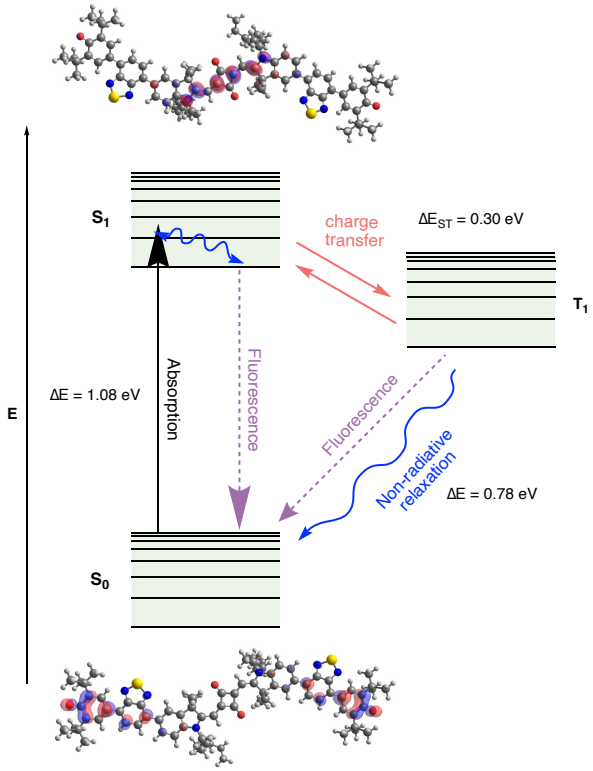

Figure 3-36. Jablonski diagram for excited state NTOs of **2.25-A** calculated at the B3LYP/def2-TZVP level of theory.

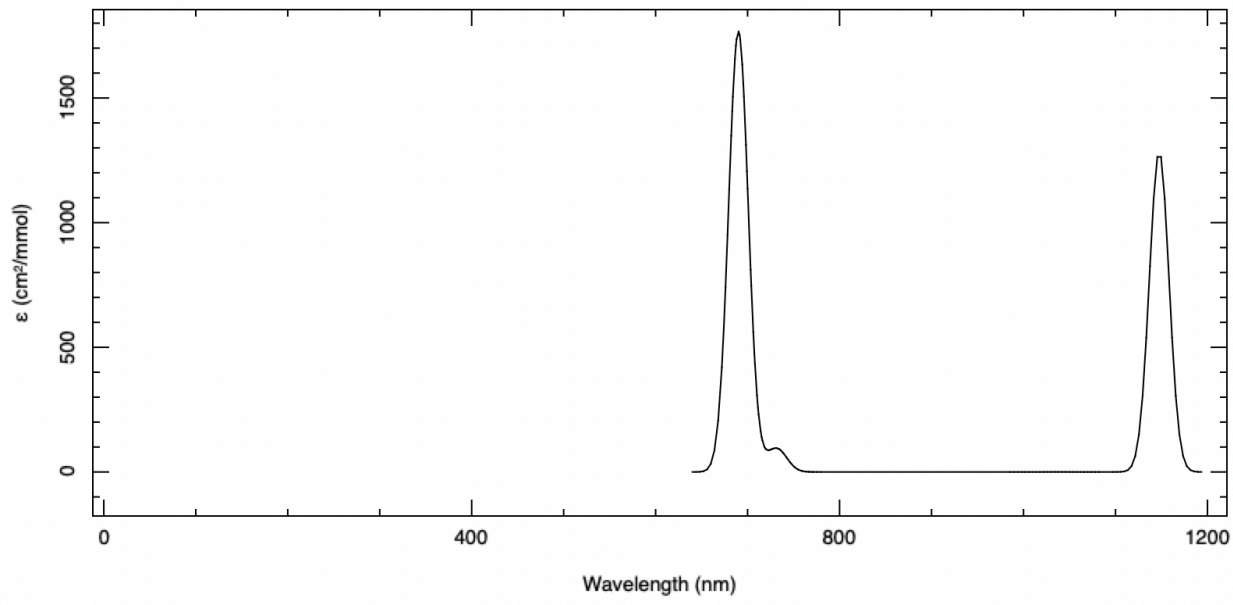

Figure 3-37. Predicted absorption spectrum of **2.25-A** calculated at the B3LYP/def2-TZVP level of theory.

3.6 Conclusion

In conclusion, the photophysical properties, along with the redox and computational studies of **2.14**, **2.15**, and **2.25** were examined. Compound **2.14** displays distinct CT character based on the solvatochromic fluorescence of the compound. The voltammogram of **2.14** displays an irreversible oxidation event at 0.76 V corresponding to the oxidation of **2.14** to **2.14-A** and the loss of a proton. Compound **2.14-A** was isolated by oxidation using $K_3Fe(CN)_6$ as oxidant. The resulting red compound displayed paramagnetism as shown using EPR spectroscopy. We also observe the appearance of two new absorbance bands in the UV-Vis spectrum. Computationally, with respect to **2.14**, a HOMO-LUMO gap of 3.19 eV was calculated using B3LYP/def2-TZVP, and the resulting predicted UV-Vis spectrum was in moderate agreement with the experimental. Conversely, the predicted α-SOMO–β-LUMO gap for **2.14-A** was predicted 1.91 eV. These results require further corroboration using TD-DFT.

2.15 was examined using UV-Vis spectroscopy and TD-DFT, and displayed an experimental λ_{max} of 410 nm. Computationally, the predicted maximum absorption was determined to be 487 nm requiring further optimization of our computational methods. Compound **2.15** underwent oxidation to form **2.36** as the two-electron oxidation product assuming a quinoid structure. This compound was characterized using TD-DFT as well as NMR and UV-Vis spectroscopy. The computational method used predicted a maximum absorption of 436 nm, compared to the experimental value of 540 nm. Again, further optimization of our computational methods are required to better validate these results.

Compound **2.25** was characterized using UV-Vis and fluorescence spectroscopy, along with CV and TD-DFT. The UV-Vis spectrum showed a solvent-dependent maximum absorption band between 665 nm and 690 nm with a molar extinction coefficient of 1.65×10^5 M^{-1} cm^{-1}. A

secondary absorption band at 410 nm with a molar extinction coefficient of $9.52x10^3$ M^{-1} cm^{-1}. Based on the fluorescence spectroscopy results, **2.25** does not have CT characteristics, however, does display increased fluorescence in non-polar solvents.

The voltammogram of **2.25** shows an oxidation event occurring at -0.69 V which is not possible to assign based on the data available to us. Computationally it is shown that the HOMO resides primarily on the cyclobutenolate core of the compound which indicates oxidation would not first occur at the phenol moieties as hoped. Attempts to oxidize **2.25** to a SFR were unsuccessful using the methods tried. We aimed instead to isolate the dianion **2.25-A** and carry out our oxidation using the product of this experiment. We characterized the deprotonation of **2.25** with sequential additions of NaHMDS by UV-Vis spectroscopy in THF. Disappearance of the main absorption band at 682 nm following the appearance of a strong absorption in the UV region showed increased CT character due to increased anionic character. Computational studies of **2.25-A** predict a λ_{max} of 690 nm and a second strong absorption at 1147 nm. Further absorption studies of **2.25-A** are necessary to confirm the validity of these results.

Chapter 4 Conclusions, and Future Work

4.1 Conclusions

As discussed in Chapter 1, the objective of this thesis was to synthesize two target squaraine dyes, **2.25** and **2.31**, functionalized with DA groups. The synthetic methodologies and characterization procedures were described in Chapter 2. The synthesis of **2.25** involved the use of SMC from precursors **2.14** and **2.24**. Surprisingly, the isolation of **2.14** and **2.15** proved to be challenging despite their relative synthetic simplicity as outlined in the retrosynthesis towards **2.25**. Nonetheless, compounds **2.14** and **2.15** were successfully isolated and characterized using UV-Vis, fluorimetry, CV, a comprehensive suite of $^{1}H/^{13}C$ NMR spectroscopy experiments, and TD-DFT. The subsequent synthesis of **2.25** was carried out without purifying the mixture of **2.14** and **2.15**, as compound **2.15** demonstrated inertness under the SMC conditions. Compound **2.25** was isolated and characterized using UV-Vis, fluorimetry, CV, $^{1}H/^{13}C$ NMR spectroscopy, HRMS, and TD-DFT.

A synthetic pathway towards the synthesis of compound **2.31** was proposed, analogous to the synthesis of **2.25**. From the available literature, only the synthesis of **2.27** has been published. With the assistance of undergraduate student Max Strasser, we succeeded in isolating **2.28a** with a yield of 31%, which was subsequently utilized for the synthesis of **2.29** with a yield of 92%. However, attempts to synthesize **2.30** using Miyaura borylation conditions were unsuccessful based on a 24-plate HTS experiment. Analysis revealed that only 3 out of the 24 conditions exhibited activity, each resulting in the formation of **2.35** as the protodeboronated squaraine. Further optimization of this reaction is required.

Chapter 3 provides a comprehensive discussion of the characterization of all relevant compounds. Both **2.14** and **2.15** exhibited qualitative fluorescence, although only **2.14** was

subjected to quantitative analysis due to its poor yields. Compound **2.14** displayed pronounced solvatochromic fluorescence characteristics typical of CT compounds. Consequently, an oxidation reaction was performed to produce SFR **2.14-A** using a mild oxidant, potassium ferricyanide. The resulting product was characterized using UV-Vis, EPR spectrometry, and TD-DFT. The absorption profile exhibited the emergence of two new bands at 500 nm and 540 nm. The EPR spectrum confirmed the presence of a paramagnetic species, while HRMS provided evidence of the radical in negative ion mode. However, these HRMS results do not confirm the presence of the radical, as the anion formed in negative ion mode can be accessed from **2.14** by deprotonating the phenolic proton. Notably, no evidence of **2.14** was found in the sample.

Compound **2.25** was obtained as a dark blue solid with an extinction coefficient of 1.65×10^5 M^{-1} cm^{-1} in DCM. Excitation at wavelengths of 400 nm and 675 nm resulted in strong emission below 700 nm in both cases. Furthermore, the emission intensity increased in non-polar solvents, with a reduction in intensity as polarity increased. Unfortunately, the emission spectra of the compound in various solvents did not exhibit any solvatochromism, indicating a loss of CT character.

TD-DFT calculations revealed that the HOMO of **2.25** predominantly localized on the cyclobutenolate core of the compound rather than the phenols. This prompted an investigation into deprotonation to form **2.25-A**, which would shift the HOMO to the phenolate peripheries. DFT analysis confirmed this hypothesis. The addition of NaHMDS resulted in the disappearance of the main absorption band between 672 nm and 692 nm, accompanied by the appearance of an absorption band at 324 nm. Based on TD-DFT, it is likely that absorbance also occurs in the NIR region beyond 1000 nm. Unfortunately, measurements beyond 1000 nm were unattainable due to the LOD of the spectrophotometer used.

Squaraine **2.29** was characterized using UV-Vis, fluorimetry, $^{1}H/^{13}C$ NMR spectroscopy, and HRMS. The λ_{max} in DCM was observed at 636 nm, with an extinction coefficient of $2.49x10^{5}$ M^{-1} cm^{-1}. Excitation at this wavelength led to emission at 646 nm. The complete assignments of proton and carbon NMR spectroscopy, as well as HRMS data, are provided in Appendix 1.

4.2 Future Work

Due to the limitations imposed by time constraints, further optimization endeavors pertaining to the synthesis of compound **2.31** could not be pursued. Building upon the outcomes derived from our primary screening in the synthesis of compound **2.30**, we propose the adoption of $B_2(Epin)_2$ as our preferred borylating agent to facilitate the formation of compound **2.30-2**, as depicted in **Figure 4-1**. This proposal is substantiated by previous literature that showcases improved stability during silica gel chromatography and higher yields.[174] Subsequently, we anticipate that the Suzuki cross-coupling reaction employed for the synthesis of compound **2.31** may encounter similar challenges as the borylation step and will necessitate careful optimization.

Should the isolation of compound **2.30-2** prove to be more intricate than that of compound **2.30**, modifications to reaction parameters such as temperature, reaction duration, or solvent choice hold promise in achieving the desired products. Additionally, as a final contingency, we suggest alternative cross-coupling methods, such as Stille coupling utilizing organotin reagents, as depicted in **Figure 4-2**.

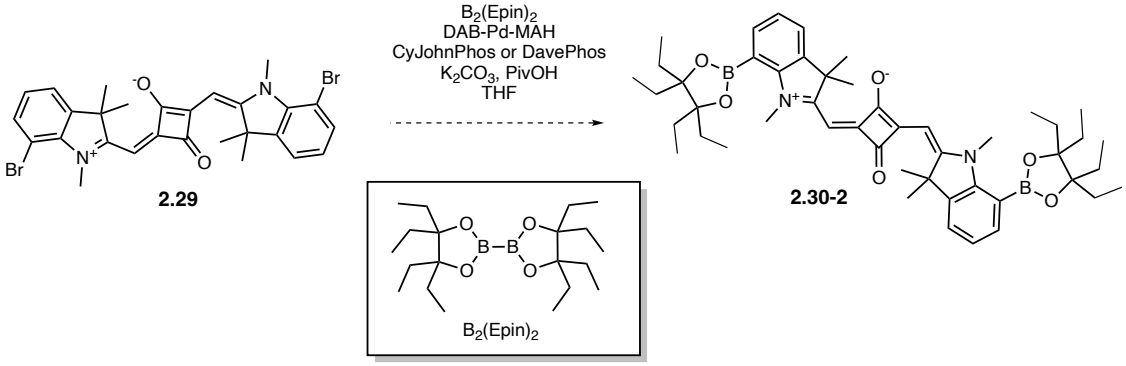

Figure 4-1. Proposed conditions towards **2.30-2**.

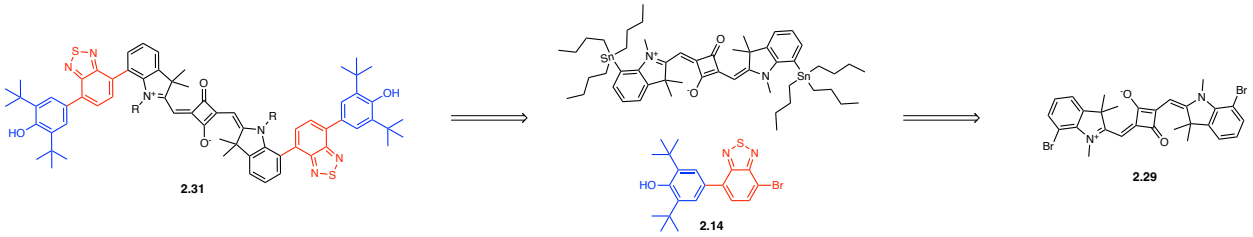

Figure 4-2. Proposed alternate synthetic route to **2.31**.

To capitalize on the promising properties of compounds **2.14** and **2.15** for potential material applications, further optimization in their synthesis is warranted based on our findings. A comprehensive characterization of **2.14-A** should involve quantitative EPR spectroscopy and stoichiometric addition of oxidant to monitor the conversion from its neutral counterpart. Currently, crystals of **2.14-A** have been cultivated, and we eagerly await the results from X-ray diffractometry, which will provide conclusive evidence confirming the isolation of SFR **2.14-A**.

Computational optimization is imperative, taking into account the outcomes obtained from our TD-DFT experiments. While experimental UV-Vis data aligns favorably with computational results in the case of **2.25**, discrepancies are apparent between computational and experimental findings for **2.14**, **2.14-A**, **2.15**, and **2.36**. Nevertheless, the distributions and energies of the HOMO and lowest unoccupied molecular orbital LUMO correspond harmoniously with those determined experimentally through CV and UV-Vis analysis.

Comprehensive characterization of all compounds presented in this thesis necessitates the determination of their FQYs and lifetime measurements. For compounds **2.14**, **2.15**, **2.25**, and **2.31**, computational evidence does not suggest the presence of TADF based on the calculated energy gap ΔE_{ST}. We propose employing single-photon measurements to ascertain fluorescence lifetimes at various temperatures for each compound. If TADF manifests in these compounds, a decrease in fluorescence lifetime is expected with decreasing temperature, as thermal energy required for RISC diminishes.

Finally, the comprehensive examination of the compounds presented in this thesis would benefit from additional CV experiments. Regrettably, due to the limited yields obtained for compounds **2.14** and **2.15**, it was not feasible to gather additional data beyond what has been presented in Chapter 3. Moreover, the solubility challenges encountered during the analysis of compound **2.25** further impeded our ability to fully characterize its redox properties. Consequently, we encourage future researchers to delve deeper into the investigation of compound **2.25-A** since computational evidence indicates that the HOMO is prominently located on the phenolic moieties, thereby facilitating easy accessibility to the corresponding SFR.

4.3 Preliminary Computational Results on 2.31

Our ongoing research focuses on the comprehensive investigation of compound **2.31** using DFT and TD-DFT. To achieve optimization, we have employed the ωB97X-3D functional and def2-TZVP level of theory, substituting the *N*-octyl chains with *N*-methyl substituents. Initial findings reveal that the HOMO predominantly resides within the cyclobutenolate core, while the LUMO extends across the indolenine and the BTD acceptor. The calculated HOMO energy is -6.53 eV, the LUMO energy is -0.97 eV, and the corresponding energy gap measures 5.56 eV. A

graphical representation of the energy diagram is illustrated in **Figure 4-3**. Similar to the observations made for **2.25**, this functional and basis set combination exhibits a relatively large HOMO-LUMO energy gap, rendering its reliability questionable despite its expected strong light absorption capabilities.

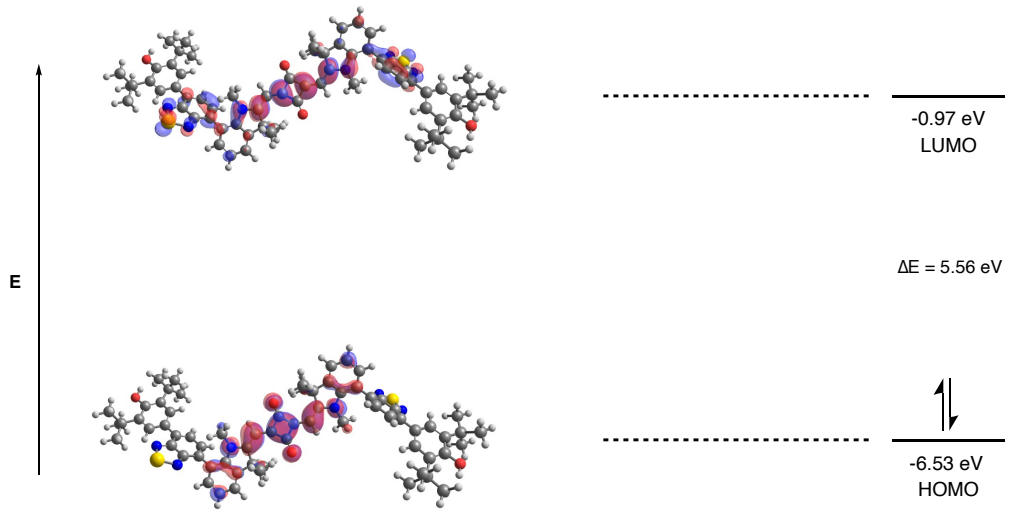

Figure 4-3. HOMO and LUMO for *N*-methylated analogue of **2.31** at the ωB97X-3D/def2-TZVP level of theory.

References

(1) Wang, H.; Wu, J.; Noble, A.; Aggarwal, V. K. Selective Coupling of 1,2-Bis-Boronic Esters at the More Substituted Site through Visible-Light Activation of Electron Donor–Acceptor Complexes. *Angew. Chem.* **2022**, *134* (18), e202202061. https://doi.org/10.1002/ange.202202061.

(2) Dávila Cerón, V.; Illicachi, L. A.; Insuasty, B. Triazine: An Important Building Block of Organic Materials for Solar Cell Application. *Molecules* **2023**, *28* (1), 257. https://doi.org/10.3390/molecules28010257.

(3) Li, X.; Yue, X.; Wang, Y.; Chen, T.; Zhou, Y.; Liu, D.; Xiang, H.; Zhang, S.; Zeng, H.; Xiang, Z. Electron Donor–Acceptor (D-A) Tuning to Achieve Soluble Covalent Organic Polymers for Optoelectronic Devices. *eScience* **2023**, *3* (1), 100084. https://doi.org/10.1016/j.esci.2022.10.009.

(4) Can, A.; Choi, G.-S.; Ozdemir, R.; Park, S.; Park, J. S.; Lee, Y.; Deneme, İ.; Mutlugun, E.; Kim, C.; Kim, B. J.; Usta, H. Meso-π-Extended/Deficient BODIPYs and Low-Band-Gap Donor–Acceptor Copolymers for Organic Optoelectronics. *ACS Appl. Polym. Mater.* **2022**, *4* (3), 1991–2005. https://doi.org/10.1021/acsapm.1c01856.

(5) Tasnim, T.; Ayodele, M. J.; Pitre, S. P. Recent Advances in Employing Catalytic Donors and Acceptors in Electron Donor–Acceptor Complex Photochemistry. *J. Org. Chem.* **2022**, *87* (16), 10555–10563. https://doi.org/10.1021/acs.joc.2c01013.

(6) Zhou, W.; Wu, S.; Melchiorre, P. Tetrachlorophthalimides as Organocatalytic Acceptors for Electron Donor–Acceptor Complex Photoactivation. *J. Am. Chem. Soc.* **2022**, *144* (20), 8914–8919. https://doi.org/10.1021/jacs.2c03546.

(7) Liu, J.; Zhang, X.; Zhang, J.; Zhang, S.; Chen, Y.; Chen, H.; Chen, H.; Lin, M. Interpenetration of Donor–Acceptor Hybrid Frameworks for Highly Sensitive Thermal Sensors. *ACS Appl. Mater. Interfaces* **2022**, *14* (21), 24575–24582. https://doi.org/10.1021/acsami.2c03578.

(8) Ling, Y.; Dong, Y.; Huang, W.; Liu, J.; Feng, S.; Huang, W. Orthogonally Responsive Donor–Acceptor Stenhouse Adduct/Poly(2-Ethylsulfonyl-2-Oxazoline) Colorimetric Sensors with Nonvolatile Memories. *ACS Appl. Polym. Mater.* **2022**, *4* (9), 6505–6513. https://doi.org/10.1021/acsapm.2c00915.

(9) Obaid Saleh, R.; Olegovich Bokov, D.; Fenjan, M. N.; Kamal Abdelbasset, W.; Altimari, U. S.; Turki Jalil, A.; Thangavelu, L.; Suksatan, W.; Cao, Y. Application of Aluminum Nitride Nanotubes as a Promising Nanocarriers for Anticancer Drug 5-Aminosalicylic Acid in Drug Delivery System. *J. Mol. Liq.* **2022**, *352*, 118676. https://doi.org/10.1016/j.molliq.2022.118676.

(10) Ghosh, R.; Mondal, S.; Mukherjee, D.; Adhikari, A.; A. Ahmed, S.; I. Alsantali, R.; S. Khder, A.; M. Altass, H.; Moussa, Z.; Das, R.; Bhattacharyya, M.; Kumar Pal, S. Oral Drug Delivery Using a Polymeric Nanocarrier: Chitosan Nanoparticles in the Delivery of Rifampicin. *Mater. Adv.* **2022**, *3* (11), 4622–4628. https://doi.org/10.1039/D2MA00295G.

(11) Lu, J.; Zhu, X.; Zhang, M.; Jiang, X.; Guo, W.; Jiang, F.; Cao, F. In Vitro and in Vivo Assessment of Structural Integrity for HPCD Complex@Liposome Nanocomposites from Ocular Surface to the Posterior Segment of the Eye. *Carbohydr. Polym.* **2023**, *315*, 120960. https://doi.org/10.1016/j.carbpol.2023.120960.

(12) Ribeiro, B. C.; Alvarez, C. A. R.; Alves, B. C.; Rodrigues, J. M.; Queiroz, M. J. R. P.; Almeida, B. G.; Pires, A.; Pereira, A. M.; Araújo, J. P.; Coutinho, P. J. G.; Rodrigues, A.

R. O.; Castanheira, E. M. S. Development of Thermo- and PH-Sensitive Liposomal Magnetic Carriers for New Potential Antitumor Thienopyridine Derivatives. *Materials* **2022**, *15* (5), 1737. https://doi.org/10.3390/ma15051737.

(13) Kumar, S.; Rajamalli, P.; Cordes, D. B.; Slawin, A. M. Z.; Zysman-Colman, E. Highly Fluorescent Emitters Based on Triphenylamine-π-Triazine (D-π-A) System: Effect of Extended Conjugation on Singlet-Triplet Energy Gap. *Asian J. Org. Chem.* **2020**, *9* (9), 1277–1285. https://doi.org/10.1002/ajoc.202000165.

(14) Goushi, K.; Yoshida, K.; Sato, K.; Adachi, C. Organic Light-Emitting Diodes Employing Efficient Reverse Intersystem Crossing for Triplet-to-Singlet State Conversion. *Nat. Photonics* **2012**, *6* (4), 253–258. https://doi.org/10.1038/nphoton.2012.31.

(15) Zhang, Q.; Li, B.; Huang, S.; Nomura, H.; Tanaka, H.; Adachi, C. Efficient Blue Organic Light-Emitting Diodes Employing Thermally Activated Delayed Fluorescence. *Nat. Photonics* **2014**, *8* (4), 326–332. https://doi.org/10.1038/nphoton.2014.12.

(16) Chan, C.-Y.; Tanaka, M.; Lee, Y.-T.; Wong, Y.-W.; Nakanotani, H.; Hatakeyama, T.; Adachi, C. Stable Pure-Blue Hyperfluorescence Organic Light-Emitting Diodes with High-Efficiency and Narrow Emission. *Nat. Photonics* **2021**, *15* (3), 203–207. https://doi.org/10.1038/s41566-020-00745-z.

(17) Baldo, M. A.; O'Brien, D. F.; You, Y.; Shoustikov, A.; Sibley, S.; Thompson, M. E.; Forrest, S. R. Highly Efficient Phosphorescent Emission from Organic Electroluminescent Devices. *Nature* **1998**, *395* (6698), 151–154. https://doi.org/10.1038/25954.

(18) Uoyama, H.; Goushi, K.; Shizu, K.; Nomura, H.; Adachi, C. Highly Efficient Organic Light-Emitting Diodes from Delayed Fluorescence. *Nature* **2012**, *492* (7428), 234–238. https://doi.org/10.1038/nature11687.

(19) Hojo, R.; T. Luppi, B.; Bergmann, K.; M. Hudson, Z. Through-Space Charge Transfer Delayed Fluorescence in Tris(Triazolo)Triazine Donor–Acceptor Copolymers. *Polym. Chem.* **2023**, *14* (22), 2742–2749. https://doi.org/10.1039/D3PY00325F.

(20) Hu, J.; Li, Q.; Wang, X.; Shao, S.; Wang, L.; Jing, X.; Wang, F. Developing Through-Space Charge Transfer Polymers as a General Approach to Realize Full-Color and White Emission with Thermally Activated Delayed Fluorescence. *Angew. Chem. Int. Ed.* **2019**, *58* (25), 8405–8409. https://doi.org/10.1002/anie.201902264.

(21) Puttock, E. V.; Ranasinghe, C. S. K.; Babazadeh, M.; Jang, J.; Huang, D. M.; Tsuchiya, Y.; Adachi, C.; Burn, P. L.; Shaw, P. E. Solution-Processed Dendrimer-Based TADF Materials for Deep-Red OLEDs. *Macromolecules* **2020**, *53* (23), 10375–10385. https://doi.org/10.1021/acs.macromol.0c02235.

(22) Ganesan, P.; Ranganathan, R.; Chi, Y.; Liu, X.-K.; Lee, C.-S.; Liu, S.-H.; Lee, G.-H.; Lin, T.-C.; Chen, Y.-T.; Chou, P.-T. Functional Pyrimidine-Based Thermally Activated Delay Fluorescence Emitters: Photophysics, Mechanochromism, and Fabrication of Organic Light-Emitting Diodes. *Chem. – Eur. J.* **2017**, *23* (12), 2858–2866. https://doi.org/10.1002/chem.201604883.

(23) Chen, T.; Zheng, L.; Yuan, J.; An, Z.; Chen, R.; Tao, Y.; Li, H.; Xie, X.; Huang, W. Understanding the Control of Singlet-Triplet Splitting for Organic Exciton Manipulating: A Combined Theoretical and Experimental Approach. *Sci. Rep.* **2015**, *5* (1), 10923. https://doi.org/10.1038/srep10923.

(24) Yang, Z.; Mao, Z.; Xie, Z.; Zhang, Y.; Liu, S.; Zhao, J.; Xu, J.; Chi, Z.; Aldred, M. P. Recent Advances in Organic Thermally Activated Delayed Fluorescence Materials. *Chem. Soc. Rev.* **2017**, *46* (3), 915–1016. https://doi.org/10.1039/C6CS00368K.

(25) Cha, J.-R.; Lee, C. W.; Lee, J. Y.; Gong, M.-S. Design of Ortho-Linkage Carbazole-Triazine Structure for High-Efficiency Blue Thermally Activated Delayed Fluorescent Emitters. *Dyes Pigments* **2016**, *134*, 562–568. https://doi.org/10.1016/j.dyepig.2016.08.023.

(26) Song, D.; Yu, Y.; Yue, L.; Zhong, D.; Zhang, Y.; Yang, X.; Sun, Y.; Zhou, G.; Wu, Z. Asymmetric Thermally Activated Delayed Fluorescence (TADF) Emitters with 5,9-Dioxa-13b-Boranaphtho[3,2,1-de]Anthracene (OBA) as the Acceptor and Highly Efficient Blue-Emitting OLEDs. *J. Mater. Chem. C* **2019**, *7* (38), 11953–11963. https://doi.org/10.1039/C9TC04115J.

(27) Che, W.; Xie, Y.; Li, Z. Structural Design of Blue-to-Red Thermally-Activated Delayed Fluorescence Molecules by Adjusting the Strength between Donor and Acceptor. *Asian J. Org. Chem.* **2020**, *9* (9), 1262–1276. https://doi.org/10.1002/ajoc.202000128.

(28) Li, W.; Li, B.; Cai, X.; Gan, L.; Xu, Z.; Li, W.; Liu, K.; Chen, D.; Su, S.-J. Tri-Spiral Donor for High Efficiency and Versatile Blue Thermally Activated Delayed Fluorescence Materials. *Angew. Chem. Int. Ed.* **2019**, *58* (33), 11301–11305. https://doi.org/10.1002/anie.201904272.

(29) Bergmann, K.; Hojo, R.; Hudson, Z. M. Uncovering the Mechanism of Thermally Activated Delayed Fluorescence in Coplanar Emitters Using Potential Energy Surface Analysis. *J. Phys. Chem. Lett.* **2023**, *14* (2), 310–317. https://doi.org/10.1021/acs.jpclett.2c03425.

(30) McClain, E. J.; Monos, T. M.; Mori, M.; Beatty, J. W.; Stephenson, C. R. J. Design and Implementation of a Catalytic Electron Donor–Acceptor Complex Platform for Radical

Trifluoromethylation and Alkylation. *ACS Catal.* **2020**, *10* (21), 12636–12641. https://doi.org/10.1021/acscatal.0c03837.

(31) Figueira-Duarte, T. M.; Lloveras, V.; Vidal-Gancedo, J.; Gégout, A.; Delavaux-Nicot, B.; Welter, R.; Veciana, J.; Rovira, C.; Nierengarten, J.-F. Changes in Electronic Couplings of Mixed-Valence Systems Due to through-Space Intramolecular Interactions. *Chem. Commun.* **2007**, No. 42, 4345–4347. https://doi.org/10.1039/B707522G.

(32) Zhu, L.; Zhong, C.; Liu, Z.; Yang, C.; Qin, J. New Intramolecular Through-Space Charge Transfer Emission: Tunable Dual Fluorescence of Terfluorenes. *Chem. Commun.* **2010**, *46* (36), 6666–6668. https://doi.org/10.1039/C0CC00136H.

(33) Wahadoszamen, M.; Margalit, I.; Ara, A. M.; van Grondelle, R.; Noy, D. The Role of Charge-Transfer States in Energy Transfer and Dissipation within Natural and Artificial Bacteriochlorophyll Proteins. *Nat. Commun.* **2014**, *5* (1), 5287. https://doi.org/10.1038/ncomms6287.

(34) Koslowski, T.; Burggraf, F.; Krapf, S.; Steinbrecher, T.; Wittekindt, C. Recent Progress in Biological Charge Transfer: Theory and Simulation. *Biochim. Biophys. Acta BBA - Bioenerg.* **2012**, *1817* (10), 1955–1957. https://doi.org/10.1016/j.bbabio.2012.02.025.

(35) Weber, S. Light-Driven Enzymatic Catalysis of DNA Repair: A Review of Recent Biophysical Studies on Photolyase. *Biochim. Biophys. Acta BBA - Bioenerg.* **2005**, *1707* (1), 1–23. https://doi.org/10.1016/j.bbabio.2004.02.010.

(36) Ansari, R.; Shao, W.; Yoon, S.-J.; Kim, J.; Kieffer, J. Charge Transfer as the Key Parameter Affecting the Color Purity of Thermally Activated Delayed Fluorescence Emitters. *ACS Appl. Mater. Interfaces* **2021**, *13* (24), 28529–28537. https://doi.org/10.1021/acsami.1c02943.

(37) Hustings, J.; Bonné, R.; Cornelissen, R.; Morini, F.; Valcke, R.; Vandewal, K.; Manca, J. V. Charge-Transfer States in Photosynthesis and Organic Solar Cells. *Front. Photonics* **2022**, *3*.

(38) Rotkiewicz, K.; Grellmann, K. H.; Grabowski, Z. R. Reinterpretation of the Anomalous Fluorescense of P-n,n-Dimethylamino-Benzonitrile. *Chem. Phys. Lett.* **1973**, *19* (3), 315–318. https://doi.org/10.1016/0009-2614(73)80367-7.

(39) Grabowski, Z. R.; Rotkiewicz, K.; Rettig, W. Structural Changes Accompanying Intramolecular Electron Transfer: Focus on Twisted Intramolecular Charge-Transfer States and Structures. *Chem. Rev.* **2003**, *103* (10), 3899–4032. https://doi.org/10.1021/cr9407451.

(40) Wang, C.; Chi, W.; Qiao, Q.; Tan, D.; Xu, Z.; Liu, X. Twisted Intramolecular Charge Transfer (TICT) and Twists beyond TICT: From Mechanisms to Rational Designs of Bright and Sensitive Fluorophores. *Chem. Soc. Rev.* **2021**, *50* (22), 12656–12678. https://doi.org/10.1039/D1CS00239B.

(41) Lippert, E.; Lüder, W.; Moll, F.; Nägele, W.; Boos, H.; Prigge, H.; Seibold-Blankenstein, I. Umwandlung von Elektronenanregungsenergie. *Angew. Chem.* **1961**, *73* (21), 695–706. https://doi.org/10.1002/ange.19610732103.

(42) Chen, C.; Fang, C. Fluorescence Modulation by Amines: Mechanistic Insights into Twisted Intramolecular Charge Transfer (TICT) and Beyond. *Chemosensors* **2023**, *11* (2), 87. https://doi.org/10.3390/chemosensors11020087.

(43) Haberhauer, G.; Gleiter, R.; Burkhart, C. Planarized Intramolecular Charge Transfer: A Concept for Fluorophores with Both Large Stokes Shifts and High Fluorescence Quantum Yields. *Chem. – Eur. J.* **2016**, *22* (3), 971–978. https://doi.org/10.1002/chem.201503927.

(44) Dereka, B.; Svechkarev, D.; Rosspeintner, A.; Tromayer, M.; Liska, R.; Mohs, A. M.; Vauthey, E. Direct Observation of a Photochemical Alkyne–Allene Reaction and of a Twisted and Rehybridized Intramolecular Charge-Transfer State in a Donor–Acceptor Dyad. *J. Am. Chem. Soc.* **2017**, *139* (46), 16885–16893. https://doi.org/10.1021/jacs.7b09591.

(45) Ratera, I.; Veciana, J. Playing with Organic Radicals as Building Blocks for Functional Molecular Materials. *Chem Soc Rev* **2012**, *41* (1), 303–349. https://doi.org/10.1039/C1CS15165G.

(46) Hicks, R. G. What's New in Stable Radical Chemistry? *Org. Biomol. Chem.* **2007**, *5* (9), 1321. https://doi.org/10.1039/b617142g.

(47) Gomberg, M. AN INSTANCE OF TRIVALENT CARBON: TRIPHENYLMETHYL. *J. Am. Chem. Soc.* **1900**, *22* (11), 757–771. https://doi.org/10.1021/ja02049a006.

(48) Bochkarev, L. N.; Molosnova, N. E.; Zakharov, L. N.; Fukin, G. K.; Yanovsky, A. I.; Struchkov, Y. T. 1-Diphenylmethylene-4-(Triphenylmethyl)Cyclohexa-2,5-Diene Benzene Solvate. *Acta Crystallogr. C* **1995**, *51* (3), 489–491. https://doi.org/10.1107/S0108270194009005.

(49) McBride, J. M. The Hexaphenylethane Riddle. *Tetrahedron* **1974**, *30* (14), 2009–2022. https://doi.org/10.1016/S0040-4020(01)97332-6.

(50) Souto, M.; Gullo, M. C.; Cui, H.; Casati, N.; Montisci, F.; Jeschke, H. O.; Valentí, R.; Ratera, I.; Rovira, C.; Veciana, J. Role of the Open-Shell Character on the Pressure-Induced Conductivity of an Organic Donor–Acceptor Radical Dyad. *Chem. – Eur. J.* **2018**, *24* (21), 5500–5505. https://doi.org/10.1002/chem.201800881.

(51) Guo, H.; Peng, Q.; Chen, X.-K.; Gu, Q.; Dong, S.; Evans, E. W.; Gillett, A. J.; Ai, X.; Zhang, M.; Credgington, D.; Coropceanu, V.; Friend, R. H.; Brédas, J.-L.; Li, F. High Stability and Luminescence Efficiency in Donor–Acceptor Neutral Radicals Not Following the Aufbau Principle. *Nat. Mater.* **2019**, *18* (9), 977–984. https://doi.org/10.1038/s41563-019-0433-1.

(52) Souto, M.; Solano, M. V.; Jensen, M.; Bendixen, D.; Delchiaro, F.; Girlando, A.; Painelli, A.; Jeppesen, J. O.; Rovira, C.; Ratera, I.; Veciana, J. Self-Assembled Architectures with Segregated Donor and Acceptor Units of a Dyad Based on a Monopyrrolo-Annulated TTF–PTM Radical. *Chem. – Eur. J.* **2015**, *21* (24), 8816–8825. https://doi.org/10.1002/chem.201500497.

(53) Prakash, N.; Rajeev, R.; John, A.; Vijayan, A.; George, L.; Varghese, A. 2,2,6,6-Tetramethylpiperidinyloxyl (TEMPO) Radical Mediated Electro-Oxidation Reactions: A Review. *ChemistrySelect* **2021**, *6* (30), 7691–7710. https://doi.org/10.1002/slct.202102346.

(54) Sugano, T.; Fukasawa, T.; Kinoshita, M. Magnetic Interactions among Unpaired Electrons in Charge-Transfer Complexes of Organic Donors Having a Neutral Radical. *Synth. Met.* **1991**, *43* (1), 3281–3284. https://doi.org/10.1016/0379-6779(91)91287-K.

(55) Li, Y.; Li, L.; Wu, Y.; Li, Y. A Review on the Origin of Synthetic Metal Radical: Singlet Open-Shell Radical Ground State? *J. Phys. Chem. C* **2017**, *121* (15), 8579–8588. https://doi.org/10.1021/acs.jpcc.6b12936.

(56) Phan, H.; Herng, T. S.; Wang, D.; Li, X.; Zeng, W.; Ding, J.; Loh, K. P.; Shen Wee, A. T.; Wu, J. Room-Temperature Magnets Based on 1,3,5-Triazine-Linked Porous Organic

Radical Frameworks. *Chem* **2019**, *5* (5), 1223–1234. https://doi.org/10.1016/j.chempr.2019.02.024.

(57) Matsushita, M. M.; Kawakami, H.; Kawada, Y.; Sugawara, T. Negative Magneto-Resistance Observed on an Ion-Radical Salt of a TTF-Based Spin-Polarized Donor. *Chem. Lett.* **2007**, *36* (1), 110–111. https://doi.org/10.1246/cl.2007.110.

(58) Matsushita, M. M.; Kawakami, H.; Sugawara, T.; Ogata, M. Molecule-Based System with Coexisting Conductivity and Magnetism and without Magnetic Inorganic Ions. *Phys. Rev. B* **2008**, *77* (19), 195208. https://doi.org/10.1103/PhysRevB.77.195208.

(59) Janoschka, T.; Hager, M. D.; Schubert, U. S. Powering up the Future: Radical Polymers for Battery Applications. *Adv. Mater.* **2012**, *24* (48), 6397–6409. https://doi.org/10.1002/adma.201203119.

(60) Chen, Z.; Li, W.; Zhang, Y.; Wang, Z.; Zhu, W.; Zeng, M.; Li, Y. Aggregation-Induced Radical of Donor–Acceptor Organic Semiconductors. *J. Phys. Chem. Lett.* **2021**, *12* (40), 9783–9790. https://doi.org/10.1021/acs.jpclett.1c02463.

(61) Poggini, L.; Cucinotta, G.; Sorace, L.; Caneschi, A.; Gatteschi, D.; Sessoli, R.; Mannini, M. Nitronyl Nitroxide Radicals at the Interface: A Hybrid Architecture for Spintronics. *Rendiconti Lincei Sci. Fis. E Nat.* **2018**, *29* (3), 623–630. https://doi.org/10.1007/s12210-018-0732-5.

(62) DaRooge, M. A.; Mahoney, L. R. Reaction of 2,4,6-Tri-Tert-Butylphenoxy Radical with Unhindered Phenols. *J. Org. Chem.* **1967**, *32* (1), 1–6. https://doi.org/10.1021/jo01277a001.

(63) Kuhn, R.; Trischmann, H. Über Verdazyle, eine neue Klasse cyclischer N-haltiger Radikale. *Monatshefte Für Chem. Verwandte Teile Anderer Wiss.* **1964**, *95* (2), 457–479. https://doi.org/10.1007/BF00901311.

(64) Tschitschibabin, A. E. Über Einige Phenylierte Derivate Des p, p-Ditolyls. *Berichte Dtsch. Chem. Ges.* **1907**, *40* (2), 1810–1819. https://doi.org/10.1002/cber.19070400282.

(65) Sprenger, H.-E.; Ziegenbein, W. Condensation Products of Squaric Acid and Tertiary Aromatic Amines. *Angew. Chem. Int. Ed. Engl.* **1966**, *5* (10), 894–894. https://doi.org/10.1002/anie.196608941.

(66) Sreejith, S.; Divya, K. P.; Ajayaghosh, A. A Near-Infrared Squaraine Dye as a Latent Ratiometric Fluorophore for the Detection of Aminothiol Content in Blood Plasma. *Angew. Chem. Int. Ed.* **2008**, *47* (41), 7883–7887. https://doi.org/10.1002/anie.200803194.

(67) Yang, X.; Yang, Z.; Wu, Z.; He, Y.; Shan, C.; Chai, P.; Ma, C.; Tian, M.; Teng, J.; Jin, D.; Yan, W.; Das, P.; Qu, J.; Xi, P. Mitochondrial Dynamics Quantitatively Revealed by STED Nanoscopy with an Enhanced Squaraine Variant Probe. *Nat. Commun.* **2020**, *11* (1), 3699. https://doi.org/10.1038/s41467-020-17546-1.

(68) Meador, W. E.; Autry, S. A.; Bessetti, R. N.; Gayton, J. N.; Flynt, A. S.; Hammer, N. I.; Delcamp, J. H. Water-Soluble NIR Absorbing and Emitting Indolizine Cyanine and Indolizine Squaraine Dyes for Biological Imaging. *J. Org. Chem.* **2020**, *85* (6), 4089–4095. https://doi.org/10.1021/acs.joc.9b03108.

(69) Yadav, Y.; Owens, E.; Nomura, S.; Fukuda, T.; Baek, Y.; Kashiwagi, S.; Choi, H. S.; Henary, M. Ultrabright and Serum-Stable Squaraine Dyes. *J. Med. Chem.* **2020**, *63* (17), 9436–9445. https://doi.org/10.1021/acs.jmedchem.0c00617.

(70) Xiao, X.; Cheng, X.-F.; Hou, X.; He, J.-H.; Xu, Q.-F.; Li, H.; Li, N.-J.; Chen, D.-Y.; Lu, J.-M. Ion-in-Conjugation: Squaraine as an Ultrasensitive Ammonia Sensor Material. *Small* **2017**, *13* (2), 1602190. https://doi.org/10.1002/smll.201602190.

(71) Hu, L.; Yan, Z.; Xu, H. Advances in Synthesis and Application of Near-Infrared Absorbing Squaraine Dyes. *RSC Adv.* **2013**, *3* (21), 7667–7676. https://doi.org/10.1039/C3RA23048A.

(72) Makowski, B. T.; Valle, B.; Singer, K. D.; Weder, C. A Melt-Processable Squaraine-Based Organic Glass for Nonlinear Optics. *J. Mater. Chem.* **2012**, *22* (7), 2848–2850. https://doi.org/10.1039/C2JM15573G.

(73) Qu, J.; Zhang, J.; Grimsdale, A. C.; Müllen, K.; Jaiser, F.; Yang, X.; Neher, D. Dendronized Perylene Diimide Emitters: Synthesis, Luminescence, and Electron and Energy Transfer Studies. *Macromolecules* **2004**, *37* (22), 8297–8306. https://doi.org/10.1021/ma0494131.

(74) Qin, C.; Wong, W.-Y.; Han, L. Squaraine Dyes for Dye-Sensitized Solar Cells: Recent Advances and Future Challenges. *Chem. – Asian J.* **2013**, *8* (8), 1706–1719. https://doi.org/10.1002/asia.201300185.

(75) Wöbkenberg, P. H.; Labram, J. G.; Swiecicki, J.-M.; Parkhomenko, K.; Sredojevic, D.; Gisselbrecht, J.-P.; Leeuw, D. M. de; Bradley, D. D. C.; Djukic, J.-P.; Anthopoulos, T. D. Ambipolar Organic Transistors and Near-Infrared Phototransistors Based on a Solution-Processable Squarilium Dye. *J. Mater. Chem.* **2010**, *20* (18), 3673–3680. https://doi.org/10.1039/B919970E.

(76) Al-horaibi, S. A.; Al-Odayni, A.-B. M.; Alezzy, A. A.; ALSaeedy, M. A.; Saeed, W. S.; El-Shishtawy, R. M. Novel D-Π-A Co-Sensitizers-Based Squaraine Dyes for Achieving

High-Performance of Dye-Sensitized Solar Cells. Rochester, NY March 16, 2023. https://doi.org/10.2139/ssrn.4380095.

(77) Alex, S.; Santhosh, U.; Das, S. Dye Sensitization of Nanocrystalline TiO2: Enhanced Efficiency of Unsymmetrical versus Symmetrical Squaraine Dyes. *J. Photochem. Photobiol. Chem.* **2005**, *172* (1), 63–71. https://doi.org/10.1016/j.jphotochem.2004.11.005.

(78) Jradi, F. M.; Kang, X.; O'Neil, D.; Pajares, G.; Getmanenko, Y. A.; Szymanski, P.; Parker, T. C.; El-Sayed, M. A.; Marder, S. R. Near-Infrared Asymmetrical Squaraine Sensitizers for Highly Efficient Dye Sensitized Solar Cells: The Effect of π-Bridges and Anchoring Groups on Solar Cell Performance. *Chem. Mater.* **2015**, *27* (7), 2480–2487. https://doi.org/10.1021/cm5045946.

(79) Li, B.; Li, W.; Xu, Y.; Li, J.; Tu, J.; Sun, S. A Simple Approach for the Discrimination of Surfactants Based on the Control of Squaraine Aggregation. *Chem. Commun.* **2015**, *51* (78), 14652–14655. https://doi.org/10.1039/C5CC06086A.

(80) Chen, G.; Sasabe, H.; Lu, W.; Wang, X.-F.; Kido, J.; Hong, Z.; Yang, Y. J-Aggregation of a Squaraine Dye and Its Application in Organic Photovoltaic Cells. *J. Mater. Chem. C* **2013**, *1* (40), 6547–6552. https://doi.org/10.1039/C3TC31243G.

(81) Merritt, V. Y.; Hovel, H. J. Organic Solar Cells of Hydroxy Squarylium. *Appl. Phys. Lett.* **2008**, *29* (7), 414–415. https://doi.org/10.1063/1.89101.

(82) Silvestri, F.; Irwin, M. D.; Beverina, L.; Facchetti, A.; Pagani, G. A.; Marks, T. J. Efficient Squaraine-Based Solution Processable Bulk-Heterojunction Solar Cells. *J. Am. Chem. Soc.* **2008**, *130* (52), 17640–17641. https://doi.org/10.1021/ja8067879.

(83) Chen, G.; Sasabe, H.; Wang, Z.; Wang, X.-F.; Hong, Z.; Yang, Y.; Kido, J. Co-Evaporated Bulk Heterojunction Solar Cells with >6.0% Efficiency. *Adv. Mater.* **2012**, *24* (20), 2768–2773. https://doi.org/10.1002/adma.201200234.

(84) Yang, D.; Sasabe, H.; Jiao, Y.; Zhuang, T.; Huang, Y.; Pu, X.; Sano, T.; Lu, Z.; Kido, J. An Effective π-Extended Squaraine for Solution-Processed Organic Solar Cells with High Efficiency. *J. Mater. Chem. A* **2016**, *4* (48), 18931–18941. https://doi.org/10.1039/C6TA08684E.

(85) Goh, T.; Huang, J.-S.; Yager, K. G.; Sfeir, M. Y.; Nam, C.-Y.; Tong, X.; Guard, L. M.; Melvin, P. R.; Antonio, F.; Bartolome, B. G.; Lee, M. L.; Hazari, N.; Taylor, A. D. Quaternary Organic Solar Cells Enhanced by Cocrystalline Squaraines with Power Conversion Efficiencies >10%. *Adv. Energy Mater.* **2016**, *6* (21), 1600660. https://doi.org/10.1002/aenm.201600660.

(86) Zheng, Y.; Huang, J.; Wang, G.; Kong, J.; Huang, D.; Mohadjer Beromi, M.; Hazari, N.; Taylor, A. D.; Yu, J. A Highly Efficient Polymer Non-Fullerene Organic Solar Cell Enhanced by Introducing a Small Molecule as a Crystallizing-Agent. *Mater. Today* **2018**, *21* (1), 79–87. https://doi.org/10.1016/j.mattod.2017.10.003.

(87) Xiao, Q.; Wu, F.; Han, M.; Li, Z.; Zhu, L.; Li, Z. A Pseudo-Two-Dimensional Conjugated Polysquaraine: An Efficient p-Type Polymer Semiconductor for Organic Photovoltaics and Perovskite Solar Cells. *J. Mater. Chem. A* **2018**, *6* (28), 13644–13651. https://doi.org/10.1039/C8TA05026K.

(88) Wang, Z.; Pradhan, A.; kamarudin, M. A.; Pandey, M.; Pandey, S. S.; Zhang, P.; Ng, C. huey; Tripathi, A. S. M.; Ma, T.; Hayase, S. Passivation of Grain Boundary by Squaraine

Zwitterions for Defect Passivation and Efficient Perovskite Solar Cells. *ACS Appl. Mater. Interfaces* **2019**, *11* (10), 10012–10020. https://doi.org/10.1021/acsami.8b22044.

(89) *The Nobel Prize in Chemistry 1912*. NobelPrize.org. https://www.nobelprize.org/prizes/chemistry/1912/sabatier/lecture/ (accessed 2023-05-08).

(90) Taylor, K. C. Automobile Catalytic Converters. In *Catalysis: Science and Technology Volume 5*; Anderson, J. R., Boudart, M., Eds.; Catalysis; Springer: Berlin, Heidelberg, 1984; pp 119–170. https://doi.org/10.1007/978-3-642-93247-2_2.

(91) Lundgren, R. J.; Stradiotto, M. Addressing Challenges in Palladium-Catalyzed Cross-Coupling Reactions Through Ligand Design. *Chem. – Eur. J.* **2012**, *18* (32), 9758–9769. https://doi.org/10.1002/chem.201201195.

(92) Wang, X.; Stanbury, D. M. Oxidation of Iodide by a Series of Fe(III) Complexes in Acetonitrile. *Inorg. Chem.* **2006**, *45* (8), 3415–3423. https://doi.org/10.1021/ic052022y.

(93) *Reactions of Alkenes with Sulfuric Acid*. Chemistry LibreTexts. https://chem.libretexts.org/Bookshelves/Organic_Chemistry/Supplemental_Modules_(Organic_Chemistry)/Reactions/Addition_Reactions/Electrophilic_Addition_Reactions/Reactions_of_Alkenes_with_Sulfuric_Acid (accessed 2023-06-29).

(94) Heck, R. F.; Nolley, J. P. Jr. Palladium-Catalyzed Vinylic Hydrogen Substitution Reactions with Aryl, Benzyl, and Styryl Halides. *J. Org. Chem.* **1972**, *37* (14), 2320–2322. https://doi.org/10.1021/jo00979a024.

(95) Barnard, B. C. Palladium-Catalysed C-C Coupling: Then and Now. *Platin. Met. Rev.* **2008**, *52* (1), 38–45. https://doi.org/10.1595/147106708X256634.

(96) Polshettiwar, V.; Len, C.; Fihri, A. Silica-Supported Palladium: Sustainable Catalysts for Cross-Coupling Reactions. *Coord. Chem. Rev.* **2009**, *253* (21), 2599–2626. https://doi.org/10.1016/j.ccr.2009.06.001.

(97) Jian, L. P. L. J. Y. H. S. P. C. Q. D. Polymer-Supported Palladium Catalysts for Heterogeneous C-C Coupling Reactions. *Prog. Chem.* **2009**, *21* (0708), 1434.

(98) Felpin, F.-X.; Ayad, T.; Mitra, S. Pd/C: An Old Catalyst for New Applications – Its Use for the Suzuki–Miyaura Reaction. *Eur. J. Org. Chem.* **2006**, *2006* (12), 2679–2690. https://doi.org/10.1002/ejoc.200501004.

(99) Wende, M.; Gladysz, J. A. Fluorous Catalysis under Homogeneous Conditions without Fluorous Solvents: A "Greener" Catalyst Recycling Protocol Based upon Temperature-Dependent Solubilities and Liquid/Solid Phase Separation. *J. Am. Chem. Soc.* **2003**, *125* (19), 5861–5872. https://doi.org/10.1021/ja029241s.

(100) Yin; Liebscher, J. Carbon−Carbon Coupling Reactions Catalyzed by Heterogeneous Palladium Catalysts. *Chem. Rev.* **2007**, *107* (1), 133–173. https://doi.org/10.1021/cr0505674.

(101) Ananikov, V. P.; Beletskaya, I. P. Toward the Ideal Catalyst: From Atomic Centers to a "Cocktail" of Catalysts. *Organometallics* **2012**, *31* (5), 1595–1604. https://doi.org/10.1021/om201120n.

(102) Arvela, R. K.; Leadbeater, N. E.; Sangi, M. S.; Williams, V. A.; Granados, P.; Singer, R. D. A Reassessment of the Transition-Metal Free Suzuki-Type Coupling Methodology. *J. Org. Chem.* **2005**, *70* (1), 161–168. https://doi.org/10.1021/jo048531j.

(103) Shimizu, K.; Koizumi, S.; Hatamachi, T.; Yoshida, H.; Komai, S.; Kodama, T.; Kitayama, Y. Structural Investigations of Functionalized Mesoporous Silica-Supported Palladium

Catalyst for Heck and Suzuki Coupling Reactions. *J. Catal.* **2004**, *228* (1), 141–151. https://doi.org/10.1016/j.jcat.2004.09.005.

(104) Schmidt, A. F.; Halaiqa, A. A.; Smirnov, V. V. Interplays between Reactions within and without the Catalytic Cycle of the Heck Reaction as a Clue to the Optimization of the Synthetic Protocol. *Synlett* **2006**, *2006* (18), 2861–2878. https://doi.org/10.1055/s-2006-951527.

(105) Devendar, P.; Qu, R.-Y.; Kang, W.-M.; He, B.; Yang, G.-F. Palladium-Catalyzed Cross-Coupling Reactions: A Powerful Tool for the Synthesis of Agrochemicals. *J. Agric. Food Chem.* **2018**, *66* (34), 8914–8934. https://doi.org/10.1021/acs.jafc.8b03792.

(106) Biajoli, A. F. P.; Schwalm, C. S.; Limberger, J.; Claudino, T. S.; Monteiro, A. L. Recent Progress in the Use of Pd-Catalyzed C-C Cross-Coupling Reactions in the Synthesis of Pharmaceutical Compounds. *J. Braz. Chem. Soc.* **2014**, *25*, 2186–2214. https://doi.org/10.5935/0103-5053.20140255.

(107) Rohand, T.; Qin, W.; Boens, N.; Dehaen, W. Palladium-Catalyzed Coupling Reactions for the Functionalization of BODIPY Dyes with Fluorescence Spanning the Visible Spectrum. *Eur. J. Org. Chem.* **2006**, *2006* (20), 4658–4663. https://doi.org/10.1002/ejoc.200600531.

(108) Tahmasbi, B.; Ghorbani-Choghamarani, A.; Moradi, P. Palladium Fabricated on Boehmite as an Organic–Inorganic Hybrid Nanocatalyst for C–C Cross Coupling and Homoselective Cycloaddition Reactions. *New J. Chem.* **2020**, *44* (9), 3717–3727. https://doi.org/10.1039/C9NJ06129K.

(109) Wang, D.; Gao, S. Sonogashira Coupling in Natural Product Synthesis. *Org. Chem. Front.* **2014**, *1* (5), 556–566. https://doi.org/10.1039/C3QO00086A.

(110) Bates, R. W.; Gabel, C. J.; Ji, J.; Rama-Devi, T. Synthesis of Phenolic Natural Products Using Palladium Catalyzed Coupling Reactions. *Tetrahedron* **1995**, *51* (30), 8199–8212. https://doi.org/10.1016/0040-4020(95)00441-A.

(111) D'Amico, F.; Papucci, C.; Franchi, D.; Reginato, G.; Calamante, M.; Zani, L.; Dessì, A.; Mordini, A. Sustainable Pd-Catalyzed Direct Arylation of Thienyl Derivatives with (Hetero)Aromatic Bromides under Air in Deep Eutectic Solvents. *ACS Sustain. Chem. Eng.* **2022**, *10* (9), 3037–3047. https://doi.org/10.1021/acssuschemeng.1c08466.

(112) Neigenfind, P.; Knyszek, D.; Handelmann, J.; H. Gessner, V. Synthesis of Sterically Encumbered Di- and Triarylamines by Palladium-Catalysed C–N Coupling Reactions under Mild Reaction Conditions. *Catal. Sci. Technol.* **2022**, *12* (11), 3447–3453. https://doi.org/10.1039/D1CY02352G.

(113) Miyaura, N.; Yamada, K.; Suzuki, A. A New Stereospecific Cross-Coupling by the Palladium-Catalyzed Reaction of 1-Alkenylboranes with 1-Alkenyl or 1-Alkynyl Halides. *Tetrahedron Lett.* **1979**, *20* (36), 3437–3440. https://doi.org/10.1016/S0040-4039(01)95429-2.

(114) Suzuki, A. Cross-Coupling Reactions Of Organoboranes: An Easy Way To Construct C□C Bonds (Nobel Lecture). *Angew. Chem. Int. Ed.* **2011**, *50* (30), 6722–6737. https://doi.org/10.1002/anie.201101379.

(115) Nicolaou, K. C.; Li, H.; Boddy, C. N. C.; Ramanjulu, J. M.; Yue, T.-Y.; Natarajan, S.; Chu, X.-J.; Bräse, S.; Rübsam, F. Total Synthesis of Vancomycin—Part 1: Design and Development of Methodology. *Chem. – Eur. J.* **1999**, *5* (9), 2584–2601. https://doi.org/10.1002/(SICI)1521-3765(19990903)5:9<2584::AID-CHEM2584>3.0.CO;2-B.

(116) Hajipour, A. R.; Rafiee, F. Synthesis of Substituted Biaryls via Suzuki, Stille and Hiyama Cross-Coupling and Homo-Coupling Reactions by CN-Dimeric and Monomeric Ortho-Palladated Catalysts. *Appl. Organomet. Chem.* **2013**, *27* (7), 412–418. https://doi.org/10.1002/aoc.2997.

(117) Fihri, A.; Bouhrara, M.; Nekoueishahraki, B.; Basset, J.-M.; Polshettiwar, V. Nanocatalysts for Suzuki Cross-Coupling Reactions. *Chem. Soc. Rev.* **2011**, *40* (10), 5181–5203. https://doi.org/10.1039/C1CS15079K.

(118) Zhang, Y.; Zhang, L.; Zhang, X.; Yang, D.; Du, C.; Wan, L.; Au, C.; Chen, J.; Xie, M. Pyridine-Based Hypercrosslinked Polymers as Support Materials for Palladium Photocatalysts and Their Application in Suzuki–Miyaura Coupling Reactions. *New J. Chem.* **2020**, *44* (35), 15202–15208. https://doi.org/10.1039/D0NJ01675F.

(119) Kim, J. K.; Kim, Y. H.; Nam, H. T.; Kim, B. T.; Heo, J.-N. Total Synthesis of Aristolactams via a One-Pot Suzuki−Miyaura Coupling/Aldol Condensation Cascade Reaction. *Org. Lett.* **2008**, *10* (16), 3543–3546. https://doi.org/10.1021/ol801291k.

(120) Fuwa, H.; Kainuma, N.; Tachibana, K.; Sasaki, M. Total Synthesis of (−)-Gambierol. *J. Am. Chem. Soc.* **2002**, *124* (50), 14983–14992. https://doi.org/10.1021/ja028167a.

(121) Okada, T.; Ngoc Thanh Luan, N.; Arata, R.; Awale, S.; Toyooka, N. Total Synthesis of 4'-O-Methylgrynullarin and Related Isoflavone Natural Products. *ChemistrySelect* **2022**, *7* (15), e202201136. https://doi.org/10.1002/slct.202201136.

(122) Wang, L.-L.; Yu, Q.; Zhang, W.; Yang, S.; Peng, L.; Zhang, L.; Li, X.-N.; Gagosz, F.; Kirschning, A. Asymmetric Total Synthesis of Antibiotic Elansolid A. *J. Am. Chem. Soc.* **2022**, *144* (15), 6871–6881. https://doi.org/10.1021/jacs.2c01133.

(123) Willemse, T.; Schepens, W.; Vlijmen, H. W. T. van; Maes, B. U. W.; Ballet, S. The Suzuki–Miyaura Cross-Coupling as a Versatile Tool for Peptide Diversification and Cyclization. *Catalysts* **2017**, *7* (3), 74. https://doi.org/10.3390/catal7030074.

(124) Hussain, I.; Capricho, J.; Yawer, M. A. Synthesis of Biaryls via Ligand-Free Suzuki–Miyaura Cross-Coupling Reactions: A Review of Homogeneous and Heterogeneous Catalytic Developments. *Adv. Synth. Catal.* **2016**, *358* (21), 3320–3349. https://doi.org/10.1002/adsc.201600354.

(125) Oger, N.; Felpin, F.-X. Heterogeneous Palladium Catalysts for Suzuki–Miyaura Coupling Reactions Involving Aryl Diazonium Salts. *ChemCatChem* **2016**, *8* (12), 1998–2009. https://doi.org/10.1002/cctc.201600134.

(126) Jiang, Y.; Qiu, H.; Liang, W.; Lin, J.; Lin, J.; Liu, W.; Wang, X.; Cui, W.; Chen, X.; Wang, H.; Zhao, L.; Liang, H. Derivatization of Marine-Derived Fascaplysin via Highly Regioselective Suzuki-Miyaura Coupling Contributing to the Enhanced Antibacterial Activity. *ChemistrySelect* **2022**, *7* (27), e202201441. https://doi.org/10.1002/slct.202201441.

(127) Qiu, S.-Q.; Chen, Y.; Peng, X.-J.; He, S.-J.; Cheng, J. K.; Wang, Y.-B.; Xiang, S.-H.; Song, J.; Yu, P.; Zhang, J.; Tan, B. Asymmetric Construction of an Aryl-Alkene Axis by Palladium-Catalyzed Suzuki–Miyaura Coupling Reaction. *Angew. Chem. Int. Ed.* **2022**, *61* (45), e202211211. https://doi.org/10.1002/anie.202211211.

(128) Hedouin, G.; Hazra, S.; Gallou, F.; Handa, S. The Catalytic Formation of Atropisomers and Stereocenters via Asymmetric Suzuki–Miyaura Couplings. *ACS Catal.* **2022**, *12* (9), 4918–4937. https://doi.org/10.1021/acscatal.2c00933.

(129) Li, X.; Liu, Y.; Zhang, L.; Dong, Y.; Liu, Q.; Zhang, D.; Chen, L.; Zhao, Z.; Liu, H. A Novel Electromagnetic Mill Promoted Mechanochemical Solid-State Suzuki–Miyaura Cross-Coupling Reaction Using Ultra-Low Catalyst Loading. *Green Chem.* **2022**, *24* (15), 6026–6035. https://doi.org/10.1039/D2GC01427K.

(130) Choy, P. Y.; Yuen, O. Y.; Leung, M. P.; Chow, W. K.; Kwong, F. Y. A Highly Efficient Monophosphine Ligand for Parts per Million Levels Pd-Catalyzed Suzuki–Miyaura Coupling of (Hetero)Aryl Chlorides. *Eur. J. Org. Chem.* **2020**, *2020* (19), 2846–2853. https://doi.org/10.1002/ejoc.202000068.

(131) Zhang, J.; Zhang, P.; Shao, L.; Wang, R.; Ma, Y.; Szostak, M. Mechanochemical Solvent-Free Suzuki–Miyaura Cross-Coupling of Amides via Highly Chemoselective N−C Cleavage. *Angew. Chem. Int. Ed.* **2022**, *61* (7), e202114146. https://doi.org/10.1002/anie.202114146.

(132) Bennett, J. A.; Davis, B. A.; Ramezani, M.; Genzer, J.; Efimenko, K.; Abolhasani, M. Continuous Ligand-Free Suzuki–Miyaura Cross-Coupling Reactions in a Cartridge Flow Reactor Using a Gel-Supported Catalyst. *Ind. Eng. Chem. Res.* **2021**, *60* (26), 9418–9428. https://doi.org/10.1021/acs.iecr.1c01531.

(133) Blakemore, D. Suzuki–Miyaura Coupling. **2016**. https://doi.org/10.1039/9781782622086-00001.

(134) Kuster, S.; Geiger, T. Strategies and Investigations on Bridging Squaraine Dye Units. *Dyes Pigments* **2012**, *95* (3), 657–670. https://doi.org/10.1016/j.dyepig.2012.06.017.

(135) Rausch, R.; Schmidt, D.; Bialas, D.; Krummenacher, I.; Braunschweig, H.; Würthner, F. Stable Organic (Bi)Radicals by Delocalization of Spin Density into the Electron-Poor

Chromophore Core of Isoindigo. *Chem. - Eur. J.* **2018**, *24* (14), 3420–3424. https://doi.org/10.1002/chem.201706002.

(136) Mutoh, K.; Yamamoto, K.; Abe, J. Excitation Wavelength- and Intensity-Dependent Stepwise Two-Photon-Induced Photochromic Reaction. *Photochem. Photobiol. Sci.* **2022**, *21* (8), 1445–1458. https://doi.org/10.1007/s43630-022-00234-y.

(137) Junge, M. J.; Kordan, M. A.; Chernick, E. T. Synthesis of Chiral Donor–Acceptor Dyes to Study Electron Transfer Across a Chiral Bridge. *J. Org. Chem.* **2020**, *85* (21), 13793–13807. https://doi.org/10.1021/acs.joc.0c01914.

(138) Shivaji, B. S.; Boddula, R.; Singh, S. P. [1]Benzothieno[3,2-b][1]Benzothiophene-Based Dyes: Effect of the Ancillary Moiety on Mechanochromism and Aggregation-Induced Emission. *Phys. Chem. Chem. Phys.* **2022**, *24* (24), 15110–15120. https://doi.org/10.1039/D2CP01934E.

(139) Ding, Z.; Chen, H.; Han, Y.; Liu, J. Molecular Engineering of π-Extended Viologens Consisting of Quinoxaline-Based Bridges for Tunable Electrochromic Devices. *J. Mol. Struct.* **2022**, *1262*, 133073. https://doi.org/10.1016/j.molstruc.2022.133073.

(140) Sifuentes-Vázquez, L. D.; Martínez-González, E.; Toscano, R. A.; Gaviño, R.; Cárdenas, J.; Rius-Alonso, C. A.; Amador-Bedolla, C.; García de la Mora, G. A.; Ugalde-Saldivar, V. M. Experimental and Theoretical Exploration of Aryl Substituent Effects on the Electronic Properties of Asymmetric 4,7-Di(Thiophene-2-Yl)-Benzo[c][2,1,5]Thiadiazole Compounds. *Polycycl. Aromat. Compd.* **2022**, *42* (3), 711–726. https://doi.org/10.1080/10406638.2020.1749858.

(141) Saber, A. F.; Elewa, A. M.; Chou, H.-H.; EL-Mahdy, A. F. M. Donor-Acceptor Carbazole-Based Conjugated Microporous Polymers as Photocatalysts for Visible-Light-

Driven H2 and O2 Evolution from Water Splitting. *Appl. Catal. B Environ.* **2022**, *316*, 121624. https://doi.org/10.1016/j.apcatb.2022.121624.

(142) Heiskanen, J. P.; Vivo, P.; Saari, N. M.; Hukka, T. I.; Kastinen, T.; Kaunisto, K.; Lemmetyinen, H. J.; Hormi, O. E. O. Synthesis of Benzothiadiazole Derivatives by Applying C–C Cross-Couplings. *J. Org. Chem.* **2016**, *81* (4), 1535–1546. https://doi.org/10.1021/acs.joc.5b02689.

(143) Amatore, C.; Jutand, A.; Le Duc, G. Kinetic Data for the Transmetalation/Reductive Elimination in Palladium-Catalyzed Suzuki-Miyaura Reactions: Unexpected Triple Role of Hydroxide Ions Used as Base. *Chem. - Eur. J.* **2011**, *17* (8), 2492–2503. https://doi.org/10.1002/chem.201001911.

(144) Huang, J.; Isaac, M.; Watt, R.; Becica, J.; Dennis, E.; Saidaminov, M. I.; Sabbers, W. A.; Leitch, D. C. DMPDAB–Pd–MAH: A Versatile Pd(0) Source for Precatalyst Formation, Reaction Screening, and Preparative-Scale Synthesis. *ACS Catal.* **2021**, *11* (9), 5636–5646. https://doi.org/10.1021/acscatal.1c00288.

(145) Reddington, M. V. Synthesis and Properties of Phosphonic Acid Containing Cyanine and Squaraine Dyes for Use as Fluorescent Labels. *Bioconjug. Chem.* **2007**, *18* (6), 2178–2190. https://doi.org/10.1021/bc070090y.

(146) Oriou, J.; Ng, F.; Hadziioannou, G.; Garbay, G.; Bousquet, M.; Vignau, L.; Cloutet, E.; Brochon, C. Synthesis of Squaraine-Based Alternated π-Conjugated Copolymers: From Conventional Cross-Coupling Reactions to Metal-Free Polycondensation. *Polym Chem* **2014**, *5* (24), 7100–7108. https://doi.org/10.1039/C4PY00896K.

(147) Barder, T. E.; Walker, S. D.; Martinelli, J. R.; Buchwald, S. L. Catalysts for Suzuki−Miyaura Coupling Processes: Scope and Studies of the Effect of Ligand

Structure. *J. Am. Chem. Soc.* **2005**, *127* (13), 4685–4696. https://doi.org/10.1021/ja042491j.

(148) Altman, R. A.; Buchwald, S. L. Pd-Catalyzed Suzuki–Miyaura Reactions of Aryl Halides Using Bulky Biarylmonophosphine Ligands. *Nat. Protoc.* **2007**, *2* (12), 3115–3121. https://doi.org/10.1038/nprot.2007.411.

(149) Immirzi, A.; Musco, A. A Method to Measure the Size of Phosphorus Ligands in Coordination Complexes. *Inorganica Chim. Acta* **1977**, *25*, L41–L42. https://doi.org/10.1016/S0020-1693(00)95635-4.

(150) Kamariza, M.; Keyser, S. G. L.; Utz, A.; Knapp, B. D.; Ealand, C.; Ahn, G.; Cambier, C. J.; Chen, T.; Kana, B.; Huang, K. C.; Bertozzi, C. R. Toward Point-of-Care Detection of Mycobacterium Tuberculosis: A Brighter Solvatochromic Probe Detects Mycobacteria within Minutes. *JACS Au* **2021**, *1* (9), 1368–1379. https://doi.org/10.1021/jacsau.1c00173.

(151) Yamaguchi, E.; Wang, C.; Fukazawa, A.; Taki, M.; Sato, Y.; Sasaki, T.; Ueda, M.; Sasaki, N.; Higashiyama, T.; Yamaguchi, S. Environment-Sensitive Fluorescent Probe: A Benzophosphole Oxide with an Electron-Donating Substituent. *Angew. Chem. Int. Ed.* **2015**, *54* (15), 4539–4543. https://doi.org/10.1002/anie.201500229.

(152) Ye, Z.; Yang, W.; Wang, C.; Zheng, Y.; Chi, W.; Liu, X.; Huang, Z.; Li, X.; Xiao, Y. Quaternary Piperazine-Substituted Rhodamines with Enhanced Brightness for Super-Resolution Imaging. *J. Am. Chem. Soc.* **2019**, *141* (37), 14491–14495. https://doi.org/10.1021/jacs.9b04893.

(153) Shin, J.; Verwilst, P.; Choi, H.; Kang, S.; Han, J.; Kim, N. H.; Choi, J. G.; Oh, M. S.; Hwang, J. S.; Kim, D.; Mook-Jung, I.; Kim, J. S. Harnessing Intramolecular Rotation To Enhance Two-Photon Imaging of Aβ Plaques through Minimizing Background

Fluorescence. *Angew. Chem. Int. Ed.* **2019**, *58* (17), 5648–5652. https://doi.org/10.1002/anie.201900549.

(154) Levitt, M. H. *Spin Dynamics: Basics of Nuclear Magnetic Resonance*; John Wiley & Sons, 2013.

(155) Shellhamer, D. F.; Beavis, Z. J.; Brady, D. L.; Bucardo, M. S.; Elwin, S. L.; Fiorella, N.; Gomez, L.; Van Horne, S.; Perry, M. C. NMR Line-Broadening and Transverse Relaxation Time Measurements Support a Di-Radical Intermediate for the Reaction of Chlorosulfonyl Isocyanate with Electron-Rich Alkenes. *Results Chem.* **2020**, *2*, 100015. https://doi.org/10.1016/j.rechem.2019.100015.

(156) Gould, S. J.; Melville, C. R. NMR Silent, Naturally-Occurring Quinones: A Case of Radicals. *Tetrahedron Lett.* **1997**, *38* (9), 1473–1476. https://doi.org/10.1016/S0040-4039(97)00133-0.

(157) Elgrishi, N.; Rountree, K. J.; McCarthy, B. D.; Rountree, E. S.; Eisenhart, T. T.; Dempsey, J. L. A Practical Beginner's Guide to Cyclic Voltammetry. *J. Chem. Educ.* **2018**, *95* (2), 197–206. https://doi.org/10.1021/acs.jchemed.7b00361.

(158) Richards, J. A.; Whitson, P. E.; Evans, D. H. Electrochemical Oxidation of 2,4,6-Tri-Tert-Butylphenol. *J. Electroanal. Chem. Interfacial Electrochem.* **1975**, *63* (3), 311–327. https://doi.org/10.1016/S0022-0728(75)80303-2.

(159) Bordwell, F. G.; Cheng, J. Substituent Effects on the Stabilities of Phenoxyl Radicals and the Acidities of Phenoxyl Radical Cations. *J. Am. Chem. Soc.* **1991**, *113* (5), 1736–1743. https://doi.org/10.1021/ja00005a042.

(160) Webster, R. D. In Situ Electrochemical-ATR-FTIR Spectroscopic Studies on Solution Phase 2,4,6-Tri-Substituted Phenoxyl Radicals. *Electrochem. Commun.* **2003**, *1* (5), 6–11.

(161) Völker, S. F.; Dellermann, T.; Ceymann, H.; Holzapfel, M.; Lambert, C. Synthesis, Electrochemical, and Optical Properties of Low Band Gap Homo- and Copolymers Based on Squaraine Dyes. *J. Polym. Sci. Part Polym. Chem.* **2014**, *52* (7), 890–911. https://doi.org/10.1002/pola.27073.

(162) Itoh, S.; Takayama, S.; Arakawa, R.; Furuta, A.; Komatsu, M.; Ishida, A.; Takamuku, S.; Fukuzumi, S. Active Site Models for Galactose Oxidase. Electronic Effect of the Thioether Group in the Novel Organic Cofactor. *Inorg. Chem.* **1997**, *36* (7), 1407–1416. https://doi.org/10.1021/ic961144a.

(163) Thomas, F. Metal Coordinated Phenoxyl Radicals. In *Stable Radicals*; John Wiley & Sons, Ltd, 2010; pp 281–316. https://doi.org/10.1002/9780470666975.ch8.

(164) Prabhananda, B. S. Spin Density Distributions and g Values in Semiquinones. *J. Chem. Phys.* **1983**, *79* (12), 5752–5757. https://doi.org/10.1063/1.445762.

(165) Saha, S.; Samanta, A. Influence of the Structure of the Amino Group and Polarity of the Medium on the Photophysical Behavior of 4-Amino-1,8-Naphthalimide Derivatives. *J. Phys. Chem. A* **2002**, *106* (18), 4763–4771. https://doi.org/10.1021/jp013287a.

(166) Baranov, M. S.; Solntsev, K. M.; Baleeva, N. S.; Mishin, A. S.; Lukyanov, S. A.; Lukyanov, K. A.; Yampolsky, I. V. Red-Shifted Fluorescent Aminated Derivatives of a Conformationally Locked GFP Chromophore. *Chem. – Eur. J.* **2014**, *20* (41), 13234–13241. https://doi.org/10.1002/chem.201403678.

(167) Rettig, W. Charge Separation in Excited States of Decoupled Systems—TICT Compounds and Implications Regarding the Development of New Laser Dyes and the Primary Process of Vision and Photosynthesis. *Angew. Chem. Int. Ed. Engl.* **1986**, *25* (11), 971–988. https://doi.org/10.1002/anie.198609711.

(168) Rettig, W. Photoinduced Charge Separation via Twisted Intramolecular Charge Transfer States. In *Electron Transfer I*; Mattay, J., Ed.; Topics in Current Chemistry; Springer: Berlin, Heidelberg, 1994; pp 253–299. https://doi.org/10.1007/3-540-57565-0_78.

(169) Yang, D.-S. 2.14 - Photoelectron Spectroscopy. In *Comprehensive Coordination Chemistry II*; McCleverty, J. A., Meyer, T. J., Eds.; Pergamon: Oxford, 2003; pp 187–196. https://doi.org/10.1016/B0-08-043748-6/01180-4.

(170) Institute of Chemistry, Jan Kochanowski University, Swietokrzyska St. 15G, PL-25406 Kielce, Poland; Jakubczyk, M. Electrochemical Behavior of Butylated Hydroxyanisole and Butylated Hydroxytoluene in Acetic Acid Solutions and Their Voltammetric Determination in Pharmaceutical Preparations. *Int. J. Electrochem. Sci.* **2018**, 4251–4266. https://doi.org/10.20964/2018.05.76.

(171) Cook, C. D.; Woodworth, R. C. Oxidation of Hindered Phenols. II. The 2,4,6-Tri-t-Butylphenoxy Radical. *J. Am. Chem. Soc.* **1953**, *75* (24), 6242–6244. https://doi.org/10.1021/ja01120a040.

(172) Manner, V. W.; Markle, T. F.; Freudenthal, J. H.; Roth, J. P.; Mayer, J. M. The First Crystal Structure of a Monomeric Phenoxyl Radical: 2,4,6-Tri-Tert-Butylphenoxyl Radical. *Chem Commun* **2008**, No. 2, 256–258. https://doi.org/10.1039/B712872J.

(173) Liu, X. W.; Zhao, W.; Wu, Y.; Meng, Z.; He, Z.; Qi, X.; Ren, Y.; Yu, Z.-Q.; Tang, B. Z. Photo-Thermo-Induced Room-Temperature Phosphorescence through Solid-State Molecular Motion. *Nat. Commun.* **2022**, *13* (1), 3887. https://doi.org/10.1038/s41467-022-31481-3.

(174) Oka, N.; Yamada, T.; Sajiki, H.; Akai, S.; Ikawa, T. Aryl Boronic Esters Are Stable on Silica Gel and Reactive under Suzuki–Miyaura Coupling Conditions. *Org. Lett.* **2022**, *24* (19), 3510–3514. https://doi.org/10.1021/acs.orglett.2c01174.

Appendices

Appendix 1 Experimental

General Methodologies

Unless otherwise stated all reactions were performed in dried glassware. All solvents and reagents were used as purchased with no further purification. Air-sensitive reactions were prepared in the glovebox under a nitrogen atmosphere and sealed before removal from the glovebox. Thin layer chromatography was performed on MACHEREYNAGEL pre-coated POLYGRAM® SIL G/UV254 TLC plates. TLC plates were visualized using UV light (254 nm).

All NMR spectra were recorded at room temperature (298 K). The ^{1}H NMR spectra were recorded on either a Bruker AVANCE 300 spectrometer or a Bruker AVANCE NEO 500 spectrometer as noted under the spectra. All ^{13}C and 2D NMR were performed solely on the Bruker AVANCE NEO 500 spectrometer. All chemical shifts are reported in ppm relative to tetramethylsilane and referenced to solvent peaks ($CDCl_3$, MeOD, or DMSO-d6). Infrared spectra were obtained using neat compounds on a Agilent 630 FTIR. Accurate masses were obtained by electrospray ionization (ESI) high-resolution mass spectrometry (HRMS) using a Thermo Scientific™ Exactive™ Plus Orbitrap Ultimate 3000 LC-MS system. EPR measurements were done using a Magnettech ESR5000 at 298 K.

Cyclic voltammetry was done using a Gamry Interface1010 potentiostat. All experiments were done in anhydrous solvent using a glassy carbon working electrode, silver wire pseudo-reference electrode, and platinum counter-electrode. All cyclic voltammograms are referenced versus ferrocene/ferrocenium with tetrabutylammonium hexafluorophosphate as electrolyte.

4,7-dibromo-2,1,3-benzothiadiazole (**2.12**)

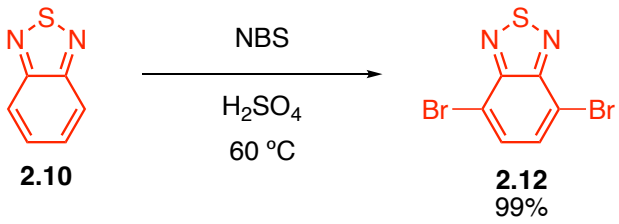

A 250 mL round bottom flask was charged with 5.17 g (0.037 mol) **2.10**, 13.54 g (0.076 mol) N-bromosuccinimide (NBS), and 50 mL concentrated sulfuric acid. The reaction was heated to 60 °C and left to stir overnight. After reaction, the mixture was cooled in an ice bath and 250 mL of distilled water was added dropwise to form a white precipitate. The aqueous solution was then extracted with 1 L toluene in five additions to yield 11.095 g **2.12** in 99% crude yield.

^{1}H NMR spectroscopy (300 MHz, $CDCl_3$, 298 K) δ(ppm): 7.72 s (2H).

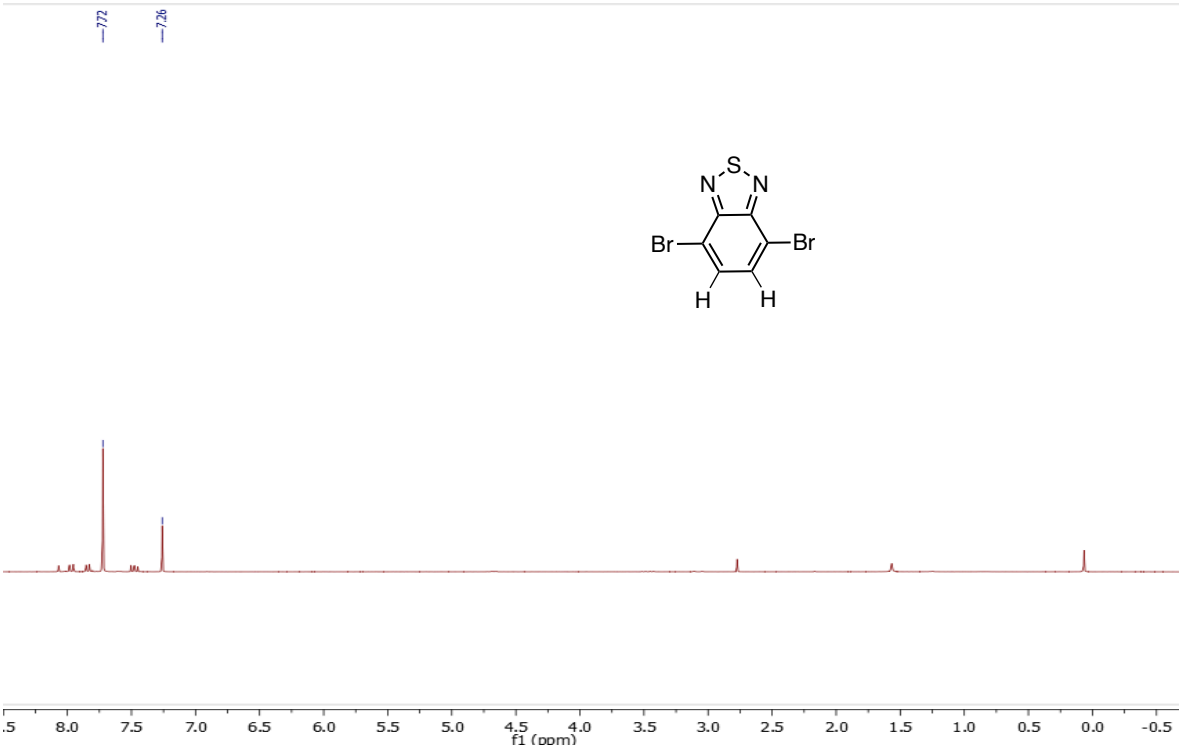

2,6-di-*tert*-butyl-4-(4,4,5,5-tetramethyl-1,3,2-dioxaborolan-2-yl)phenol (**2.13**)

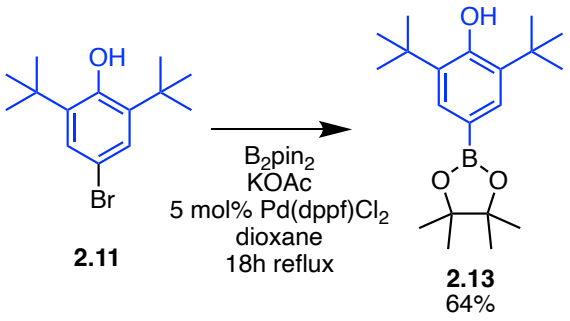

A 250 mL round bottom flask was charged with 90 mL of dioxane, 2.04 g (7.015 mmol) **2.11**, 2.4213 g (9.535 mmol) bis(pinocolato)diboron, 0.2347 g Pd(dppf)Cl_2 (5 mol%), and 1.866 g (19 mmol) KOAc. The solution was degassed and then heated to 90 C under inert atmosphere and left to stir overnight. The crude reaction mixture was filtered and the solvent was removed on the rotary evaporator to yield a black solid. The mixture was purified using column chromatography over silica gel using a 2:1 mixture of pentane to DCM to yield 1.5077 g (4.537 mmol) **2.13** in 64% yield.

^{1}H NMR spectroscopy (300 MHz, $CDCl_3$, 298 K) δ(ppm): 7.63 s (2H), 5.45 s (1H), 1.46 s (18H), 1.31 s (12H)

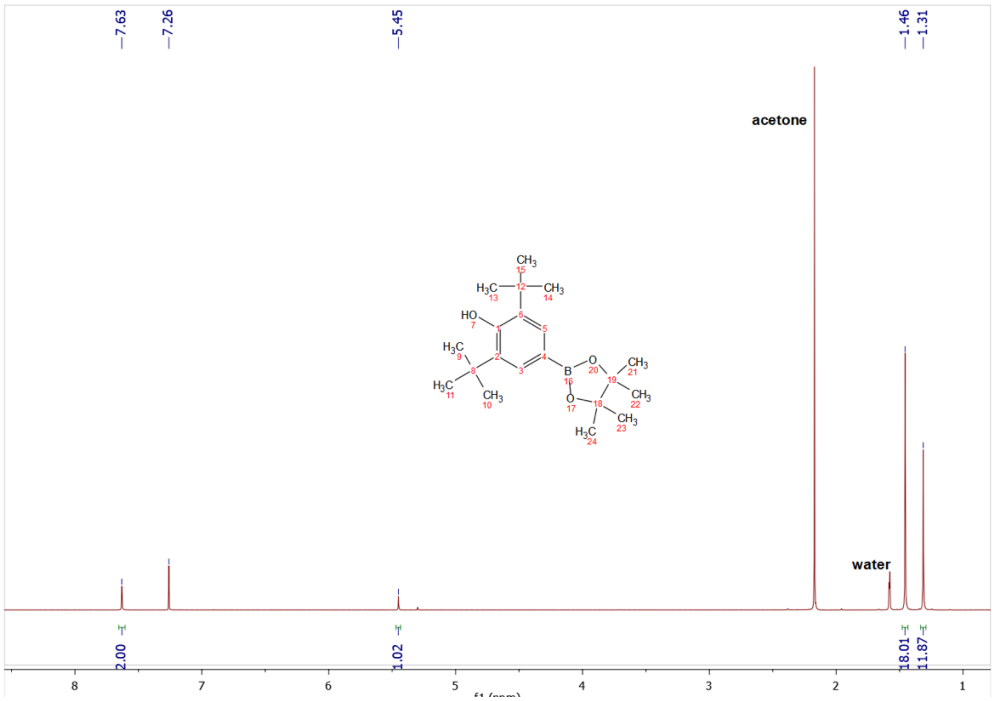

4-(7-bromobenzo[*c*][1,2,5]thiadiazol-4-yl)-2,6-di-*tert*-butylphenol (**2.14**)

4,4'-(benzo[*c*][1,2,5]thiadiazole-4,7-diyl)bis(2,6-di-*tert*-butylphenol) (**2.15**)

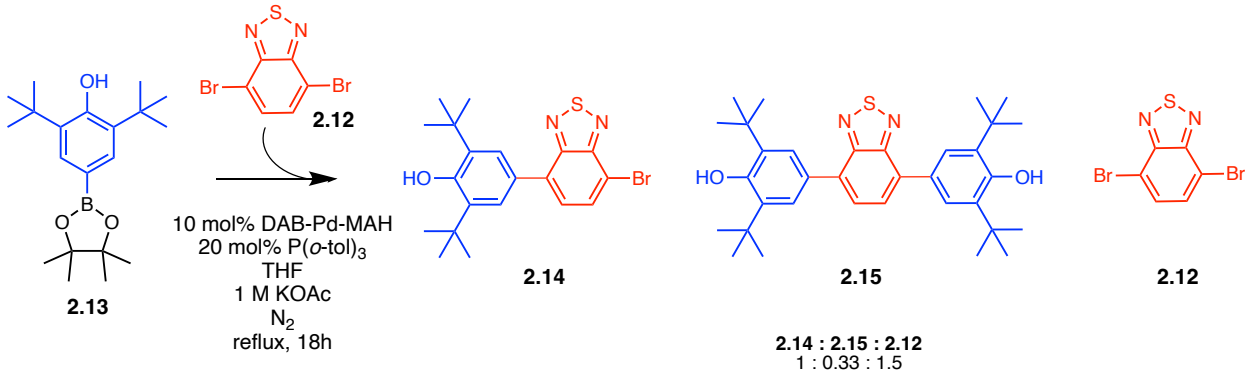

A 50 mL round bottomed flask was charged with **2.13** (1.0119 g, 1 eq), **2.12** (0.8209 g, 0.9 eq), DAB-Pd-MAH (0.1229 g, 10 mol%), P(*o*-tol)$_3$ (0.0599 g, 20 mol%), KOAc (0.8000 g), 1.4 mL water and 7 ml THF. The solution was heated to reflux and left to stir overnight. After cooling, the resulting solution was filtered and concentrated on the rotary evaporator. The resulting solid was subjected to column chromatography over silica gel using a 1:1 mixture of light petroleum

ether and DCM to yield a mixture of **2.14**, **2.15** and **2.12** in a 1 : 0.33 : 1.5 ratio in a crude yield of 22% (0.2310 g). Crude NMR is shown below.

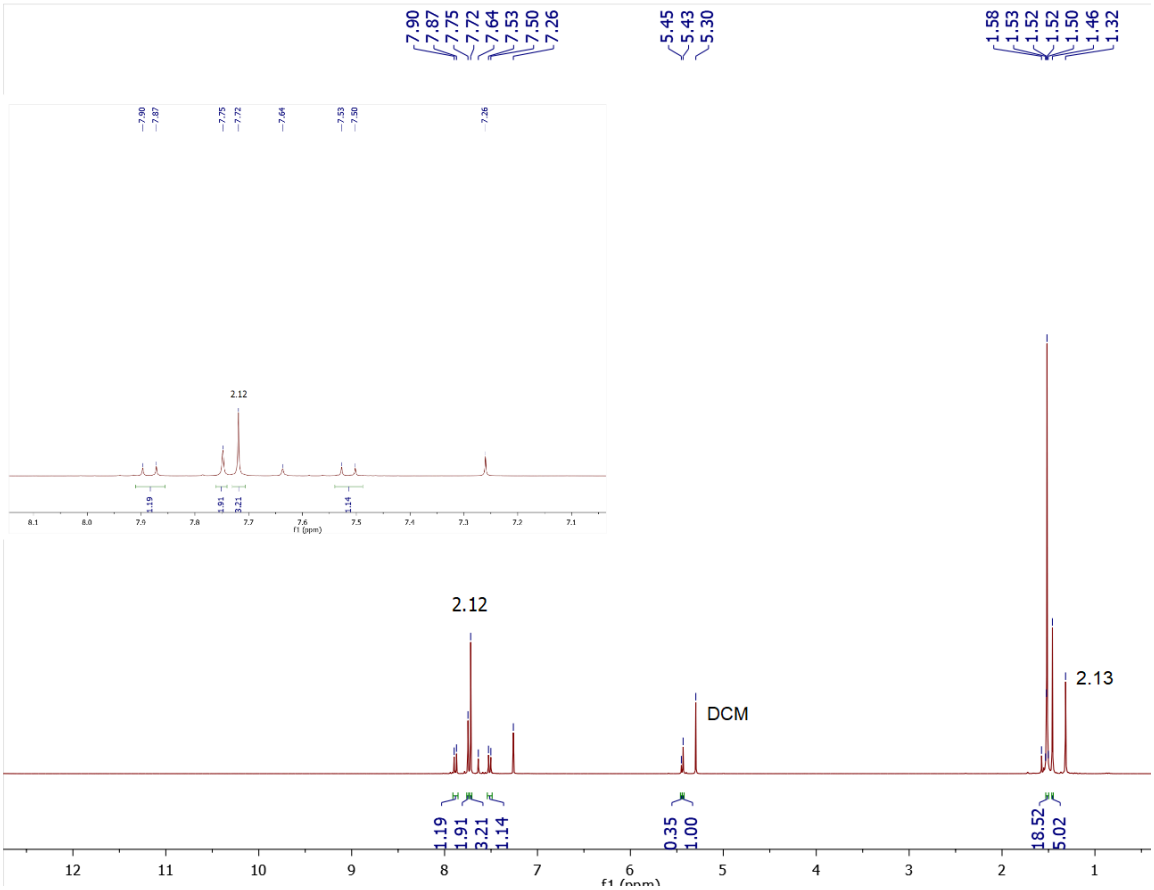

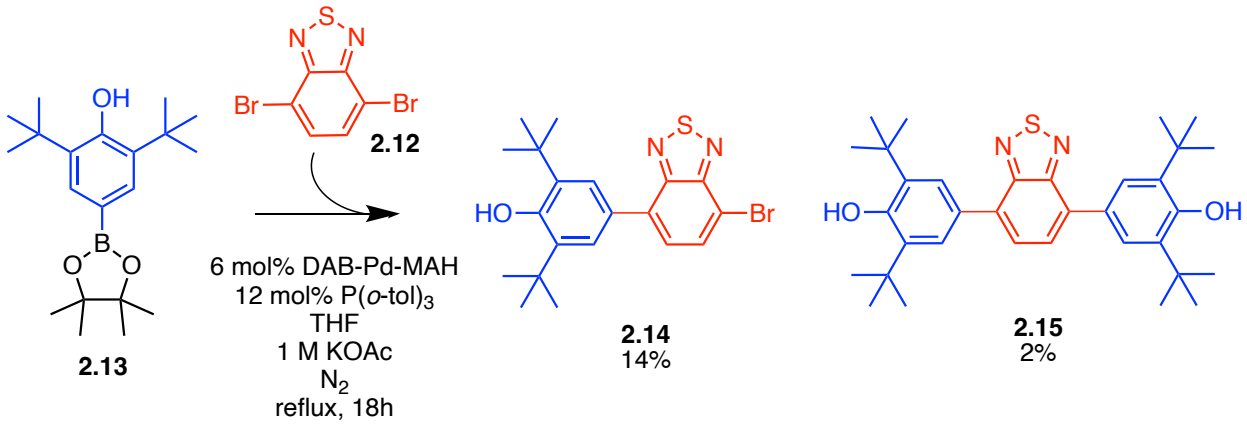

A 100 mL round bottomed flask was charged with DAB-Pd-MAH (0.0291 g, 0.062 mmol, 6 mol%) and P(*o*-tol)$_3$ (0.0377 g, 0.124 mmol, 12 mol%) 5 mL THF. The solution was degassed

and then **2.13** (0.6243 g, 1.879 mmol), **2.12** (0.2670 g, 0.908 mmol), and 1.5 mL 1 M aqueous KOAc were added. The solution was heated to 85 °C and left to stir overnight under inert atmosphere. The crude reaction mixture was extracted using DCM and washed with 3 x 50 mL water before being dried over anhydrous $MgSO_4$ and then filtered and dried under vacuum. The crude solid was purified using column chromatography over silica gel using 100% DCM as eluent. Compounds **2.14** and **2.15** were collected as yellow solids in 14% and 2% yields respectively.

2.14

^{1}H NMR spectroscopy (500 MHz, $CDCl_3$, 298 K) δ (ppm) = 7.89 d (1H, ^{3}J = 8 Hz), 7.75 s (2H), 7.52 d (1H, ^{3}J = 8 Hz), 5.44 s (1H), 1.52 s (18H)

^{13}C NMR spectroscopy (500 MHz, $CDCl_3$, 298 K) δ (ppm) = 154.66, 153.93, 153.45, 136.12, 134.95, 132.35, 127.75, 127.35, 126.31, 111.77, 34.54, 30.35

HR-MS: calculated for $C_{20}H_{23}BrN_2OS$ $[M]^+$: 419.07873. Found: 419.07884

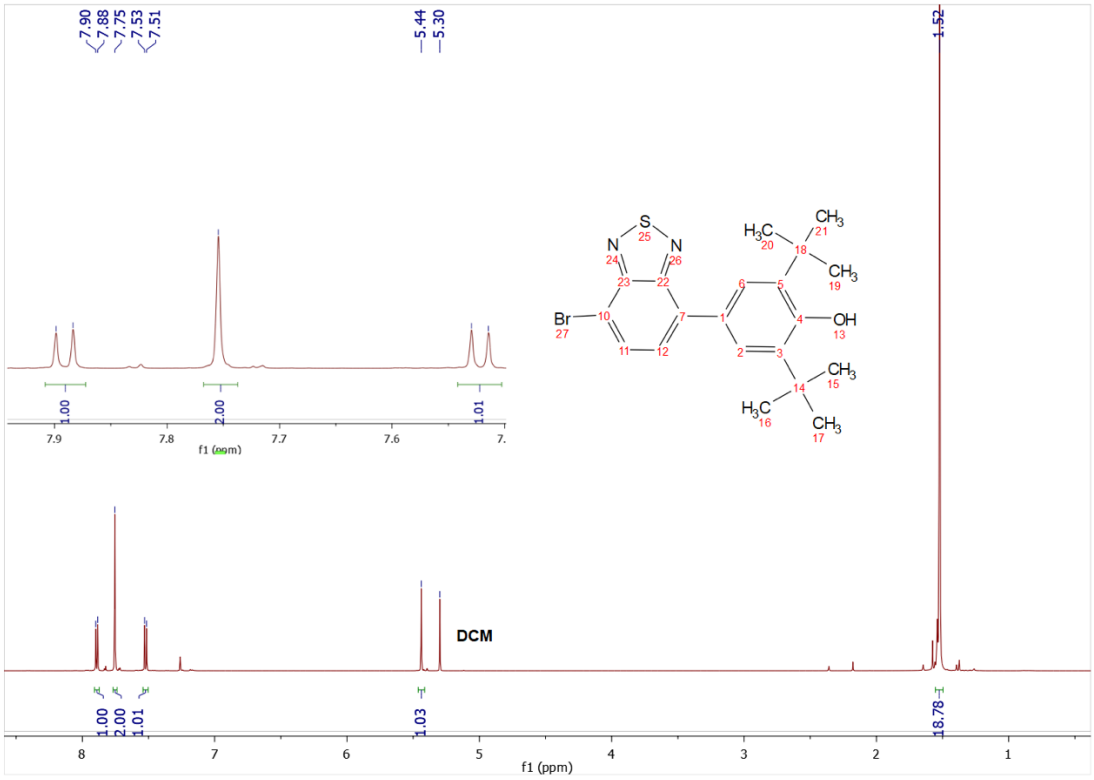
7.90
7.88
7.75
7.53
7.51
5.44
5.30
1.52
DCM
1.00
2.00
1.01
1.03
18.78
f1 (ppm)

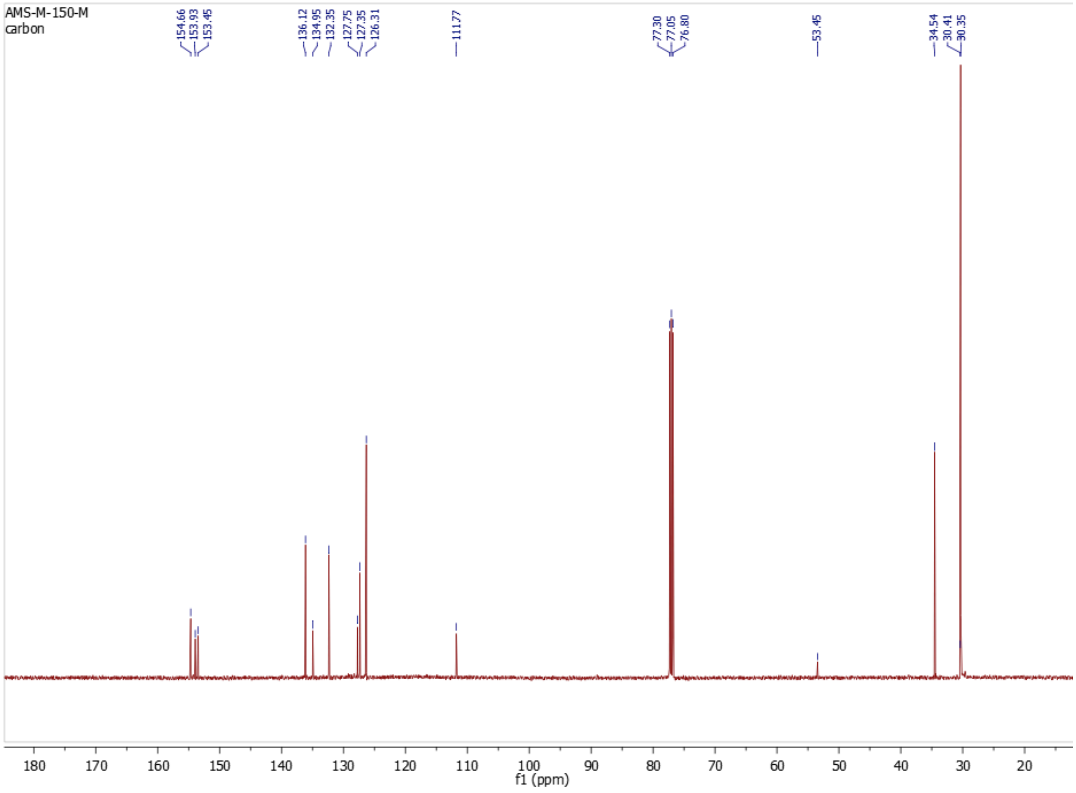
AMS-M-150-M
carbon
154.66
153.93
153.45
136.12
134.95
132.35
127.75
127.35
126.31
111.77
77.30
77.05
76.80
53.45
34.54
30.41
30.35
f1 (ppm)

2.15

^{1}H NMR spectroscopy (500 MHz, $CDCl_3$, 298 K) δ (ppm) = 7.82 s (4H), 7.71 s (2H), 5.39 s (2H), 1.53 s (36H)

^{13}C NMR spectroscopy (500 MHz, $CDCl_3$, 298 K) δ (ppm) = 154.41, 154.22, 135.91, 133.24, 128.76, 127.37, 126.29, 34.54, 30.39

HR-MS: calculated for $C_{34}H_{44}N_2O_2S$ $[M]^+$: 545.31963. Found: 545.31979

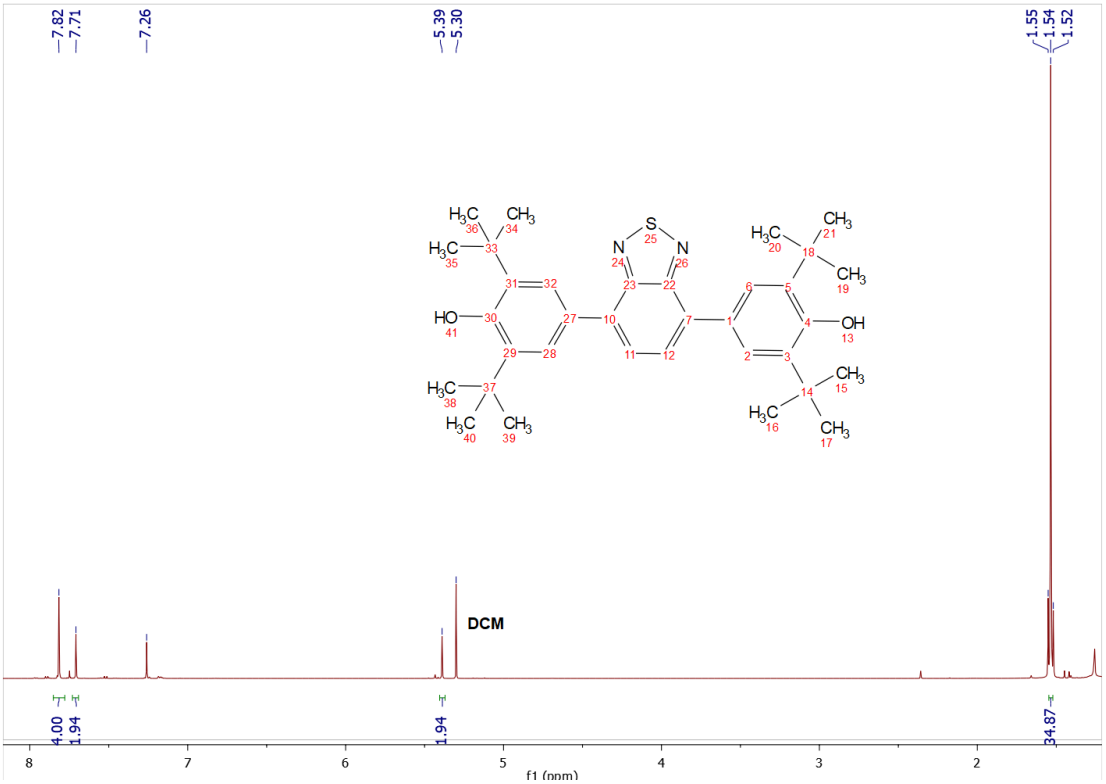

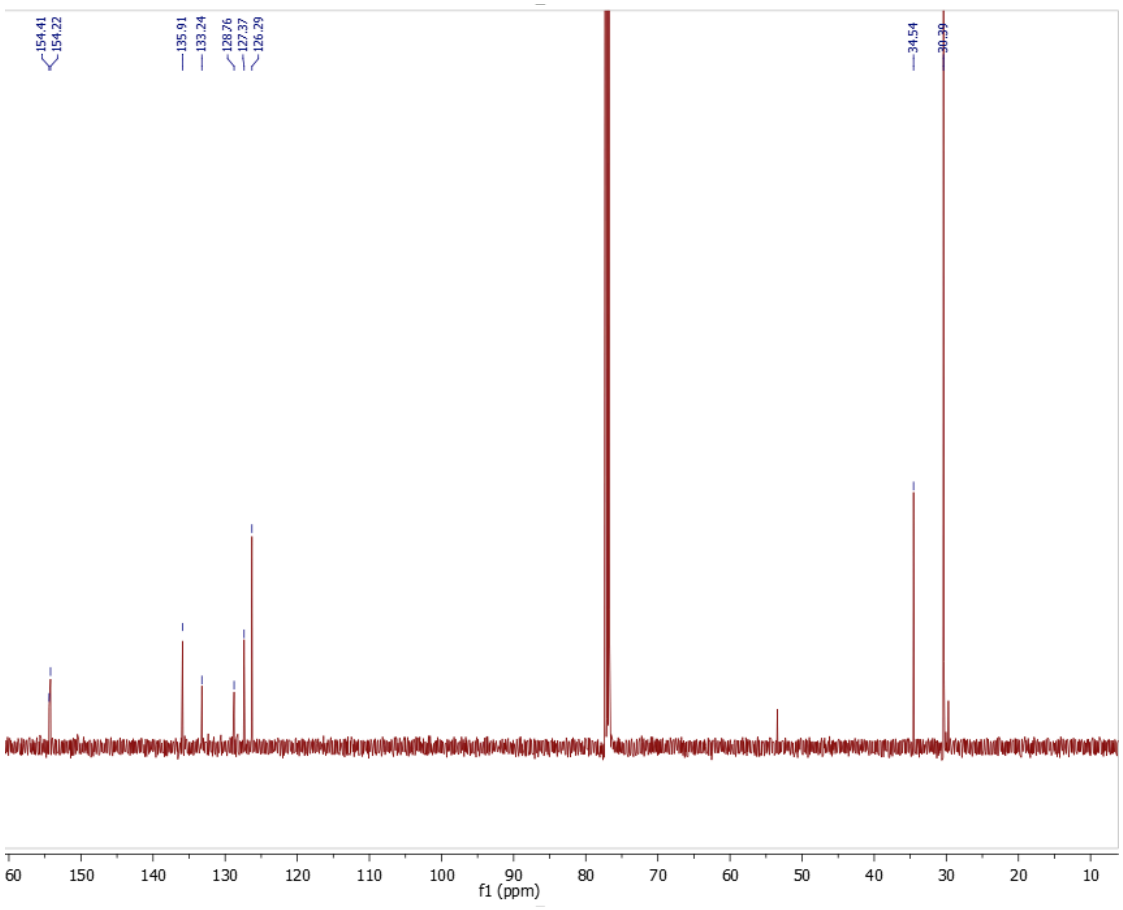

5-bromo-2,3,3-trimethyl-3*H*-indole (**2.19**)

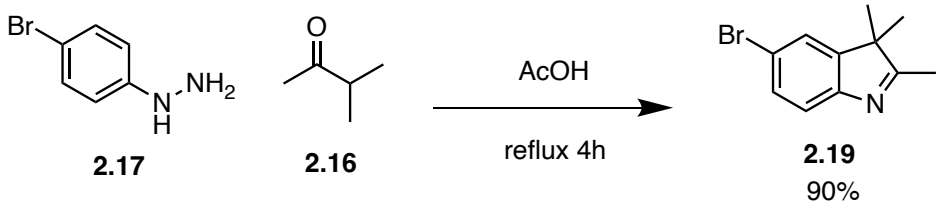

2.17 **2.16** **2.19**
90%

A 250 mL round bottomed flask was charged with 160 mL acetic acid, 32 mL (0.3 mol) **2.16** and 25.00 g (0.11 mol) **2.17**. The solution was heated to 130 °C and stirred for 4 hours. The red reaction mixture was cooled to room temperature and the solvent was removed on the rotary evaporator. The crude reaction mixture was dissolved in 120 mL diethyl ether, and washed with 3 x 50 mL water before being dried over anhydrous $MgSO_4$ and filtered. The remaining solvent was evaporated on the rotary evaporator to yield 24.00 g **2.19** as a red oil in 90% yield.

^{1}H NMR spectroscopy (300 MHz, $CDCl_3$, 298 K) δ (ppm) = 7.41 m (2H), 7.39 d (1H, ^3J = 8 Hz), 2.27 s (3H), 1.29 s (6H)

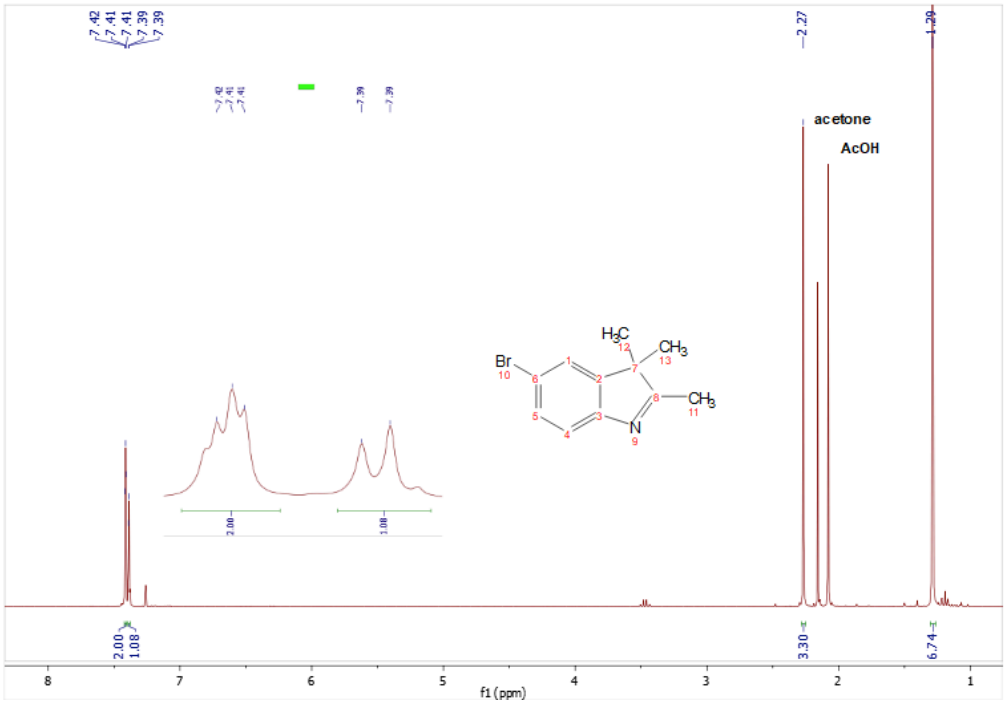

5-bromo-1-hexadecyl-2,3,3-trimethyl-3*H*-indol-1-ium iodide (**2.33**)

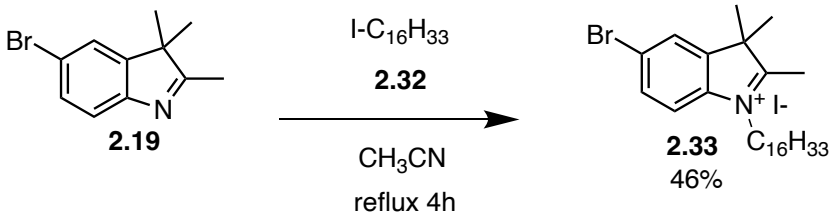

In a 100 mL round bottom flask, 5.0214 g **2.19**, 7.715 g **2.32** and 15 mL acetonitrile were combined and heated to reflux and left for 4 hours. The dark red solution was cooled after reaction. Solvent was removed on the rotary evaporator and the resulting solid was washed with hexanes to yield **2.33** in 46% yield.

^{1}H NMR spectroscopy (300 MHz, $CDCl_3$, 298 K) δ (ppm) = 7.72 dd (1H, ^3J = 8 Hz, ^4J = 2 Hz), 7.69 d (1H, ^4J = 2 Hz), 7.54 d (^3J = 8 Hz), 4.67 t (2H, ^3J = 8 Hz), 3.08 s (3H), 1.88 – 0.87 m (37H), 1.67 s (6H)

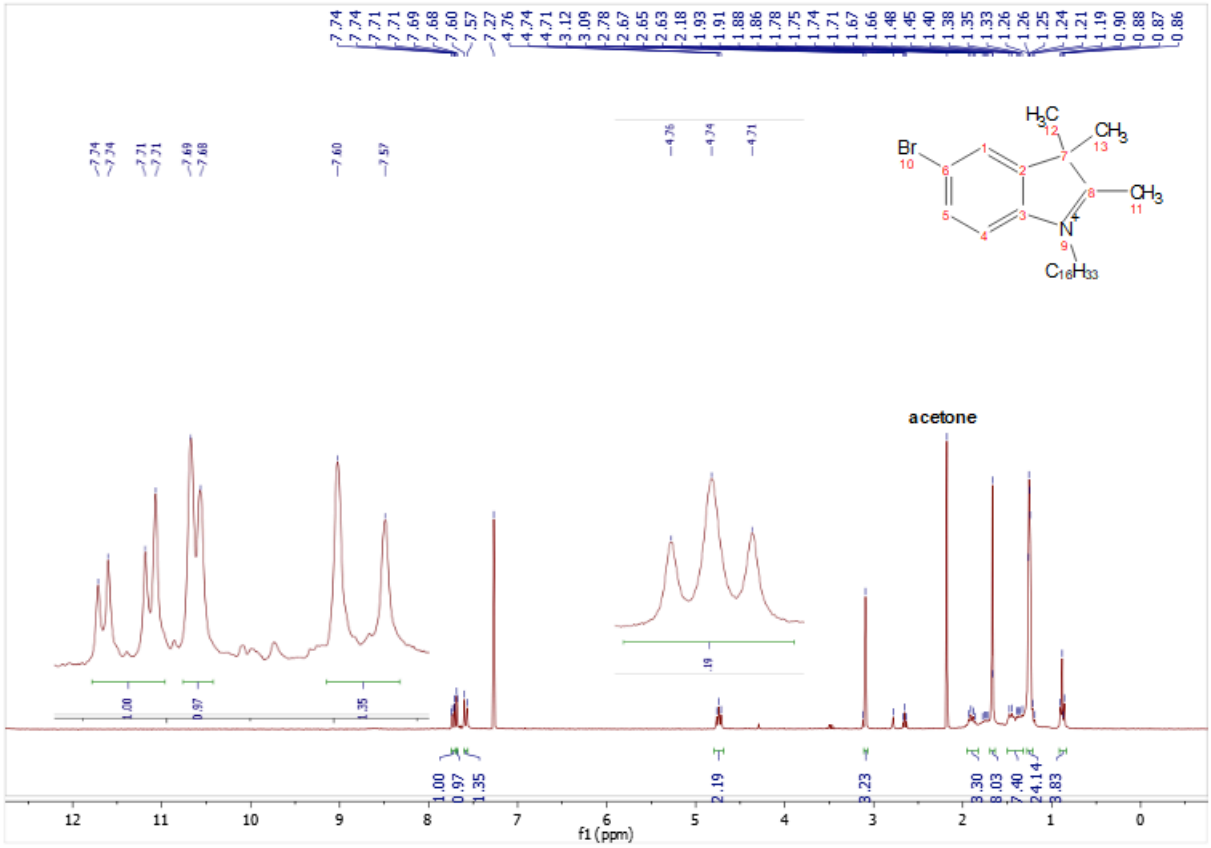

5-bromo-2,3,3-trimethyl-1-octyl-3*H*-indol-1-ium (**2.21**)

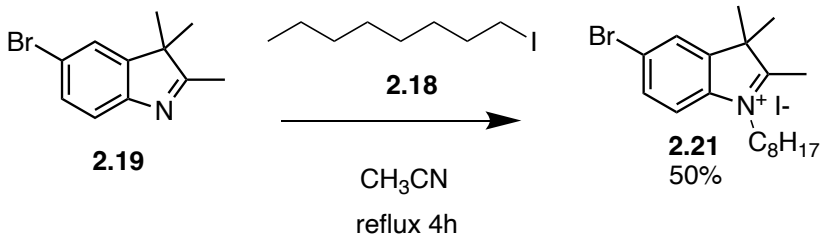

A 100 mL round bottomed flask was charged with 10 mL acetonitrile, 19.69 g (0.08 mol) **2.19** and 31.22 g (0.13 mol) **2.18**. The reaction was heated to reflux and left to stir for 4 hours.

After reaction, the crude reaction mixture was added to 1 L diethyl ether and the residual precipitate was filtered to yield 19.13 g (50%) of pure **2.21** as a reddish-purple solid.

^{1}H NMR spectroscopy (300 MHz, $CDCl_3$, 298 K) δ (ppm) = 7.72 dd (1H, ^{3}J = 8 Hz, ^{4}J = 2 Hz), 7.69 d (1H, ^{4}J = 2 Hz), 7.53 d (^{3}J = 8 Hz), 4.66 t (2H, ^{3}J = 8 Hz), 3.08 s (3H), 1.88 – 0.87 m (17H), 1.68 s (6H)

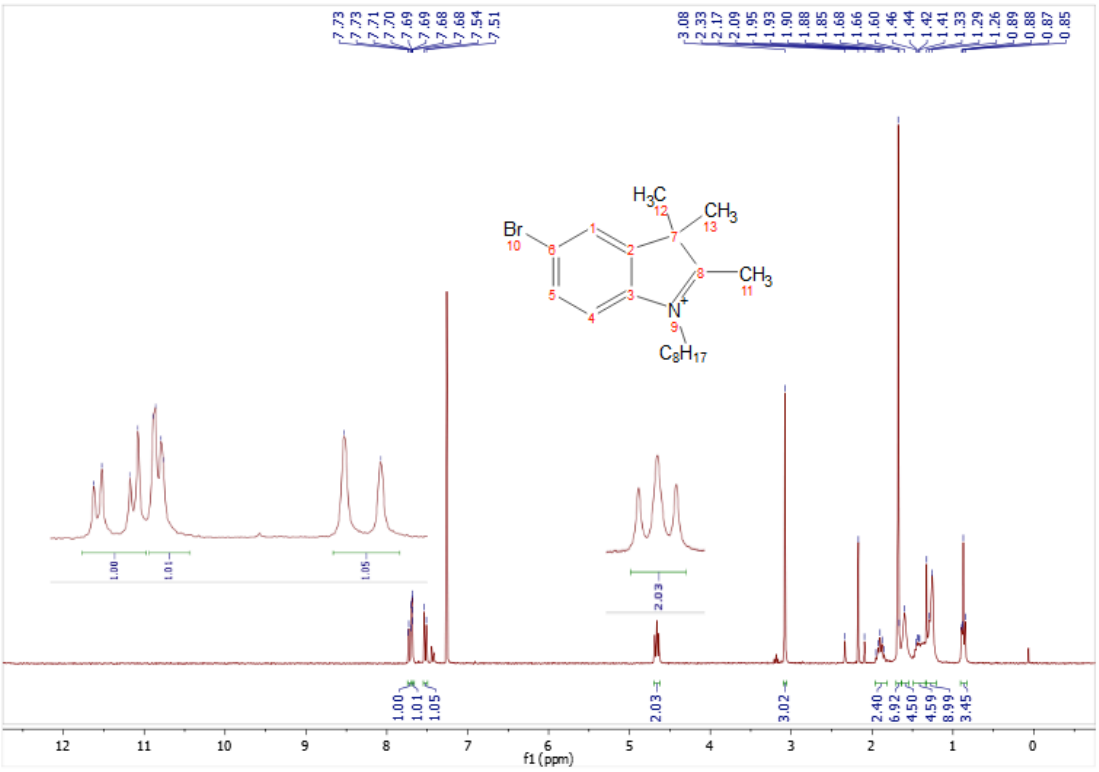

4-((5-Bromo-3,3-dimethyl-1-octyl-3H-indolium-2-yl)methylene)-2-((5-bromo-3,3- dimethyl-1-octylindolin-2-ylidene)methyl)-3-oxocyclobut-1-enolate (**2.22**)

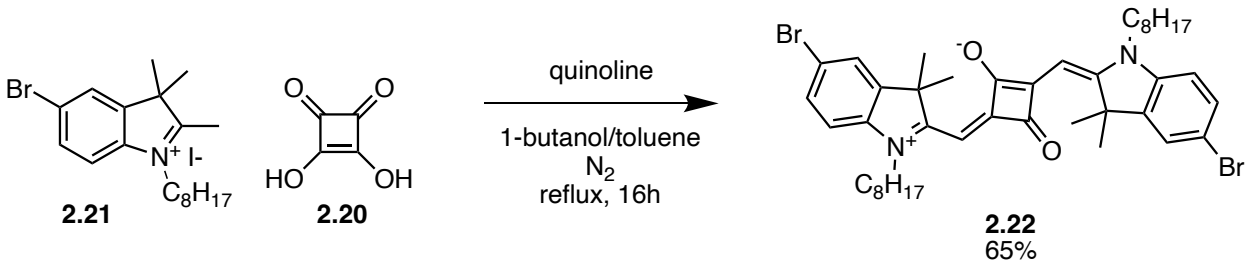

A 250 mL round bottomed flask was charged with 50 mL of a 1:1 mixture of toluene and 1-butanol, 7.9633 g (0.0167 mol) of **2.33**, 10 mL (0.084 mol) quinoline, and 0.9496 g (0.0083 mol) of **2.20**. The reaction mixture was purged and backfilled with nitrogen. The mixture was then heated to reflux and left overnight. The reaction mixture turned from red to dark blue after 30 minutes. The residue of the reaction was dissolved into 50 mL ethanol which was then added to 250 mL of a 5% aqueous citric acid solution and stirred for 30 minutes. The precipitate was then filtered and dissolved into 50 mL chloroform. The organic solution was washed with 50 mL 10% aqueous citric acid, and then 50 mL 10% aqueous potassium carbonate before being dried over anhydrous magnesium sulfate and filtered. The solvent was then removed in vacuo to yield 7.2013 g **2.22** in 65% yield as a iridescent green solid.

^{1}H NMR spectroscopy (300 MHz, $CDCl_3$, 298 K) δ(ppm) = 7.44 d (2H, ^{4}J = 2 Hz), 7.42 dd (2H, ^{3}J = 8 Hz, ^{4}J = 2 Hz), 6.83 d (2H, ^{3}J = 8 Hz), 5.94 s (2H), 3.93 s br (4H), 1.78 – 0.85 m (46H)

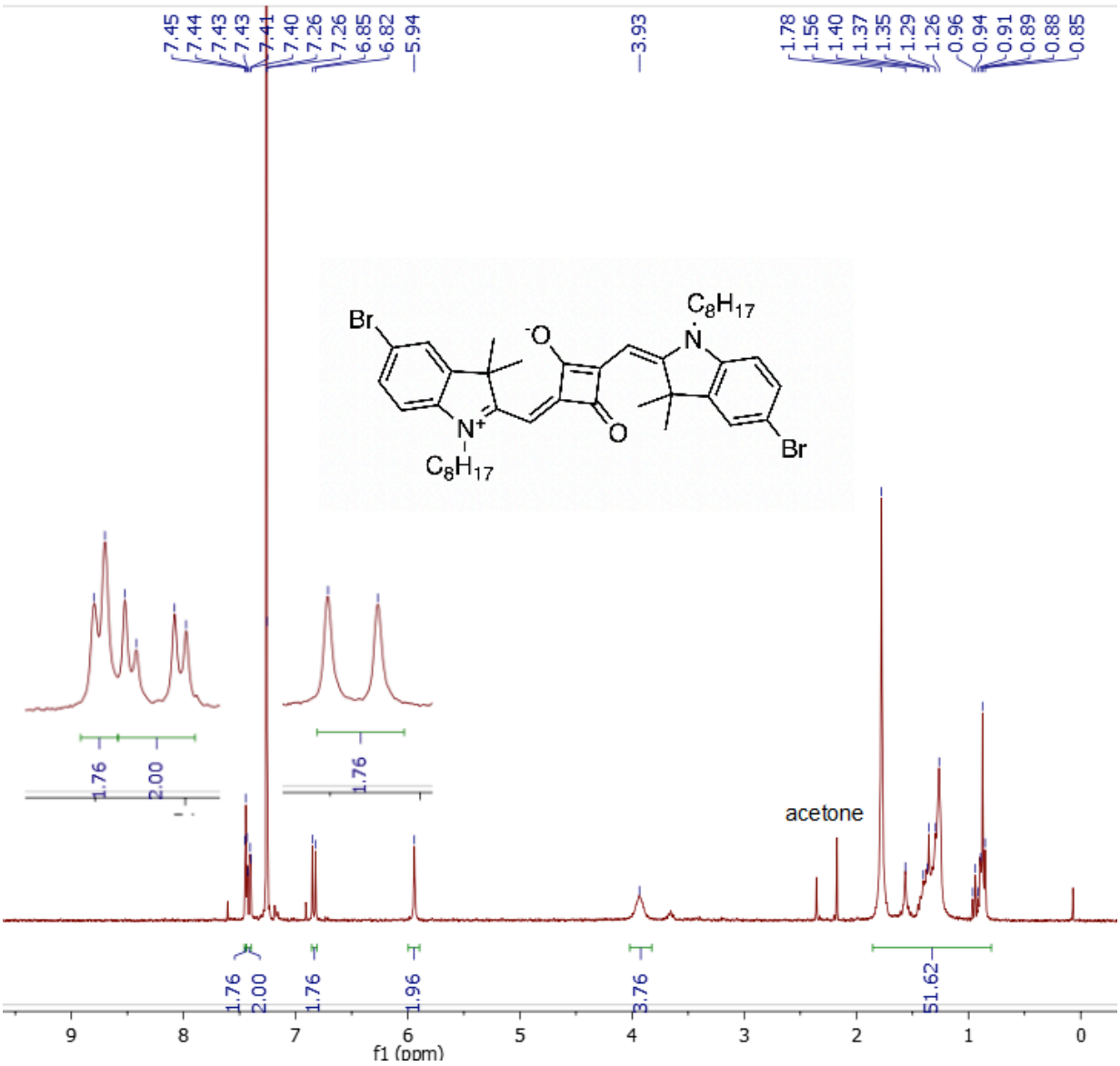
7.45
7.44
7.43
7.43
7.41
7.40
7.26
7.26
6.85
6.82
5.94
3.93
1.78
1.56
1.40
1.37
1.35
1.29
1.26
0.96
0.94
0.91
0.89
0.88
0.85
Br
O
N
C8H17
N+
C8H17
O
Br
1.76
2.00
1.76
acetone
1.76
2.00
1.76
1.96
3.76
51.62
9
8
7
6
5
4
3
2
1
0
f1 (ppm)

4-((5-Bromo-3,3-dimethyl-1-octyl-3H-indolium-2-yl)methylene)-2-((5-bromo-3,3- dimethyl-1-hexadecylindolin-2-ylidene)methyl)-3-oxocyclobut-1-enolate (**2.23**)

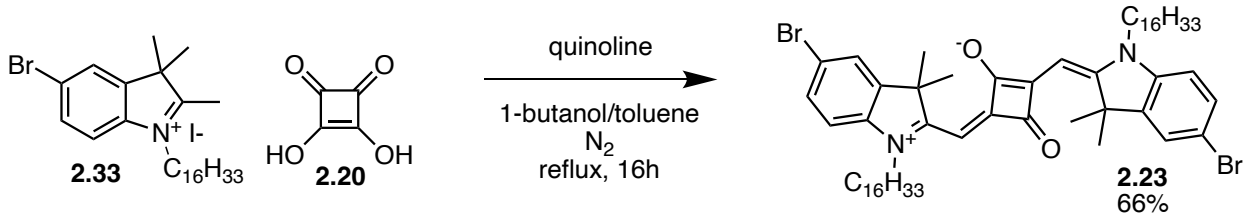

A 50 mL round-bottomed flask was charged with 5 mL of a 1:1 toluene/1-butanol mixture, **2.33** (1.0280 g, 1.74 mmol), **2.20** (0.1214 g, 1.06 mmol), and quinoline (0.0728 g, 0.56 mmol). The solution was sparged with N_2 and then heated to reflux for 16 hours. After cooling to room temperature, the solvent was removed on the rotary evaporator. The resulting mixture was purified via column chromatography over silica gel using a 0.75:0.25 mixture of petroleum ether and ethyl acetate to yield **2.23** in 66% yield (0.5705 g, 0.86 mmol) as a sticky reddish/blue solid.

^{1}H NMR spectroscopy (300 MHz, $CDCl_3$, 298 K) δ(ppm) = 7.44 d (2H, ^{4}J = 2 Hz), 7.41 dd (2H, ^{3}J = 8 Hz, ^{4}J = 2 Hz), 6.83 d (2H, ^{3}J = 8 Hz), 5.94 s (2H), 3.93 s br (4H), 1.78 – 0.85 m (97H)

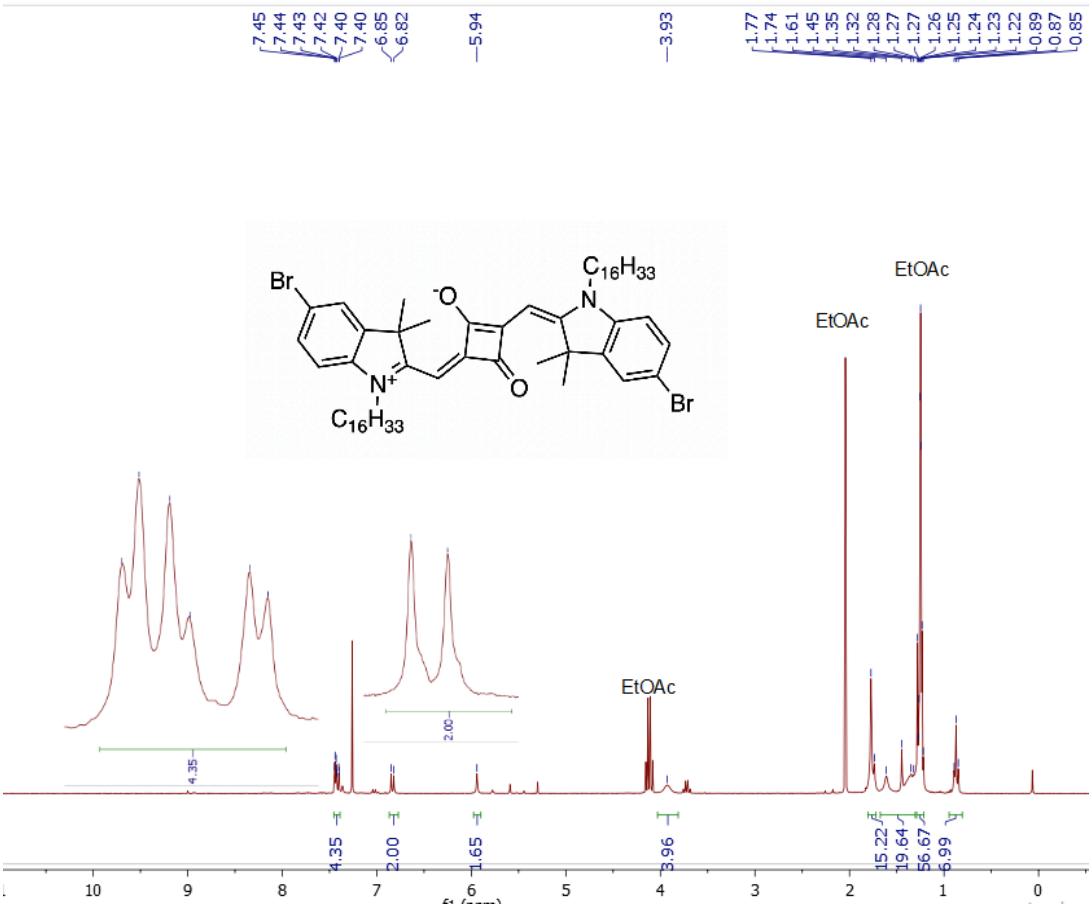

4-((3,3-Dimethyl-1-octyl-5-(4,4,5,5-tetramethyl-1,3,2-dioxaborolan-2-yl)-3Hindolium-2-yl)methylene)-2-((3,3-dimethyl-1-octyl-5-(4,4,5,5-tetramethyl-1,3,2- dioxaborolan-2-yl)indolin-2-ylidene)methyl)-3-oxocyclobut-1-enolate (**2.24**)

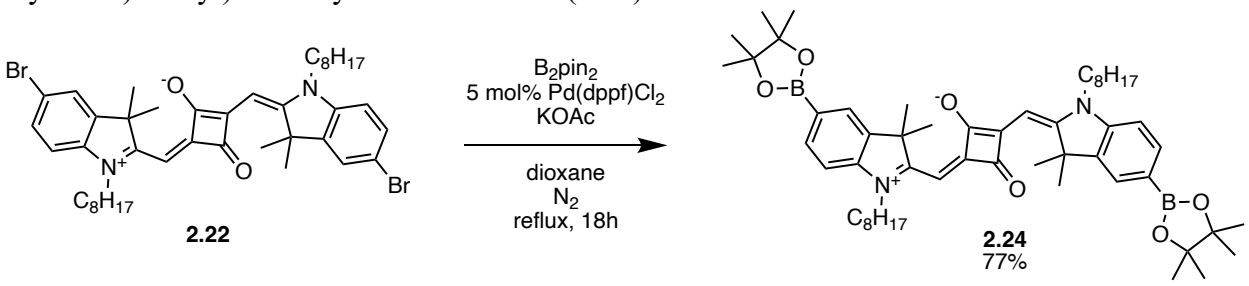

A 100 mL round bottomed flask was charged 50 mL dioxane, **2.22** (0.9979 g, 1.28 mmol), bis(pinacolato)diboron (0.9770 g, 3.84 mmol), $Pd(dppf)Cl_2$ (0.04800 g, 5 mol%), and KOAc (0.6292 g, 6.4 mmol). The solution was heated to reflux and stirred overnight. The resulting solution was cooled to room temperature, filtered, and the solvent was removed on the rotary evaporator to yield **2.24** in 77% (0.8603 g) yield as a shiny bright green solid.

^{1}H NMR spectroscopy (300 MHz, $CDCl_3$, 298 K) δ (ppm) = 7.78 d (2H, ^{4}J = unresolved), 7.78 dd (2H, ^{3}J = 8 Hz , ^{4}J = unresolved), 6.97 d (2H, ^{3}J = 8 Hz), 5.99 s (2H), 3.98 s br (4H), 1.78 – 0.85 m (46H), 1.36 s (24H)

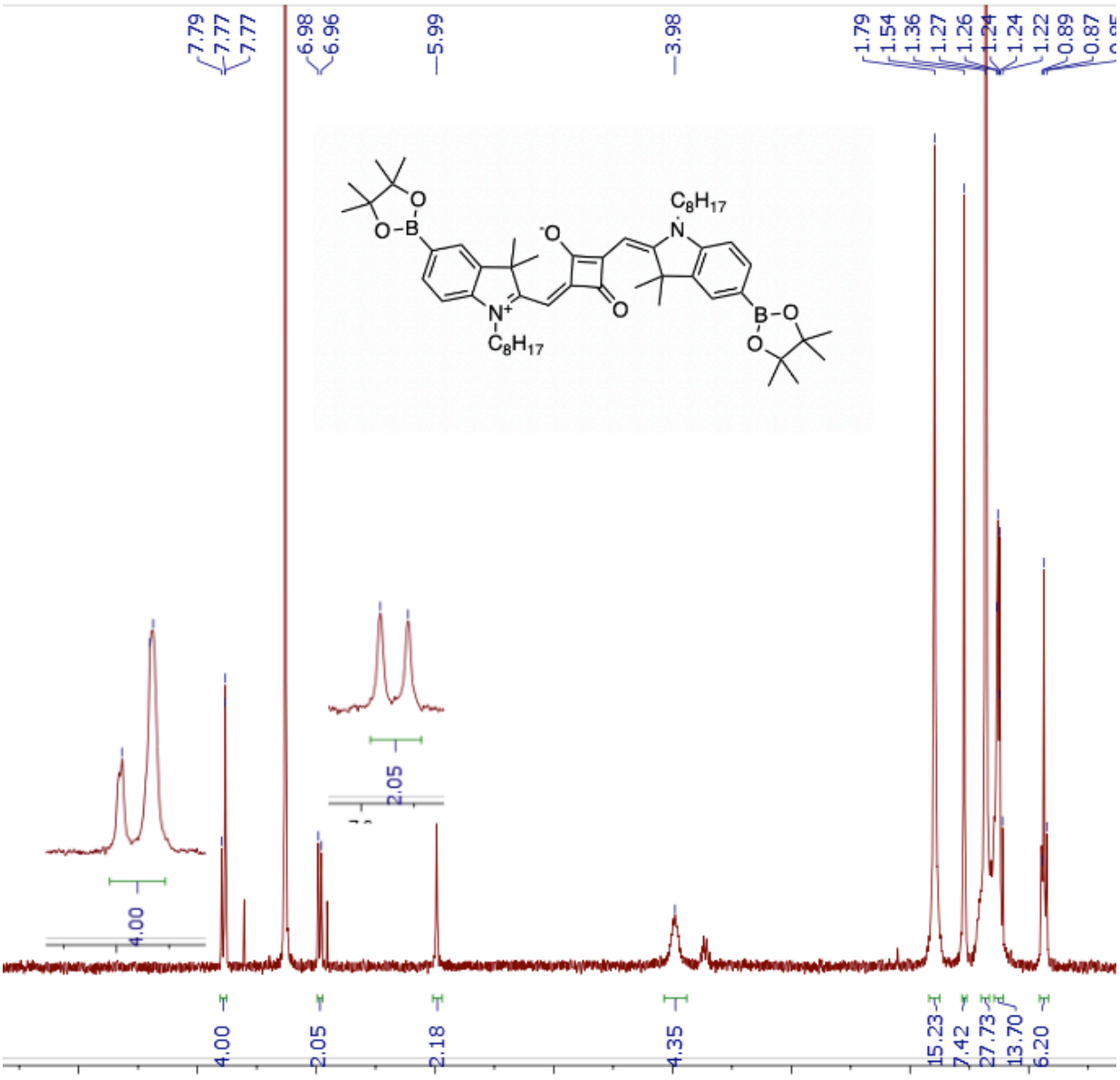

(*E*)-4-((5-(7-(3,5-di-*tert*-butyl-4-hydroxyphenyl)benzo[*c*][1,2,5]thiadiazol-4-yl)-3,3-dimethyl-1-octyl-3*H*-indol-1-ium-2-yl)methylene)-2-(((*E*)-5-(7-(3,5-di-*tert*-butyl-4-hydroxyphenyl)benzo[*c*][1,2,5]thiadiazol-4-yl)-3,3-dimethyl-1-octylindolin-2-ylidene)methyl)-3-oxocyclobut-1-en-1-olate (**2.25**)

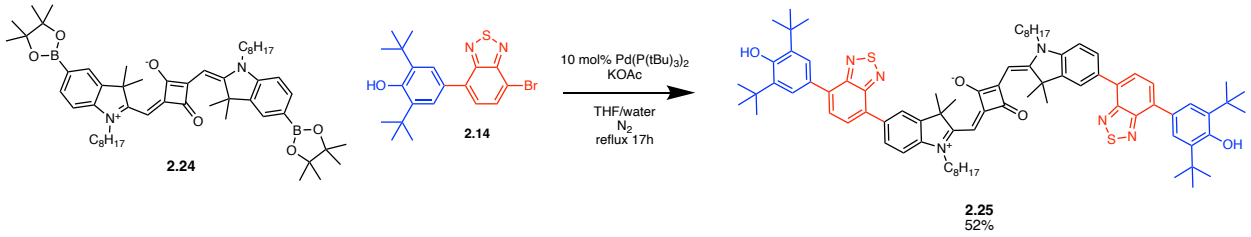

To a 100 mL two-neck round bottomed flask, 2.0 mL THF and 2.0 mL water was added with $Pd(P(tBu)_3)_2$ (0.0148 g, 10 mol%). The solution was degassed, and **2.24** (0.0990 g, 0.113 mmol)**,** **2.14** (0.0970 g, 0.231 mmol) and KOAc (0.0940 g, 0.959 mmol) was added under inert atmosphere. The solution was heated at 85 °C for 18 hours. The green solution was concentrated under vacuum and the product was purified by recrystallization in ethanol to yield **2.25** in 52% yield (0.0765 g) as a greenish-blue iridescent solid.

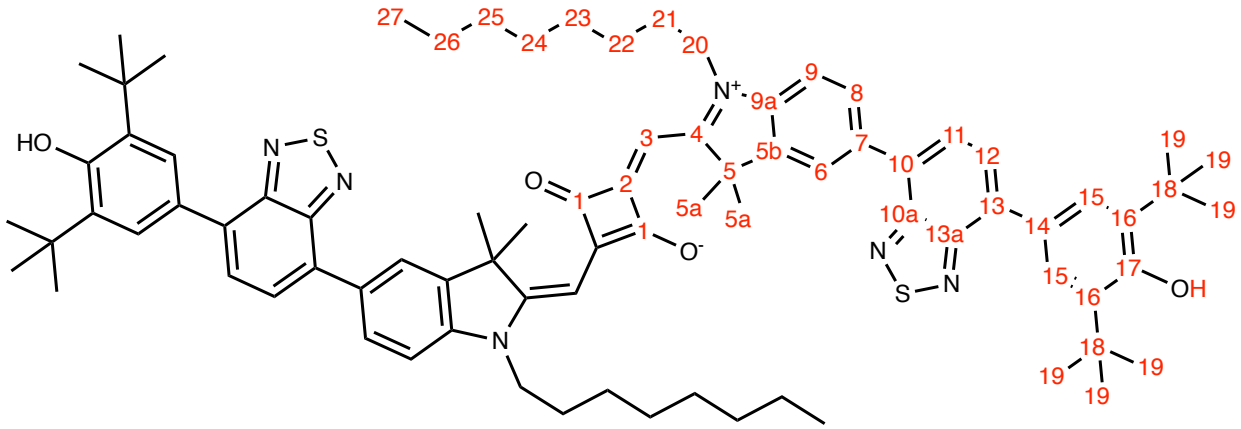

^{1}H NMR spectroscopy (500 MHz, $CDCl_3$, 298 K) δ (ppm) = 8.02 dd (2H, H_8, $^{3}J_{8,9}$ = 8 Hz, $^{4}J_{8,6}$ = 1 Hz) 7.92 d (2H, H_6 $^{4}J_{6,8}$ = 1 Hz) 7.84 s (4H, H_{15}), 7.79 d (2H, H_{11}, $^{3}J_{11,12}$ = 7 Hz) 7.74 d (2H, H_{12}, $^{3}J_{12,11}$ = 7 Hz) 7.15 d (2H, H_9, $^{3}J_{9,8}$ = 8 Hz) 6.05 s, br (2H, H_3), 5.42 s (2H, O**H**), 4.05 s, br (4H, H_{20}), 1.90 s (12H, H_{5a}), 1.54 s (36H, H_{19}), 1.50 – 1.25 m (24H, $H_{21\text{-}26}$) 0.89 t (3H, H_{27}, $^{3}J_{27,26}$ = 7 Hz)

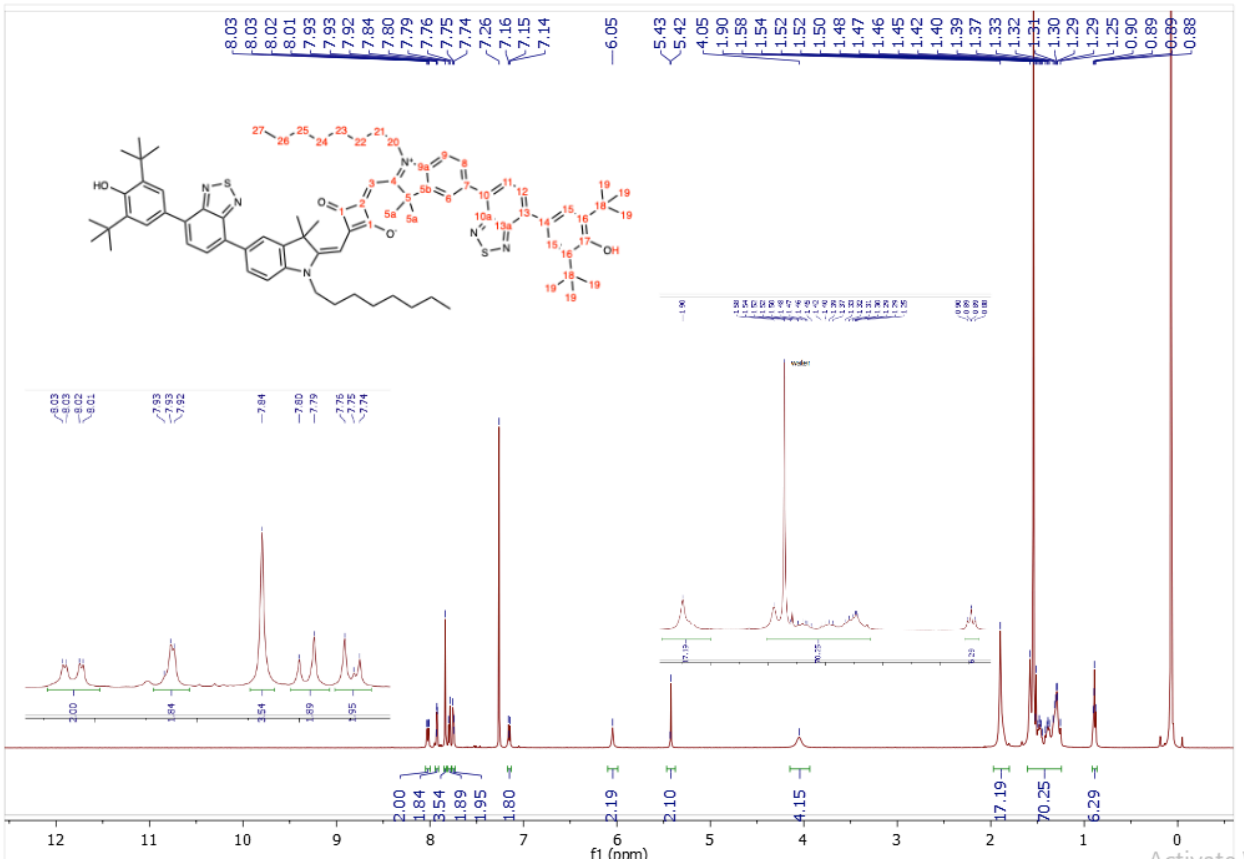

^{13}C NMR spectroscopy (500 MHz, $CDCl_3$, 298K) δ (ppm) = 179.84 (C_1), 170.11 (C_4), 154.61 (C_{14}), 154.58 (C_{17}), 154.33 (C_{10a}), 142.95 (C_{5b}), 142.70 (C_{9a}), 136.20 (C_{16}), 134.33 (C_{13}), 133.56 (C_7), 132.52 (C_2), 131.90 (C_{10}), 129.35 (C_8), 128.68 (C_{13a}), 128.06 (C_{11}), 127.43 (C_{12}), 126.53 (C_{15}), 123.31 (C_6), 109.56 (C_9), 87.42 (C_3), 49.61 (C_5), 44.16 (C_{20}), 34.74 (C_{18}), 31.96 (C_{21}), 30.56 (C_{19}), 30.51 (C_{22}), 29.56 (C_{23}), 29.37 (C_{24}), 27.39 (C_{5a}), 27.33 (C_{25}), 22.80 (C_{26}), 14.27 (C_{27})

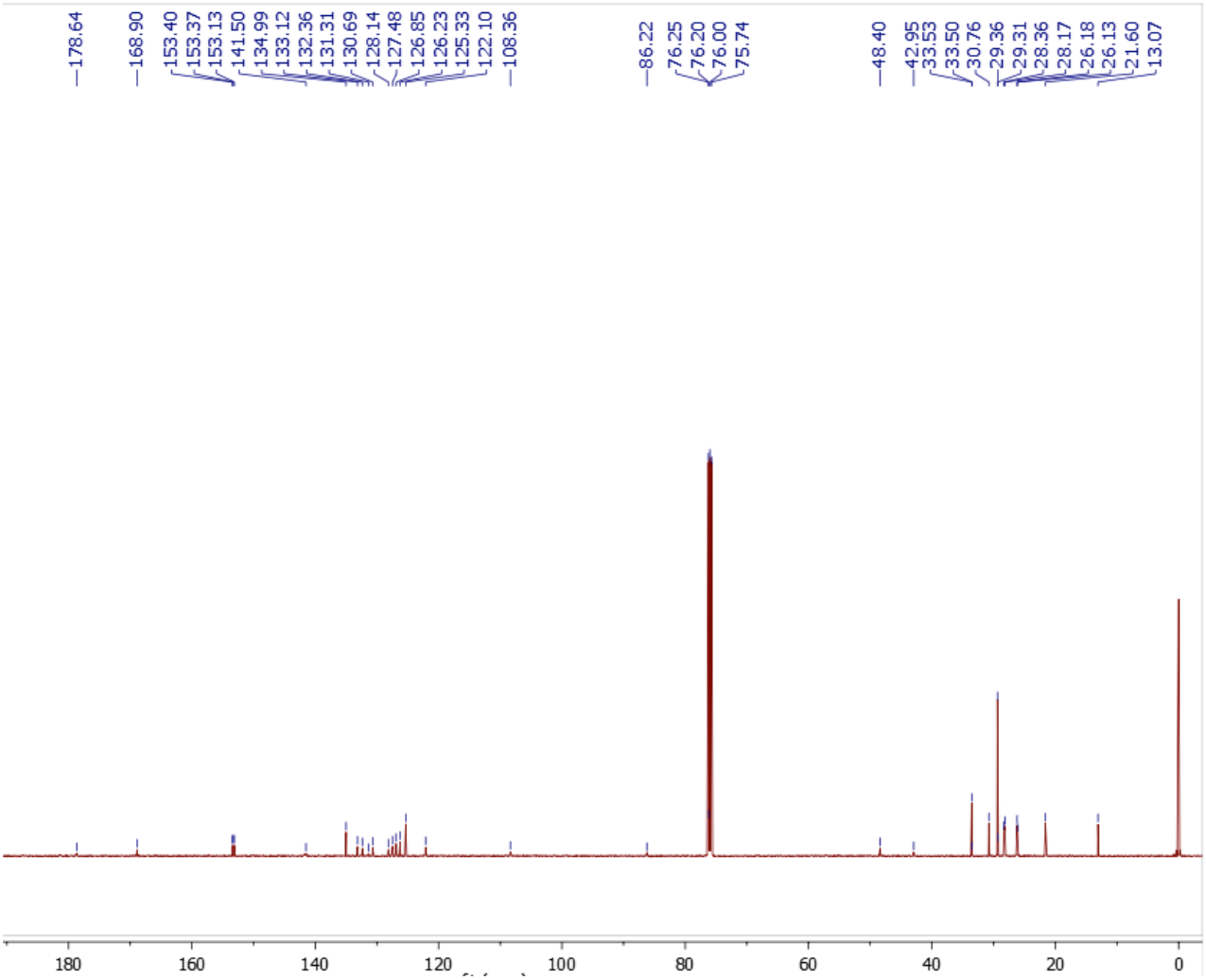

HR-MS: calculated for $C_{82}H_{100}N_6O_4S_2$ $[M]^+$: 1297.73203. Found: 1297.73239

7-bromo-2,3,3-trimethyl-3*H*-indole (**2.27**)

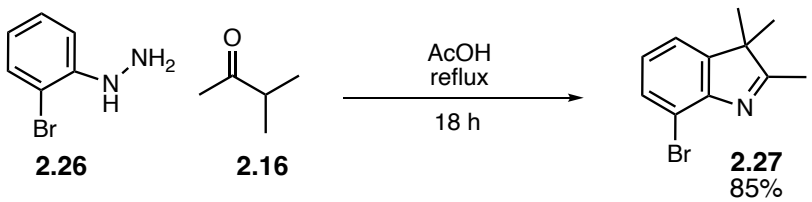

A 100 mL round-bottomed flask was charged with 15 mL acetic acid, **2.26** (2.03 g, 0.0109 mol), and **2.16** (1.24 g, 0.0144 mol). The solution was heated to reflux and left overnight. The

resulting reaction mixture was then cooled to room temperature and extracted with 3 x 100 mL diethyl ether. The ether was removed on the rotary evaporator to afford **2.27** as a red oil in 85% (2.20 g) yield.

^{1}H NMR spectroscopy (300 MHz, $CDCl_3$, 298 K) δ (ppm) 7.44 dd (1H, ^3J = 7 Hz, ^4J = 1 Hz), 7.19 dd (1H, ^3J = 7 Hz, ^4J = 1 Hz), 7.06 t (1H, ^3J = 7 Hz), 2.32 s (3H), 1.29 s (6H)

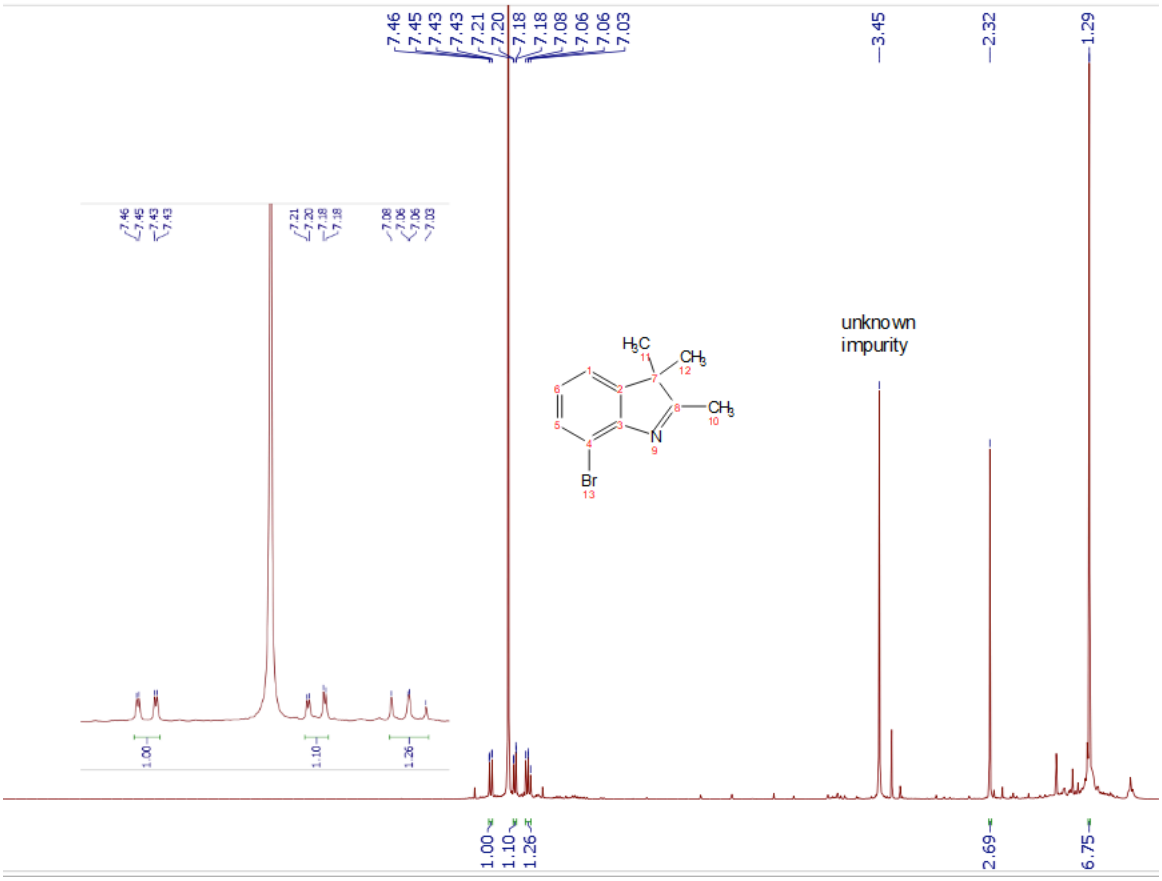

7-bromo-1,2,3,3-tetramethyl-3*H*-indol-1-ium iodide (**2.28a**)

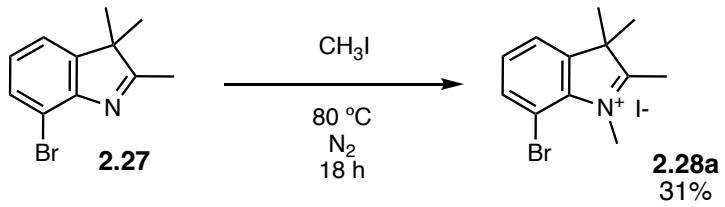

A 4 dram vial was charged with **2.27** (1.0098 g, 4.2 mmol) and CH_3I (5.0014 g, 35 mmol, 12 eq), sealead and then heated at 80 °C overnight. After cooling, the resulting brown solid was washed with ice-cold THF to yield **2.28a** in 31.4% (0.5060 g) yield.

^{1}H NMR spectroscopy (500 MHz, d_6-dmso, 298 K) δ(ppm) = 7.87 d (1H, H_4 $^3J_{4,5}$ =), 7.83 d (1H, H_6, $^3J_{6,5}$ =), 7.53 t (1H, H_5, $^3J_{5,4,6}$ =), 4.18 s (3H, H_8), 2.79 s (3H, H_{2a}), 1.54 s (6H, H_{3b})

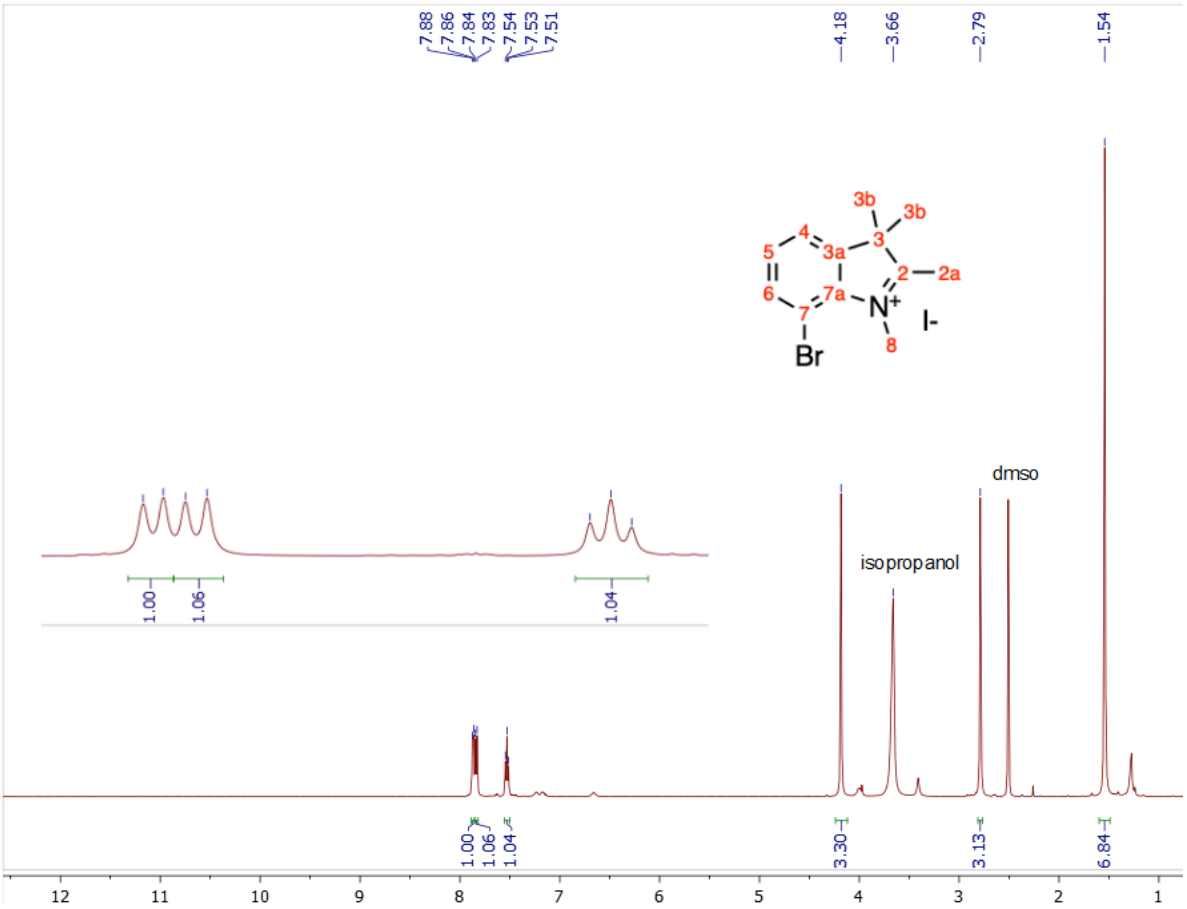

\13C NMR spectroscopy (500 MHz, $CDCl_3$, 298K) δ(ppm) = 198.71 (C_2), 145.21 (C_{3a}), 139.03 (C_{7a}), 134.74 (C_6), 130.71 (C_5), 123.04 (C_4), 107.50 (C_7), 53.76 (C_3), 40.13 (C_8), 21.73 (C_{3b}), 14.76 (C_{2a})

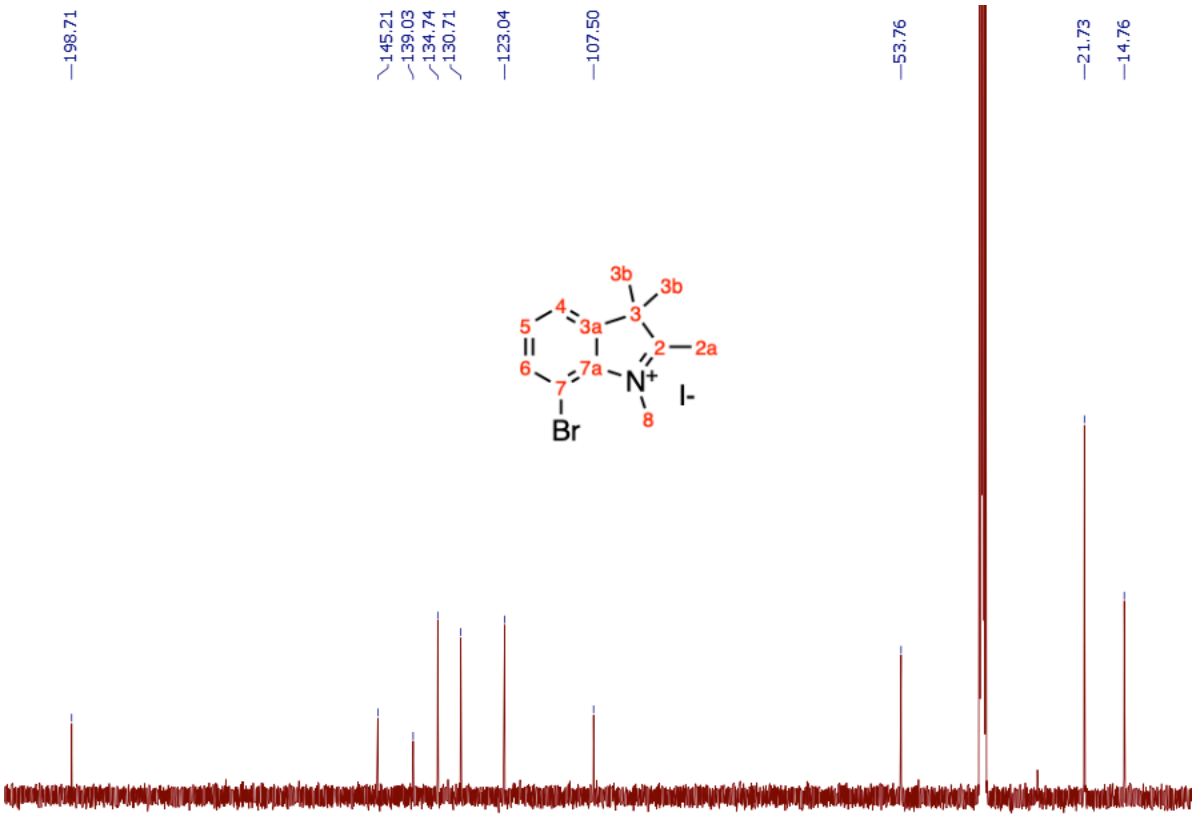

4-((7-Bromo-3,3-dimethyl-1-methyl-3H-indolium-2-yl)methylene)-2-((7-bromo-3,3- dimethyl-1-methylindolin-2-ylidene)methyl)-3-oxocyclobut-1-enolate (**2.29**)

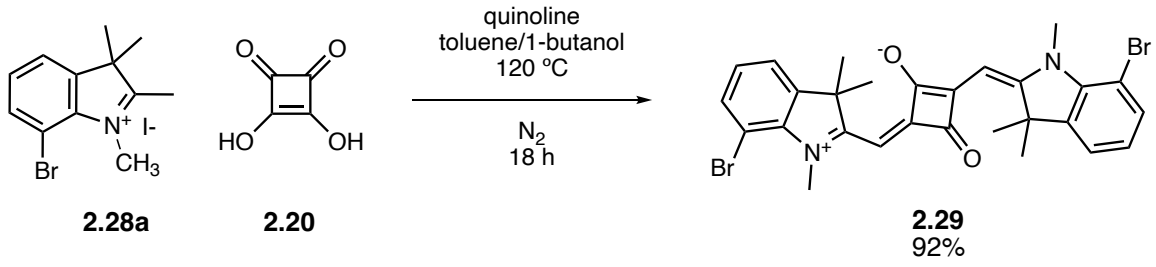

2.28a **2.20** **2.29** 92%

To a 250 mL round-bottomed flask, **2.28a** (8.000 g, 22.2 mmol), **2.20** (1.09 g, 9.5 mmol), 10 mL quinoline and 50 mL of a 1:1 mixture toluene and 1-butanol. The solution was heated to 120 °C after which it quickly began to turn dark blue. The reaction was left to stir overnight. After cooling to room temperature, the reaction mixture was added to a 250 mL 5% aqueous citric acid

solution to yield a shiny blue precipitate. The solid was filtered and oven-dried to yield **2.29** in 93% yield (5.68 g) as a shiny blue solid.

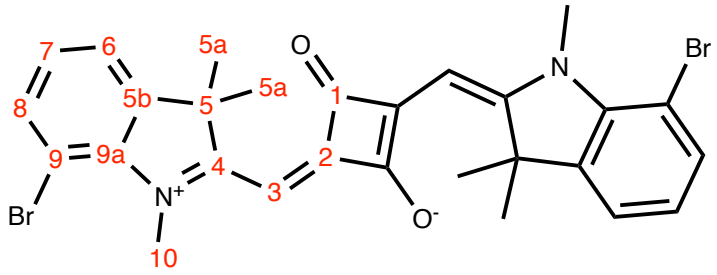

^{1}H NMR spectroscopy (500 MHz, $CDCl_3$, 298 K) δ (ppm) = 7.45 d (2H, $^{3}J_{2,7}$ = 8 Hz), 7.27 d (2H, $^{3}J_{2,7}$ = 8 Hz, H_7), 6.98 t (2H, ^{3}J = 8 Hz, H_7), 5.98 s (2H, H_3), 4.00 s (6H, H_6), 1.76 s (12H, H_{5a})

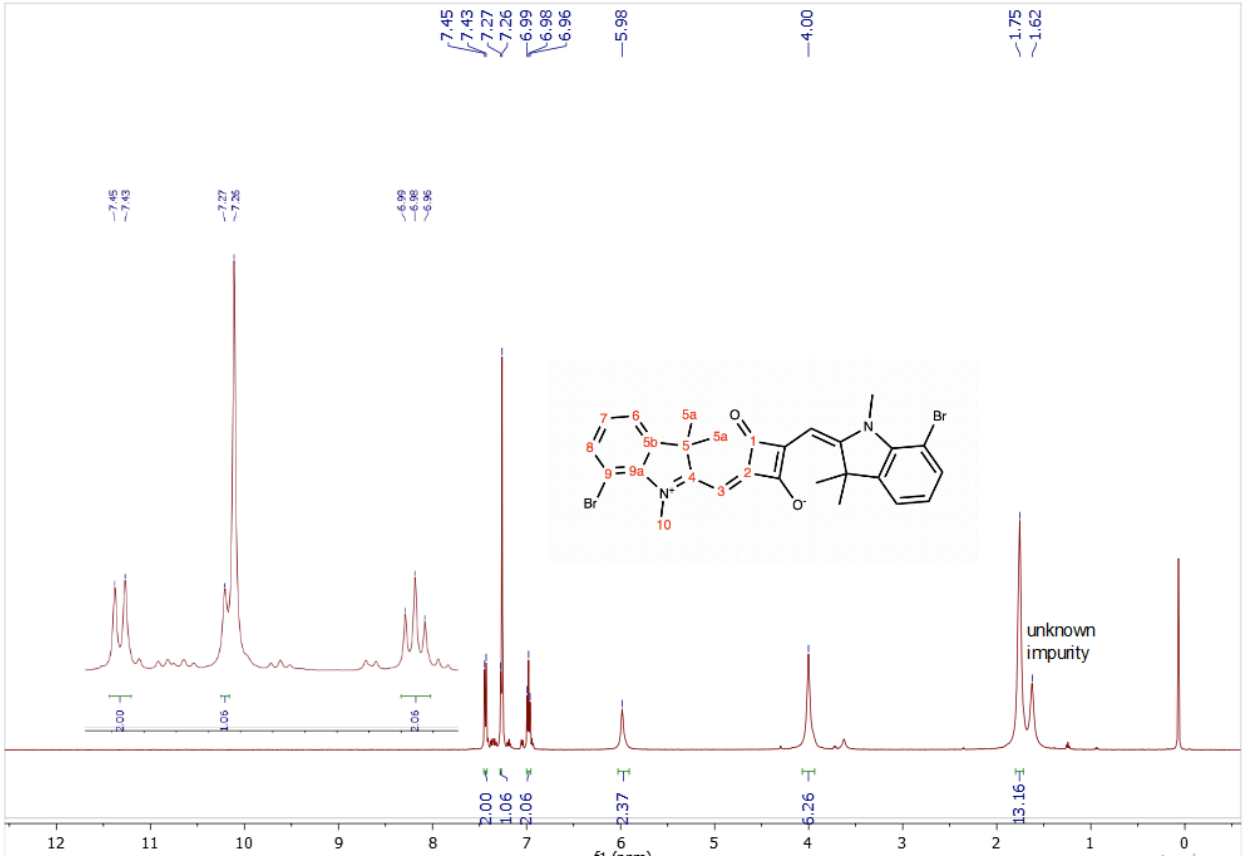

^{13}C NMR spectroscopy (500 MHz, $CDCl_3$, 298K) δ (ppm) = 182.13 (C_1), 172.34 (C_4), 140.03 (C_{9a}), 134.20 (C_8), 128.13 (C_2), 125.10 (C_7), 121.63 (C_6), 121.56 (C_{5b}), 103.48 (C_9), 88.20 (C_3), 49.04 (C_5), 27.75 (C_{5a})

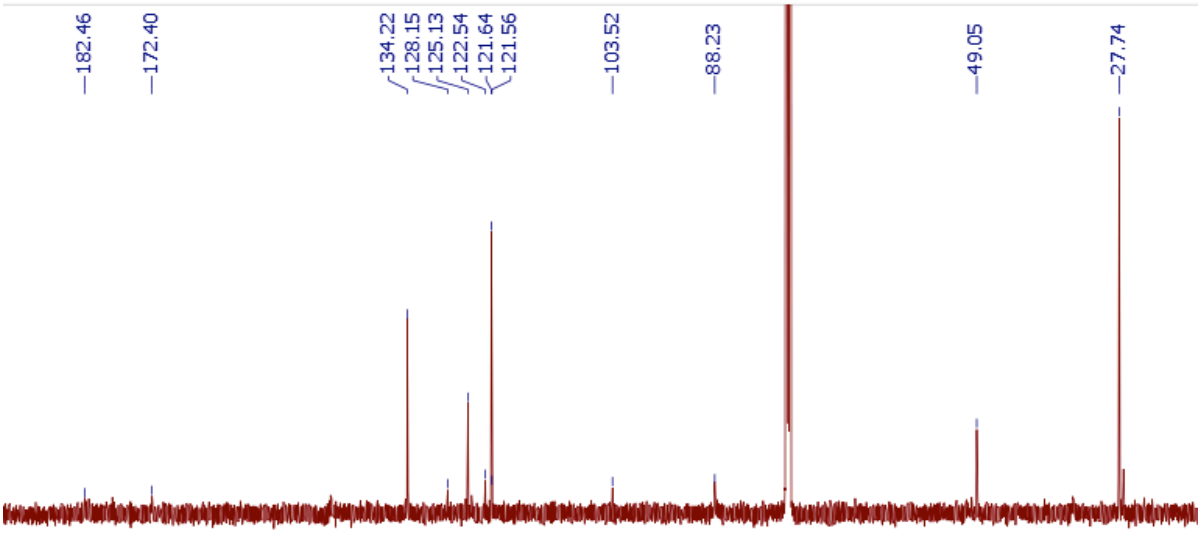

HR-MS: calculated for $C_{28}H_{26}Br_2N_2O_2$ $[M]^+$: 583.04134. Found: 583.04135

4,4'-(benzo[*c*][1,2,5]thiadiazole-4,7-diylidene)bis(2,6-di-*tert*-butylcyclohexa-2,5-dien-1-one) (**2.36**)

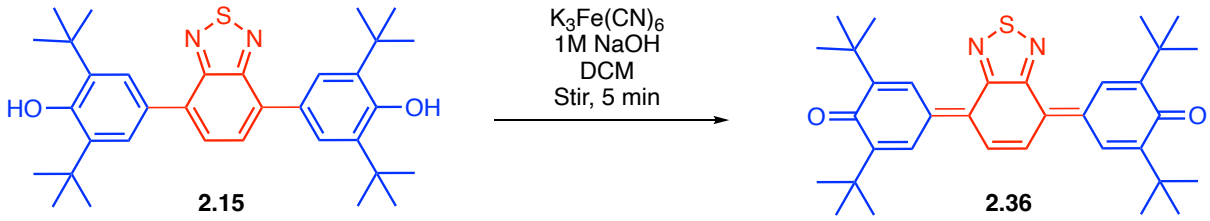

To a 1-dram vial, 1 mg **2.15**, 50 mg potassium ferricyanide, 1 mL DCM and 0.3 mL 1 M NaOH were added and stirred under regular atmosphere. The yellow solution turned to an opaque magenta after 30 seconds. The organic phase was separated, and solvent was removed on the rotary evaporator to yield a purple solid in quantitative yield.

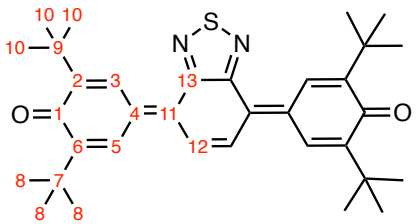

^{1}H NMR spectroscopy (500 MHz, $CDCl_3$, 298 K) δ (ppm) = 9.35 s, br (2H, H_5), 7.86 s (2H, H_{12}), 7.74 s, br (2H, H_3), 1.41 s (18H, H_{10}), 1.40 s (18H, H_8)

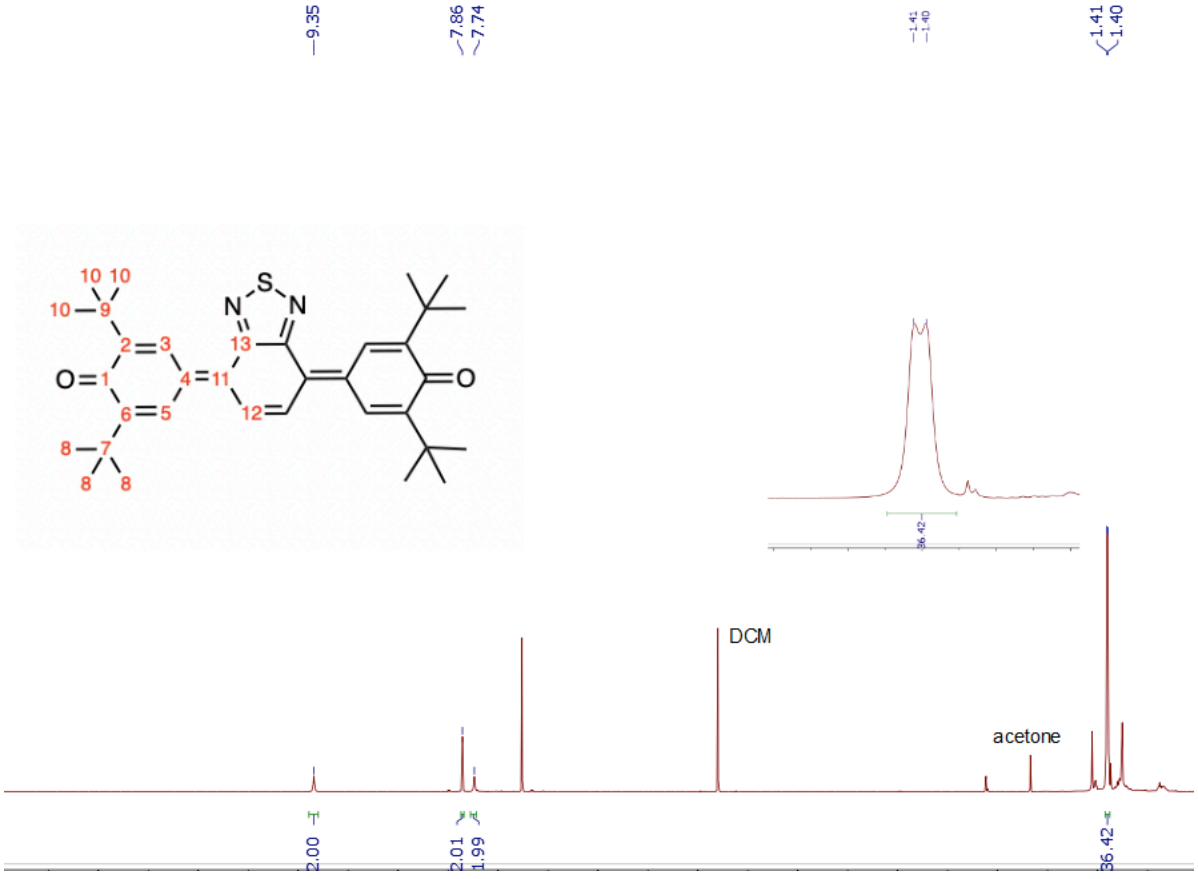

^{13}C NMR spectroscopy (500 MHz, $CDCl_3$, 298K) δ (ppm) = 186.60 (C_1), 156.30 (C_{13}), 151.27 (C_2), 150.08 (C_6), 134.99 (C_4), 131.59 (C_{11}), 130.98 (C_5), 127.85 (C_{12}), 126.46 (C_3), 36.52 (C_9), 36.34 (C_7), 30.13 (C_{10} or C_8), 30.05 (C_{10} or C_8)

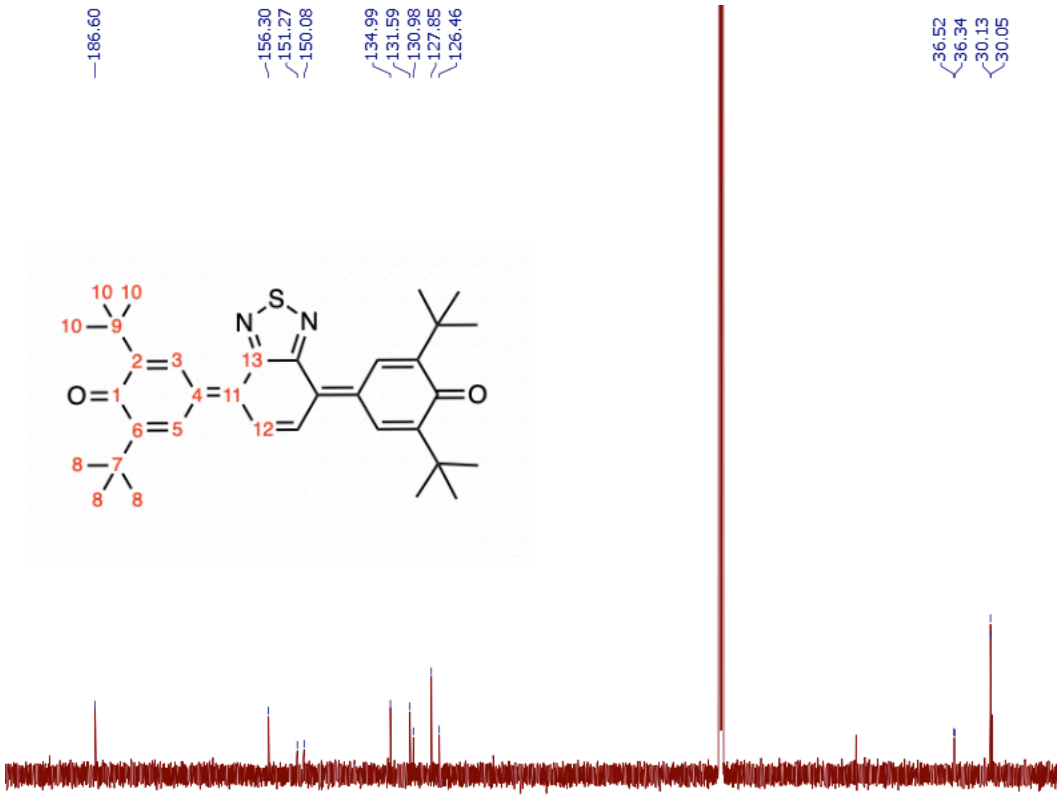

(**2.14-A**)

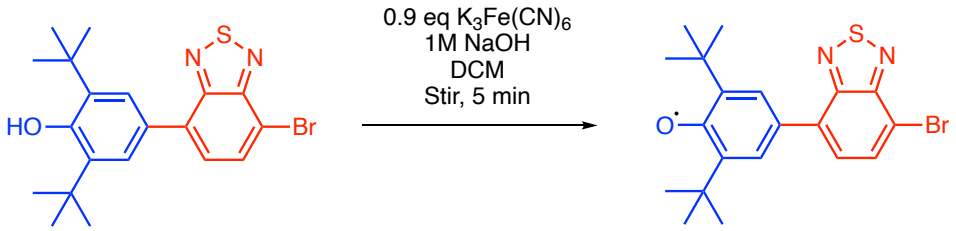

2.14 **2.14-A**

A 1-dram vial was charged with **2.14** (52.2 mg, 0.12 mmol), $K_3Fe(CN)_6$ (38.8 mg, 0.12 mmol, 1 eq), DCM (2 mL), and 1 M NaOH (0.12 mL, 1.2 mmol, 10 eq). The vial was sealed and then stirred without nitrogen. After moments, the solution changed color from yellow to red. After 5 minutes, the solution was filtered to remove any remaining inorganic components. The resulting organic phase was concentrated to isolate **2.14-A** in an unknown yield.

FT-IR (ν_{max}/cm^{-1}): 3350, 2039, 1439.

HR-MS: calculated for $C_{20}H_{22}BrN_2OS\bullet$ $[M]^-$: 417.06362. Found: 417.06476

Appendix 2 2D NMR Spectroscopy

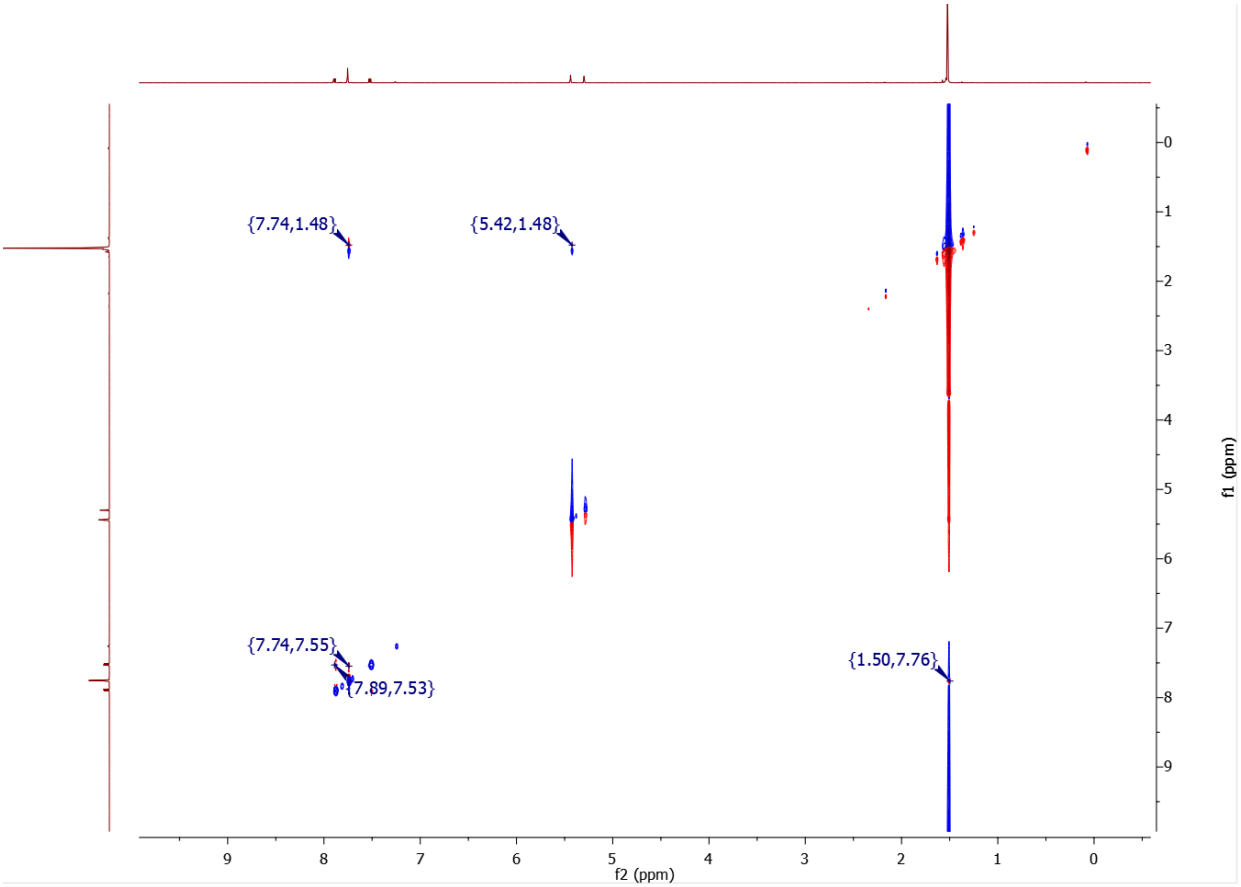

Appendix 2.10. ^{1}H-^{1}H NOESY NMR spectroscopy for **2.14**.

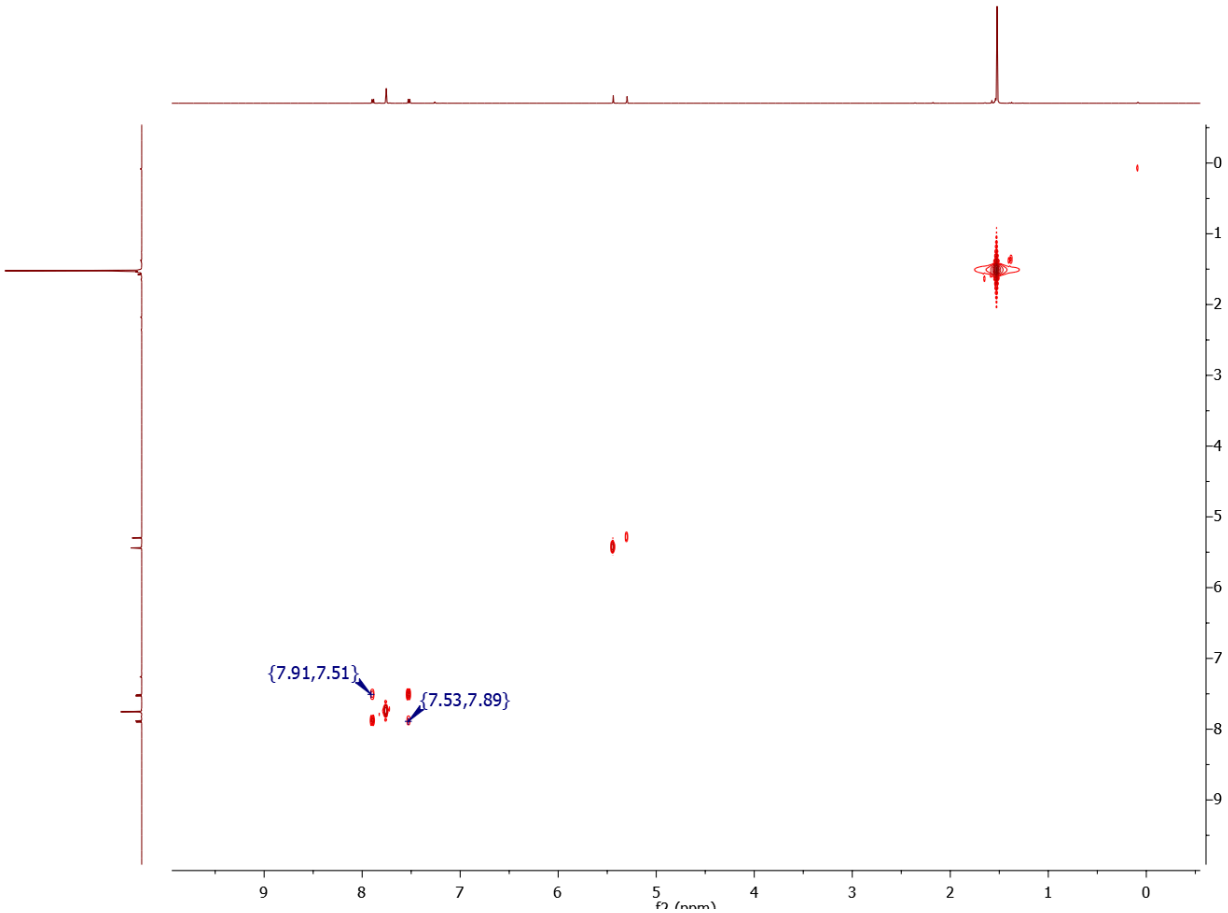

Appendix 2.11. ^{1}H-^{1}H COSY NMR spectroscopy for **2.14**.

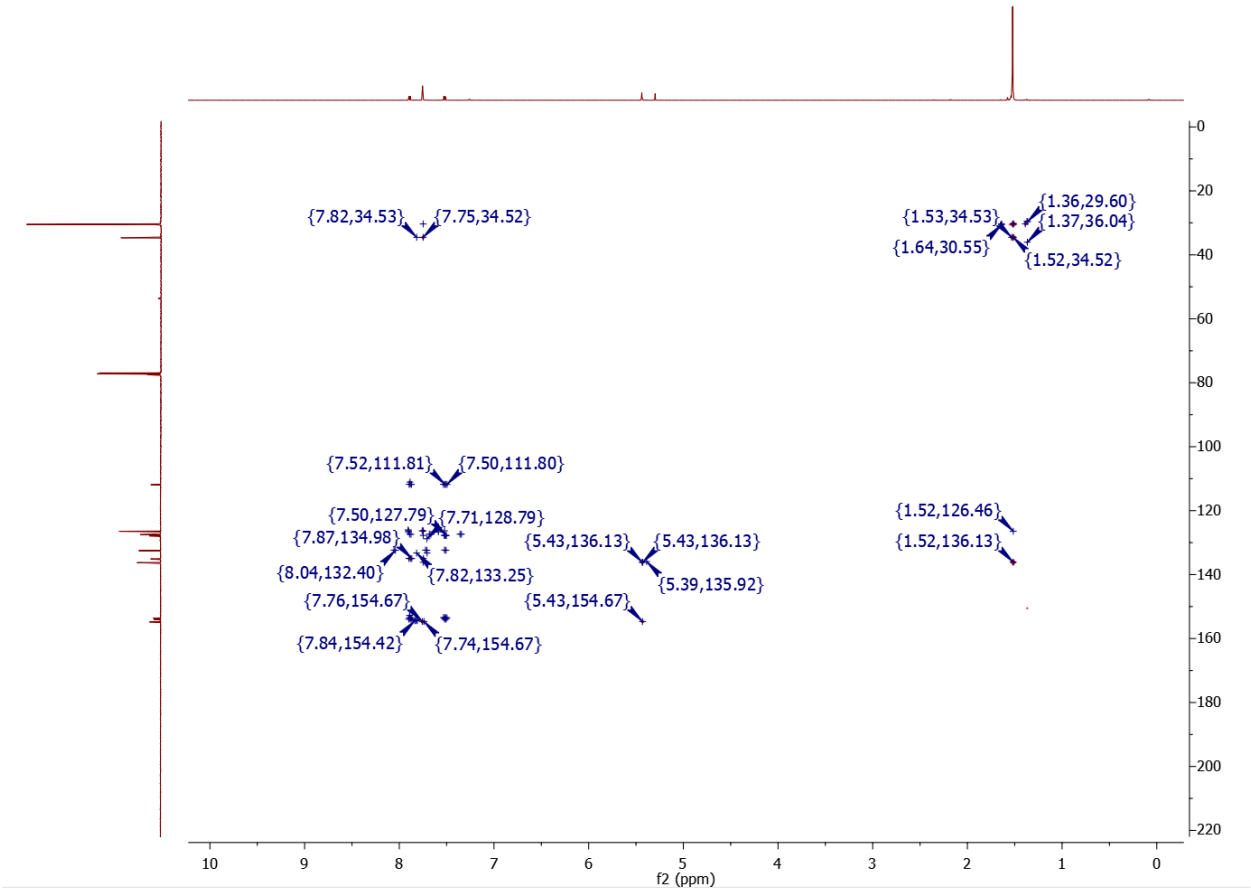

Appendix 2.12. ^{1}H-^{13}C HMBC NMR spectroscopy for **2.14**.

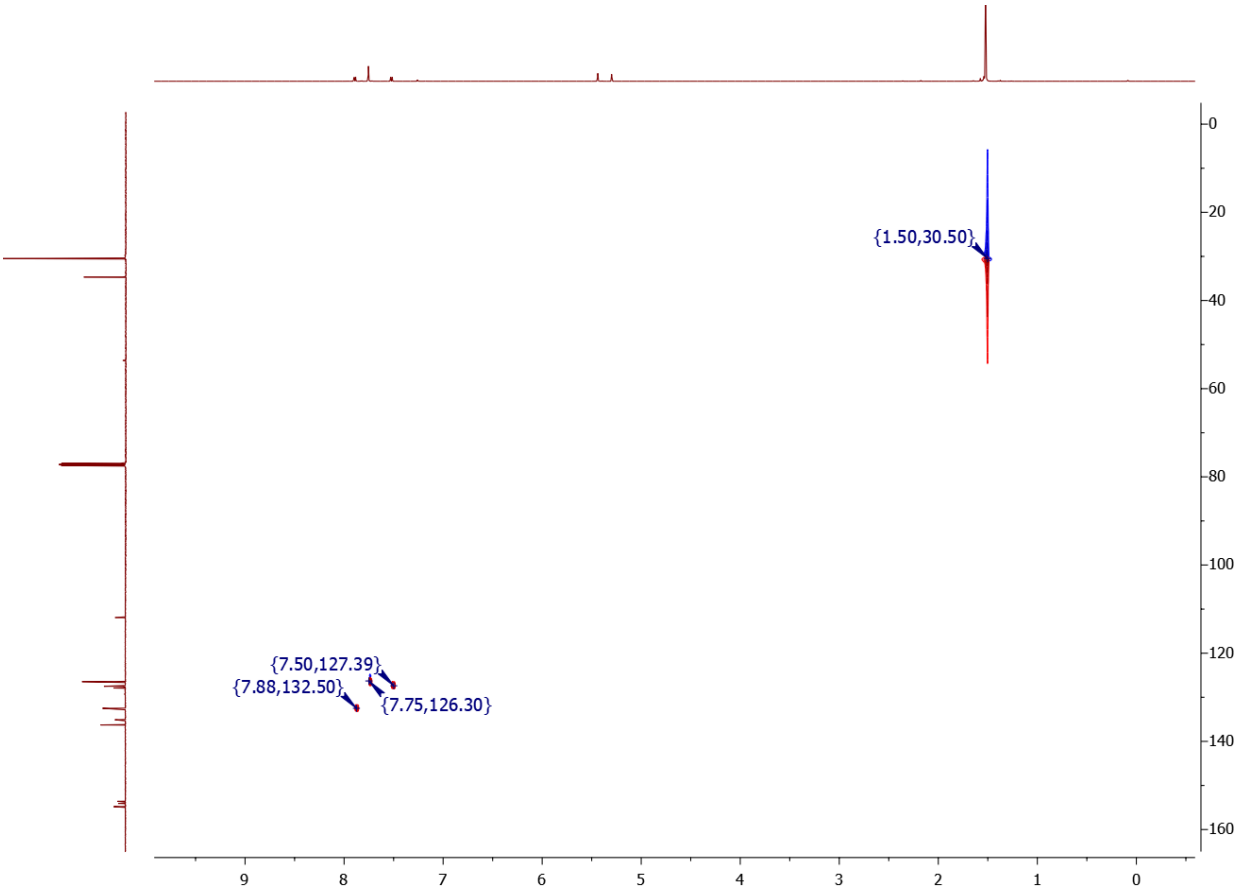

Appendix 2.14. ^{1}H-^{13}C HSQC NMR spectroscopy for **2.14**.

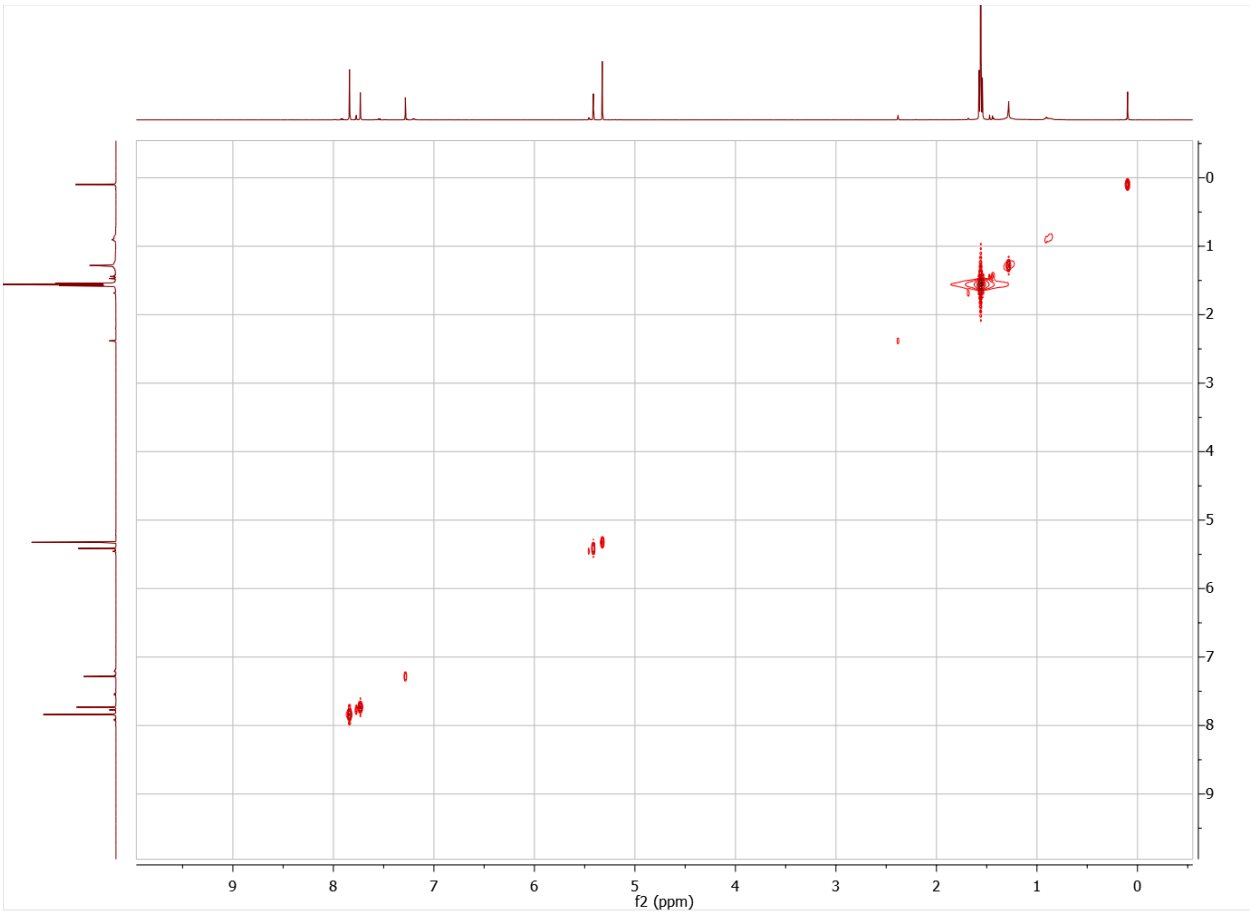

Appendix 2.15 ^{1}H-^{1}H COSY NMR spectroscopy for **2.15.**

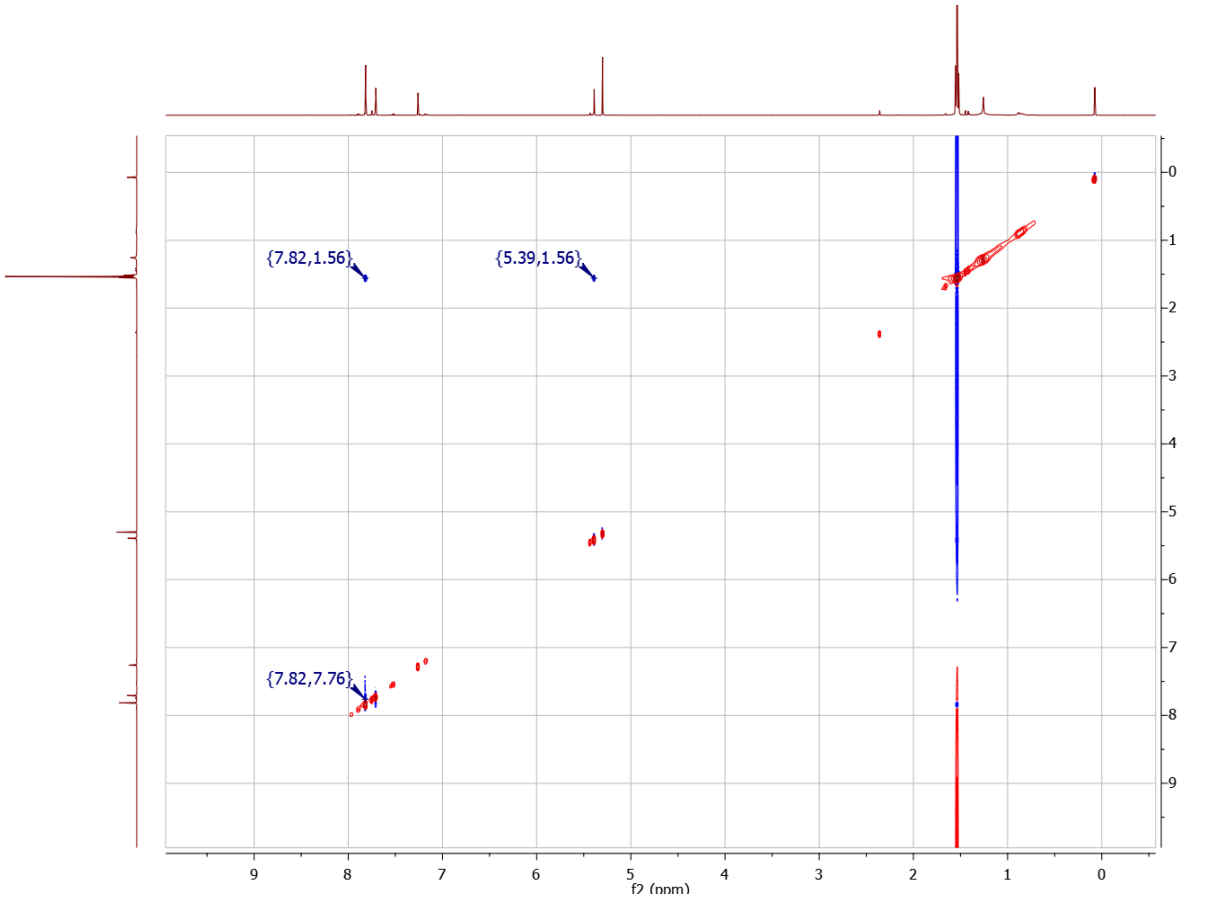

Appendix 2.16 ^{1}H-^{1}H NOESY NMR spectroscopy for **2.15.**

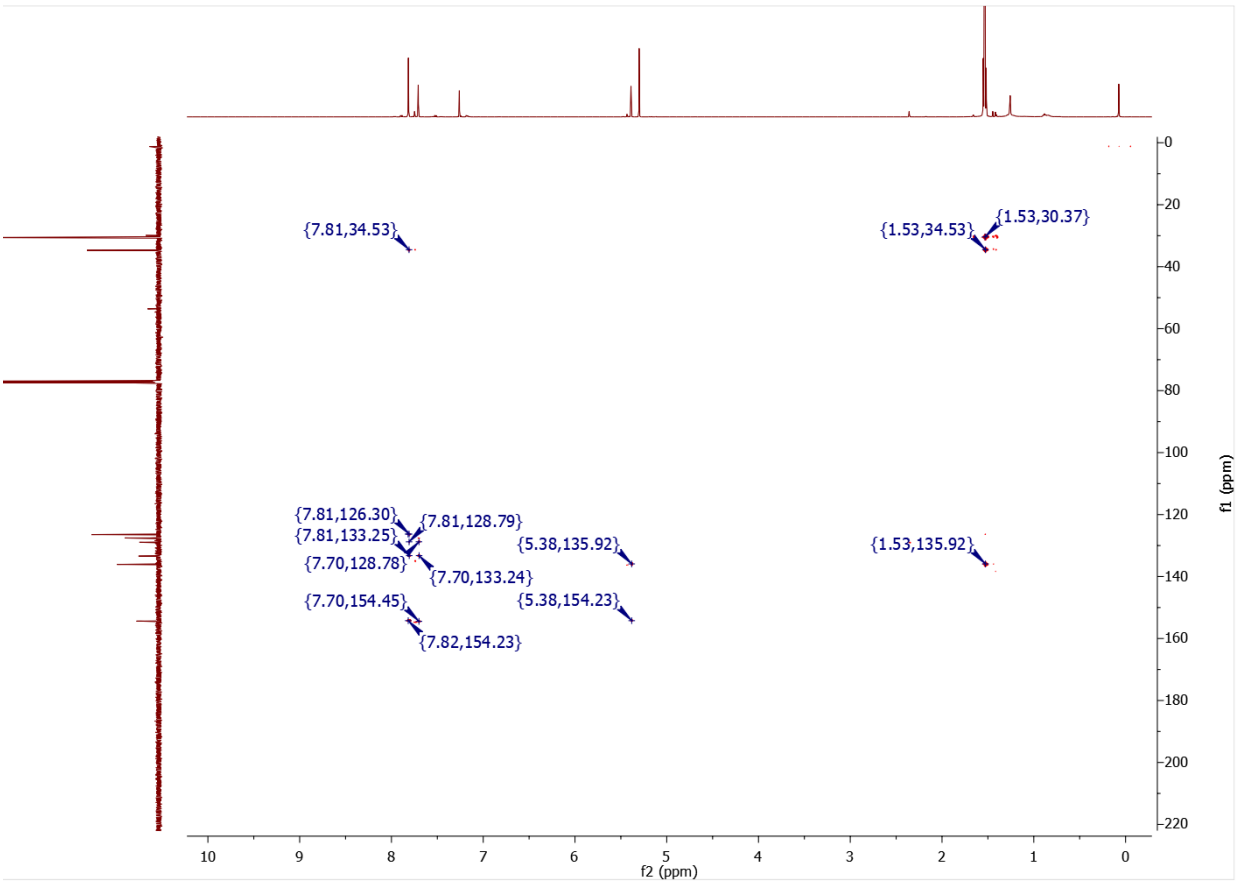

Appendix 2.17. ^{1}H-^{13}C HMBC for **2.15**.

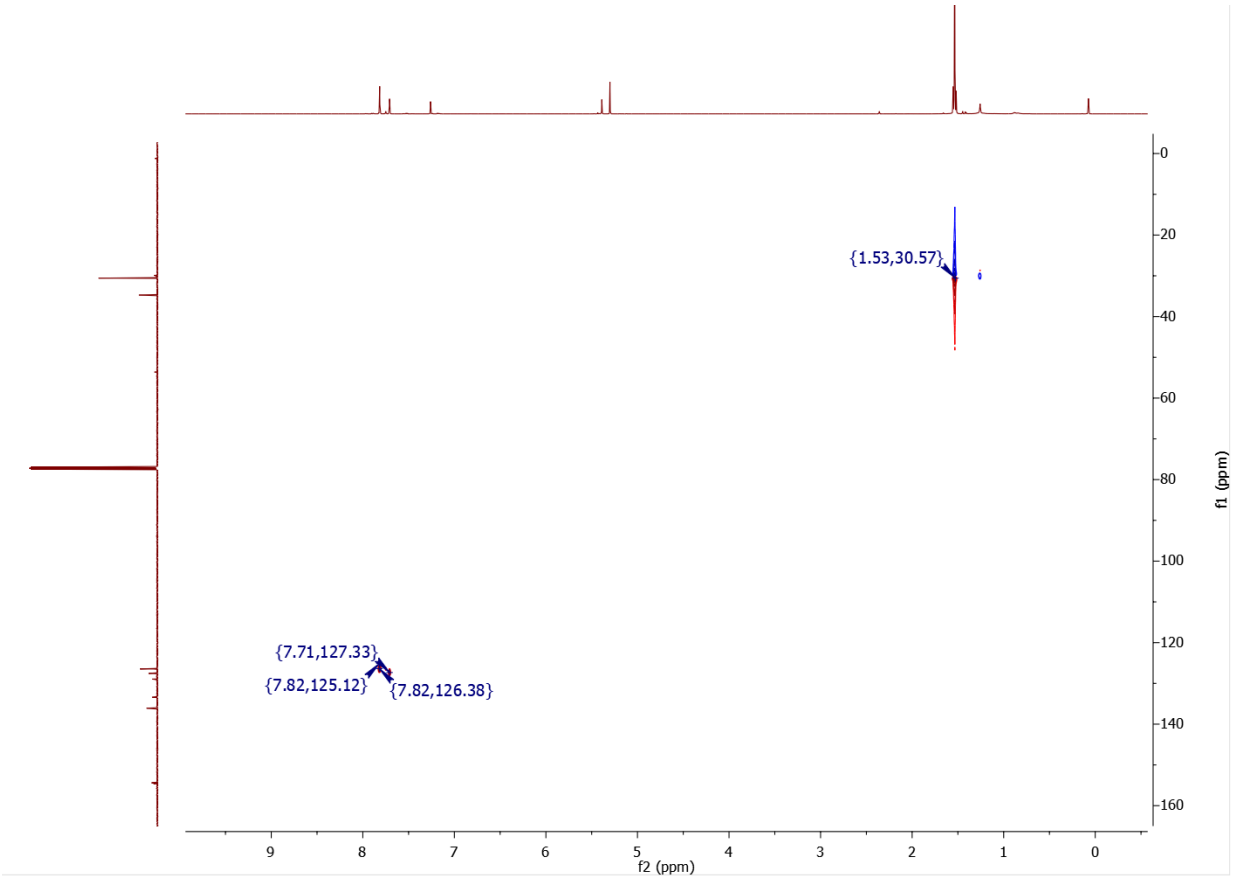

Appendix 2.18. ^{1}H-^{13}C HSQC for **2.15**.

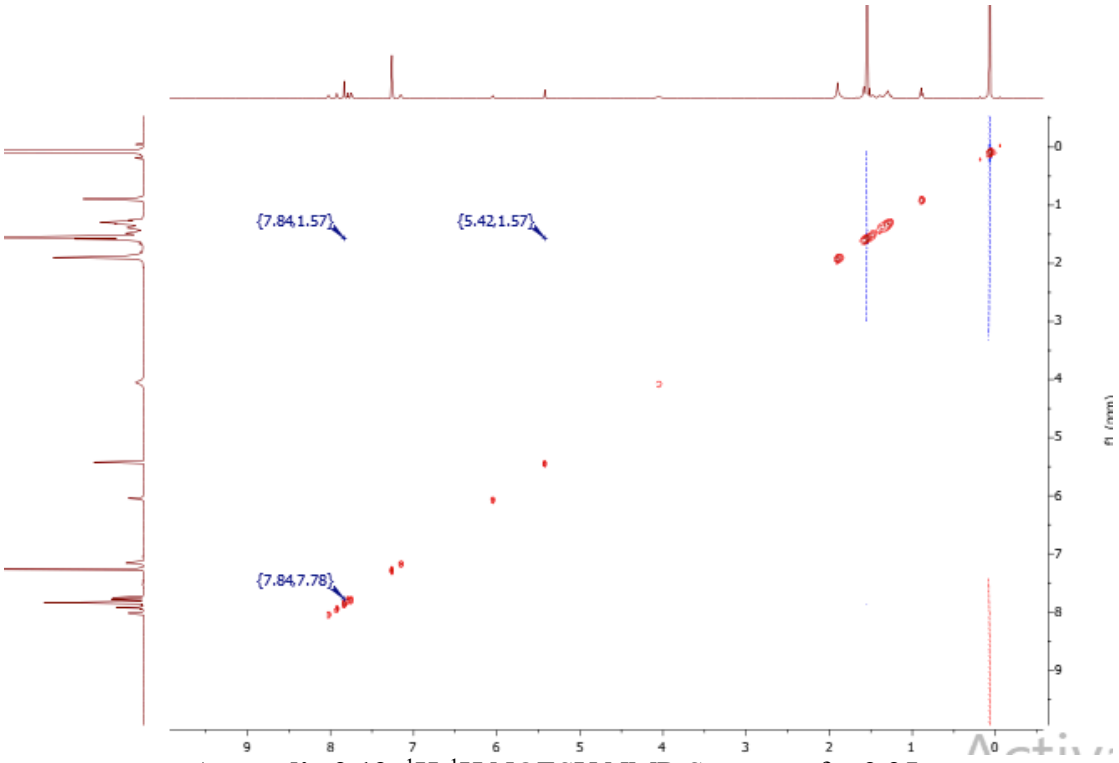

Appendix 2.19. ^{1}H-^{1}H NOESY NMR Spectrum for **2.25**.

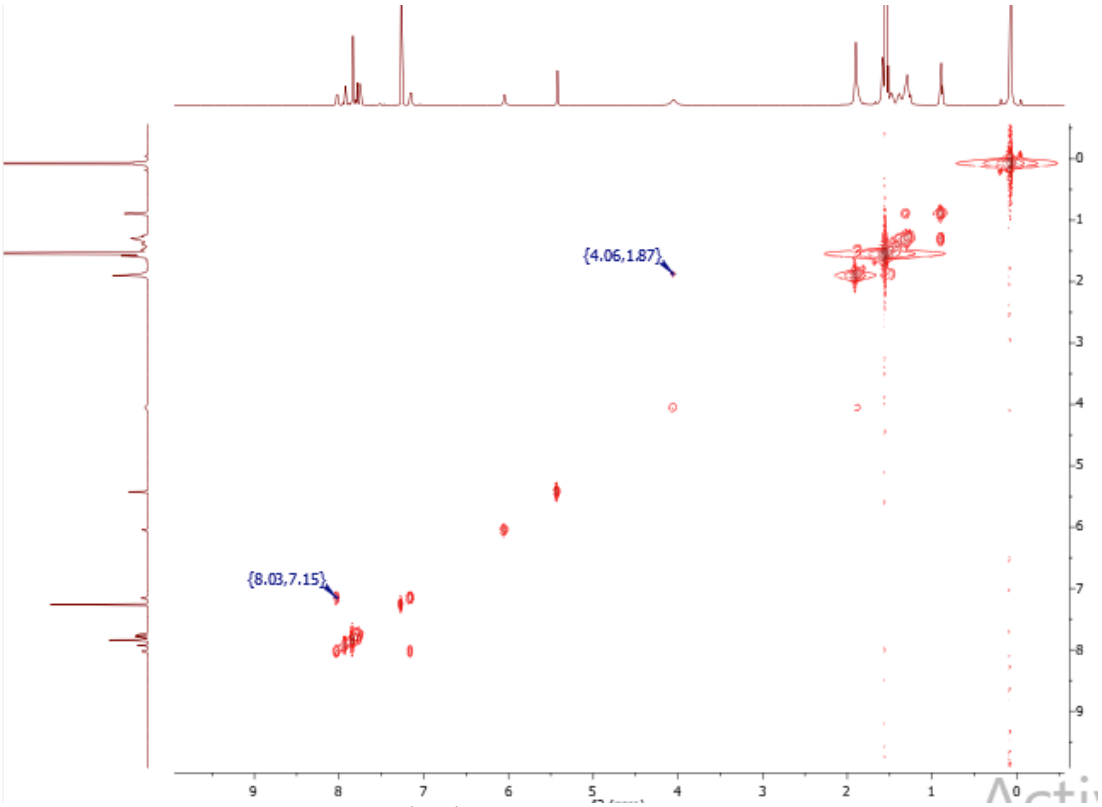

Appendix 2.20. ^{1}H-^{1}H COSY NMR Spectrum for **2.25**.

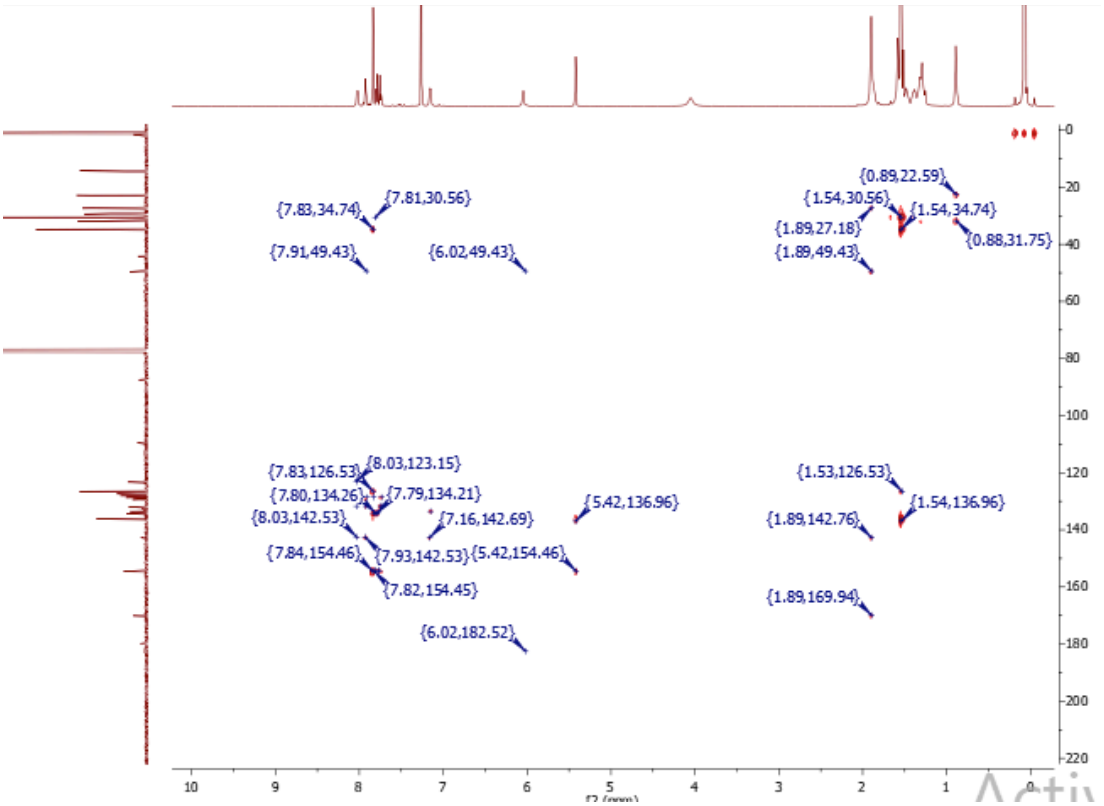

Appendix 2.21. ^{1}H-^{13}C HMBC NMR Spectrum for **2.25**.

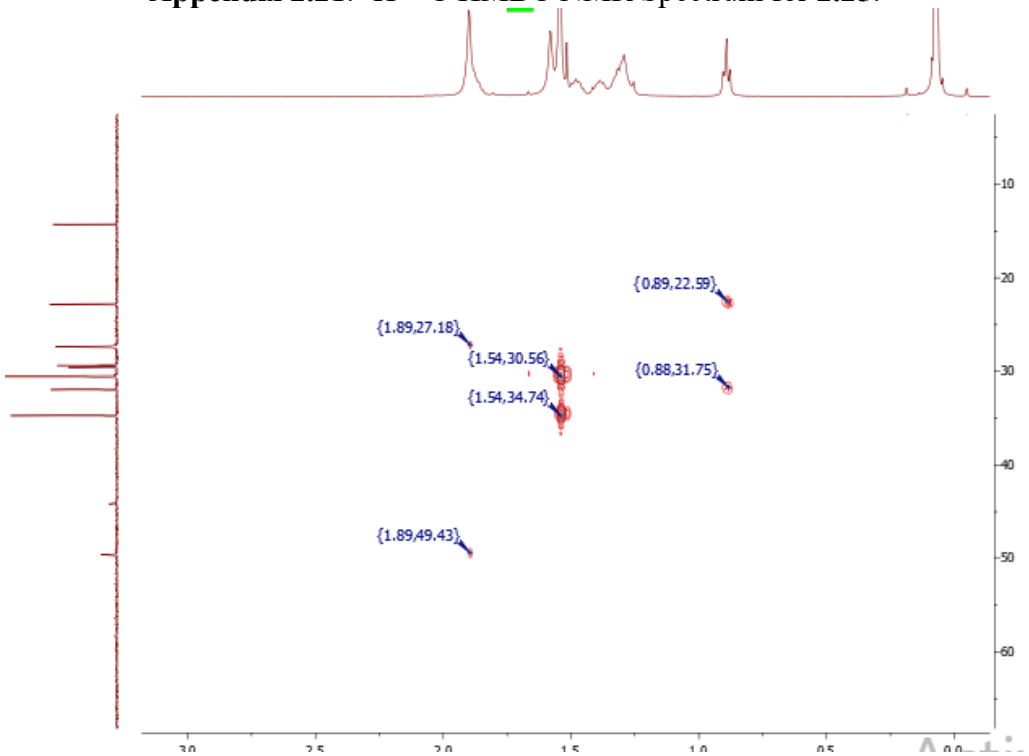

Blow-up HMBC **2.25**.

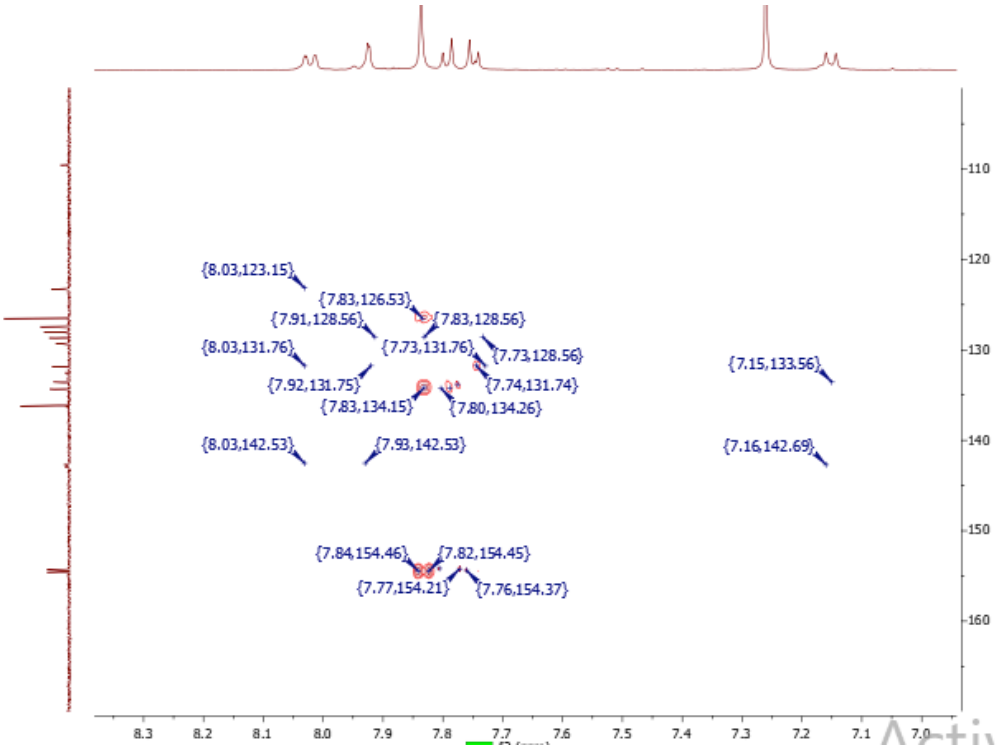

Blow-up HMBC **2.25**.

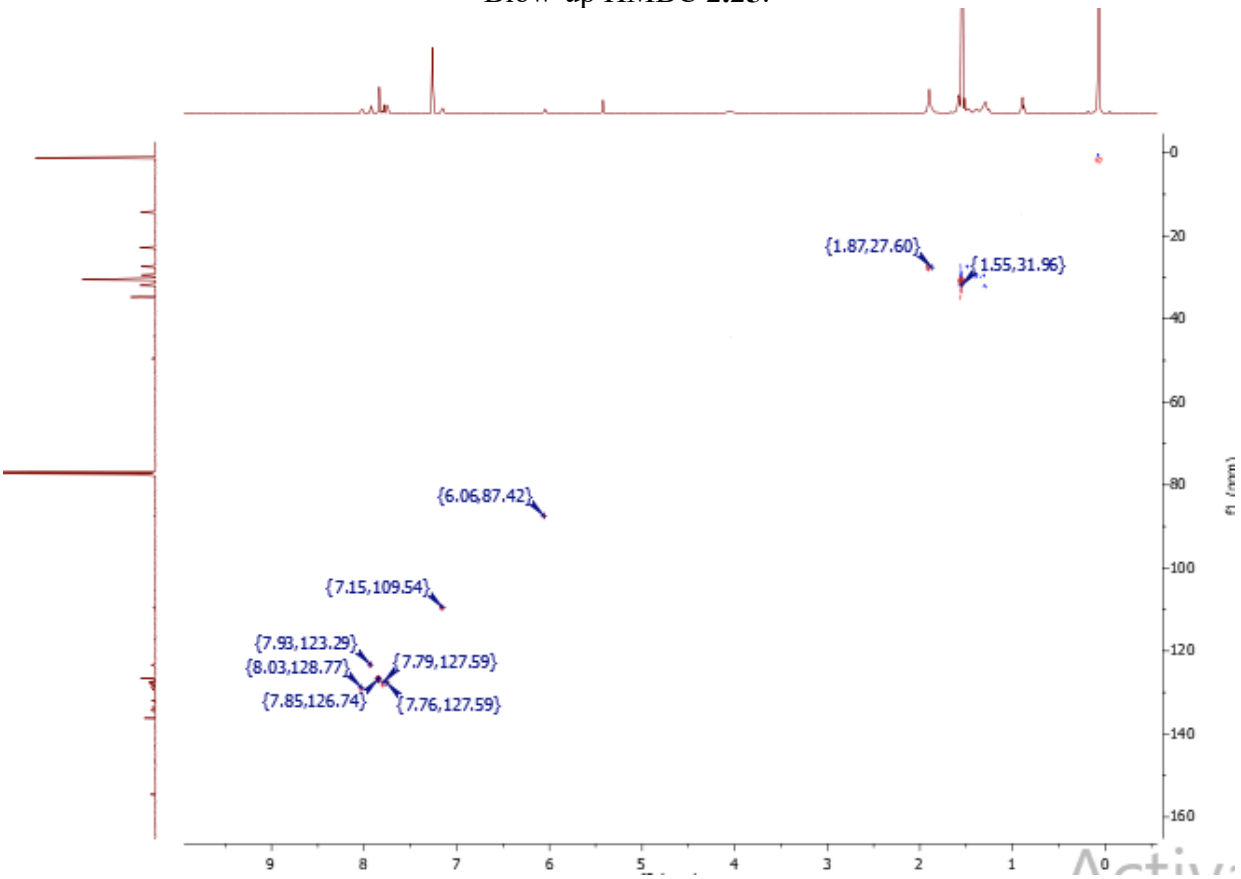

Appendix 2.22. ^{1}H-^{13}C HSQC NMR Spectrum for **2.25**.

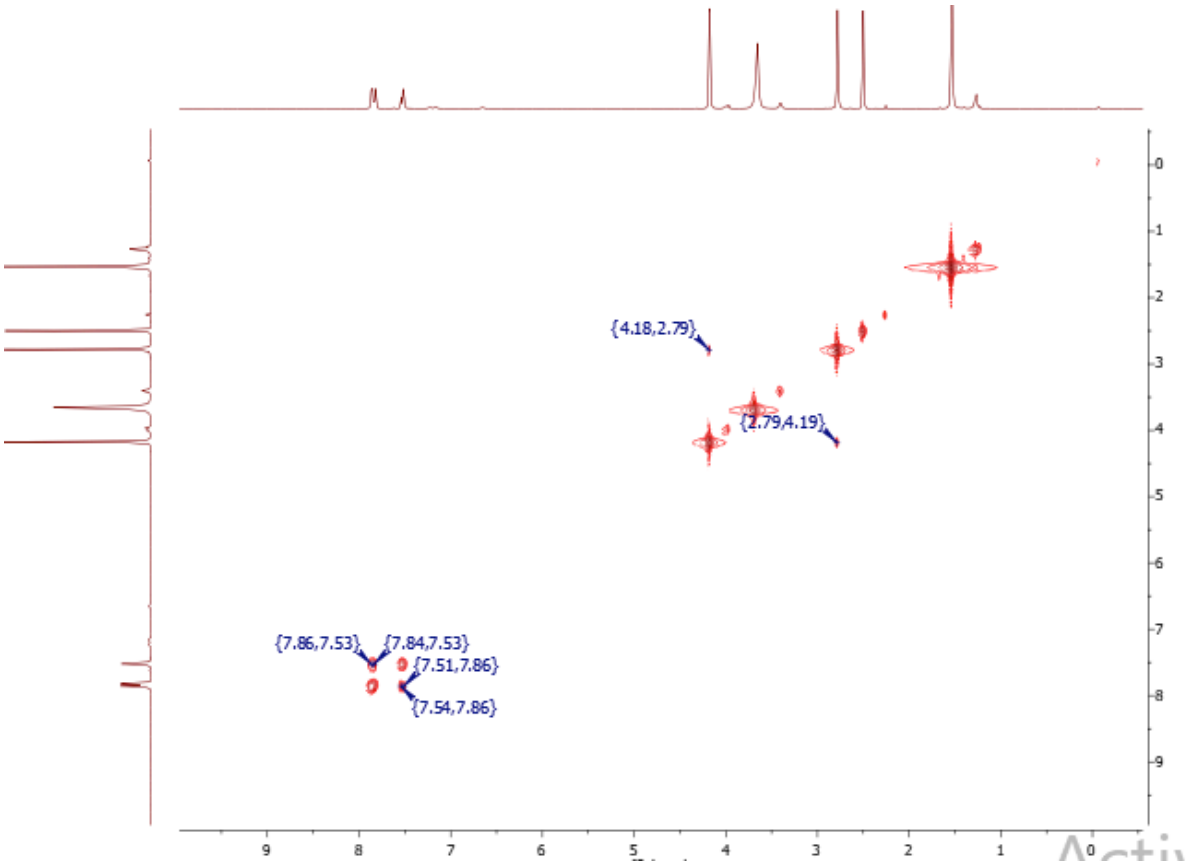

Appendix 2.23. ^{1}H-^{1}H COSY NMR Spectrum for **2.28a**.

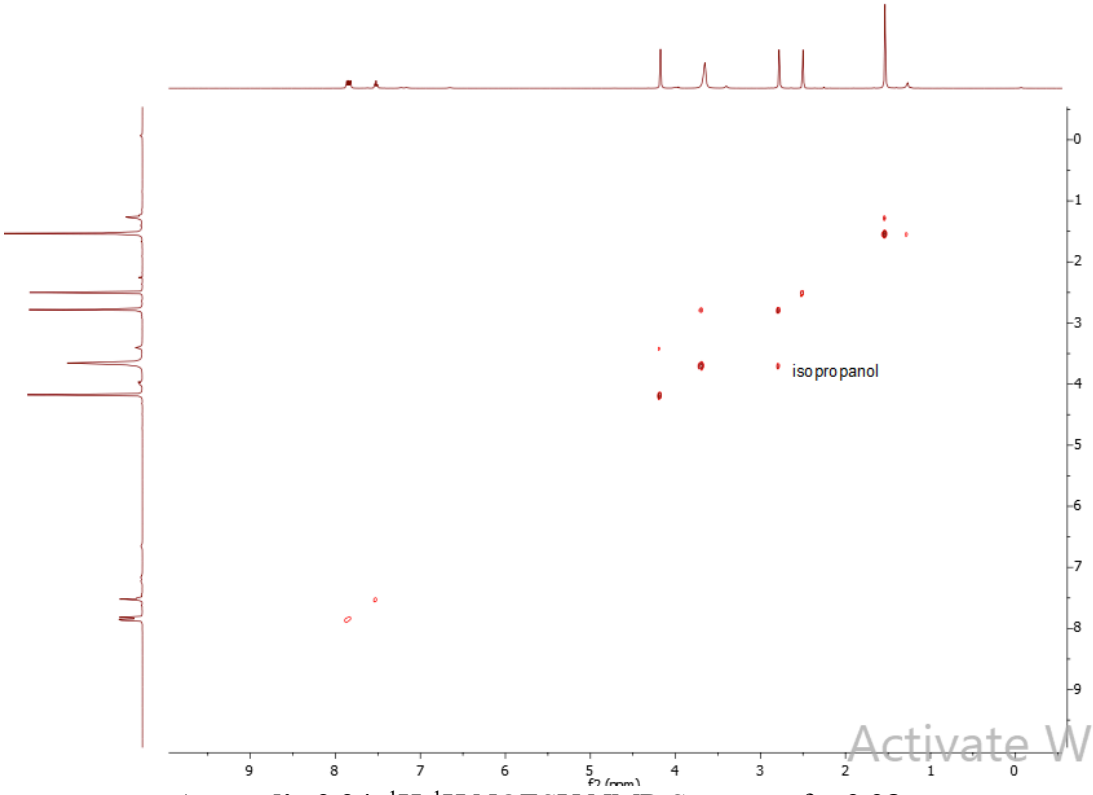

Appendix 2.24. ^{1}H-^{1}H NOESY NMR Spectrum for **2.28a**.

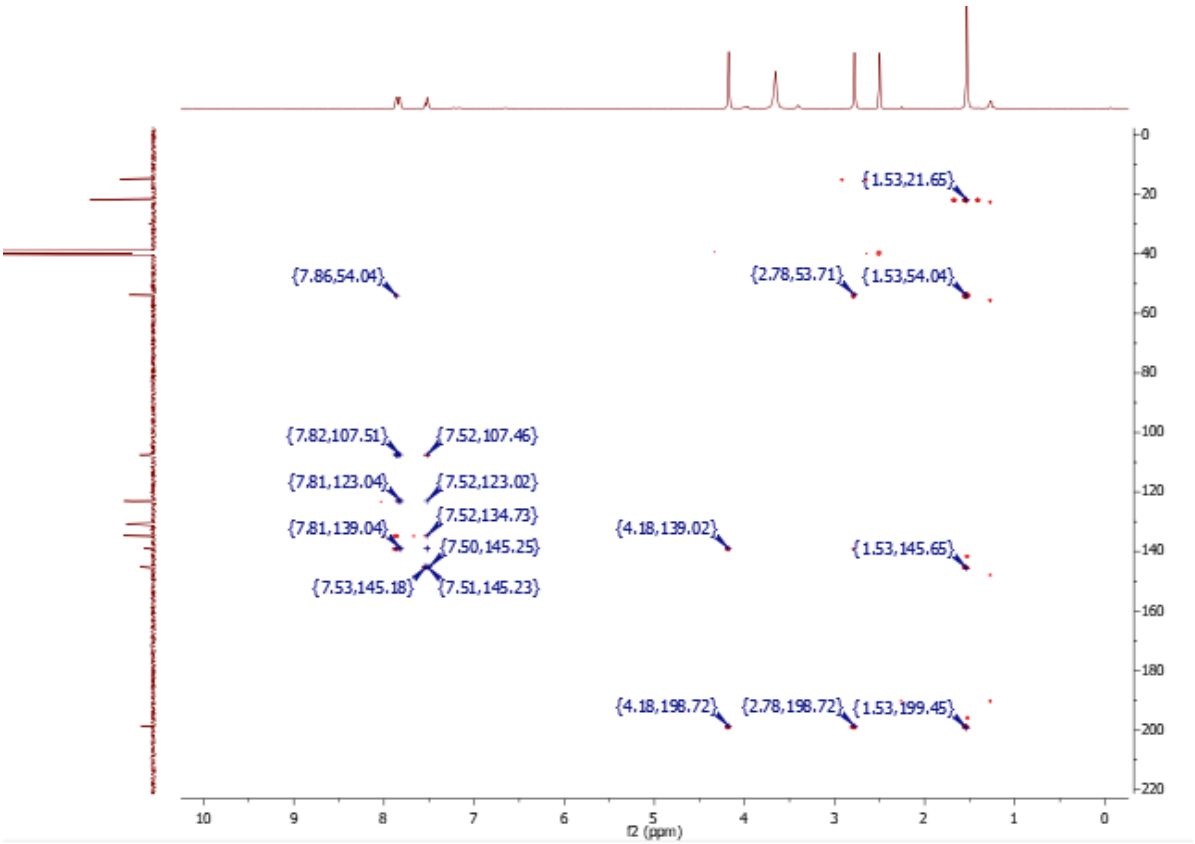

Appendix 2.25. ^{1}H-^{13}C HMBC NMR Spectrum for **2.28a**.

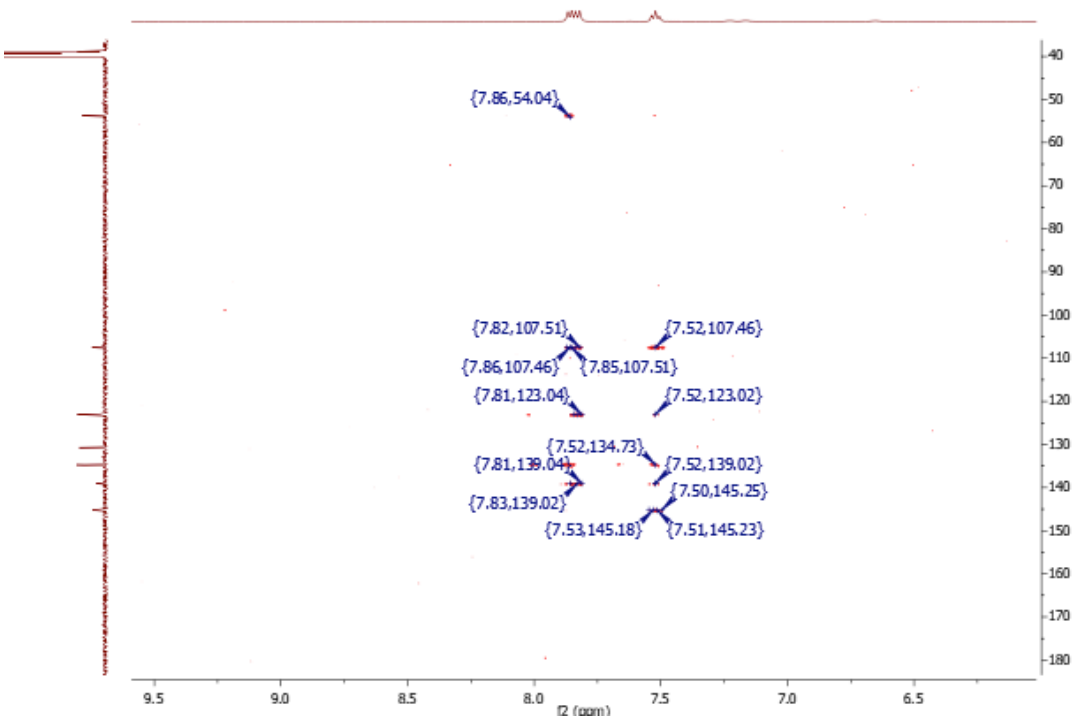

Blow-up HMBC **2.28a**.

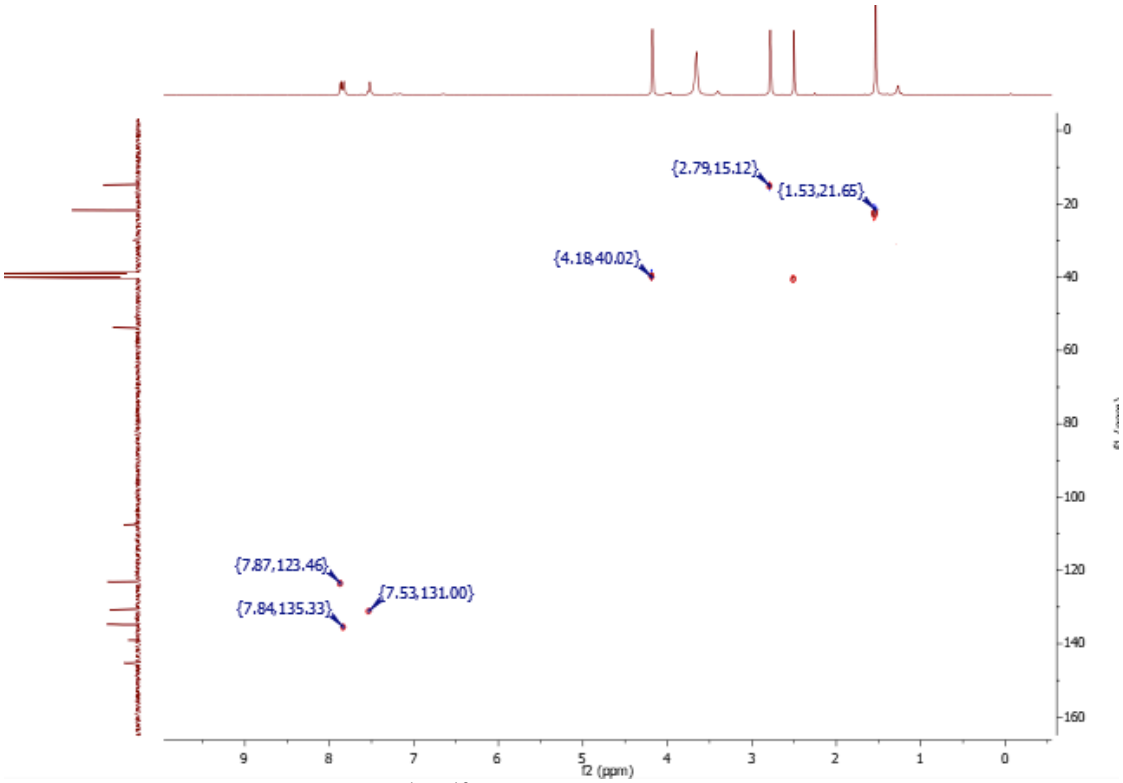

Appendix 2.26. ^{1}H-^{13}C HSQC NMR Spectrum for **2.28a**.

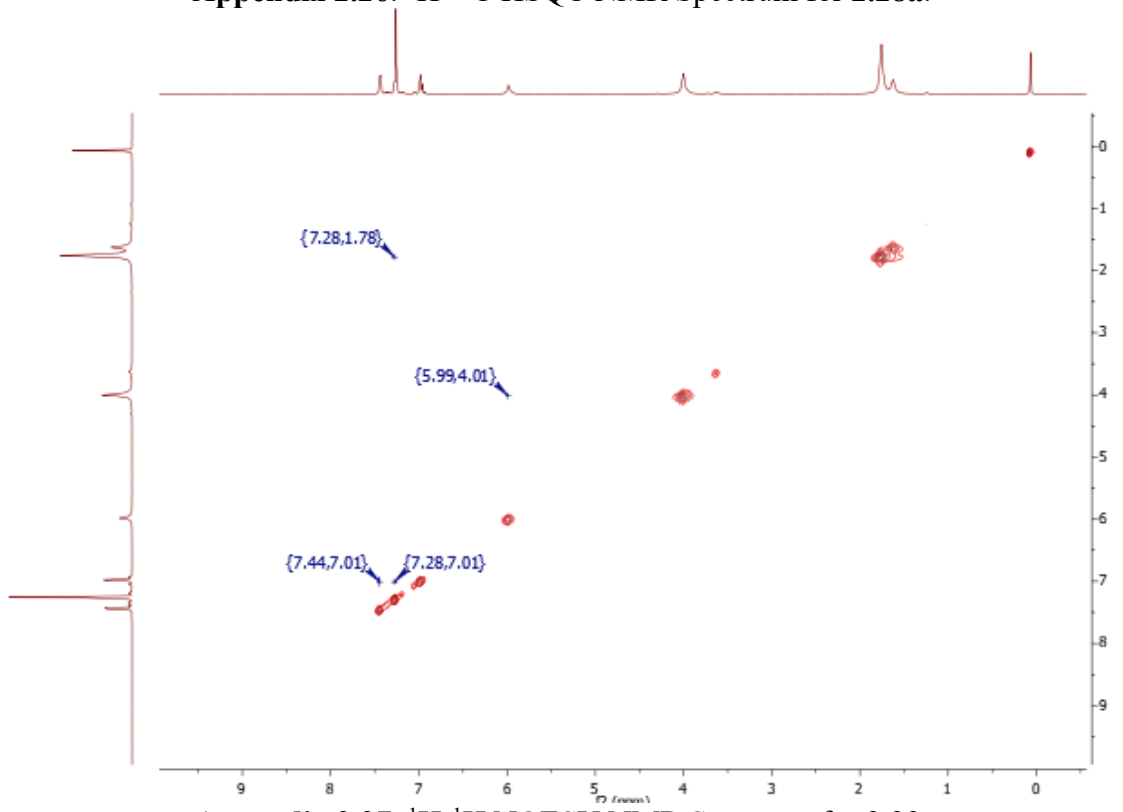

Appendix 2.27. ^{1}H-^{1}H NOESY NMR Spectrum for **2.29**.

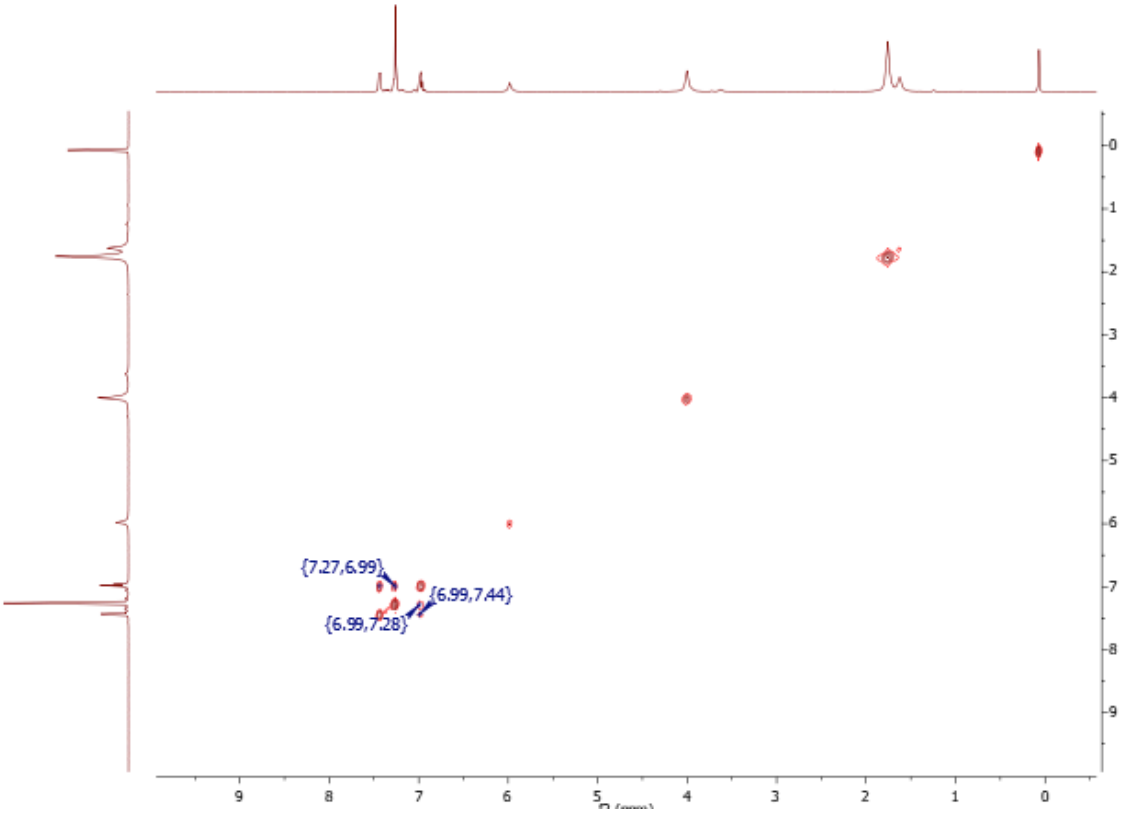

Appendix 2.28. ^{1}H-^{1}H COSY NMR Spectrum for **2.29**.

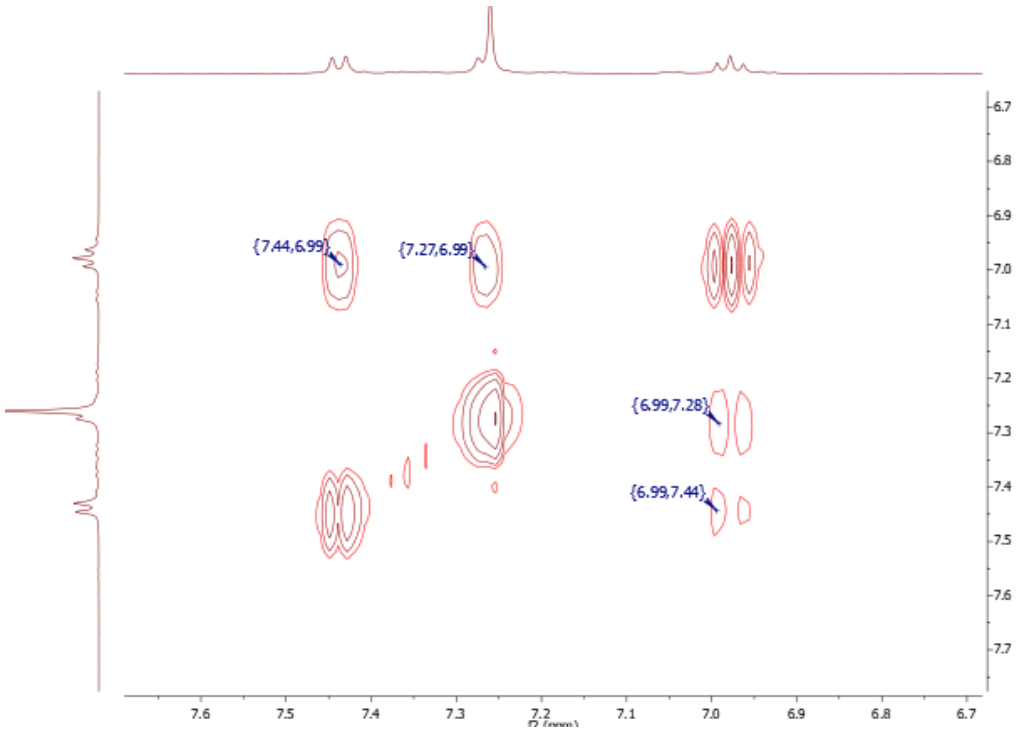

Blow-up COSY **2.29**

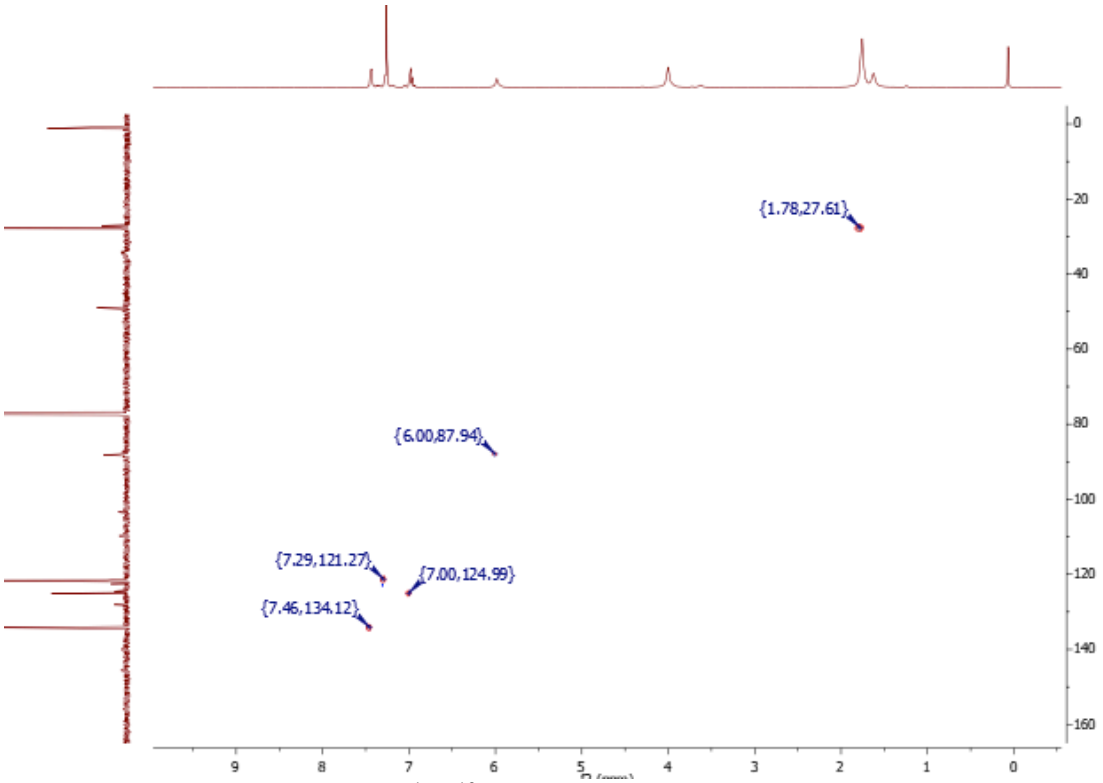

Appendix 2.29. ^{1}H-^{13}C HSQC NMR Spectrum for **2.29**.

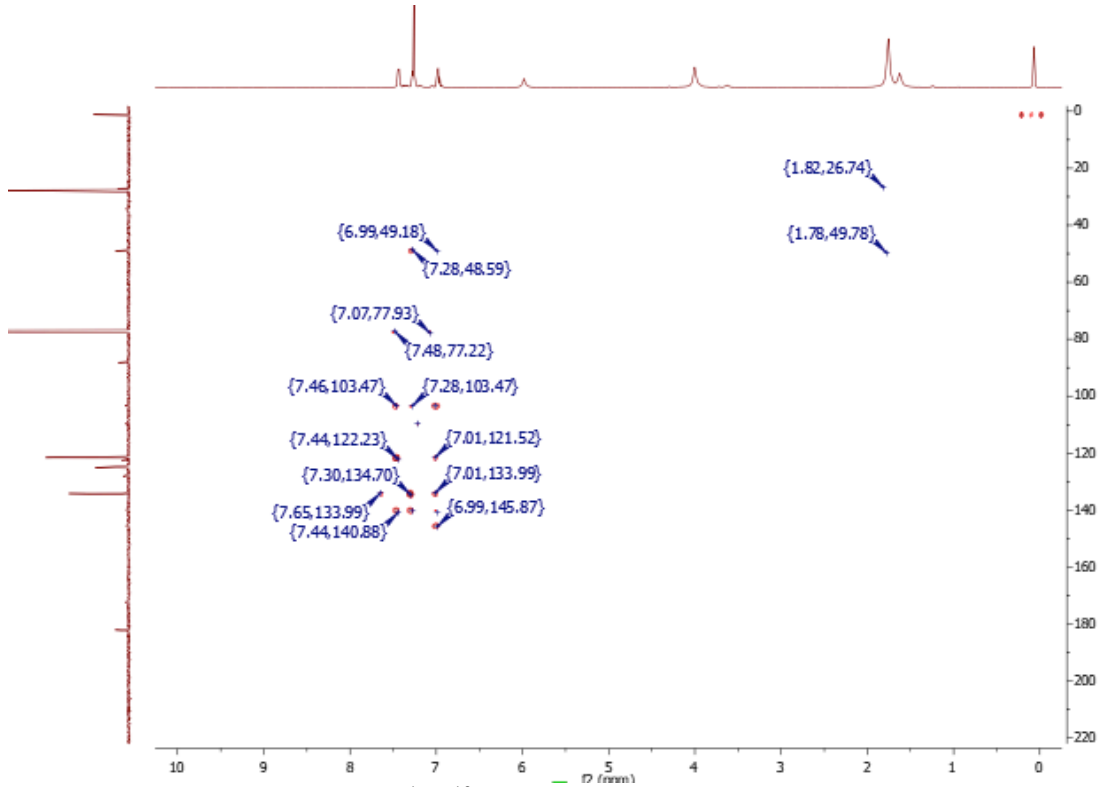

Appendix 2.30. ^{1}H-^{13}C HMBC NMR Spectrum for **2.29**.

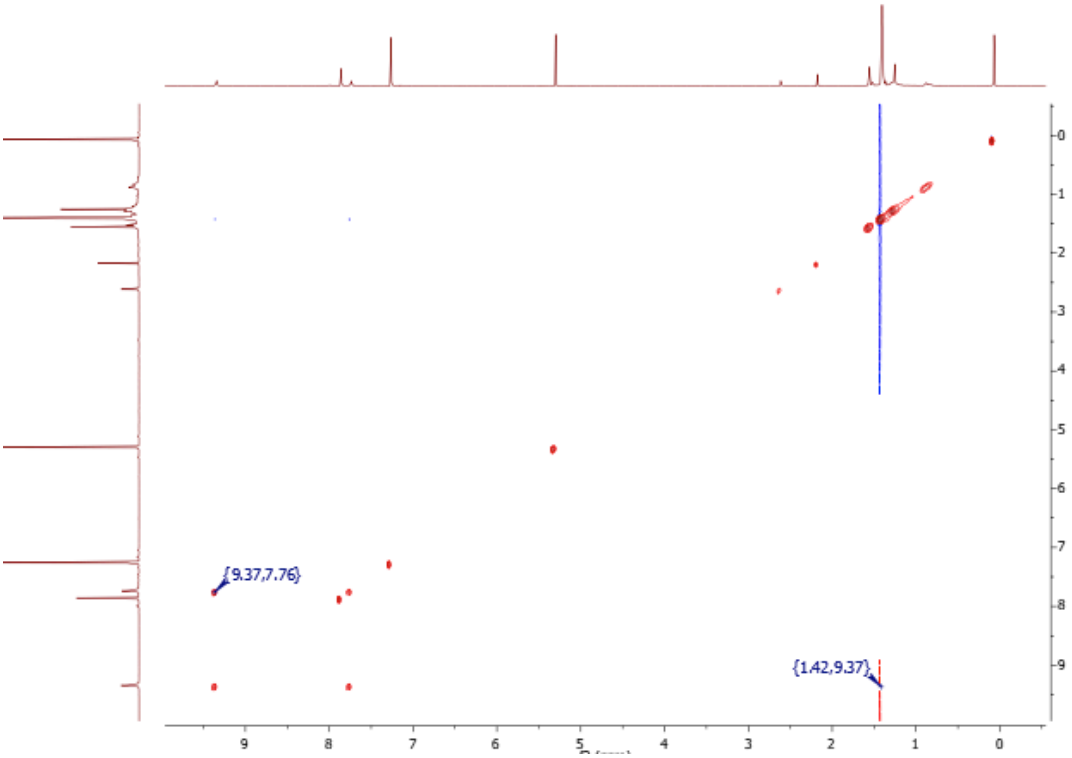

Appendix 2.31. ^{1}H-^{1}H NOESY NMR Spectrum for **2.36**.

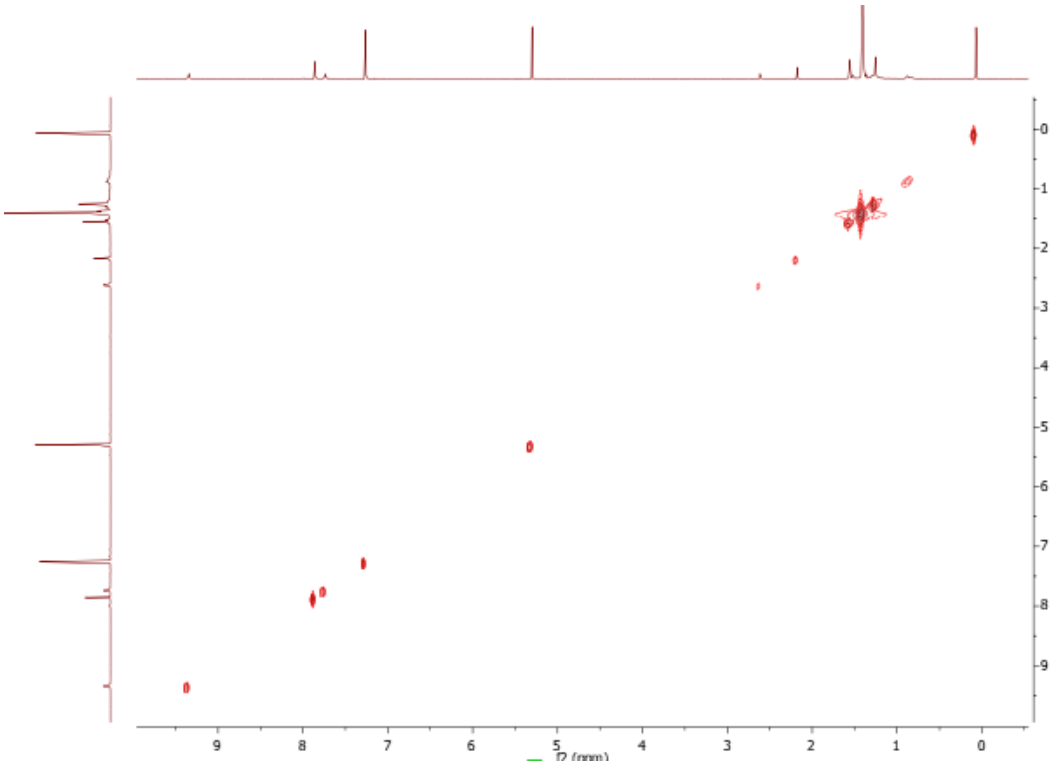

Appendix 2.32. ^{1}H-^{1}H COSY NMR Spectrum for **2.36**.

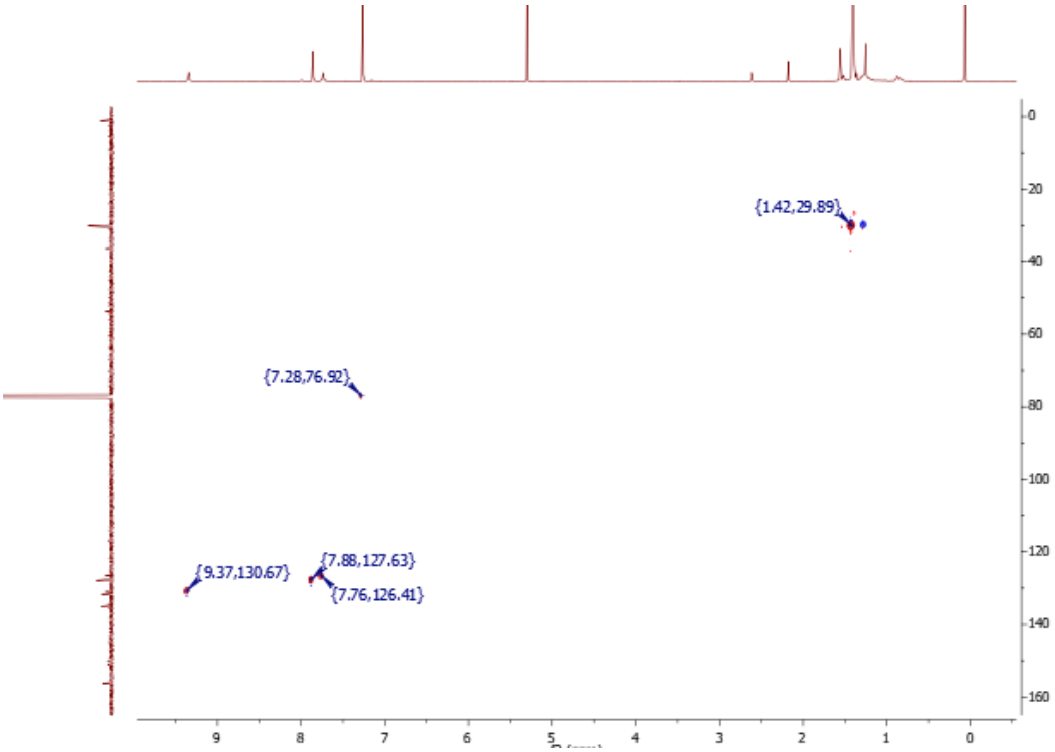

Appendix 2.33. ^{1}H-^{13}C HSQC NMR Spectrum for **2.36**

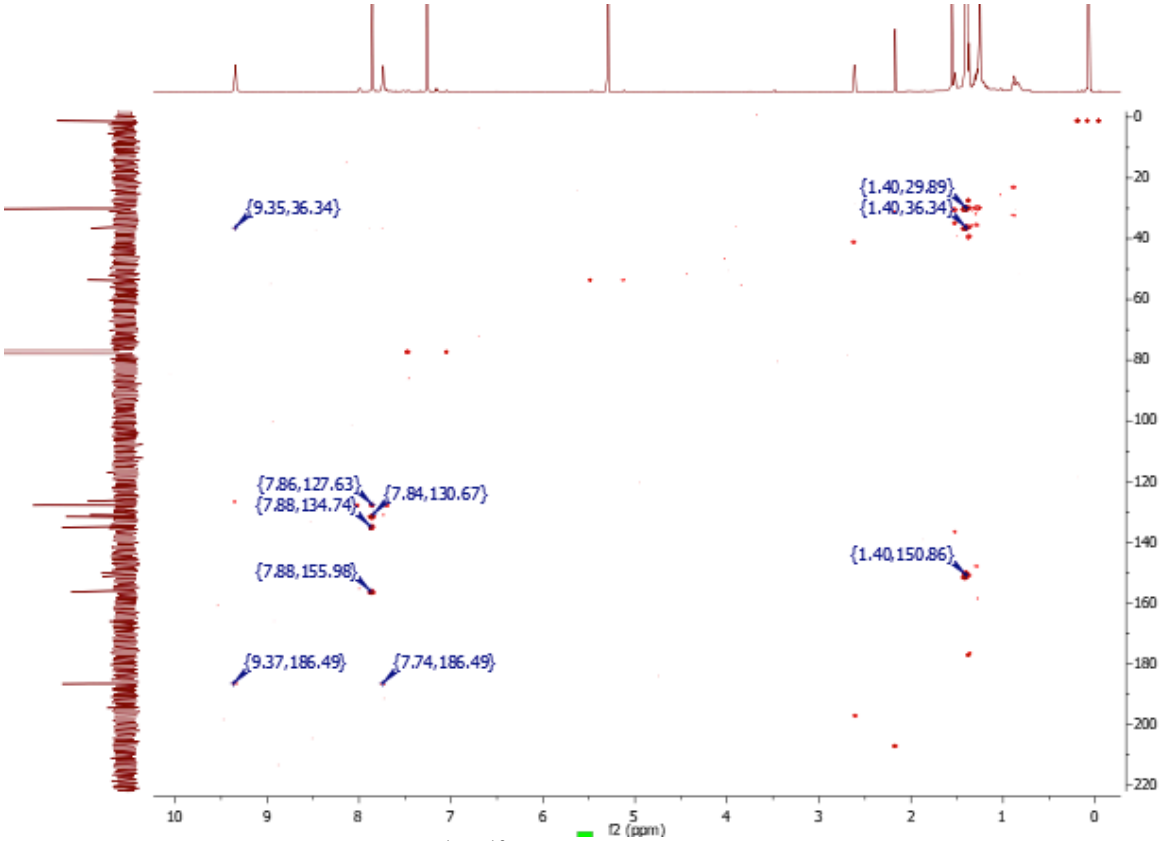

Appendix 2.34. ^{1}H-^{13}C HMBC NMR Spectrum for **2.36**

Appendix 3 UV-Visible spectroscopy, IR spectroscopy, and HRMS

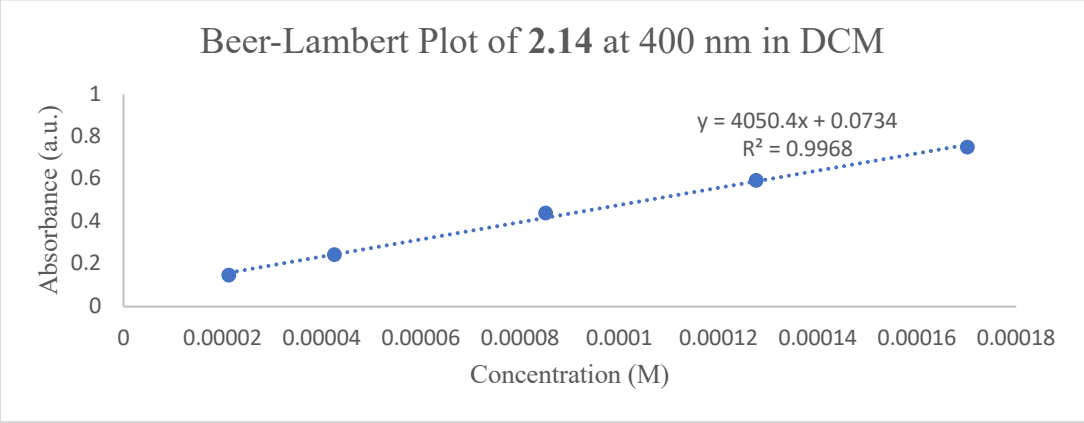

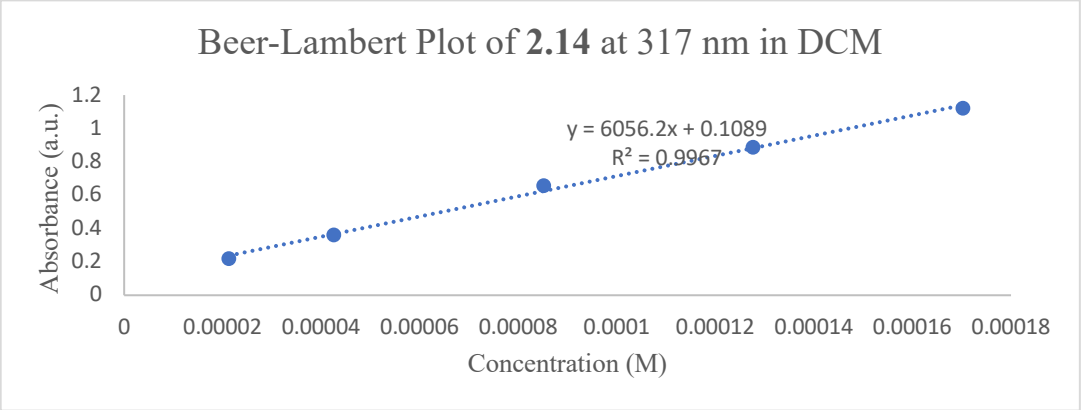

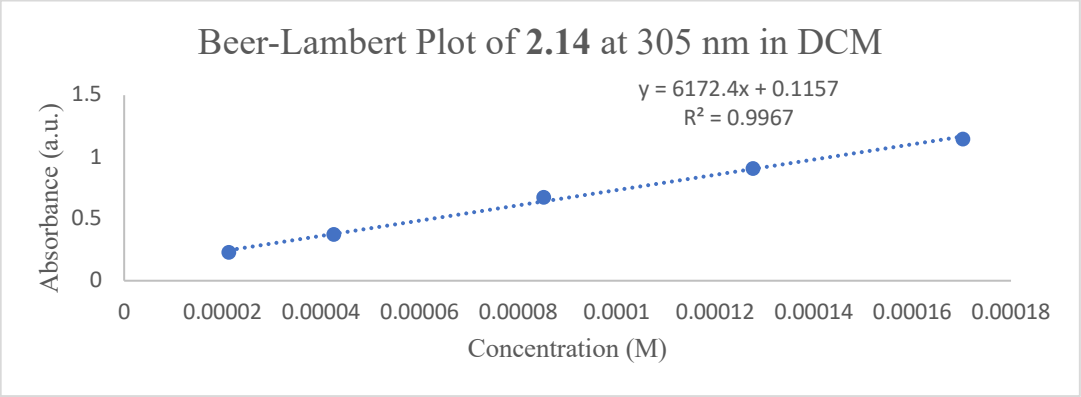

Appendix 3.01. Beer-Lambert plots for **2.14** in DCM.

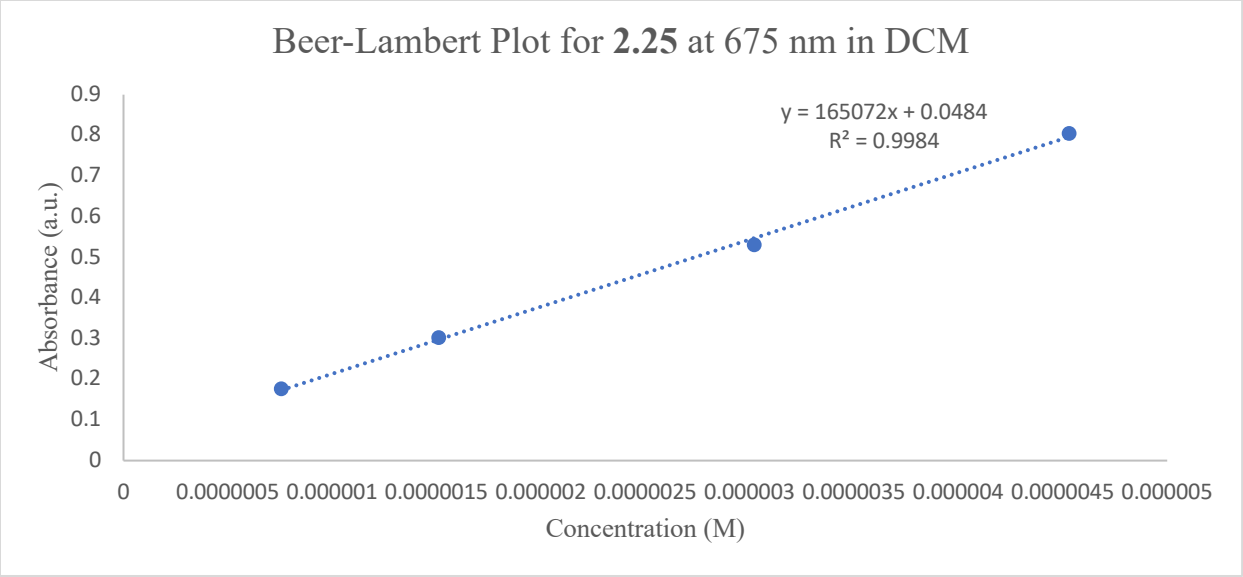

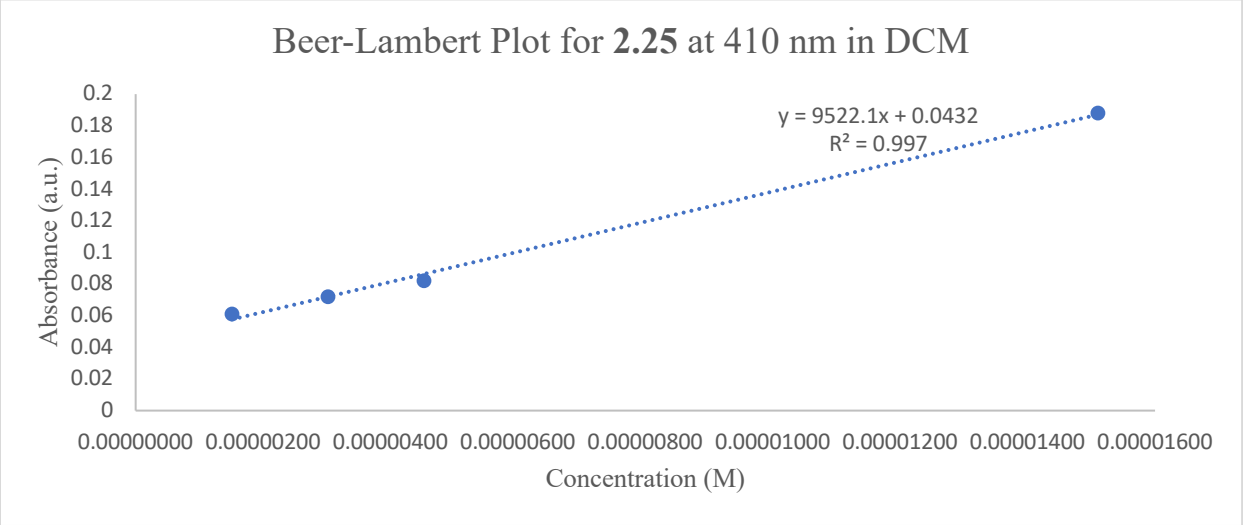

Appendix 3.02. Beer-Lambert plots for **2.25** in DCM.

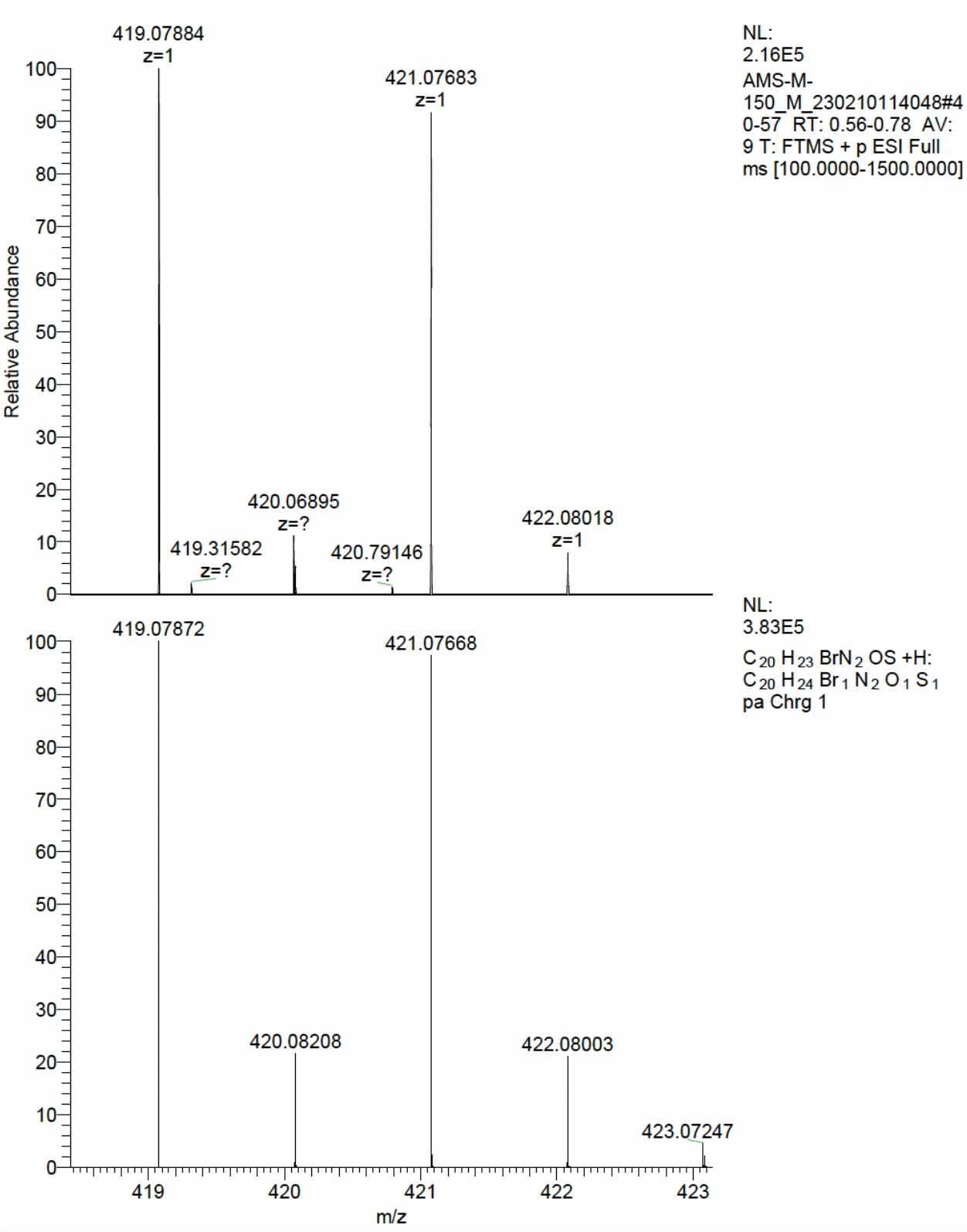

Appendix 3.03. HRESI-MS spectrum for **2.14**. Top – experimental; Bottom – Predicted

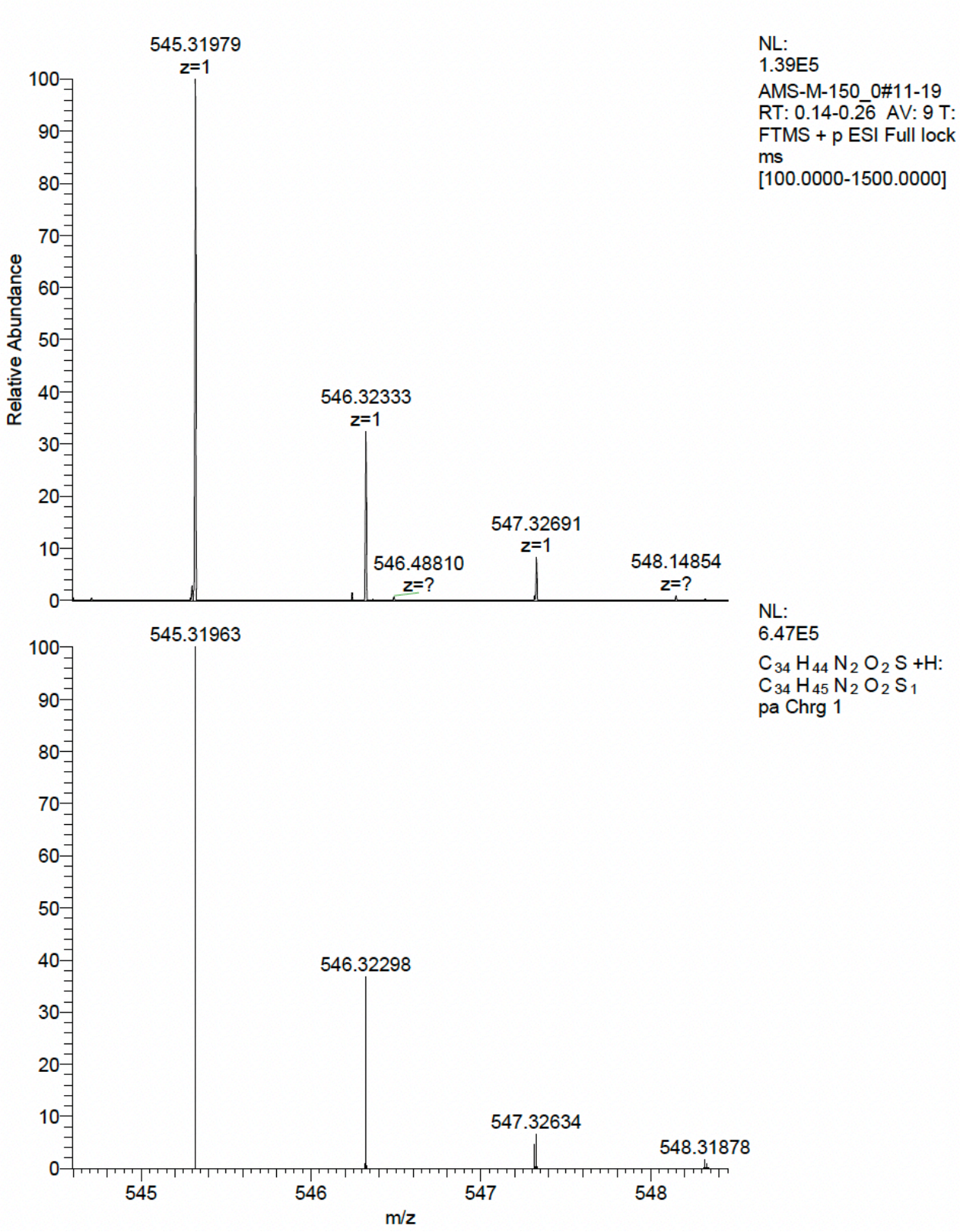

Appendix 3.04. HRESI-MS spectrum for **2.15**. Top – experimental; Bottom – Predicted

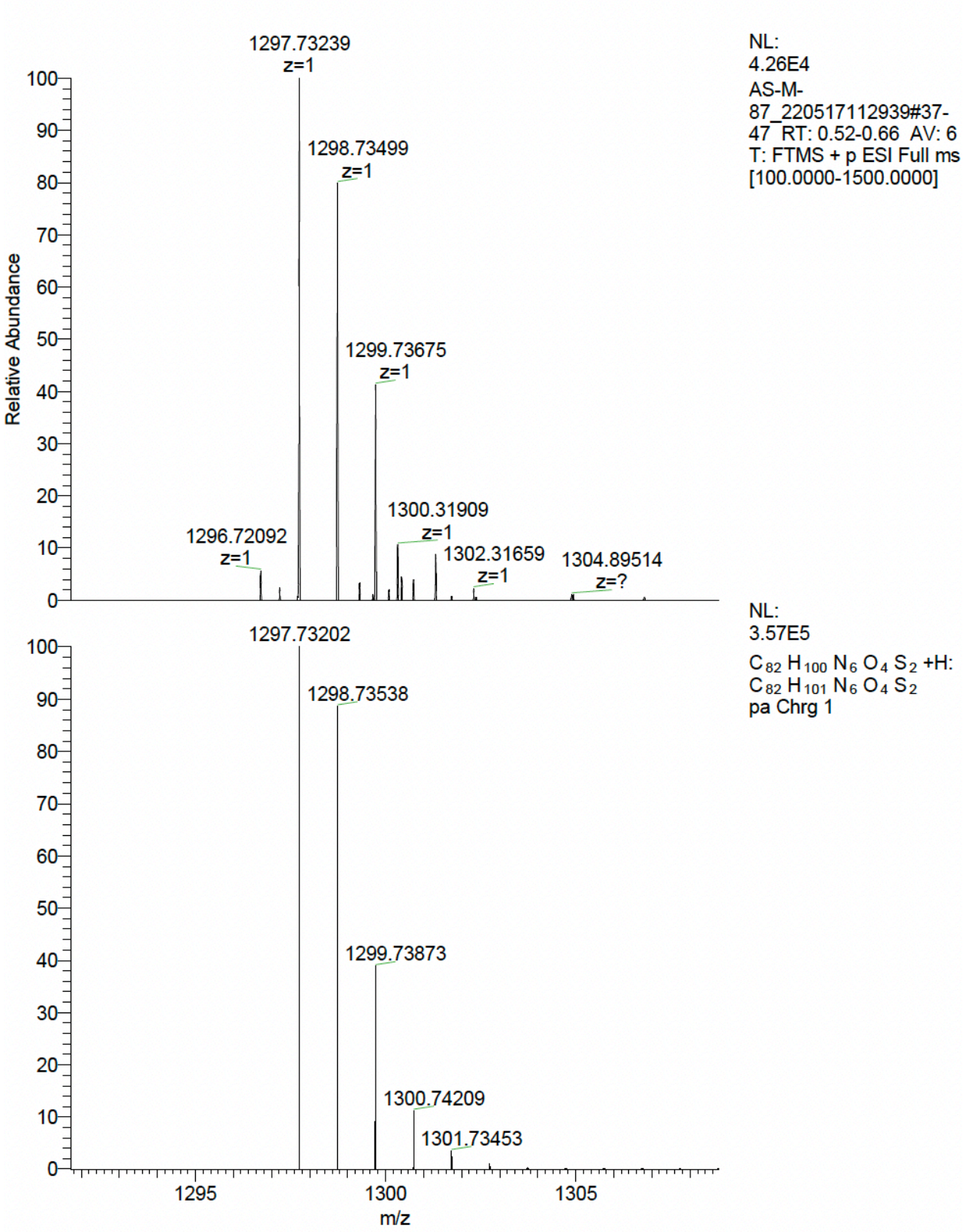

Appendix 3.05. HRESI-MS spectrum for **2.25**. Top – experimental; Bottom – Predicted

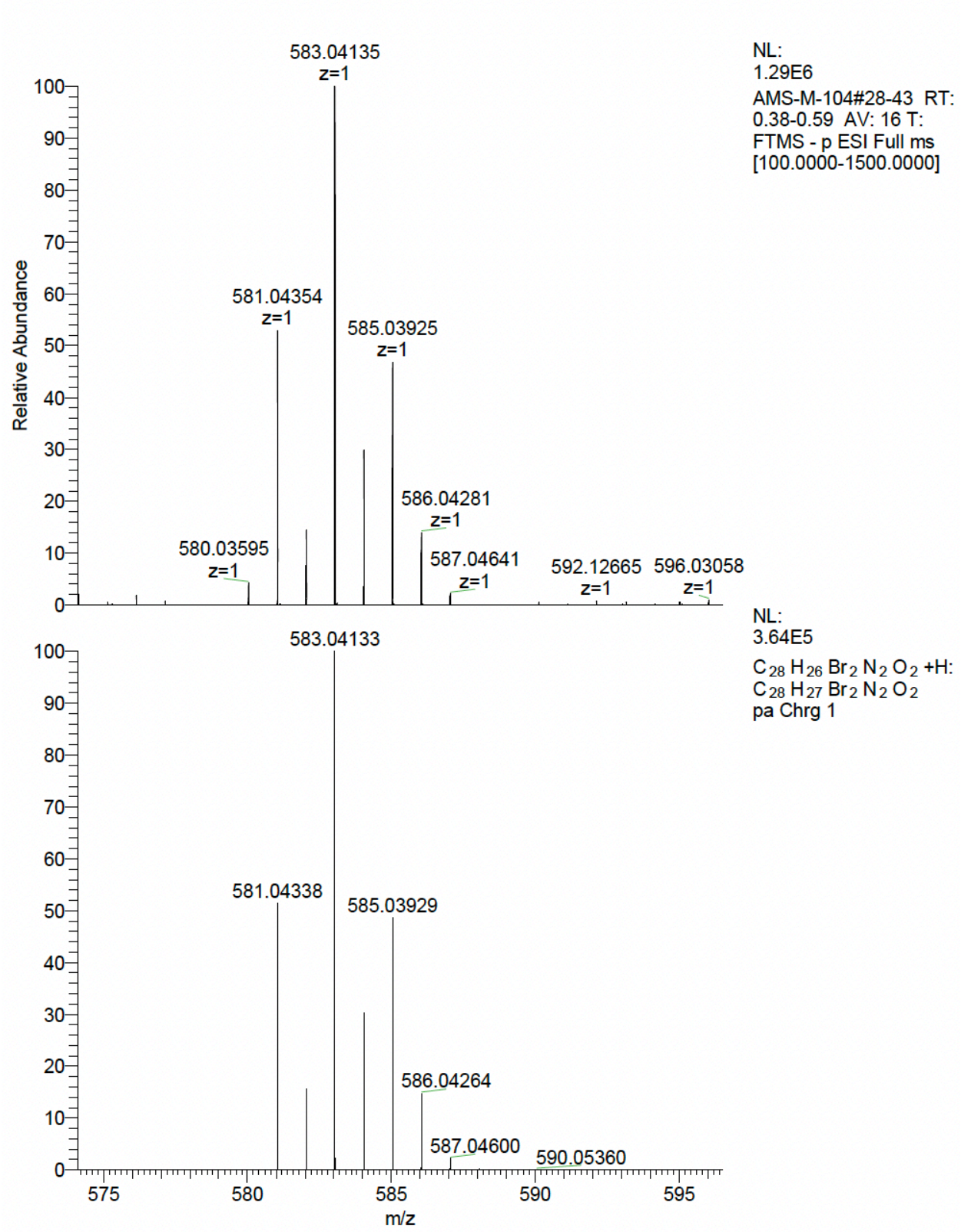

Appendix 3.06. HRESI-MS spectrum for **2.29**. Top – experimental; Bottom – Predicted

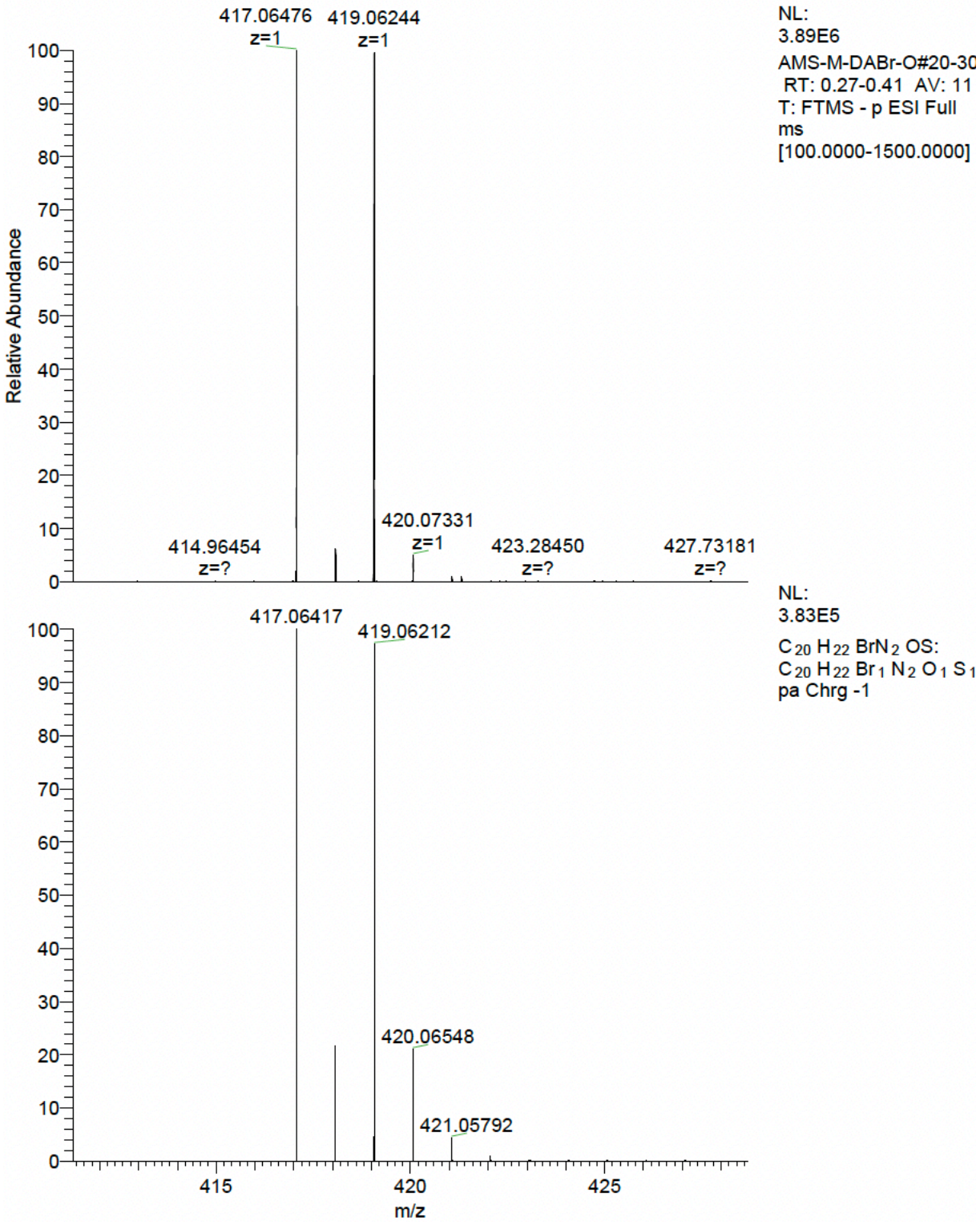

Appendix 3.07. HRESI-MS spectrum for **2.14-A**. Top – experimental; Bottom – Predicted

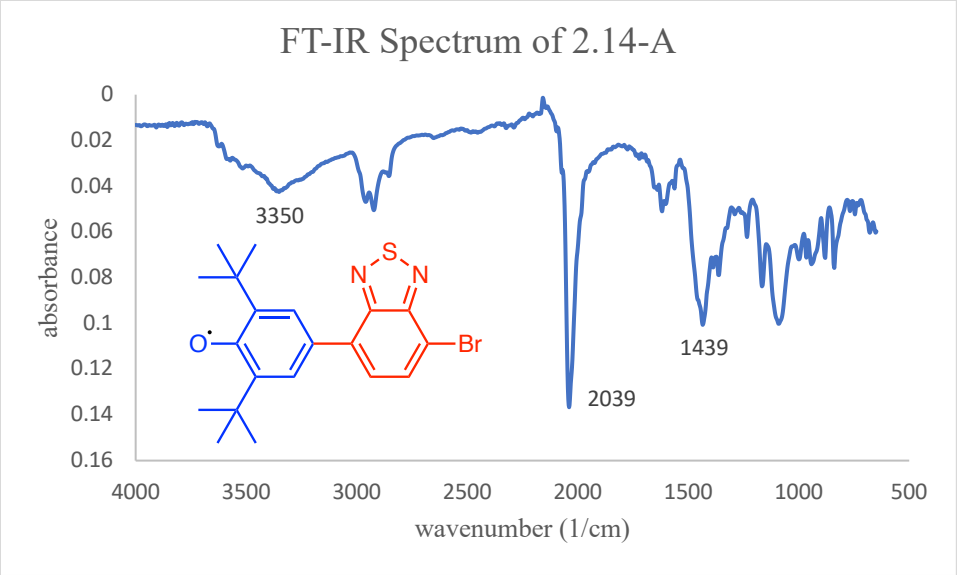

Appendix 3.08. FT-IR spectrum of **2.14-A**.

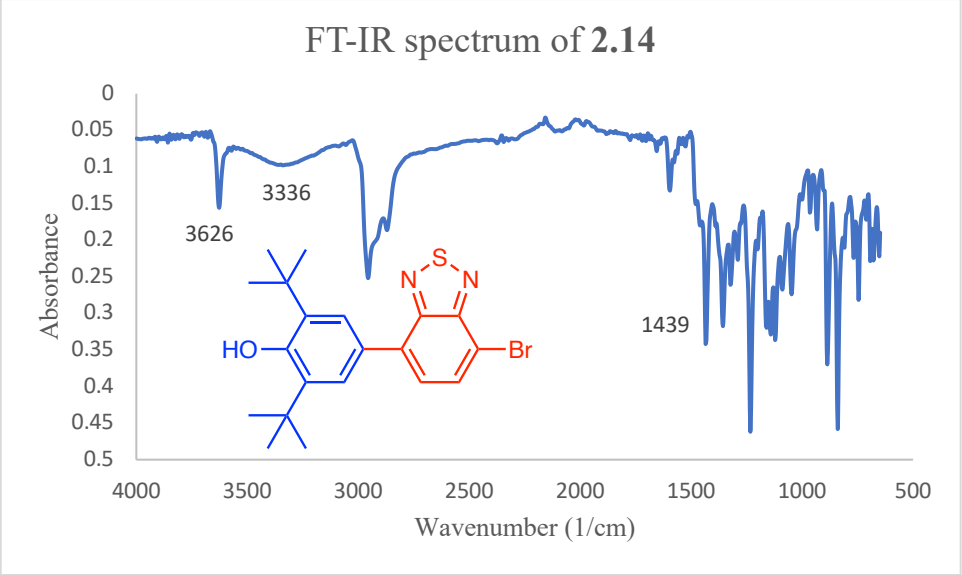

Appendix 3.09. FT-IR spectrum of **2.14**.

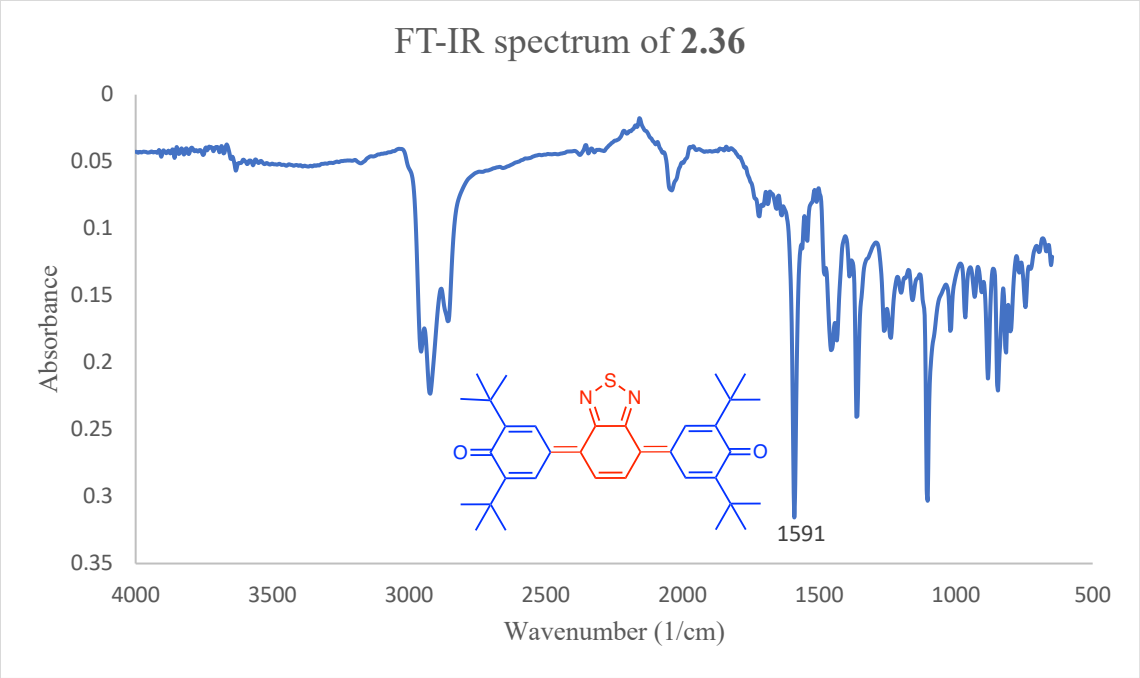

Appendix 3.10. FT-IR spectrum of **2.36**.

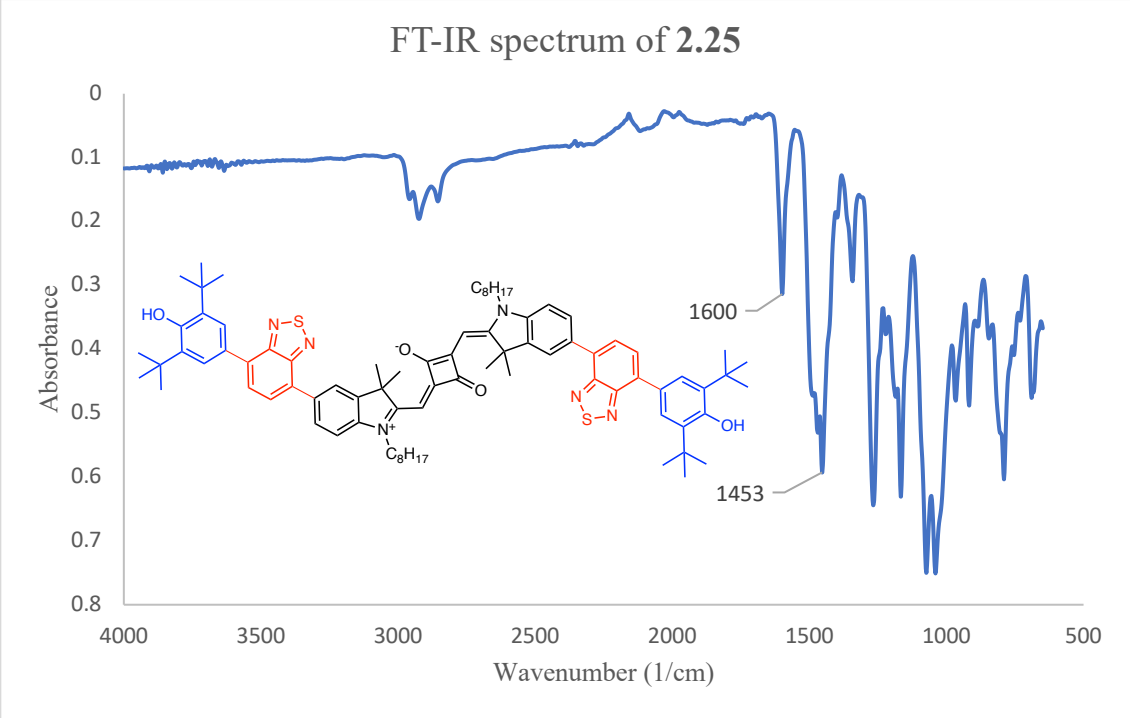

Appendix 3.11. FT-IR spectrum of **2.25** .